



HAL
open science

Non-invasive spline-based shape optimization strategies development for experimental mechanics

Morgane Chapelier

► **To cite this version:**

Morgane Chapelier. Non-invasive spline-based shape optimization strategies development for experimental mechanics. Mechanics of materials [physics.class-ph]. INSA de Toulouse, 2021. English. NNT : 2021ISAT0016 . tel-03610673

HAL Id: tel-03610673

<https://theses.hal.science/tel-03610673>

Submitted on 16 Mar 2022

HAL is a multi-disciplinary open access archive for the deposit and dissemination of scientific research documents, whether they are published or not. The documents may come from teaching and research institutions in France or abroad, or from public or private research centers.

L'archive ouverte pluridisciplinaire **HAL**, est destinée au dépôt et à la diffusion de documents scientifiques de niveau recherche, publiés ou non, émanant des établissements d'enseignement et de recherche français ou étrangers, des laboratoires publics ou privés.



THÈSE

En vue de l'obtention du
DOCTORAT DE L'UNIVERSITÉ DE TOULOUSE
Délivré par l'Institut National des Sciences Appliquées de
Toulouse

Présentée et soutenue par
Morgane CHAPELIER

Le 15 novembre 2021

**Développement de stratégies d'optimisation de forme non-
intrusives basées sur les splines pour la mécanique
expérimentale**

Ecole doctorale : **MEGEP - Mécanique, Energétique, Génie civil, Procédés**

Spécialité : **Génie mécanique, mécanique des matériaux**

Unité de recherche :
ICA - Institut Clément Ader

Thèse dirigée par
Jean-Charles PASSIEUX et Robin BOUCLIER

Jury

M. Thomas ELGUEDJ, INSA Lyon, *Rapporteur*
M. François HILD, ENS Paris-Saclay, *Rapporteur*
M. Ludovic CHAMOIN, ENS Paris-Saclay, *Président*
Mme Nathalie BARTOLI, ONERA, *Examinatrice*
Mme Pauline LECOMTE-GROSBRAS, Ecole Centrale de Lille, *Examinatrice*
M. Jean-Charles PASSIEUX, INSA Toulouse, *Directeur de thèse*
M. Robin BOUCLIER, INSA Toulouse, *Co-directeur de thèse*
Mme Sylvie TESTE, TopSolid, *Invitée*



Remerciements

Je garderai un excellent souvenir des trois années de thèse qui viennent de se terminer, ce que je dois aux personnes fantastiques que j'ai croisées de plus ou moins près pendant ces trois ans.

Mes premiers remerciements vont à mes directeurs de thèse Robin Bouclier et Jean-Charles Passieux. Merci pour ce sujet, tout d'abord, et votre aide précieuse pour lui faire prendre quelques virages sans embuches. Merci pour votre honnêteté, votre bienveillance et votre écoute, qui m'ont permis de me sentir en confiance. Merci pour votre disponibilité, qualité qui s'apprécie d'autant plus connaissant vos nombreuses autres responsabilités. Merci enfin pour votre pédagogie et vos bonnes idées, à la fois sur le fond scientifique et la façon de le présenter au mieux au reste de la communauté.

Je souhaite également remercier chaleureusement tous les membres de mon jury, en particulier Thomas Elguedj et François Hild, pour leur relecture attentive de mon manuscrit, leurs remarques, et les discussions intéressantes soulevées par leurs questions. Merci également à Ludovic Chamoin d'avoir présidé ce jury, à Nathalie Bartoli et Pauline Lecomte d'avoir amené leur expertise pour compléter ce jury, ainsi qu'à Sylvie Testé d'avoir représenté le monde industriel dans ce jury.

Si tout s'est bien passé pendant trois ans, c'est aussi et surtout grâce aux bureaux formidables que j'ai eus, et qui sont tous d'une gentillesse infinie. Au GMM, d'abord : merci Clément pour ta bonne humeur communicative et ton implication partout où tu vas ; merci Jessica pour la force inspirante que tu dégages et ta sincérité ; merci Alban pour ta sympathie et le plaisir que tu as à aider autour de toi ; et merci Cyriel de nous avoir accueillis à bras ouverts dans le bureau 120 avec énormément d'amabilité. C'était très agréable de partager votre bureau, et merci également à tous les quatre pour vos réponses claires à mes questions de maths pas toujours claires. A l'ICA, ensuite : merci Guillaume pour ta bienveillance, merci de nous avoir appris ce que tu savais sur le fonctionnement du labo, et j'ai été heureuse que nos travaux réunis puissent mener à une publication ; et merci Ali pour à peu près tout, des morceaux de code spline aux quelques séances de sport/balade/jardinage/cuisine, en passant par les questions de méca ou de maths, toujours souriant et avec un altruisme incroyable. Les derniers moments avant Covid auront été des chouettes moments avec vous dans le bureau BR2030.

En-dehors du bureau, je tiens à remercier les autres doctorants / post-docs / ATER / ingés de l'ICA, en particulier les habitués du resto de l'IAS, et ceux qui ont fait et font vivre le laboratoire, par leurs actions ou simplement par leur présence, leur soutien et leur bonne humeur : merci Simon V., Adeline, Adama, Thibaut, Julien, Alexandra, Tohme, Louis, John-Eric, Yohan, Edouard, Charles, Malo, Sabine, Khouloud, Guillermo, Evgeniia, Marie, Noémie, Jim, Simon E.,

Renaud, Florent... Malheureusement, le Covid et la fermeture de l'IAS font que je connais moins les doctorants plus jeunes mais je leur souhaite de créer plein d'évènements sympas au labo. Du côté des permanents, un grand merci Jean-Noël pour la team image (dont je remercie tous les membres), Luchon et tes histoires passionnantes ; merci Philippe pour l'organisation des 10 ans de l'ICA, les JPO, ton entrain et tes idées pour faire du labo un espace plus convivial ; merci Paul et merci Eduard pour nos échanges intéressants, scientifiques ou non. Et merci Valérie, Myriam et Marie-Odile de nous accompagner aussi bien.

J'aimerais souligner aussi l'ambiance chaleureuse et presque familiale qui règne au GMM. Je salue notamment l'entente et l'entre-aide entre tous, quel que soit le statut. Merci particulièrement aux passionnés et passionnants Fred et Aude pour m'avoir permis de mieux comprendre l'optimisation, et également à Firas, Léo, Jean-Yves, Sandrine B., Marlène, Anthony, Béatrice, Violaine, Romain, Lorick, Sandrine, Loïc, Mélisande, Olivier M., Olivier R., Géraldine, Sandrine S., Adeline, Cathy, Florent, Laure, Aldéric, David, Charles, Simona, Pascal...

Du côté de l'école doctorale, je souhaite remercier Kamila Koziura grâce à qui tout le côté administratif de la thèse s'est passé sans accroc.

Je dois également remercier mes amis Cachanais, en particulier Ronan, David, Willy et Kévin pour leurs mails dignes de Molière et de Stéphane de Groodt qui à chaque fois m'ont donné la pêche pour le reste de la journée, mais aussi Clotilde, Roméo, Jean, Filippo, Déborah et ceux qui ont pris ou donné des nouvelles, ce qui fait toujours plaisir. Pour les mêmes raisons, je remercie aussi des amis de prépa et d'avant qui me sont toujours chers aujourd'hui : Amicie, Léa, Lucie, Mathilde, JB, Antonin, Maxime, Solange, Elsa...

Enfin, un grand merci à ma famille et celle de Raphaël pour votre soutien pendant ces trois ans. Et merci Raphaël ; j'aurais pu te citer presque à chaque paragraphe, car en tant que cobureau, tu m'as aidée à résoudre bien des problèmes, et à l'ICA tu t'es fortement investi pour organiser des choses sympa comme les olympiades, pour ne citer que ça. Et alors que tu menais souvent plusieurs tâches importantes en parallèle, tu as toujours été là pour moi et pour embellir mes journées. Pour tout ça, merci infiniment.

Résumé

Abstract

Non-invasive spline-based shape optimization strategies development for experimental mechanics

Keywords: B-spline reduced basis, Free-Form Deformation, Multilevel design, Non-invasive implementation, Digital Image Correlation, Material constitutive parameters identification.

Digital Image Correlation (DIC) techniques have spread widely over the last few decades. They allow performing full-field measurements, which serves several purposes in the experimental mechanics domain, typically to measure shapes, displacement fields or to identify material constitutive parameters on mechanical specimens. However, obtaining an accurate measured field is not straightforward, as it comes from the resolution of an ill-posed inverse problem. Setting an approximation subspace for the solution field is thus necessary. Among other choices, the Finite Element (FE) space allows for a direct coupling between the measured field and the simulated one, by using the same mesh for both fields. Yet, fine meshes, which ensure good simulation results, may lead to irregular noisy measured fields because of the ill-posedness of the problem. Generally, a Tikhonov regularization, based on the addition of a penalization term, is used, but this technique tends to alter parts of the true solution. Interestingly, structural shape optimization brings comparable concerns. To avoid getting unrealistic geometries, the use of FE degrees of freedom as design variables for shape optimization has soon been replaced with the use of coarser, smoother tools such as CAD models, which imply the use of spline functions. Several methods, such as multilevel strategies, or the use of Free-Form Deformation (FFD) spline morphing boxes, have been developed in the shape optimization domain to improve the optimization process. In this work, we draw inspiration from shape optimization to regularize several optimization problems in experimental mechanics, such as displacement measurement, shape measurement and also the improvement of the specimen shape to minimize identification uncertainties. Linking the FE space to the spline space, we propose a non-invasive regularization for DIC problems, based on the use of a well-chosen projection, first on a boundary-fitted (analysis-suitable) CAD model of the specimen, then extending the method to any geometry described with an arbitrary FE mesh thanks to a morphing box. A multilevel procedure is used by coupling coarse graining in DIC with the refinement properties of splines functions. Solutions are proposed to tackle conditioning issues occurring with the FFD method by handling non-influential control points, and a novel procedure based on additional projections over local directions complements the FFD method for full efficiency in 3D mesh-based shape measurement. The proposed method was successfully applied to real images coming from experimental tests and compared to the commonly used Tikhonov regularization.

The developed tools are then used to optimize the fine (FE) description of the geometry of a pre-existing specimen with very few design variables in order to improve the identification of constitutive parameters. Morphing boxes are adapted to ensure that all design variables are useful, and mesh deformation propagation is carried out to avoid remeshing at each geometry update. A specific care is taken to define a cost function and constraint functions guaranteeing that the improved specimen geometry is physically sound and adapted to the associated mechanical experiment. Attention is also paid to the effect of boundary conditions on the constitutive parameters sensitivity. Eventually, the developed algorithm is validated on a simple traction beam and then applied to a more complex specimen to identify several parameters at once, leading to a significant reduction of the identification uncertainty.

Résumé court

Développement de stratégies d'optimisation de forme non-intrusives basées sur les splines pour la mécanique expérimentale

Mots-clés : Base réduite B-spline, Free-Form Deformation, Design multiniveaux, Implémentation non-intrusive, Corrélation d'Images Numériques, Identification de paramètres matériau.

Les techniques de Corrélation d'Image Numérique (CIN) se sont largement répandues ces dernières décennies. Elles permettent de réaliser des mesures de champs complets, et ont diverses utilisations en mécanique expérimentale, par exemple pour la mesure de forme, de champ de déplacement, ou l'identification de paramètres de comportement de matériaux sur des éprouvettes mécaniques. Cependant, l'obtention du champ mesuré n'est pas immédiate et vient de la résolution d'un problème inverse. Il est alors nécessaire de choisir l'espace de recherche du champ solution. Entre autres, le sous-espace vectoriel des champs Eléments Finis (EF) permet un couplage direct entre un champ mesuré et un champ simulé, grâce à l'utilisation du même maillage pour les deux champs. Toutefois, les maillages de simulation, assez fins, peuvent conduire à la mesure de champs irréguliers à cause du caractère mal-posé du problème à résoudre. En général, une régularisation de Tikhonov est utilisée (ajout d'un terme de pénalisation), mais cette technique a tendance à altérer certaines parties de la vraie solution. Il est intéressant de constater que le domaine de l'optimisation de forme traite de préoccupations similaires. En effet, pour éviter d'obtenir des géométries non réalistes, l'utilisation de degrés de liberté (ddl) EF a rapidement fait place à l'utilisation d'outils plus réguliers avec moins de ddl, comme les modèles CAO, qui font intervenir des fonctions splines. Différentes méthodes ont ensuite été développées dans la communauté d'optimisation de forme pour améliorer le processus d'optimisation, comme des stratégies multi-niveaux, ou l'utilisation d'enveloppes splines FFD (de l'anglais Free-Form Deformation). Dans cette thèse, nous nous inspirons des stratégies d'optimisation de forme pour régulariser trois problèmes d'optimisation en mécanique expérimentale : la mesure de champ de déplacement, de forme, et l'amélioration de la forme d'une éprouvette mécanique pour minimiser des incertitudes d'identification. En CIN, un lien entre l'espace EF et l'espace spline permet de proposer une régularisation non-intrusive basée sur une projection bien choisie, d'abord sur un modèle CAO de l'éprouvette, adapté à l'analyse, puis en généralisant la méthode à n'importe quelle géométrie décrite par un maillage EF quelconque, grâce à une enveloppe FFD. Une procédure multiniveau couplant une stratégie d'agrégation de pixels avec les propriétés de raffinement des fonctions splines est utilisée. Des solutions sont pro-

posées pour résoudre les problèmes de conditionnement survenant avec la méthode FFD en gérant les points de contrôle non influents, et une nouvelle procédure de projections supplémentaires sur des directions locales complète avantageusement la méthode FFD pour la mesure de forme sur un maillage 3D. La méthode proposée a été appliquée avec succès à des images réelles issues d'essais expérimentaux et comparée à la régularisation de Tikhonov, qui est la plus couramment utilisée. Les outils développés sont ensuite utilisés pour optimiser la description fine (EF) de la géométrie d'une éprouvette préexistante, avec peu de variables de design afin d'améliorer l'identification des paramètres matériau. Les enveloppes FFD sont adaptées pour que toutes les variables de design soient utiles, et une propagation de la déformation du maillage permet d'éviter le remaillage à chaque itération. Un soin particulier est apporté à la définition de la fonction coût et des fonctions contraintes, garantissant que la géométrie finale de l'éprouvette est physiquement acceptable et est adaptée à l'essai mécanique associé. L'effet des conditions aux limites sur la sensibilité aux paramètres matériau est également traité. Enfin, l'algorithme développé est validé sur une poutre simple en traction, puis appliqué à une éprouvette plus complexe dans le but d'identifier plusieurs paramètres à la fois, menant à une réduction significative de l'incertitude sur les paramètres identifiés.

Résumé long en français

La langue choisie pour la rédaction de ce manuscrit étant l'anglais, voici un résumé plus long, en langue française, de son contenu. Ce résumé vient compléter le résumé court.

Dans ce manuscrit, nous montrons le potentiel des fonctions splines dans le cadre de trois problèmes d'optimisation : la mesure de champs de déplacement Eléments Finis (EF) par Corrélation d'Images Numériques (CIN), la mesure de forme 3D basée sur des maillages EF par stéréo-CIN, ainsi que l'optimisation de forme d'une éprouvette mécanique vis-à-vis de l'identification de paramètres de comportement de matériaux.

Le premier chapitre, à travers une revue de la littérature, présente les trois problèmes d'optimisation et identifie certains de leurs verrous. Pour la CIN basée sur les EF (CIN-EF), l'utilisation de maillages EF adaptés à l'analyse (*analysis-suitable FE meshes* en anglais), nécessaire pour le couplage direct avec des logiciels de simulation EF, génère des résultats bruités, autant pour la mesure de forme que de champs de déplacement. Ce bruit vient du trop grand nombre de nœuds EF (et donc de variables de design) par rapport à la quantité de données, et de la faible régularité entre éléments EF. Pour le problème d'optimisation de forme de l'éprouvette mécanique, l'optimisation paramétrique n'offre qu'un faible éventail de géométries. De l'autre côté, l'optimisation topologique (en particulier celle basée sur la méthode SIMP) nécessite de faire un choix (fastidieux) de paramètres de pénalisation, et de procéder à une étape de post-traitement avant d'obtenir une géométrie qui ait un sens physique, et ce à cause d'un trop grand nombre de variables de design et de la faible régularité des bords obtenus. Dans tous les cas étudiés, les défauts rencontrés viennent de la trop grande dimension de l'espace de recherche, ainsi que des fonctions de base de cet espace qui ne sont pas suffisamment régulières. Les fonctions splines sont parfaitement appropriées pour résoudre ces problèmes. Leur grande régularité, ainsi que leurs autres propriétés comme leur support local et leurs procédures automatiques de raffinement, sont idéales dans le cadre de l'optimisation de forme, et de manière générale dans tout problème

d'optimisation régulier. De plus, elles forment un sous-espace vectoriel de l'espace vectoriel EF, ce qui fait des fonctions splines d'excellentes candidates pour une approche CAO non-intrusive. Une approche plus générale basée sur le concept FFD (de *Free-Form Deformation*) permet d'étendre l'utilisation de variables de design spline à des champs définis en des points physiques quelconques.

Dans le second chapitre, la stratégie CAO non-intrusive que nous avons développée est présentée, et appliquée au problème de mesure de forme 3D EF. L'extracteur de Lagrange (ou son approximation dans le cas des NURBS) est exprimé sous forme d'une matrice globale, puis appliqué aux opérateurs CIN de mesure de forme, après une étape de projection selon la normale exprimée elle aussi sous forme matricielle, et qui permet d'éviter des corrections de forme qui ne modifient pas la géométrie. Une approche multiniveaux couplant les étapes d'agrégation des pixels dans les images avec différents niveaux de raffinement des splines permet d'obtenir une convergence plus rapide de l'algorithme de mesure de forme. Une attention particulière est portée aux conditions lumineuses pour prendre en compte des réflexions spéculaires sur l'éprouvette. La méthode est ensuite validée sur des images réelles d'une plaque trouée dans deux configurations : une configuration où l'éprouvette subit une légère torsion, et une configuration plane. La stratégie CAO non-intrusive multiniveaux convient au cas où un maillage CAO adapté à l'analyse est disponible, et elle fournit à la fois un champ CAO et son expression comme un champ EF. Elle permet donc de réaliser une vraie mesure de forme CAO, et ce uniquement grâce aux logiciels EF classiques. Cependant, d'un point de vue champ EF, la méthode est restreinte aux maillages EF qui sont inclus dans l'espace vectoriel CAO. Ils sont donc obligatoirement composés d'éléments quadrangles $Q9$ (et non $Q8$) lorsqu'on travaille en degré 2.

Le troisième chapitre ouvre la possibilité d'utiliser une plus grande variété de maillages EF (géométrie et type d'éléments quelconques), et plus seulement des maillages EF qui découlent de modèles CAO adaptés à l'analyse. L'approche développée, basée sur le concept FFD, consiste à immerger la description EF de la géométrie dans une enveloppe spline (*spline morphing box* en anglais). L'enveloppe est choisie comme un hyperrectangle de dimension δ (segment si $\delta = 1$, rectangle si $\delta = 2$, parallélépipède rectangle si $\delta = 3$), de telle sorte que le mapping entre le domaine paramétrique et le domaine physique soit l'identité. Cette approche peut être vue comme une généralisation de l'approche CAO, et nous montrons qu'elle aboutit à un schéma non-intrusif similaire, basé sur une projection sur un espace plus régulier (spline) grâce à un opérateur creux. Un parallèle est tiré entre la méthode proposée et les approches de type domaine fictif, puis avec les approches modèles réduits. De façon similaire à ce qui est fait dans la communauté domaine fictif, nous proposons un critère pour éliminer les variables de design non influentes qui détériorent le conditionnement du problème. Le critère proposé est simple et rapide à calculer car il dépend uniquement de sommes sur les lignes de l'opérateur creux déjà créé. Notre stratégie FFD est appliquée au problème de mesure de champ de déplacement CIN-EF, puis au problème de mesure de forme en stéréo-CIN-EF. Une comparaison avec la régularisation de Tikhonov, assez répandue dans ce domaine, est effectuée sur la mesure du champ de déplacement d'une poutre en flexion. Cet exemple montre le potentiel de la stratégie FFD pour régulariser sans ajouter d'artefacts, et la facilité de définir une longueur de régularisation. Notre stratégie FFD est ensuite appliquée à la plaque trouée déjà étudiée lors de l'approche CAO, dans la configuration en torsion, et cette stratégie améliore encore plus la régularité de l'espace de recherche grâce à l'absence des lignes C^0 (qui étaient nécessaires pour créer une CAO adaptée à l'analyse). Enfin, une preuve de concept sur une structure 3D plus complexe est

présentée : la mesure de forme d'une calotte sphérique. Plusieurs verrous propres à ce problème de mesure de forme ont alors dû être traités :

- Des images ont été prises à 360° tout autour de la structure, et donc la fonctionnelle à minimiser doit prendre toutes ces images en compte. En conséquence, une somme sur toutes les paires de caméras est réalisée.
- Chaque caméra ne voit qu'une partie de la structure. Un masque a donc été ajouté pour ne sélectionner que les éléments visibles par chaque caméra indépendamment, et le produit de deux masques permet de sélectionner les éléments visibles par une paire de caméras.
- Sur une structure initialement plane, bouger les nœuds EF selon la normale est équivalent à bouger les points de contrôle FFD dans cette même direction. Sur des structures 3D plus complexes, définir une normale aux points de contrôle n'est pas évident car ils ne sont pas situés sur le maillage, et surtout, les directions définies sur le maillage spline le plus grossier fixent les directions pour tous les niveaux de raffinement de ce maillage spline (car on utilise les procédures de raffinement spline exactes). Ainsi, nous proposons de définir un champ de "normales" aux nœuds EF, et les points de contrôle FFD définissent un champ scalaire qui représente la norme du champ de correction de forme.
- Pour définir un champ de "normales" aux nœuds EF, l'utilisateur peut choisir d'imposer des directions "globales" ou "locales", dépendant du type de correction de forme recherché. Il est courant de chercher des corrections "globales" dans un premier temps, puis de chercher des corrections de plus en plus "locales". Quelques exemples de champs sont donnés, qui peuvent également être utilisés conjointement à une approche multiniveaux.

Un petit exemple numérique simple sur la mesure d'un champ de déplacement moins régulier, et où l'enveloppe FFD est raffinée en tenant compte de la carte des résidus CIN, montre le potentiel de l'approche FFD à être appliquée à des cas plus complexes. Notre approche FFD offre la possibilité de régulariser un champ mesuré sur n'importe quel maillage EF, ce qui est particulièrement intéressant pour le mécanicien expérimental qui aurait en sa possession uniquement un maillage EF pour faire ses mesures.

Le dernier chapitre applique l'approche FFD au problème d'optimisation de forme d'une éprouvette mécanique vis-à-vis de l'identification de paramètres de comportement de matériaux. Dans ce cas, nous choisissons l'enveloppe FFD de telle sorte que tous les points de contrôle soient influents. Pour cela, nous créons des enveloppes qui épousent les bords de la géométrie, quitte à en créer plusieurs et à utiliser des splines périodiques. Un opérateur, composé du lien FFD non-intrusif, d'un opérateur de symétrie, et d'une matrice de réduction de Guyan, lie la position des points de contrôle à la position des nœuds EF. Cet opérateur global est utilisé tout au long de la procédure d'optimisation et évite des étapes de remaillage. Une attention particulière a également été portée à la modélisation du problème d'optimisation :

- La fonction coût est basée sur la matrice de covariance des paramètres à identifier (qui est aussi la hessienne du problème d'identification), et des approximations ayant du sens physique sont proposées pour prendre en compte la taille de l'éprouvette et le fait que cette matrice de covariance doit être calculée sans images (puisque cette optimisation s'effectue en amont des essais).
- Les champs de sensibilité sont calculés analytiquement.
- Une expression semi-analytique du gradient est proposée pour la fonction coût dans le cas de l'identification d'un seul paramètre matériau.

-
- Une fonction contrainte qui prend en compte le déterminant du jacobien de la transformation EF permet d'assurer que le maillage EF obtenu est toujours adapté pour l'analyse.
 - Une fonction contrainte basée sur une contrainte mécanique équivalente maximale évite d'obtenir une éprouvette qui serait endommagée pendant l'essai, et surtout, cette fonction garantit que les gains obtenus en termes de sensibilité aux paramètres ne pourraient pas être surpassés par une simple augmentation de l'intensité des conditions limites appliquées.

La stratégie d'optimisation proposée est validée sur une poutre pleine en traction, puis la forme de trous dans une autre éprouvette en traction a été améliorée vis-à-vis de l'identification de paramètres de comportement élastique linéaire orthotrope, ce qui a mené à une division par 30 de l'incertitude maximale sur les paramètres à identifier.

Les résultats obtenus sur les trois problèmes d'optimisation considérés confirment la capacité des splines à être utilisées de manière non-intrusive pour régulariser l'espace de recherche. Dans le cas de la mesure de champs par CIN, l'avantage de l'utilisation des splines par rapport à d'autres techniques de régularisation est souligné, en particulier le lien direct entre le niveau de raffinement d'un maillage spline et la définition d'une longueur caractéristique de régularisation, et la possibilité de réaliser des mesures par CIN lorsque les maillages EF sont trop fins pour permettre de telles mesures dans l'espace de recherche EF. Dans les trois problèmes étudiés, une méthode CAO, et plus généralement, FFD, peut être utilisée pour remplacer un espace de recherche trop grand et irrégulier par un espace de recherche plus régulier, grâce à une matrice de projection creuse et simple à implémenter, et qui fait le lien entre le formalisme spline et les routines EF. Enfin, une approche multiniveaux peut être facilement adoptée grâce aux propriétés de raffinement exact des fonctions spline.

Contents

Remerciements	iii
Résumé	v
Introduction	1
1 The power of splines for numerical optimization in experimental mechanics	7
1.1 Some optimization problems in experimental mechanics	7
1.1.1 Optimization problem	8
1.1.2 Displacement field measurement	8
1.1.3 Shape measurement	10
1.1.4 Identification of constitutive parameters	12
1.1.4.1 Constitutive parameters identification methods . . .	12
1.1.4.2 Improvement of the identification experimental tests	13
1.1.5 Issues in common and envisaged routes	16
1.1.5.1 Sources of irregularity	16
1.1.5.2 Solutions to irregularity in structural shape optimization	17
1.2 Spline tools for optimization	18
1.2.1 Splines	19
1.2.2 Isogeometric analysis	22
1.2.3 Non-invasive CAD-based optimization	22
1.2.4 FFD-based optimization	28
2 CAD-based regularization of DIC problems	31
2.1 Mesh-based shape measurement	33
2.1.1 Camera model	33
2.1.2 Coupled calibration and shape measurement problem	33
2.2 Geometric regularization based on Bézier extraction	37
2.2.1 Splines: basics and shape modification	37
2.2.2 IG-FE bridge	39
2.2.2.1 Principle	40
2.2.2.2 Construction: case of B-splines	41
2.2.2.3 Construction: case of NURBS	41
2.2.3 Proposed methodology	43
2.3 Examples	44
2.3.1 Pre-processing: construction of the geometric model and FE mesh	46
2.3.2 Results: twisted configuration	46
2.3.2.1 Classic FE-based shape measurement without any regularization	46

2.3.2.2	Use of standard Tikhonov regularization	47
2.3.2.3	Use of the proposed geometric regularization	48
2.3.2.4	A note regarding brightness and contrast correction	50
2.3.3	Results: flat configuration	50
3	FFD-based regularization of DIC problems	53
3.1	Free-Form Deformation projection	54
3.1.1	Creating the morphing box	55
3.1.2	Linking the deformation of the FE mesh to that of the morphing box	57
3.1.3	Implementation: projection over the morphing box	60
3.1.4	Conditioning concerns	61
3.2	Digital Image Correlation (DIC)	62
3.2.1	Mesh-based DIC	63
3.2.2	2D digital image correlation: Bending of a beam	64
3.3	A less regular case	67
3.4	Shape measurement	69
3.4.1	Mesh-based shape measurement: generalization to n_{cam} cameras	70
3.4.2	FFD projection of the shape measurement problem	71
3.4.3	Twisted plate with a hole	73
3.4.4	Spherical cap	75
4	Shape optimization for constitutive parameters identification	81
4.1	Parameter identification	82
4.1.1	FEMU method	82
4.1.2	Covariance matrix	84
4.1.2.1	Noise modeling in the images	84
4.1.2.2	Noise impact on the measured displacement field	84
4.1.2.3	Noise impact on the identified constitutive parameters	84
4.2	Appropriate modeling of the specimen shape optimization problem	85
4.2.1	Cost function	85
4.2.1.1	Preliminaries	85
4.2.1.1.1	Approximating the unknown DIC matrix	85
4.2.1.1.2	Choosing numerical constitutive parameter values	86
4.2.1.1.3	Computing parameter sensitivities analytically	86
4.2.1.2	For a single parameter	87
4.2.1.2.1	Expression	87
4.2.1.2.2	Semi-analytical sensitivity	87
4.2.1.3	For several parameters	88
4.2.1.3.1	Physical meaning of the eigenvalues	88
4.2.1.3.2	Defining a criterion over eigenvalues	88
4.2.2	Normalizing coefficient	90
4.2.3	Restricting to permissible geometries	93
4.2.3.1	Transformation Jacobian determinant	93
4.2.3.2	Specimen integrity	94
4.2.3.3	Constraint function formulations	94
4.2.4	Validation on a beam	95
4.2.4.1	Analytical developments	95
4.2.4.2	Numerical test	96
4.2.4.3	Example with more design variables	96

4.2.5	Influence of boundary conditions	96
4.3	Improving a specimen shape with a robust FFD-based optimization strategy	100
4.3.1	Shape modification with FFD	100
4.3.1.1	Choice of the FFD morphing box	100
4.3.1.1.1	Solution 1	100
4.3.1.1.2	Solution 2	101
4.3.1.1.3	Solution 3	101
4.3.1.2	Link between design variables and complete mesh	102
4.3.2	Optimizing hole shapes	103
4.3.2.1	First optimization phase	104
4.3.2.2	Second optimization phase	106
4.3.2.3	Overview of the results	108
4.3.3	An ill-posed problem	109
	General conclusion	113
	A Appendix	117
A.1	Interactions between Python and <i>Abaqus</i>	117
A.1.1	<i>Abaqus</i> job creation	117
A.1.2	Calling <i>Abaqus</i> from Python	119
A.1.3	Reading <i>Abaqus</i> data	119
	Notations	121

Introduction

The growing capacities of our computers in terms of computing power over the past decades paved the way to the use of increasingly efficient tools in many areas, especially in the mechanical engineering field. These tools are all the more essential today with the pressing need to reduce carbon dioxide emissions and rely less on fossil energies. The environmental situation, together with the current socioeconomic context and the competitive global market, call for constant innovation from companies, in the final product design as well as in every step of the engineering process, and particularly in the test and certification phases. Among others, these tools allow processing and analyzing massive amounts of data, extracting more information from it, or designing systems that are optimized with respect to desired behavior and constraints. It has direct applications in experimental solid mechanics, where more complex tests can be numerically designed and optimized, and where full-field measurements can be derived from the resolution of inverse problems thanks to the fusion of data coming from a set of sensors (acoustic holography, digital image correlation, tomography, thermography, etc). These tools provide all sorts of valuable information (localization of sound source, displacement field or shape measurement, cracks and damage monitoring, constitutive parameters identification for material characterization, non-destructive testing, microstructure analysis, etc), which, for instance, help characterize new materials, validate the often nonlinear mechanical behavior of complex structures that have been optimized, or control structure integrity all along their life-cycle.

Digital Image Correlation (DIC), which is also referred to as image registration in the computer vision and applied mathematics communities, is one of these tools. It has become one of the most commonly used techniques to obtain full-field measurements on structures, because of its simplicity (it is noncontact and makes use of multipurpose reusable hardware) and its modularity (no intrinsic physical scale), which are huge advantages compared to standard mechanical gauges. Depending on the imaging devices, it is possible to derive 2D surface, 3D surface, or even 3D volume displacement fields by taking pictures of a structure at different loading states and solving an inverse problem. The associated method can be classified as 2D-DIC (or simply DIC) [Lucas and Kanade, 1981, Sutton et al., 1983, Sun et al., 2005, Hild and Roux, 2012, Fedele et al., 2013, Wittevrongel et al., 2015], stereo-DIC [Sutton et al., 2000, Garcia and Orteu, 2001, Dufour et al., 2015a, Pierré et al., 2017, Balcaen et al., 2017] and Digital Volume Correlation (DVC) [Bay et al., 1999, Roux et al., 2008, Gomes Perini et al., 2014], respectively. In the case of stereo-DIC, a similar set up allows to measure the shape of a 3D mechanical surface [Beaubier et al., 2014, Dufour et al., 2016, Pierré et al., 2017, Colantonio et al., 2020], which is actually a fundamental step prior to any experiment for 3D surface displacement field measurements.

Among multiple variants of the method, Finite-Element (FE) mesh-based techniques (also named global- or FE-DIC) [Sun et al., 2005, Besnard et al., 2006, Hild

and Roux, 2012, Fedele et al., 2013, Wittevrongel et al., 2015, Pierré et al., 2017, Passieux et al., 2018b] have widely spread because of their ability to be directly coupled with simulation software in view of performing data assimilation [Périé et al., 2009, Réthoré, 2010, Mathieu et al., 2015], and they pave the way to a better integration of models and experiments in solid mechanics [Réthoré et al., 2013, Dufour et al., 2015b, Pierré et al., 2017, Serra et al., 2017, Passieux et al., 2018b]. The interaction of measurement and simulation becomes fast and friendly, as both kinematic fields are defined at the nodes of the same mesh. The measured field is sought in the space generated by the FE functions associated with the FE mesh that is used for computational mechanics.

More precisely, this direct coupling is of great interest when characterizing a material constitutive law thanks to mechanical experiments. This characterization comes with the identification of the constitutive parameters of a chosen law, which is carried out through the optimization of these parameters with respect to certain quantities. One of the well-known identification procedure, which benefits from the FE direct coupling, is the *Finite Element Model Updating method* (FEMU), which consists in comparing the measured displacement field with the simulated displacement field obtained on a virtual twin with the same FE mesh and the chosen constitutive law. The (properly weighted) squared difference between these two fields is then minimized by adjusting the constitutive parameters values. The FEMU method can be easily applied to a large variety of constitutive laws, and allows for the identification of several parameters at the same time.

Yet, an experiment is generally not sensitive enough to all parameters of a chosen constitutive law (or at least not equally sensitive to all parameters), which explains the use of several different experiments used for different parameters of the same constitutive law nowadays [D3518/D3518M, 1994]. These numerous experiments, though, are costly and time consuming. This observation led to the development of more complex specimen shapes to improve the sensitivity to all constitutive parameters, and thus reduce the number of needed experimental tests [Pottier et al., 2012, Schmaltz and Willner, 2014, Mitukiewicz and Głogowski, 2016, Schemmann et al., 2018]. More recently, a few works were carried out to optimize the specimen geometry with respect to quantities that aim at solving two issues: being sensitive to all sought constitutive parameters, and improving the sensitivity to each parameter [Feld et al., 2015, Bertin et al., 2016, Chamoin et al., 2020, Conde et al., 2021, Zhang et al., 2021]. In particular, the quantity to minimize chosen by Feld et al., Bertin et al. and Chamoin et al. is well adapted when the constitutive law, and therefore the set of sought parameters, is chosen. However, this optimization problem can contain several local minima, especially if several constitutive parameters are to be identified, and this issue is compounded by the use of search spaces of high dimension for the design variables that define the specimen shape.

Interestingly, displacement measurement and shape measurement via FE-DIC also suffer from the high dimension of the search space because of too many degrees of freedom to describe a field. Simulation FE meshes are generally quite fine, since they need to accurately capture the numerical solution over structures of potentially complex geometries. In this work, such meshes that are designed for accurate simulation results will be referred to as *analysis-suitable* meshes. When directly used to describe the kinematic measured field in DIC, they may lead to ill-posed problems since the meshes contain too many degrees of freedom (dof) to optimize compared to the data provided by the experimental instrumentation (camera resolution, speckle pattern resolution, etc). Such a problematic is even more exacerbated in case of mesh-based shape measurement since the shape of the specimen is generally rather

smooth and regular, and thus should require less dof than the corresponding simulated displacement field. To tackle this issue in FE-DIC, the common practice consists in resorting to what is referred to as the Tikhonov regularization technique in the field, *i.e.* to add a specific term to the initial DIC objective function that penalizes a norm of each component of the measured field or its derivatives (typically the L_2 -norm of the gradient [Passieux and Périé, 2012, Pierré et al., 2017, Dufour et al., 2016]). Yet, this treatment may create important artifacts, especially when the kinematic transformation involves global rotations, as will be shown in this work (see, for instance, Section 2.3.2.2 or Section 3.2.2).

Therefore, there is a need for a regularization method that would allow working with FE meshes while keeping a low number of design variables. A desirable feature of this method would be its non-invasiveness with respect to the standard FE approach so that all operators could be computed using usual FE routines.

In the structural shape optimization community, a way of reducing the number of design variables together with enforcing the regularity of the optimized shape is the use of spline functions. These functions are very common in Computer-Aided Design (CAD) to describe geometries, and therefore offer a relevant basis in the context of shape optimization [Braibant and Fleury, 1984, Wall et al., 2008, Hirschler et al., 2019b] or to measure a shape or a shape correction [Beaubier et al., 2014, Dufour et al., 2016, Jiang et al., 2015, Jiang et al., 2019]. Furthermore, their regularity properties make them appropriate to define search spaces for more general optimization problems, in particular when the optimized quantity is a field defined in a given domain. Typically, displacement field measurement can also benefit from spline functions properties [Elguedj et al., 2011, Réthoré et al., 2010, Dufour et al., 2015a, Kleinendorst et al., 2015].

In this context, we propose to draw inspiration from the shape optimization community and to use spline functions to define the search space in three optimization problems that arise in experimental mechanics:

- FE-DIC displacement field measurement, where the displacement field on a structure is sought through the minimization of differences between images taken of the same structure at two different load states;
- FE-DIC shape measurement, where a shape correction field is sought through the minimization of a graylevel mismatch between images taken of the same structure at the same load state (usually the initial load state) from different viewpoints;
- shape optimization of a mechanical test specimen with regard to constitutive parameters identifiability, where a shape modification is sought through the minimization of an appropriate quantity.

Several approaches will be presented, which all allow non-invasive coupling with FE software. By non-invasive, we mean that the FE routines can be used as black boxes. It allows using the advantages of spline functions while relying on standard, widely-used, robust FE software, and without recoding equivalent spline software. When working on these three optimization problems, particular attention will also be paid to the specificity of each problem, through the handling of special and real test-cases designed to show the potential offered by spline functions.

Following these opening remarks, this manuscript is made of four chapters.

The first chapter details the issues encountered in the three optimization problems, and some spline tools that may be of high interest to tackle these issues. First, general optimization problems are briefly presented and the mathematical expression is given, together with basic vocabulary that will be used in the rest of the manuscript. Then, each problem is illustrated thanks to the literature and the regularity issues are pointed out. For FE-DIC problems, the commonly used Tikhonov regularization method and associated artifacts are presented. Then, the issues are explained in the light of what is done in the shape optimization community.

In the second section, spline functions are presented and a focus is made on their interesting properties (smoothness, exact refinement, finite support). An interesting use of refinement in IGA (IsoGeometric Analysis) shape optimization procedure is shown, in which different refinement levels are associated to different models of the exact same structure, with different purposes. Then, two approaches that can help link spline functions to FE functions, namely the CAD-based and the FFD-based (Free-Form Deformation) approaches, are briefly presented with the help of literature and first tests and examples.

The second chapter focuses on the developed modern CAD-based approach, applied to FE-DIC shape measurement. After a short introduction, the basics of mesh-based shape measurement are given, and the chosen coupled calibration and shape measurement procedure are explained.

Then, the proposed CAD-based approach is fully detailed. The used Lagrange extractor is presented in the case of B-splines and NURBS, and its implementation in a non-invasive way with the standard FE-DIC software is presented. A multilevel scheme based on both coarse graining and spline refinement is built.

Finally, results on a plate with a hole are shown in two configurations. First, pictures of the plate installed in the clamping jaws of a tensile testing machine allow measuring a twisted configuration with shape corrections up to the tenth of a millimeter. Particular attention is paid to contrast correction as it affects the solution on the center part of the specimen. Then, the same specimen is studied unclamped, in a flat configuration, with corrections of the order of a hundredth of a millimeter. In both cases, the results are validated with subset-based-DIC shape measurement results.

The third chapter presents our developed FFD-based regularization scheme for FE-DIC problems, which can be seen as a generalization of the CAD-based approach established in the second chapter. A full understanding of FFD is given, from the creation of the morphing box to its non-invasive implementation, and parallels were made with the fictitious domain and reduced basis classes of methods. A criterion is then proposed to deal with problematic degrees of freedom.

A multilevel scheme is also proposed and the method is applied the case of FE-DIC displacement field measurement. After some theoretical aspects on this method are given, our approach is validated on real images of a bending beam, and compared to a classic regularization method. A numerical example also shows the potential of the method to be used on a less regular displacement field.

Then, we apply our FFD-based approach to FE-DIC shape measurement problems. First, a generalization of the stereo-DIC problem to n_{cam} cameras is made, and a specific care is paid to the projection of the sought field along the normal in this multilevel context. The method is validated on the same twisted plate as earlier but we show that the mesh does not have to derive from a spline mesh and can be chosen arbitrarily. Finally, our method is applied to a more complex 3D

structure with pictures taken at 360° , and we show that it both efficiently smooths the measured shape and makes the problem more robust to initialization.

The fourth chapter deals with the third optimization problem, namely the shape optimization of mechanical specimen with regard to constitutive parameters identifiability. First, essential concepts related to constitutive parameter identification and identification quality, in particular the covariance matrix, are explained.

Then, all choices that we have performed to define the optimization problem are given. The cost function is constructed in the case of one or several sought constitutive parameters, based on the literature. Physical observation help us finely enrich the cost function formulation, define adequate constraint functions and adjust thresholds for the inequality constraints. The problem definition is validated on a simple tension beam.

Finally, the choices regarding the shape handling through FFD are explained, and its non-invasive implementation which allows the use of FE routines is described. For validation purposes, the complete framework is applied to the shape optimization of holes in a tension beam to identify the constitutive parameters of an orthotropic linear elastic law.

Chapter 1

The power of splines for numerical optimization in experimental mechanics

Introduction

Our work aims at improving the resolution of optimization problems in experimental mechanics, thanks to spline functions.

In this chapter, we focus on and explicit three different optimization problems that occur in experimental mechanics, namely FE-DIC (Finite Element Digital Image Correlation) displacement field measurement, FE-DIC shape measurement and shape optimization of a mechanical specimen with regard to constitutive parameter identification. Note that these three optimization problems can be part of one single experiment, in which a material constitutive law has to be characterized. In this case, a specimen shape would be optimized to improve the experiment sensitivity to the sought constitutive parameters, and then, DIC would be used during the experiment to carry out full-field measurement of the shape if needed, and the displacement field required to identify the constitutive parameters. After these three optimization problems and their issues are presented through a literature review, spline basics are given to start understanding what their advantages are with respect to these issues, and how they could be used in a non-invasive way. This non-invasive property is desirable so that the usual FE software can be used. FE software is omnipresent in the mechanical engineering domain and is still very powerful thanks to decades of research and developments. A spline-based non-invasive scheme seems to be a beneficial way of introducing splines and their advantages into the engineering community.

1.1 Some optimization problems in experimental mechanics

Optimization problems arise at various levels in experimental mechanics. In our case for instance, full-field measurement such as shape or displacement field measurement involve solving inverse problems, which is achieved through the minimization of a functional thanks to optimization algorithms. Optimization tools also typically help designing complex experiments that offer more sensitivity to one or several measured quantities.

In this section, we focus on three continuous optimization problems related to the

process of characterizing a material using full-field measurement, namely FE-DIC displacement field measurement, FE stereo-DIC shape measurement and the design of a test specimen for constitutive parameter identification via FEMU-DIC (Finite Element Model Updating method based on Digital Image Correlation measurement).

1.1.1 Optimization problem

Optimization problems consist in making something optimal with regard to certain quantities and with respect to certain constraints. The standard formulation for continuous mono-objective optimization problems is the following:

$$\text{Find } \underline{s} = \arg \min_{\underline{s} \in \mathcal{D}} f(\underline{s}), \quad (1.1)$$

where $f : \mathbb{R}^{n_{dv}} \rightarrow \mathbb{R}$ is the function to minimize, called *cost function* (also called *objective function*), $\underline{s} \in \mathbb{R}^{n_{dv}}$ contains the *design variables* and \mathcal{D} is the *search space* (of dimension n_{dv}), sometimes called *design space* in the context of shape optimization. *Constraint functions* can be added to restrain the possible solutions, which makes the general definition of \mathcal{D} as follows:

$$\mathcal{D} = \{ \underline{s} \in \mathbb{R}^{n_{dv}}, g_i(\underline{s}) \leq 0 \text{ and } h_j(\underline{s}) = 0, \forall i \text{ and } \forall j \}, \quad (1.2)$$

where $g_i : \mathbb{R}^{n_{dv}} \rightarrow \mathbb{R}$ are inequality constraints and $h_j(\underline{s}) : \mathbb{R}^{n_{dv}} \rightarrow \mathbb{R}$ are equality constraints. Bounds on \underline{s} are also sometimes written separately (*e.g.* in [Kiendl, 2011, Kiendl et al., 2014]), but they can be written in the form of two inequality constraints g .

In this work, equality constraints will not be used, and inequality constraints will only be used in Chapter 4 for the shape optimization of a test specimen with respect to constitutive parameters identification.

1.1.2 Displacement field measurement

The first optimization problem is the measurement of a displacement field via what is referred to DIC in the experimental mechanics community. The same problem is also known as *image registration* in the Computer Vision, Applied Mathematics and Biomechanical Engineering communities for image processing [Fehrenbach and Masmoudi, 2008, Sotiras et al., 2013]. To perform DIC, pictures are taken of a specimen or structure, generally covered with a contrasted speckle pattern. An image (or several images in the case of stereo-DIC [Sutton et al., 2000, Garcia, 2001]) is taken in a reference state, when the specimen is *in-situ*, still, and unloaded. The same camera (or camera rig) is used to get an image (or several images) in a deformed state, while the specimen is under load. The displacement field of the surface of the specimen is then derived from the resolution of an inverse problem based on the assumption that the graylevel associated with a physical point is the same in the reference and deformed state images. This inverse problem is ill-posed and is expressed as the minimization of a functional in order to be solved (see [Passieux, 2015] and Section 3.2.1 for further details).

There are two main ways of performing DIC, namely *local* and *global* DIC [Hild and Roux, 2012]. In local DIC, the displacement field is sought in the search space defined by elementary deformations of small parts of the region of interest, called *subsets*. Historically, it was the first DIC method, developed in the Computer Vision community [Lucas and Kanade, 1981] and then applied to mechanical problems by [Sutton et al., 1983, Sutton et al., 2009, Orteu, 2009] and it is well developed today. Nevertheless, coupling these measurements with simulation results is not

straightforward and induces errors when expressing this field in a new space, typically defined by FE functions [Lava et al., 2020]. Conversely, global DIC aims at directly coupling DIC measurements with simulation results, by using the simulation (generally FE) mesh and the associated vector space to define the search space for the inverse problem [Sun et al., 2005, Besnard et al., 2006]. Apart from its great benefit in hybrid approaches (using FE simulation to regularize measurements, to estimate boundary conditions or to complete partial measurements for instance), using the simulation FE mesh for the measurement makes test-simulation dialogue easier, and is for example particularly useful to identify constitutive parameters via FEMU (which is detailed Section 4.1.1).

Yet the measured FE displacement fields are often noisy, especially on the edges, as can be seen on Figure 1.1. This high frequency noise, with a typical wavelength of two FE elements, disturbs the measurement and makes the strain and stress fields difficult to derive because of noise propagation when taking the derivative. This issue comes from the chosen FE meshes, which are very fine as they have to be analysis-suitable. When directly used to describe the kinematic measured field in DIC, they usually lead to problems such as Equation (1.1) that are ill-posed since the meshes contain too many degrees of freedom (dof) to optimize compared to the data provided by the experimental instrumentation (camera resolution, speckle pattern resolution, etc).

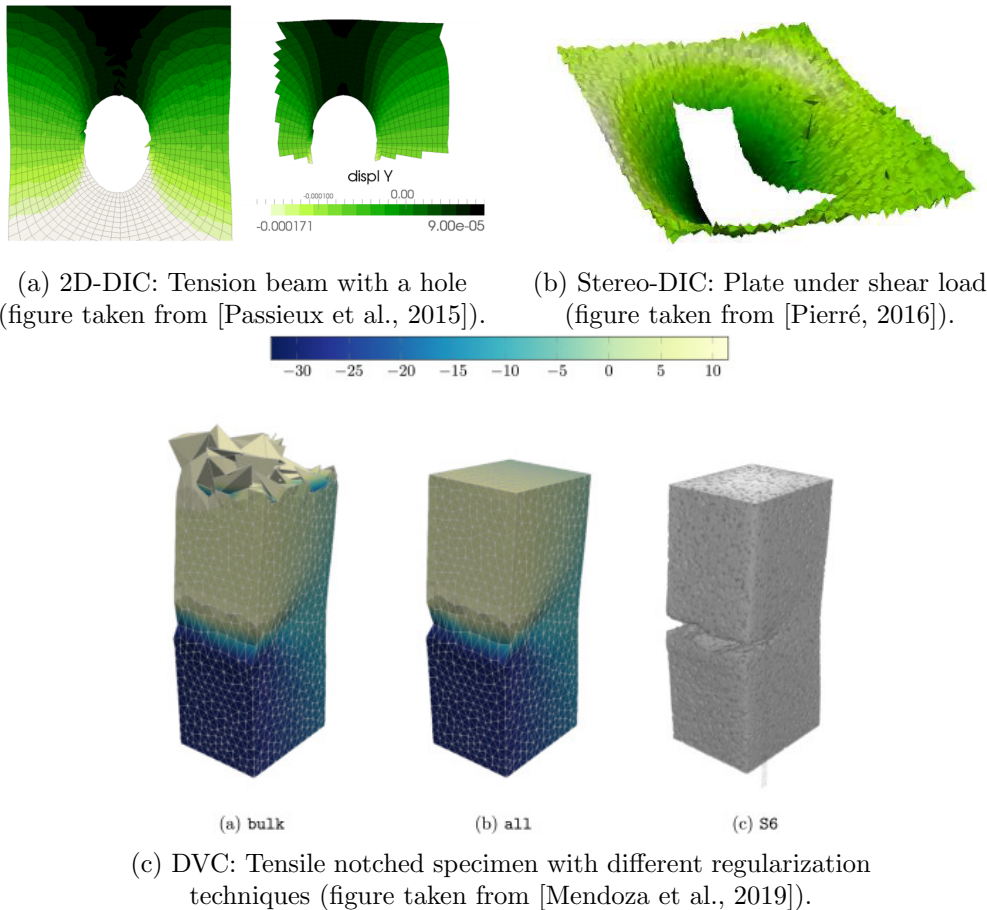


Figure 1.1: Measured displacement fields with global FE-DIC methods. The results are noisy, especially on the edges.

As a remedy, regularization techniques have been proposed, that incorporate physical knowledge or assumptions on the sought field. For instance, time regu-

larity can be taken into account [Passieux et al., 2018a, Berny et al., 2018, Jailin et al., 2018] (see PGD-DIC regularization shown Figure 1.2), elastic regularization adds a mechanical-sound penalization term [Réthoré et al., 2009a, Leclerc et al., 2011, Mendoza et al., 2019, Rouwane et al., 2021], and Tikhonov regularization shown Figure 1.3 also adds a penalization term based on the gradient of the sought displacement field [Pierré, 2016].



Figure 1.2: Physical regularization using time regularity knowledge for vibrations. (figure taken from [Passieux et al., 2018a]).

Among these methods, Tikhonov regularization is widely used because it is non-invasive with respect to FE-DIC operators computation, it can be adapted to a large variety of DIC problems, and it does not necessitate *a priori* mechanical knowledge on the material behavior. However, this regularization technique has some drawbacks, namely the handling of global rotations (the method minimizes the gradient, yet this gradient can be part of the sought solution), the definition of an equivalent regularization length that is indirect [Leclerc et al., 2012], and the handling of the edges (for illustration, see Figure 1.3). At this stage, we refer the interested reader to [Colantonio et al., 2020, Chapelier et al., 2021] and indicate that the problematic will be deeply tackled in the remaining of the manuscript (see, *e.g.*, Sections 2.3.2.2 and 3.2.2).

1.1.3 Shape measurement

The second optimization problem, which shares similarities with the first one, is the mesh-based shape measurement procedure occurring in FE-DIC. This step is essential before performing any experiment with 3D stereo-DIC displacement field measurement so that the reference FE mesh of the specimen is as close as possible to the real reference geometry (incorporating manufacturing defects, pre-load or relaxation of residual stresses, etc). To this end, several cameras take pictures of the specimen in the reference state with different points of view. After a calibration procedure used to characterize the cameras intrinsic parameters (focal length, skew...) and extrinsic parameters (cameras positions and orientations) [Garcia, 2001], the shape is sought as a field of FE node positions update. To do so, the assumption is made that the graylevel associated with a physical point is the same in every image, from every point of view (see Sections 2.1 and 3.4.1 and [Pierré, 2016] for more details).

The search space is once again the FE space associated with the FE mesh of the specimen, and the design variables are position updates for each FE node.

In the case of global shape measurements, additional sources of ill-posedness occur compared to DIC displacement field measurement. Moving the position of a node along the surface of the specimen does not modify the geometry [Pierré,

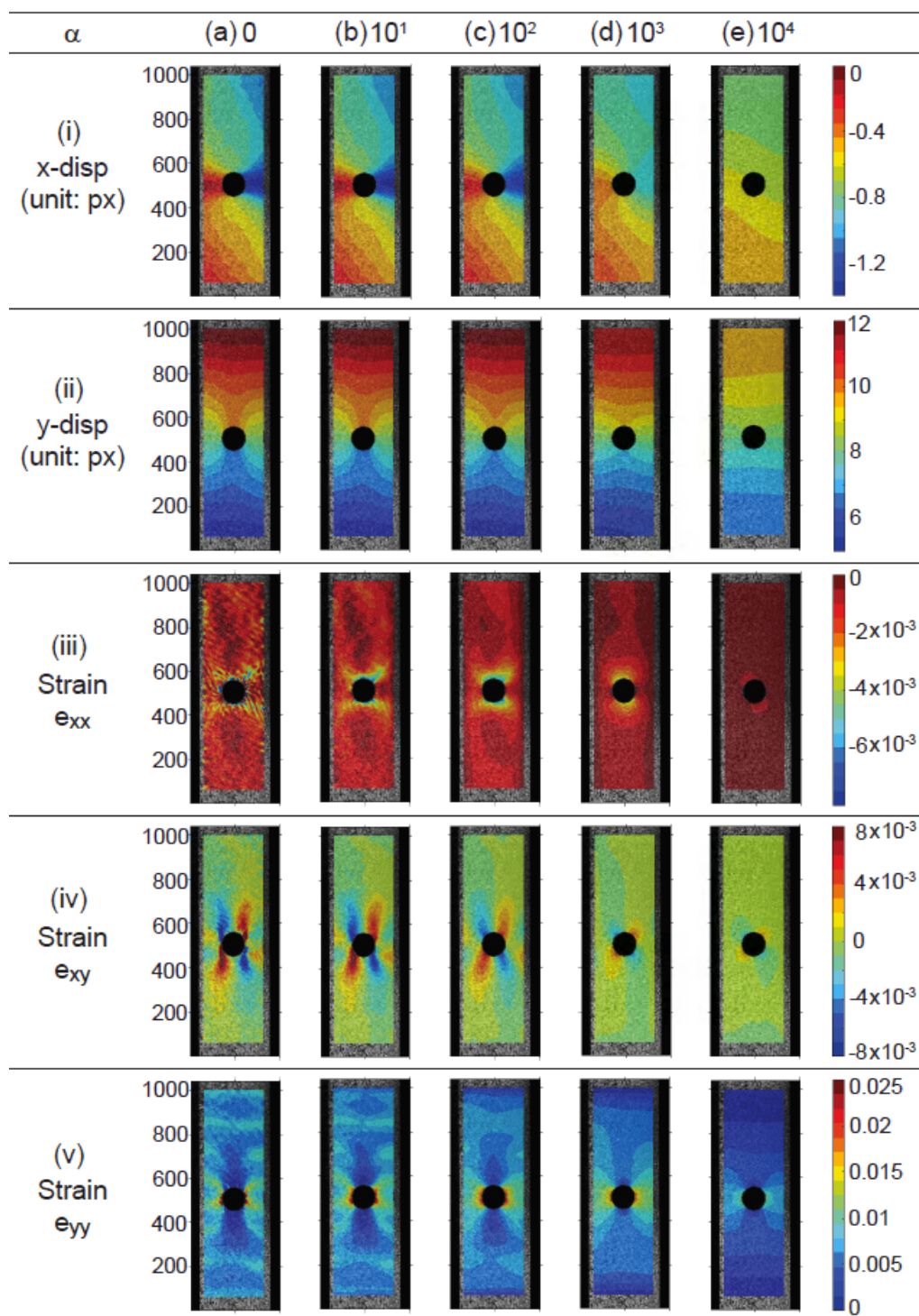


Figure 1.3: Tikhonov regularization with several penalization coefficient values α .
(figure taken from [Yang, 2021]).

2016, Dubreuil et al., 2016] (see Figure 1.4), and thus the functional value is almost the same for all these corrections. This problem comes from the fact that the FE mesh is not attached to the specimen yet, and the shape correction affects how both images in each pair are processed (contrary to displacement field measurement where the displacement field affects how the deformed state image is processed, but not the reference state image). To tackle this issue, the shape correction is often

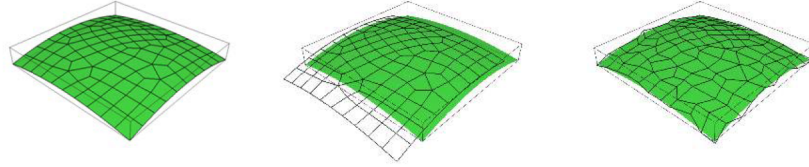


Figure 1.4: Sources of ill-posedness for shape measurement. The nodes can move along the surface without changing the shape. The mesh can "slide" (the edges do not match and the measured shape does not correspond to the region of interest anymore, see the middle figure), or interior nodes can move (see the figure on the right). (figure taken from [Pierré, 2016]).

measured only along the normal to the surface, which is computed on the initial uncorrected FE mesh (the measured corrections are supposed to be small) [Dubreuil et al., 2016, Pierré, 2016]. In this case, a scalar field is sought, and the design variables are the normal corrections at each FE node.

Yet the other sources of ill-posedness make the measured shape correction noisy, even when the measured correction is along the normal (see Figure 1.5). One of them is similar to what makes measured displacement fields noisy. Indeed, the analysis-suitable FE mesh contains too many design variables compared to available information. Such a problematic is even more exacerbated in case of mesh-based shape measurements since the shape of the specimen is generally rather smooth and regular, and thus should require even less dof than the corresponding simulated displacement field which may comprise important gradients [Colantonio et al., 2020]. Once again, Tikhonov regularization can help regularizing the measured shape correction field, but it also degrades parts of the true solution, in particular global rotations (see Figure 1.5 again).

1.1.4 Identification of constitutive parameters

The third optimization problem that we will focus on is the identification of constitutive parameters, and more precisely, how to design the shape of the test specimen to improve constitutive parameters identification ability.

1.1.4.1 Constitutive parameters identification methods

Knowing the constitutive parameter values is necessary to describe the physical behaviour of a material, once a constitutive law has been chosen. They are determined by carrying out experimental tests on specimens, and solving an inverse problem based on the comparison of the measured field with a model. Several different identification methods have been developed over the last decades: the Finite Element Model Updating (FEMU) method [Kavanagh and Clough, 1971], the constitutive equation error [Ladevèze et al., 1994], the virtual fields method [Grediac, 1989] or the equilibrium gap method [Claire et al., 2004], to name the most common methods. Recently, Roux and Hild [Roux and Hild, 2020] have shown that all these

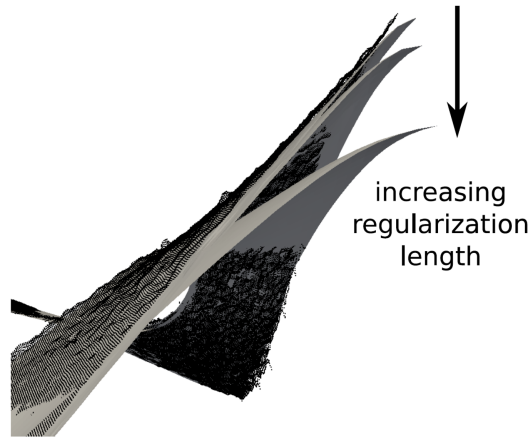


Figure 1.5: Unregularized FE shape measurement (black mesh) and shape measurement with Tikhonov regularization with increasing penalization coefficients (gray surfaces). The unregularized measurement is noisy. Tikhonov regularization smoothes the shape but deteriorates the measured field. (figure taken from [Colantonio et al., 2020]).

methods actually consist in the minimization of a metric measuring the distance between the measured and the simulated displacement fields which differ only in the choice of the quadratic (semi-)norm used. The study concludes that the optimal metric with respect to the identification sensitivity to measurement noise is a norm associated with the inverse of the measured displacements covariance matrix, which corresponds, in the literature, to the so-called weighted FEMU method. More details on the FEMU method are given in Section 4.1.

Note that some more integrated methods also exist [Réthoré, 2010, Leclerc et al., 2009], that do not require two steps for the displacement field measurement and the identification of the constitutive parameters, such as, for instance, Integrated DIC (IDIC) [Leclerc et al., 2009, Mathieu et al., 2015]. Yet, it has been shown that under the assumption of small noise levels (in particular coming from the FE mesh refinement level), IDIC and FEMU are equivalent and lead to the same identified parameters covariance matrix [Mathieu et al., 2015]. Our later developments with the FEMU method in Chapter 4 can therefore be transposed to IDIC.

1.1.4.2 Improvement of the identification experimental tests

Experimental tests to identify constitutive parameters are generally designed to calibrate one (or few) parameter at a time. In addition, they are usually quite basic (simple geometry and loading), which does not guarantee that the constitutive parameter values are accurately identified, and requires performing several tests for each constitutive parameter. The FEMU functional often shows a valley, either because of constitutive parameters that are less identifiable than others or because of constitutive parameters whose uncertainties are strongly correlated (see Figure 1.6). This valley causes the identified set of constitutive parameters to highly depend on the initialization if only few experiments are carried out [Decultot, 2009].

To reduce the costs coming from this identification procedure, specific tests have been designed for specific needs. For instance, designs for a cruciform specimen that allow reaching higher plastic strain levels before fracture in the test section have been proposed [Mitukiewicz and Głogowski, 2016, Schemmann et al., 2018]. Other works focused on the heterogeneity of the strain or stress field in order to

activate the maximum of constitutive parameters in a single test [Pottier et al., 2012]. Sensitivity studies were also carried out to determine the effect of a geometry modification of the specimen on a resultant force or displacement field derivative with respect to the constitutive parameters [Affagard et al., 2017]. Comparisons of different specimen shapes were made, by juxtaposing the identified model results with experimental results [Schmaltz and Willner, 2014] or by performing several identification tests and deriving the standard deviation on the identified parameters for each geometry [Lecompte et al., 2007]. In all these works, the authors propose their ideas for better test designs. Conversely, other articles relied on optimization algorithms to find new designs that improve some quantities linked to the parameters identifiability. They focus on getting high and homogeneous strain levels where the gauge is, in the center of cruciform specimens [Demmerle and Boehler, 1993], on increasing the heterogeneity level of strain or stress fields to improve the mechanical richness of the test [Conde et al., 2021, Zhang et al., 2021], or on the covariance matrix of the identified parameters to take into account the metrological chain [Feld et al., 2015, Bertin et al., 2015, Bertin et al., 2016, Chamoin et al., 2020].

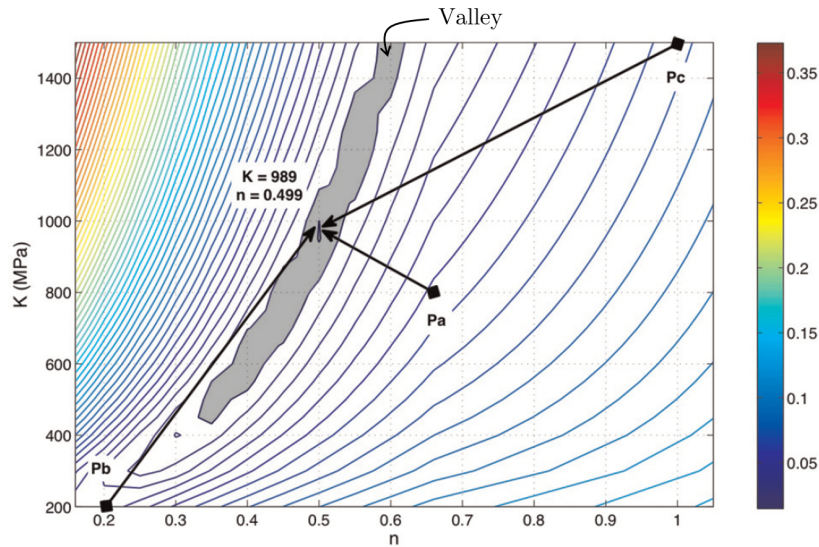


Figure 1.6: FEMU functional for the identification of two isotropic hardening parameters. A valley is clearly visible and highlighted in gray. (figure taken from [Robert et al., 2012]).

When comparing two cruciform geometries, Lecompte et al. draw an interesting conclusion [Lecompte et al., 2007]. The geometry with a hole makes a more heterogeneous deformation field but leads to higher standard deviations for the identified parameter values. They argue that these heterogeneities are possibly harder to measure correctly with the DIC setup, which causes errors in the measured field. This observation justifies taking the measurement process into account when designing an experimental test, rather than relying solely on heterogeneity quantities. In addition, many of the works that focus on criteria on the strain or stress field do not incorporate *a priori* knowledge about the nature of the constitutive parameters to identify. This approach is suitable to design identification tests when the constitutive law is not known, but does not ensure the sensitivity to specific constitutive parameters.

In this work, we will suppose that a constitutive law has been chosen *a priori*.

Our study thus draws on the articles of Feld et al., Bertin et al. and Chamoin et al., which are founded on uncertainty propagation from the camera sensor to the sought constitutive parameters, and use quantities coming from the constitutive parameters covariance matrix to define their cost function [Feld et al., 2015, Bertin et al., 2016, Chamoin et al., 2020]. Feld et al. and Bertin et al. propose methodologies based on what is generally called *parametric optimization*. It means that the design variables are simple geometry parameters that do not fundamentally change the modified features: circles remain circles, lines remain lines, etc. Feld et al. have two design variables that represent the position of a hole (and its symmetry) in a tension beam (see Figure 1.7). Bertin et al. work on fillet radii on a cruciform specimen (see Figure 1.8). They first make them vary together as one design variable, and in a second phase, the optimized radii are fixed one by one after four one-design-variable optimization procedures, which leads to four different radii. These works pave

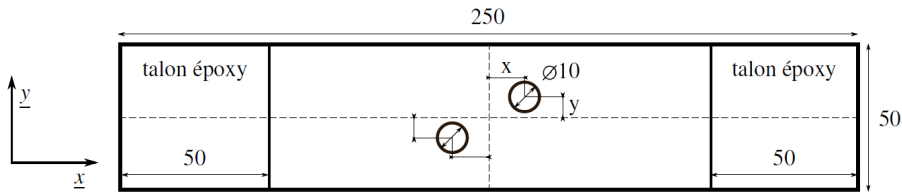


Figure 1.7: Specimen proposed in [Feld et al., 2015]. x and y are the design variables. (figure taken from [Feld et al., 2015]).

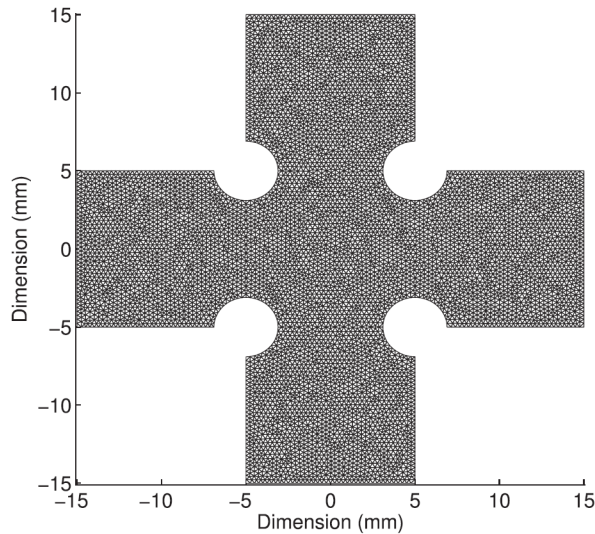
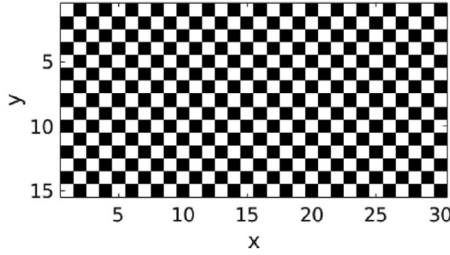


Figure 1.8: Specimen proposed in [Bertin et al., 2016]. The radii of the four circles are the design variables. (figure taken from [Bertin et al., 2016]).

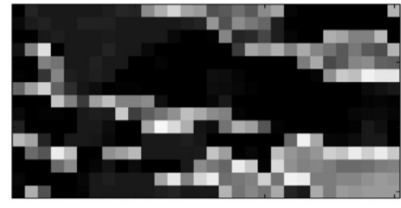
the way for optimization of experimental tests with respect to the identifiability of chosen constitutive parameters. Yet they have few design variables and the latter are quite restrictive regarding the possible final specimen geometries.

To widen the scope of possible geometries, Chamoin et al. use *topology optimization*, which means that holes can be created or removed throughout the optimization process [Chamoin et al., 2020]. They apply the SIMP method, where the structure is divided into elements and the design variables are the densities of each element (see

Figure 1.9(a)). These densities can vary from 0 (void) to 1 (matter) and a penalization term in the cost function forces them to be close to 0 or 1. This methodology



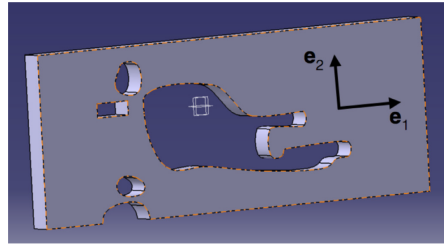
(a) SIMP checkerboard initialization. The squares densities are the design variables.



(b) Raw optimal solution obtained for a volume fraction of 0.6, before filtering.



(c) Optimized geometry obtained for a volume fraction of 0.8, after filtering the raw optimal solution.



(d) Final CAD geometry obtained for a volume fraction of 0.8. Non-physically-sound parts have been removed and edges have been smoothed.

Figure 1.9: Specimen proposed in [Chamoin et al., 2020]. The elements densities are the design variables. (figures taken from [Chamoin et al., 2020]).

allows to get various geometries, yet it has several drawbacks. First, penalty factors in the cost function have to be chosen, which requires running numerical tests, especially since the choice of these factors may be problem-dependent. Then, a filtering step is needed (see fig. 1.9) to set low densities at 0 and high densities at 1 (see Figure 1.9(c)), and the optimized geometry has to be transferred into a physically-sound CAD model (see Figure 1.9(d)), which can affect the identification properties of the specimen. In this step, non-physically-sound parts of the specimen, such as the small part inside the big hole in Figure 1.9(c), are removed. Finally, the high number of design variables implies high computational costs to compute the cost function gradient in the optimization process, and above all, makes the search space dimension high, which generally increases the number of local minima in which we can end. As a matter of fact, only few developments on topology optimization are made by Chamoin et al. with the more complex cost function in the case when more than one constitutive parameter is to be identified.

1.1.5 Issues in common and envisaged routes

1.1.5.1 Sources of irregularity

In the three optimization problems described above, similar issues occur, that lead to noisy, non-physically-sound results. These issues come from the search space choice. The chosen search spaces are too rich and lack regularity. In the displacement field and shape measurement problems, the FE space is used and the number of design variables is proportional to the number of FE nodes. Since FE meshes are generally analysis-suitable (*i.e.* adapted to mechanical analysis problems solving) to make a

direct coupling between measurement and simulation, these FE meshes can be very fine and lead to search spaces of large dimension. As a result, the measured fields contain one-element-wavelength noise that inherits the C^0 properties of FE basis functions (see Figures 1.1 and 1.5). In the shape measurement problem, using the FE space as a search space is even less physically sound, because the used FE mesh refinement is adapted to the mechanical analysis, not to the sought shape correction. The latter has features whose desired typical length is generally greater than a few FE elements. For this optimization problem and the mechanical one, the natural roughness of the FE modeling, which is suitable for analysis, is not adapted. Finally, in the topology optimization for identification problem [Chamoin et al., 2020], each square element density is a design variable, so the search space dimension is often several hundreds or more. Additional cumbersome precautions are needed to generate a smooth, physically sound geometry (see Figure 1.9).

To circumvent these issues, we therefore propose to draw inspiration from the shape optimization community and to use a more regular spline space as a search space. Many articles in that community use a spline space for shape optimization, they only deal with different cost functions, such as, for instance, the minimization of compliance [Wall et al., 2008, Kiendl et al., 2014, Hirschler et al., 2019b]. We aim at benefiting from advances made in this field.

1.1.5.2 Solutions to irregularity in structural shape optimization

As we have seen, dealing with a large number of dof causes unrealistic geometries, especially with FE which are of low regularity (see Figure 1.10). The following example highlights the main steps of dealing with regularity issues in the shape optimization community. Therefore the use of FE dof as design variables is usually

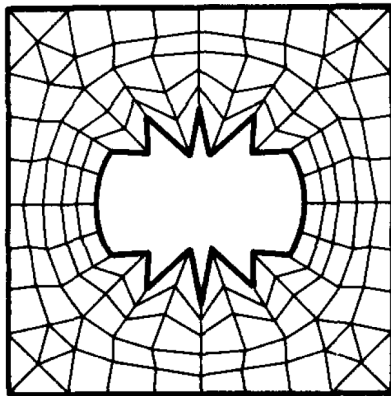


Figure 1.10: Node-based shape optimization of a hole, leading to irregular edges. (figure taken from [Braibant and Fleury, 1984]).

combined in this field of research with the use of smoothing filters [Le et al., 2011, Firl et al., 2013, Bletzinger, 2014, Hojjat et al., 2014]. Another classic approach, sometimes referred to as CAD-based approach, consists in considering a CAD model, *i.e.* made of spline functions (typically B-splines or NURBS [Cohen et al., 1980, Piegl and Tiller, 1997]), to define the design variables [Braibant and Fleury, 1984, Olhoff et al., 1991, Wall et al., 2008, Kiendl, 2011, Kiendl et al., 2014]. The spline functions are well suited for shape optimization since they have been built for geometric modeling in CAD and computer graphics; they are of higher regularity and thus imply

few dof (mainly associated with the control point positions of the spline entities) to describe a geometry and, more importantly, a geometry update. They also allow reaching a wide variety of different geometries, as long as the topology remains the same. Shape optimization techniques that rely on them are sometimes referred to as *geometric shape optimization* [Dapogny and Frey, 2014], which is richer than parametric optimization and less complex than topology optimization. Yet, from a purely mathematical point of view, geometric optimization is just a generalization of parametric optimization.

Taking the reasoning even further, the spline technology actually provides a natural regularization framework for general optimization problems since it allows to look for the solution in a more regular approximation subspace [Bouclier and Hirschler, 2021]. In this respect, some work has been performed to regularize DIC problems using B-spline and NURBS functions. First, the ability of B-spline functions to accurately measure displacement fields along with their derivatives in 2D-DIC was established [Cheng et al., 2002, Elguedj et al., 2011, Kleinendorst et al., 2015]. Then, B-spline functions were also used for smooth 3D shape measurements [Beaubier et al., 2014, Dufour et al., 2016, Jiang et al., 2015, Jiang et al., 2019] before being investigated for real 3D surface displacement measurements [Dufour et al., 2015a] in the context of stereo-DIC. From a global point of view, all these methods are similar to FE-DIC, but instead of using FE basis functions, they consider B-spline functions to describe the specimen geometry, the sought measured fields, and hence to compute all the operators needed for the resolution. As a result, besides the effort to implement spline functions in the DIC framework, the user ends up with an experimental displacement field that is not directly comparable with the output provided by most of today’s simulation tools, which was the core interest of global approaches in DIC. Other works on shape optimization for identification of constitutive parameters, such as [Conde et al., 2021], use B-spline to describe the specimen shape edges and give the obtained spline geometry as an input to *Abaqus*. The geometry is then meshed with FE. Such a technique may require a lot a remeshing steps.

Our goal is to take advantage of the spline properties and use them in a non-invasive way so that usual FE simulation software can be used, possibly without remeshing. To this end, we build the spline space so that it is a vector subspace of the FE vector space (same philosophy as in [Tirvaudey et al., 2019]).

Note that other works propose different smooth FE subspaces, such as [Etievant et al., 2020], with the use of free vibration modes as a search space basis for shape measurement. Yet in our case, we aim at benefitting from the finite support of spline functions, which offers the possibility to modify a field locally. As a consequence, spline functions lead to a sparse projection matrix with regard to vibration modes, which reduces computational costs. In addition, we enforce less pronounced *a priori* knowledge so as to be able to regularize a large range of FE optimization problems. Indeed, we only prescribe smoothness of the reduced basis by resorting to spline functions.

In the next chapters of this manuscript, several approaches will be detailed and adapted to our three optimization problems.

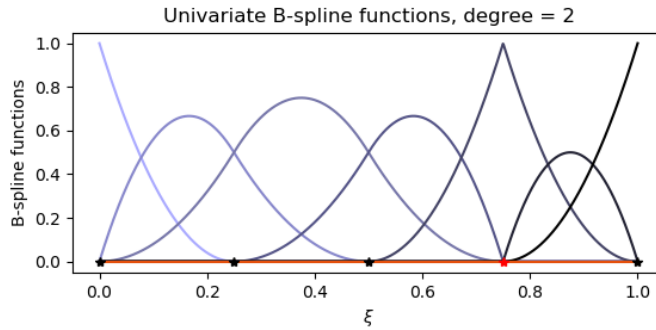
1.2 Spline tools for optimization

Before entering into the details regarding our developed work for optimization in experimental mechanics, some necessary ingredients on spline tools are given in this section.

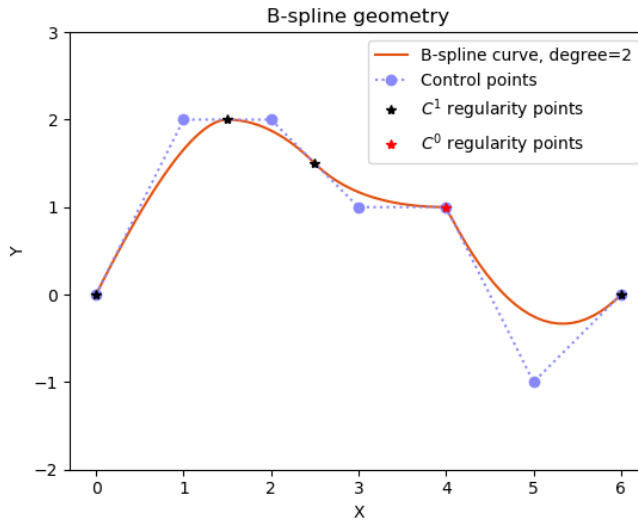
B-spline and NURBS functions are well-known to describe geometries and are classically used to describe CAD models [Cohen et al., 1980, Piegl and Tiller, 1997, Farin, 2002]. In 2005, they have been reintroduced by Hughes et al. for mechanical analyses, leading to an active field of research [Hughes et al., 2005]. Some developed tools, in the mechanical field as well as in other fields where splines are used for shape optimization or image registration, are briefly presented in this section.

1.2.1 Splines

B-spline functions map a δ -orthotope, called the *parametric domain* (e.g. a segment when $\delta = 1$, a rectangle when $\delta = 2$, a parallelepiped when $\delta = 3$, etc), to a continuous geometry of intrinsic dimension δ that lives in a space of dimension D (D can be greater than δ , see Figure 1.11). This geometry is usually called a *patch*. This mapping is entirely defined thanks to a B-spline function basis and



(a) Univariate 2nd-degree B-spline basis associated with the knot vector $\{0, 0, 0, 0.25, 0.5, 0.75, 0.75, 1, 1, 1\}$. The repeated knot decreases the regularity at this parameter value.



(b) B-spline curve defined by the basis of Figure 1.11(a) and the given control point positions.

Figure 1.11: B-spline mapping from the 1D parametric domain to the 2D physical domain. Each control point in Figure 1.11(b) is associated with a B-spline function in Figure 1.11(a).

the coefficients associated with each function, which are control points coordinates.

Mathematically, it reads:

$$\begin{aligned} \underline{\mathcal{S}} &: I \subset \mathbb{R}^\delta \longrightarrow \mathbb{R}^D \\ \underline{\xi} &\longmapsto \underline{\mathcal{S}}(\underline{\xi}) = \sum_{i=1}^{n_{IG}} \tilde{N}_i(\underline{\xi}) \tilde{\mathbf{X}}_i = \underline{\tilde{\mathbf{N}}}^T \underline{\tilde{\mathbf{X}}}, \end{aligned} \quad (1.3)$$

where $\underline{\xi}$ is a parameter living in I the parametric domain, and $(\tilde{N}_i)_{i=1..n_{IG}}$ are the p^{th} -degree δ -variate spline functions associated with the n_{IG} control points $(\tilde{\mathbf{X}}_i)_{i=1..n_{IG}}$ that have D coordinates in the physical space. $\underline{\tilde{\mathbf{N}}}$ gathers all spline functions (that depend on $\underline{\xi}$) in a $D n_{IG} \times D$ matrix and $\underline{\tilde{\mathbf{X}}}$ gathers the positions of all control points in a vector.

The univariate ($\delta = 1$) B-spline basis is entirely defined by a degree p and a knot vector. The knot vector divides the parametric domain into *knot spans* (or *elements*) and controls the continuity between the elements (see Figure 1.11(a)). The B-spline functions are defined recursively and can be evaluated thanks to the Cox-de-Boor algorithm [Piegl and Tiller, 1997]. The δ -variate B-spline basis is constructed as a tensor product of several univariate B-spline bases, as shown in Figure 1.12. Note

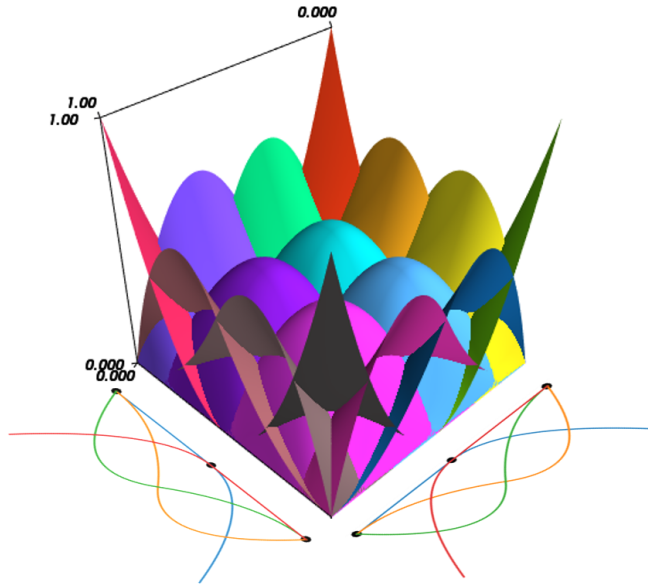


Figure 1.12: Bivariate B-spline basis, made of two 2-element 2^{nd} -degree univariate B-spline bases.

that when knots are repeated, they create zero-size knot spans, that will generally not be counted as elements, as in Figure 1.11(b) description for instance.

B-splines have several interesting properties. The most important for this work is their smoothness. A p^{th} -degree B-spline curve is C^{p-m} -continuous on knots that are repeated m times (see Figure 1.11). Along with their smoothness comes a low number of degrees of freedom to define or control a geometry [Tirvaudey et al., 2017]. Moreover, the B-spline functions support is finite, of size $p + 1$ knot spans, as can be seen in Figure 1.11(a). It means that each control point has a local influence on the B-spline curve geometry. B-splines can also be degree-elevated (degree elevation is sometimes referred to as *p-refinement*), and knots are added to the knot vector without any modification of the geometry (this is called *knot insertion*, or sometimes

h-refinement, see Figure 1.13). *k-refinement* is used to increase both the number of spline elements and the degree while ensuring a maximum regularity (degree elevation is performed before inserting knots) [Hughes et al., 2005, Cottrell et al., 2007]. The algorithms can be found in [Piegl and Tiller, 1997]. Knots can be

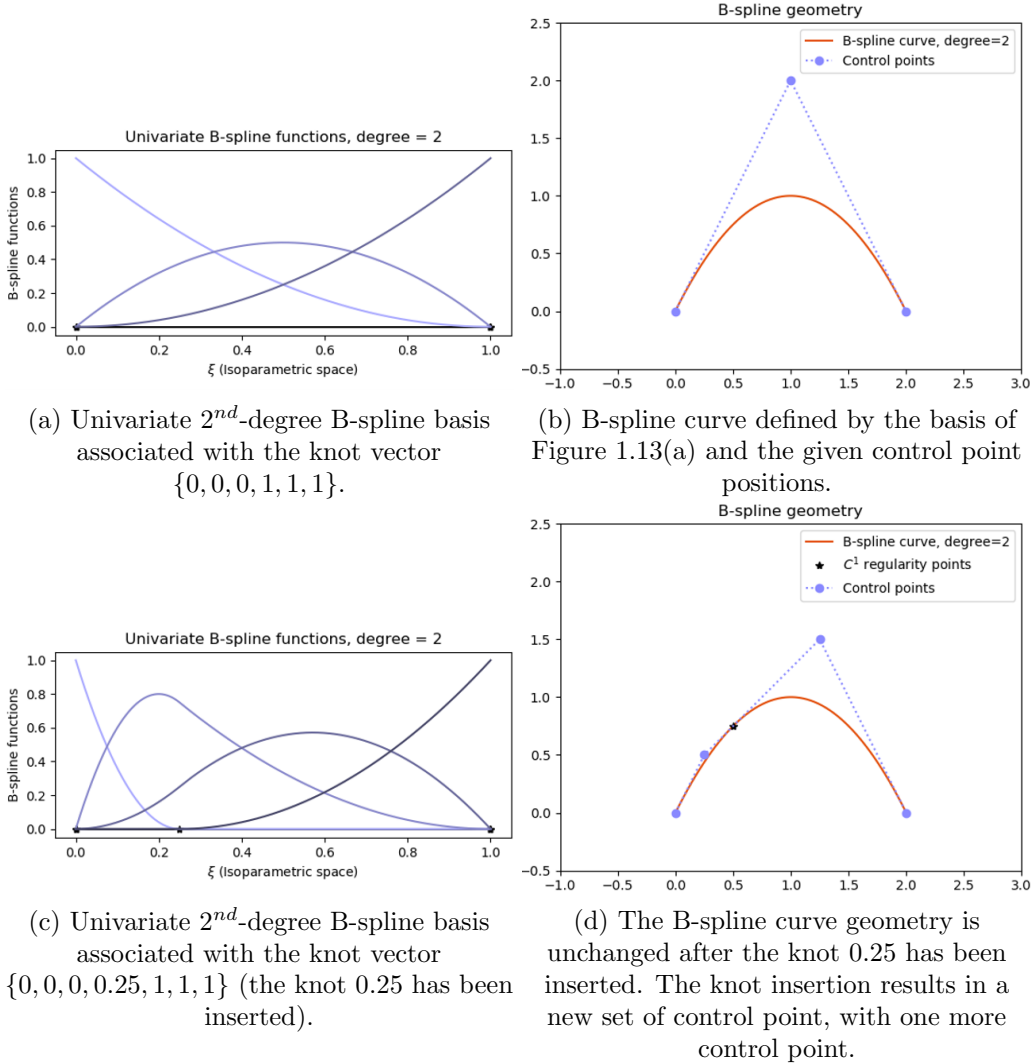


Figure 1.13: Knot insertion to split a 1-element B-spline curve into 2 elements of different sizes. The basis is modified, a control point is added and the positions of the control points are modified. The B-spline curve geometry is unchanged.

inserted on pre-existing knots with the same algorithm. In this case, it increases the multiplicity of the knots. When knot insertion leads to each knot being repeated p times, the process is called *Bézier decomposition* [Borden et al., 2011], and it results in C^0 element boundaries. Both knot insertion and degree elevation process can be implemented as matrices that only depend on knot vectors and degree and then act on the basis or position of the control points [Piegl and Tiller, 1997, Lee and Park, 2002]:

$$\underline{\underline{\tilde{\mathbf{N}}}}^c = \underline{\underline{\mathbf{C}}}_{\text{ref}} \underline{\underline{\tilde{\mathbf{N}}}}^f \quad \text{and} \quad \underline{\underline{\tilde{\mathbf{X}}}}^f = \underline{\underline{\mathbf{C}}}_{\text{ref}}^T \underline{\underline{\tilde{\mathbf{X}}}}^c, \quad (1.4)$$

where $\underline{\underline{\tilde{\mathbf{N}}}}^c$ (resp. $\underline{\underline{\tilde{\mathbf{N}}}}^f$) are the spline functions associated with the coarse (resp. fine) spline mesh, $\underline{\underline{\tilde{\mathbf{X}}}}^c$ (resp. $\underline{\underline{\tilde{\mathbf{X}}}}^f$) are the spline control point positions associated with the coarse (resp. fine) spline mesh, and $\underline{\underline{\mathbf{C}}}_{\text{ref}}$ is the refinement matrix.

NURBS (Non-Uniform Rational B-Spline) functions are built from B-spline functions (they are fractions of B-splines), and they offer an exact representation of conics (circles, ellipses, etc). Therefore, they share most of their properties with B-spline functions. An example is given Figure 1.14 and further information can be found in [Piegl and Tiller, 1997, Cottrell et al., 2007] and in Chapter 2.

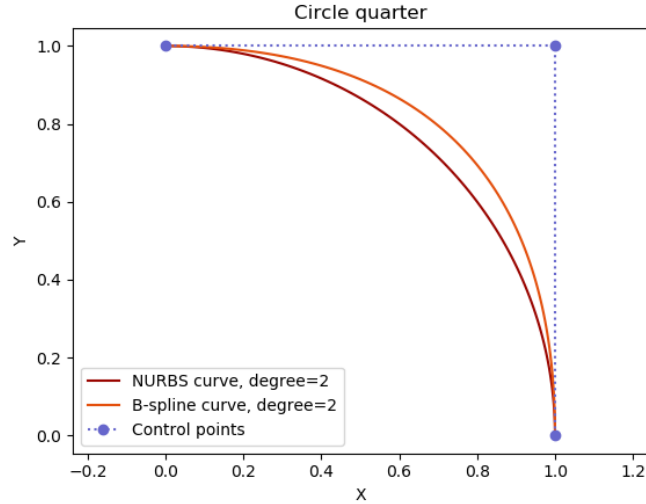


Figure 1.14: Comparison of a NURBS curve with circle weights on control points, and a B-spline curve with the same control points. The weight $\frac{1}{\sqrt{2}}$ for the middle control point allows the NURBS curve to exactly represent a circle.

1.2.2 Isogeometric analysis

Once a geometry is created, it is possible to solve mechanical problems in the spline vector space defined by the spline mesh, similarly to what is done with FE. This way of performing the mechanical analysis in the spline space, called *IsoGeometric Analysis* (IGA), has been introduced by [Hughes et al., 2005]. It was then applied to shape optimization by [Wall et al., 2008]. The exact refinement procedures, and especially knot insertion, were finally used to create several levels of refinement for different purposes [Nagy et al., 2011, Nagy et al., 2013, Kiendl et al., 2014, Hirschler et al., 2019b], as can be seen in Figure 1.15.

Creating boundary-fitted analysis-suitable geometries with splines for standard IGA is not straightforward. Complex CAD models generally imply trimmed curves or surfaces to describe almost any geometry (see *e.g.* Figure 1.16) but the link toward an analysis-suitable model is not automatic and may require defining several spline patches [Bouclier, 2020].

Yet, with a single patch and a well-chosen parameterization, it is possible to create geometries with simple topology but complex edges. Figure 1.17 shows an example with a geometry similar to the specimen of Figure 1.9 but with a single hole. With this geometry, we obtain sensitivity fields that are close to the ones of [Chamoïn et al., 2020] (see Fig. 1.18).

1.2.3 Non-invasive CAD-based optimization

Another advantage of B-spline functions is that they are naturally part of the FE vector space and thus generate a vector subspace of the FE space. Splines are

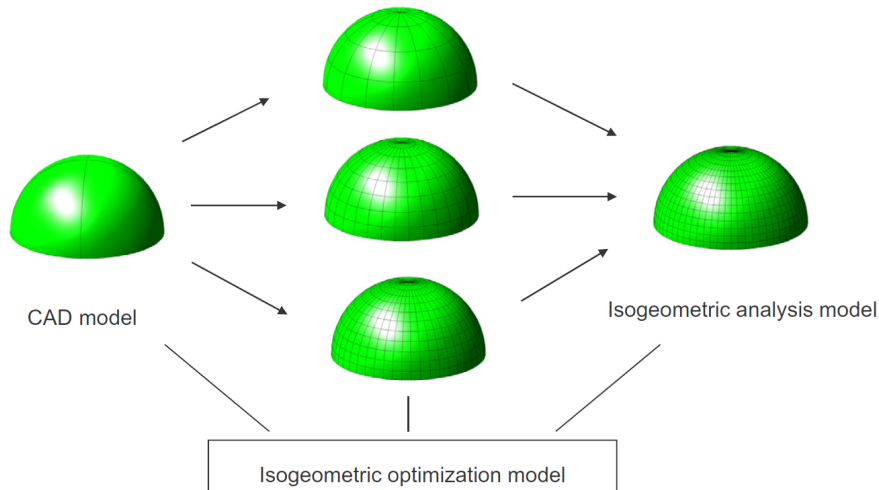


Figure 1.15: Different models with different levels of refinement. The *CAD model* is the coarsest mesh to describe the initial geometry. The *optimization model*, or *design model* is refined at the right level to define a search space with control point positions. A fine design model allows for more geometry modifications but regularizes less the optimization problem. The *analysis model* is refined enough to get reasonably small errors coming from the discretization space to solve the mechanical problem. The advantage of spline functions is that the analysis model and the design model define the exact same geometry thanks to the spline exact refinement procedures. Furthermore, this refinement can be done with a matrix that has to be computed only once between two given refinement levels (see Equation (1.4)). (figure taken from [Kiendl et al., 2014]).

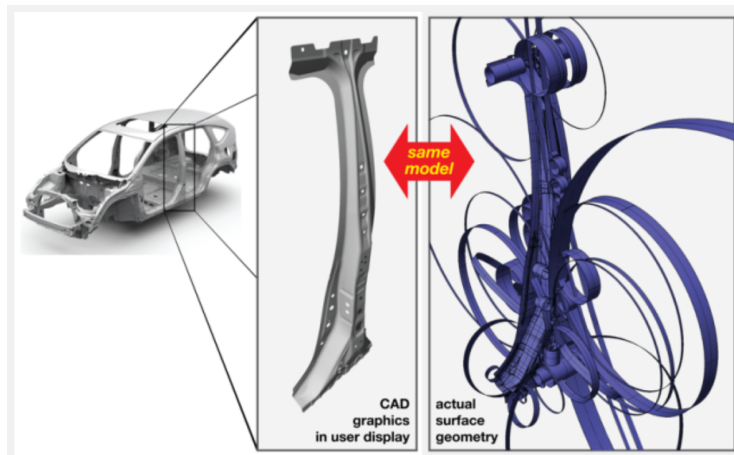


Figure 1.16: Conventional CAD model of an automotive part. The left figure shows the graphic display and the right figure shows the data structure. The geometry is made of more than 1200 trimmed surfaces. (figure taken from [Urick and Marussig, 2017]).

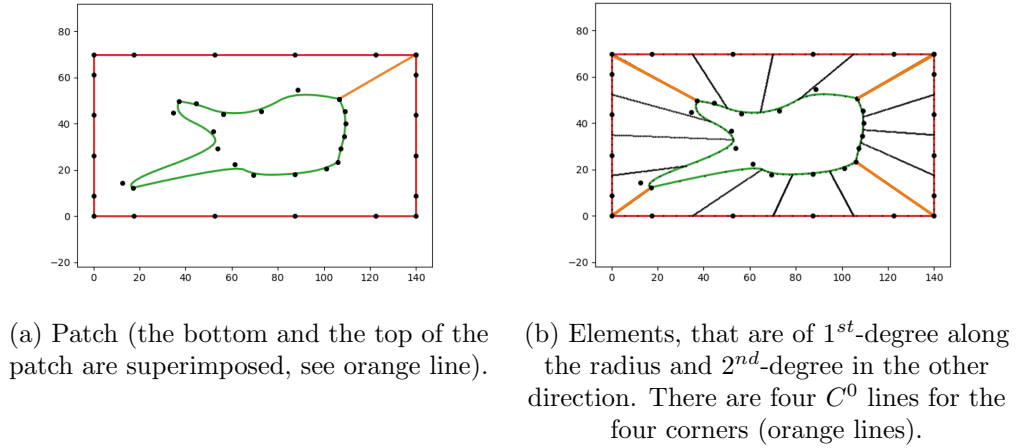
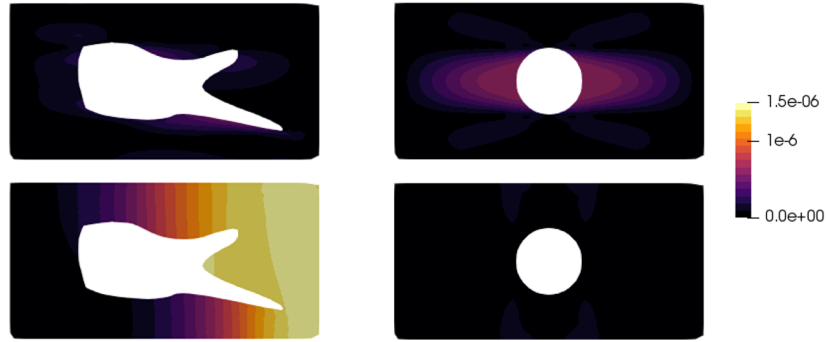
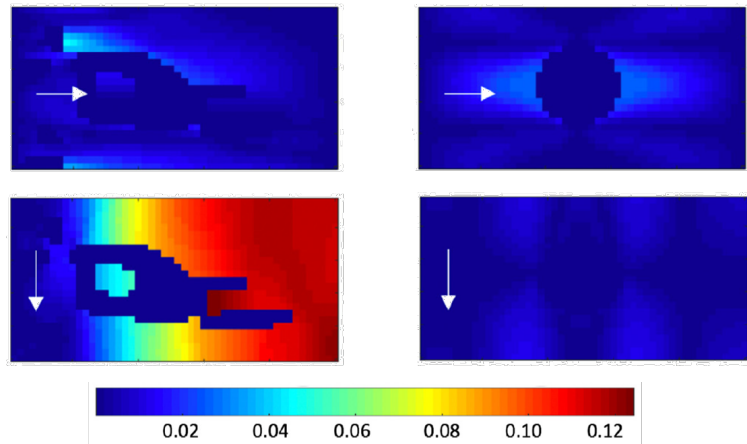


Figure 1.17: Boundary-fitted bivariate B-spline geometry for a specimen with a complex hole.



(a) IGA results. Scale in mm/MPa. The constitutive law is an orthotropic linear elastic law with $E_1 = 1 \times 10^5$ MPa, $E_2 = 1.9 \times 10^5$ MPa, $\nu_{12} = 0.3$ and $G_{12} = 1 \times 10^4$ MPa. The boundary conditions are a fixed upper left corner, the down left corner can move only along y , and a displacement is imposed only along x on the right edge (it is free along y).

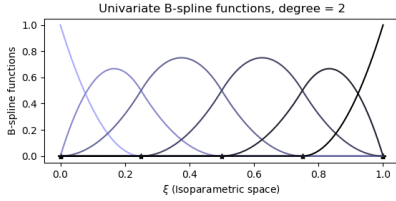


(b) Figure taken from [Chamoin et al., 2020].

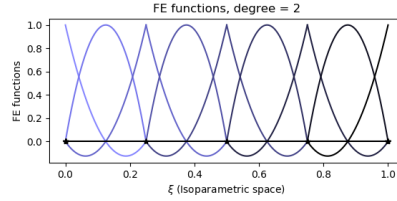
Figure 1.18: Sensitivity to the shear modulus $\frac{dU}{dG_{12}}$.

1.2. SPLINE TOOLS FOR OPTIMIZATION

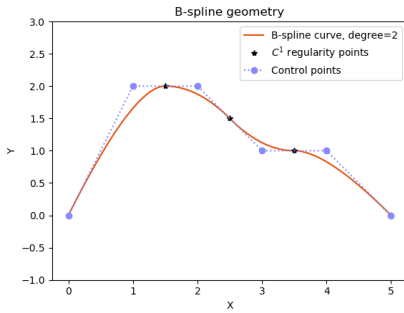
defined piecewise by polynomials of degree p . Therefore, they can be written inside an element as a linear combination of $p+1$ Lagrange polynomials of degree p defined in the same element, *i.e.* by standard FE functions defined on the same mesh. Note that a C^{p-1} B-spline basis (or even a less regular B-spline basis if knots are repeated) can be expressed as a linear combination of C^0 FE functions, but the reverse is not true (see Figure 1.19 for an example); the C^0 features cannot be obtained without changing the spline basis to decrease its regularity (by increasing knots multiplicity thanks to Bézier decomposition [Borden et al., 2011]). The regular spline space is thus included in the corresponding C^0 FE space.



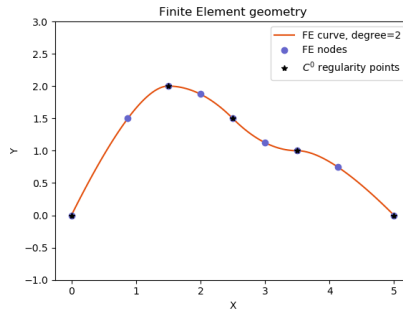
(a) Univariate 2^{nd} -degree B-spline basis with 4 elements (knot vector: $\{0, 0, 0, 0.25, 0.5, 0.75, 1, 1, 1\}$).



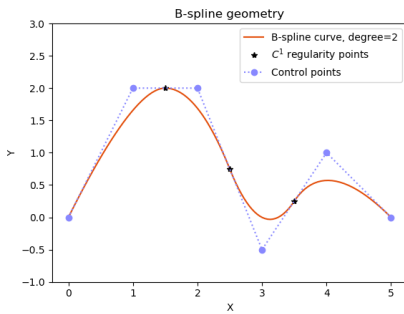
(b) 2^{nd} -degree standard FE basis with 4 elements.



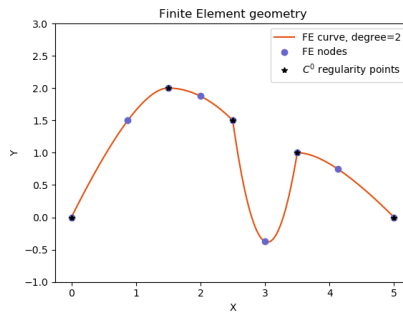
(c) B-spline geometry associated with the basis of Figure 1.19(a) and the given control point positions.



(d) Exact same geometry as Figure 1.19(c), described with the FE basis of Figure 1.19(b).



(e) It is not possible to generate the same geometry as Figure 1.19(f) with the regular B-spline basis. Moving just one control point preserves the C^1 continuity.



(f) C^0 geometry obtained by moving a FE node.

Figure 1.19: 2^{nd} -degree example of the link between B-spline basis and FE basis. The B-spline basis can be constructed from standard FE functions, so a B-spline geometry can be exactly described by a FE geometry, but the reverse is not true. The C^1 B-spline vector space is contained within the C^0 FE vector space.

Hence, a direct link, called *Lagrange extractor*, exists between the B-spline basis

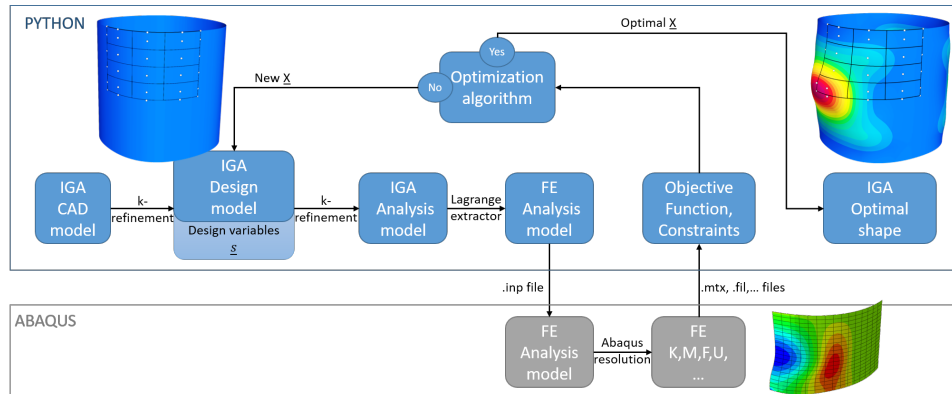
and the FE basis. It can be seen as an extraction of the regular part of the FE space, which is the IGA space. This link can be written in a matrix form [Schillinger et al., 2016, Tirvaudey et al., 2019]. The same matrix also links the control point positions to the FE node positions, similarly to Equation (1.4):

$$\underline{\tilde{\mathbf{N}}} = \underline{\mathbf{C}}_{\text{Lag}} \underline{\mathbf{N}} \quad \text{and} \quad \underline{\mathbf{X}} = \underline{\mathbf{C}}_{\text{Lag}}^T \underline{\tilde{\mathbf{X}}}, \quad (1.5)$$

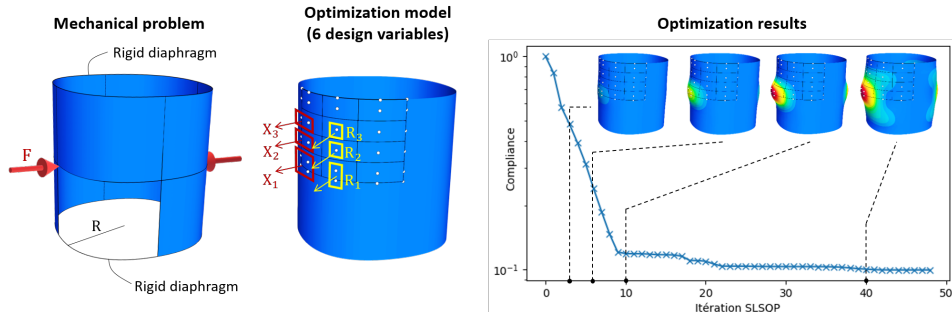
where $\underline{\tilde{\mathbf{N}}}$ (resp. $\underline{\mathbf{N}}$) are the shape functions associated with the spline (resp. FE) mesh, $\underline{\tilde{\mathbf{X}}}$ are the spline control point positions associated with the spline mesh, $\underline{\mathbf{X}}$ are the FE nodes positions associated with the FE mesh, and $\underline{\mathbf{C}}_{\text{Lag}}$ is the Lagrange extractor matrix.

Note that in the case of rational splines such as NURBS, the spline vector space is not strictly contained within the FE vector space. However, an approximate link can still be defined. Further information can be found in [Schillinger et al., 2016, Tirvaudey et al., 2019] and in Chapter 2. This link makes possible the use of FE mechanical operators in an IGA framework, and thus eases the coupling of IGA software with FE software.

Following the idea of several refinement levels for different models proposed by [Kiendl et al., 2014], it is possible to use this link in a shape optimization process, in order to perform the analysis on a FE mesh, which we validated with the shape optimization of a pinched cylinder with respect to compliance [Hirschler et al., 2019b], thanks to a coupling between our Python algorithms and *Abaqus* (see Figure 1.20 and Appendix A.1). In this work, an analysis-suitable CAD model of a



(a) CAD-based shape optimization framework with *Abaqus*.



(b) Shape optimization process for the pinched cylinder.

Figure 1.20: CAD-based shape optimization. Results shown in [Bouclier et al., 2019].

cylinder has been created with Python. Thanks to symmetries in loading, geometry and boundary conditions, only one eighth of the cylinder has been modeled,

with a single 2^{nd} -degree one-element B-spline patch (see Figure 1.20(b) on the left). This CAD model has then been refined into a 3×4 -element design (or optimization) model, and 12 control points have been selected to define 6 design variables. Some control points have been grouped in order to preserve G^1 continuity at symmetry boundaries (see Figure 1.20(b) in the middle). Then, a refinement level for the analysis model is chosen and the refinement operator $\underline{\underline{\mathbf{C}}}_{\text{ref}}$ is computed (see Equation (1.4)). The matrix form of the Lagrange extractor $\underline{\underline{\mathbf{C}}}_{\text{Lag}}$ can also be computed at this time.

After this initialization phase, the optimization phase starts. At each iteration, the IGA analysis model is created thanks to $\underline{\underline{\mathbf{C}}}_{\text{ref}}$, then the Lagrange extractor $\underline{\underline{\mathbf{C}}}_{\text{Lag}}$ gives the FE nodes positions that define the exact same geometry with $Q9$ FE elements (2^{nd} -degree quadrangles with 9 nodes). Note that these two steps can be done at once by multiplying the two matrix operators $\underline{\underline{\mathbf{C}}}_{\text{ref}}$ and $\underline{\underline{\mathbf{C}}}_{\text{Lag}}$. The FE analysis model is given to *Abaqus* to compute the desired mechanical quantities (stiffness matrix, mass matrix, force or displacement vectors for instance), that are then read by a Python script to calculate the cost and constraint functions values. These values are taken into account by a chosen optimization algorithm that either proposes a new set of values for the design variables for the next iteration, or ends the optimization phase if a given criterion is met. The final design is expressed on the IGA design model. It can also easily be expressed on the analysis FE mesh thanks to the refinement operator and the Lagrange extractor.

This approach is therefore different from isogeometric shape optimization, in the sense that no routines have been developed to compute the spline shell mechanical quantities. We used the exact link between B-spline functions and FE functions, which means that the FE mechanical operators such as the stiffness matrix and the mass matrix could then be projected exactly in the IGA space [Schillinger et al., 2016, Tirvaudey et al., 2019], and the only requirement to get these matrices was to provide the right FE node positions as an input. This non-invasive approach allows using FE software for IGA purposes, and in the context of shape optimization, this non-invasive CAD-based optimization method takes advantage of spline properties and of all complex mechanical behaviors that are already implemented in industrial FE software.

This non-invasive CAD-based approach will be used in Chapter 2. However, the cost function is different and other mechanical operators are involved. The Python framework that has been developed here for the minimization of compliance on a pinched cylinder and shown Figure 1.20(a) in the blue frame will be used with another FE software dedicated to digital image correlation instead of *Abaqus*.

Remark 1 *The cylinder has been described by B-spline functions to get an exact link with $Q9$ FE functions but NURBS functions would have been more adapted to describe an exact circle. As we have seen earlier, using NURBS functions stops us from having an exact link with FE standard functions. Yet the quality of the approximated link to go from a NURBS geometry to a FE geometry increases as the mesh is refined [Tirvaudey et al., 2019], which makes it acceptable in this case where the link is used for the fine analysis model.*

Remark 2 *$Q9$ elements could not be used with *Abaqus*. Thus, we performed an additional approximation by removing the center node of each FE element to get a $Q8$ FE mesh (2^{nd} -degree quadrangles with 8 nodes). The FE mesh was supposed to be fine enough so that it would not affect the results too much.*

1.2.4 FFD-based optimization

To modify complex geometries without creating a boundary-fitted spline model of the initial geometry, the *Computer Graphics* field has introduced the *Free-Form Deformation* (FFD) concept [Sederberg and Parry, 1986]. It consists in embedding the initial geometry, which can be defined by a set of points for instance, into a morphing box. Then, the user deforms the morphing box, and the embedded geometry is deformed accordingly (see Figure 1.21 and Figure 3.1). A spline basis is generally chosen to describe the morphing box deformation, because of their smoothness and the low number of dof needed to describe geometries. This tool has also been used in

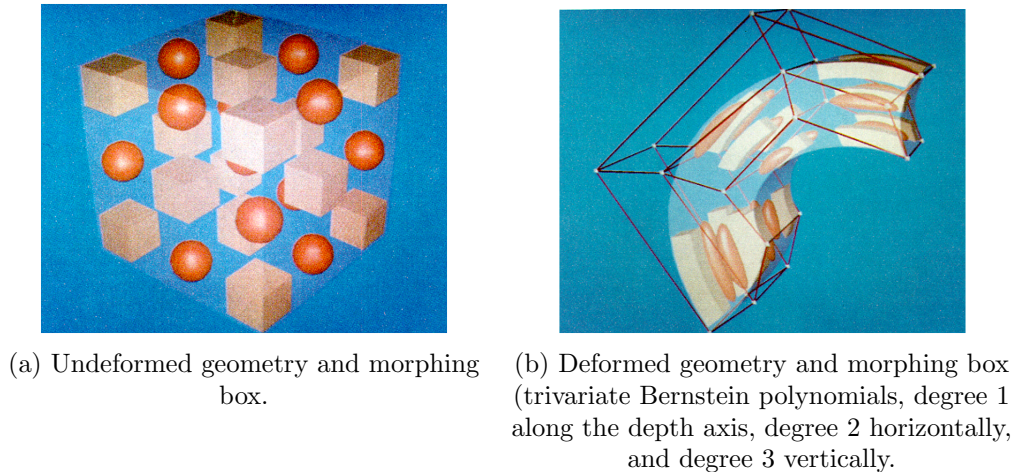


Figure 1.21: Free-Form Deformation. (figure taken from [Sederberg and Parry, 1986]).

the mechanical engineering field for the shape optimization of plane wings [Kenway et al., 2010, Lassila and Rozza, 2010]. In the aeronautical industry, FE meshes of structures are often given *a priori* and using FFD allows to slightly update the geometry without modifying the mesh and its connectivity, typically while optimizing the wing shape with respect to aerodynamics quantities.

A FFD-based approach is interesting because it decouples the design space from that of the geometry description. For instance, the geometry can be described by an analysis-suitable FE mesh (arbitrarily defined, which means that it does not necessarily comes from an analysis-suitable CAD mesh) and the design space can be a smooth spline space with much less dof than the FE mesh. The spline functions are thus not defined on the same mesh as the FE functions and the defined spline vector space is not necessarily contained within the FE vector space. It gives the opportunity to work with possibly any structure geometry and any FE mesh with spline design variables.

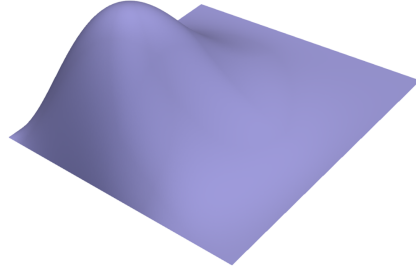
Still in the case when a FE mesh is embedded, we can apply the morphing box deformation to the FE nodes (it could also be applied to any point of the FE mesh, see Section 3.1.2 for more details). Each FE node position is defined as a linear combination of the morphing box control point positions, and moving a control point deforms the FE mesh accordingly. This linear combination can be written in a matrix form:

$$\underline{\mathbf{X}} = \underline{\mathbf{C}}_{\text{FFD}}^T \tilde{\mathbf{X}}_{\text{mb}}, \quad (1.6)$$

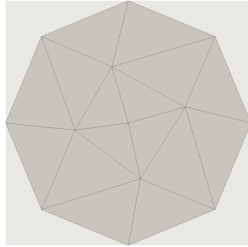
where $\underline{\mathbf{X}}$ are the FE node positions associated with the FE mesh, $\tilde{\mathbf{X}}_{\text{mb}}$ are the spline control point positions associated with the spline mesh of the morphing box, and

$\underline{\underline{\mathbf{C}}}_{\text{FFD}}$ is the FFD matrix.

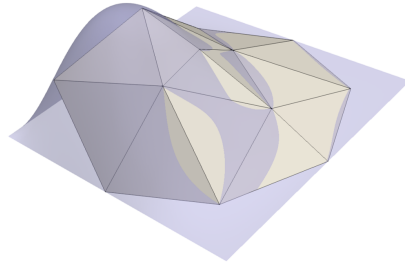
Note that we do not have the same relation on the shape functions $\underline{\mathbf{N}}$ and $\underline{\tilde{\mathbf{N}}}_{\text{mb}}$. In fact, $\underline{\underline{\mathbf{C}}}_{\text{FFD}} \underline{\mathbf{N}}$ provides a restriction and a discretization of spline functions (see Figure 1.22).



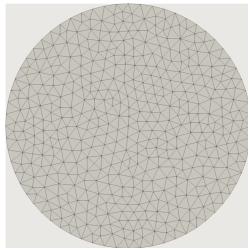
(a) A bivariate 2^{nd} -degree B-spline shape function for a 2×2 -element patch, in the spline morphing box parametric domain.



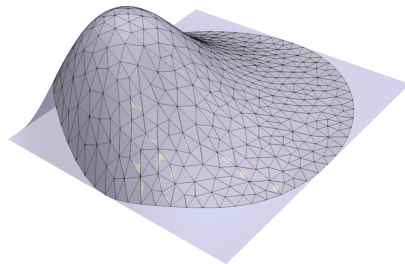
(b) Coarse FE mesh of a disk, in the spline morphing box parametric domain.



(c) Result of $\underline{\underline{\mathbf{C}}}_{\text{FFD}} \underline{\mathbf{N}}$ for the spline function of Figure 1.22(a) and the coarse FE mesh, in the spline morphing box parametric domain.



(d) Fine FE mesh of a disk, in the spline morphing box parametric domain.



(e) Result of $\underline{\underline{\mathbf{C}}}_{\text{FFD}} \underline{\mathbf{N}}$ for the spline function of Figure 1.22(a) and the fine FE mesh, in the spline morphing box parametric domain.

Figure 1.22: Illustration of the restriction and discretization resulting from $\underline{\underline{\mathbf{C}}}_{\text{FFD}} \underline{\mathbf{N}}$ on a bivariate quadratic B-spline function. This figure clearly shows that

$$\underline{\tilde{\mathbf{N}}}_{\text{mb}} \neq \underline{\underline{\mathbf{C}}}_{\text{FFD}} \underline{\mathbf{N}}.$$

Yet the matrix formulation allows for a non-invasive approach thanks to a projection on the smoother space defined by the set of discretized spline functions that can be seen as smooth modes. This approach will be further detailed in Chapter 3.

Note that in the case when the morphing box and the FE mesh describe the same domain (within the accuracy due to facetization), $\underline{\underline{\mathbf{C}}}_{\text{FFD}} \underline{\underline{\mathbf{N}}}$ provides a discretization only of spline functions, and the geometry of the morphing box becomes the geometry of interest. This approach will be used in Chapter 4 to describe the geometry of a specimen hole edges.

Conclusion

We have seen that the three studied optimization problems share similar issues, caused by the choice of a search space that is both too large and not regular enough. To tackle these issues, we propose to use spline functions, typically B-spline and NURBS functions. They present some interesting properties, for instance their high regularity, their finite support and their capacity to be exactly refined or degree-elevated. Thanks to the Lagrange extractor, an exact link can be created between a spline description and a standard FE description of a structure. This link will be studied in the next chapter in the context of FE-DIC shape measurement, and a non-invasive implementation will be proposed. An FFD-based generalization will then be used in Chapters 3 and 4.

Chapter 2

CAD-based regularization of DIC problems

This chapter is extracted from [Colantonio et al., 2020].

Introduction

When carrying out experiments to measure 3D displacement fields on structure surfaces, a first calibration step is necessary. This step consists in determining the camera parameters and the actual shape of the structure. For the latter, an analysis-suitable FE mesh has to be used to get a direct coupling between the measured fields and FE simulation results. In FE simulations, and thus in FE stereo-DIC (FE-SDIC), a unique interpolation subspace is generally used for both the approximation of the geometry and of the displacement (basic principle of isoparametric finite elements), and the associated unique mesh that describes the geometry has to be corrected to take into account the real structure shape. However, the shape of the specimen is generally rather smooth and regular and it should require less degrees of freedom than the displacement field which may comprise important gradients.

As has been seen in the previous chapter, the shape measurement problem shares similarities with standard shape optimization problems. Indeed, the shape measurement problem consists in finding a shape correction that minimizes a functional based on the grayscale mismatch between several images (see Section 2.1.2). This functional can be understood as the cost function of an optimization problem. Therefore, we draw inspiration from techniques that have been developed in the shape optimization community. Among them, the computer-aided-design (CAD)-based approach relies on the same spline-based functions as in CAD software to describe the geometry [Cohen et al., 1980, Piegl and Tiller, 1997, Farin, 2002]. The design variables are this time the spatial location of the control points of the spline entities, which allows to get a light and smooth parametrization of the geometry and of its update [Braibant and Fleury, 1984, Olhoff et al., 1991]. The difficulty in this second family of methods is then transferred to the connection of the (spline-based) geometric and (FE-based) analysis models [Hasan Imam, 1982, Bletzinger et al., 1992]. To answer this issue, one way to naturally proceed is to use the isogeometric analysis (IGA) framework [Hughes et al., 2005, Cottrell et al., 2009] which allows to discretize the structure with its intrinsic, spline-based, CAD geometric definition. Isogeometric (IG) shape optimization has thus been successfully applied to a

wide range of applications (see [Nagy et al., 2011, Nagy et al., 2013, Kiendl et al., 2014, Hirschler et al., 2019b, Wang et al., 2018] among others). More precisely, it is based on a multilevel design concept offered by the spline technology in which one can refine the geometry without altering its initial shape and regularity [Cottrell et al., 2007]. As a consequence, different refinement levels of the same spline-based geometry are considered to define both design and analysis spaces. The coarser level is dedicated to the parametrization of the shape to get "realistic" structures while the finer level defines the analysis model and is set to ensure good quality of the mechanical solution (see Figure 1.15).

A first attempt in applying IGA to shape measurement has been recently performed by Dufour *et al.* [Beaubier et al., 2014, Dufour et al., 2015a, Dufour et al., 2016]. In these pioneering works, the authors considered a higher-order B-spline (monolevel) parametrization of the surface (thereby acting on a geometrical object which is consistent with CAD) both for shape and displacement measurements. The authors also went towards the identification of mechanical models by comparing the measured IG displacement field with a computed one using a dedicated IG code [Dufour et al., 2015b]. However, besides the effort to implement spline functions in the SDIC framework, the problem is that the user ends up with an experimental displacement field that is expressed on a spline basis, whereas most simulation tools are based on finite elements. Splines clearly provide flexibility for shape and displacement measurements but make connection with most of today's numerical models more complex, which is the key advantage of global approaches in DIC.

In this chapter, we build a hybrid IG-FE methodology for mesh-based shape measurement that draws up the best of each technology. On the one hand, we consider as input and output the FE mesh that is fine enough to properly describe the underlying mechanics. In the second step, the FE mesh will thus be suitable for displacement measurement using stereo-correlation and this resulting kinematic field will be easily compared to a computed one obtained from existing, standard FE codes. On the other hand, we undertake to use the splines along with the IG multilevel design concept (performed in shape optimization, see Figure 1.15) for the description of the geometry and of its update in the shape measurement process. The idea here is to couple the multilevel optimization process [Kiendl et al., 2014] with the multiscale initialization of shape measurement [Pierré, 2016] to get different approximation spaces which naturally follow, at each level, the resolution of the image. The regularization level is thus given by the refinement of the spline spaces which is chosen in accordance with the coarsening of the images (no needs of additional regularization terms). Since it is based on functions coming from the geometric design community, the proposed regularization scheme has a strong geometrical meaning, that is why we refer to geometric regularization to characterize the technique.

The additional ingredient of our approach is to make use of a recently developed global bridge between IGA and FE analysis (FEA) [Tirvaudey et al., 2019] to be able to communicate between the different approximation subspaces for the geometry (multilevel spline-based parametrizations) and for the displacement (analysis-suitable FE mesh). Based on the original idea behind Bézier extraction [Borden et al., 2011] and on more recent Lagrange extraction [Schillinger et al., 2016], this global transformation goes from Lagrange polynomials to (possibly rational) spline basis, thus allowing to recover an IG operator without implementing IGA but simply by projecting an FE operator onto the reduced, more regular, IG basis. As a result, besides its attractive regularizing features, the implementation of the proposed strategy is non-invasive with respect to FE-SDIC (as has been seen in Section 1.2.3).

The chapter is organized as follows: after this introduction, Section 2.1 specifies the calibration phase occurring in FE-SDIC with a particular emphasis on the shape measurement problem. Then, Section 2.2 is devoted to the development of the proposed geometric regularization scheme while Section 2.3 assesses the performance of the methodology through the analysis of several real images and comparisons with other published techniques. This brings us to the last section where concluding remarks are drawn.

2.1 Mesh-based shape measurement

Let us assume that we have an existing description (say a CAD model) of the nominal geometry of the specimen. Let Ω_s be a surface domain referred to as Region of Interest (ROI) and such that $\Omega_s \subset \mathbb{R}^3$ corresponds to the visible surface of the theoretical shape. This representation does not correspond exactly to the actual shape of the specimen, because of surface roughness, manufacturing defects, pre-load or relaxation of residual stresses, to name a few. In SDIC, the estimation of the real surface is of the utmost importance because it is an essential prerequisite for 3D surface displacement measurement. It may also be used to update the model geometry in validation and/or identification procedures, since kinematic fields may significantly depend on it.

2.1.1 Camera model

As classically done in SDIC [Sutton et al., 1999], each camera c is equipped with a camera model \underline{P}_c that maps any 3D point $\underline{X} \in \Omega_s$ expressed in the world reference system \mathcal{R}_w to the corresponding coordinates in pixels \underline{x}_c in the image frame and is written as:

$$\underline{P}_c : \mathbb{R}^3 \rightarrow \mathbb{R}^2, \quad \underline{X} \mapsto \underline{x}_c = \underline{P}_c(\underline{X}, \underline{p}_c), \quad \forall \underline{X} \in \Omega_s, \quad (2.1)$$

where \underline{p}_c is a vector collecting the model parameters. More precisely, camera models \underline{P}_c can be either linear (in homogeneous coordinates) or non-linear to take into account lens distortions. It depends on two sets of parameters: the intrinsic parameters (focal length, image center, horizontal/vertical aspect ratio, skew and possible distortion parameters) and the extrinsic parameters (3 rotations and 3 translations that map the reference frame of the specimen \mathcal{R}_w to that of the imaging sensor \mathcal{R}_c). The calibration of these parameters must be conducted prior to any measurement. In this study, intrinsic parameters are calibrated using calibration targets and a classic photogrammetric technique as described in [Lavest et al., 1998, Garcia, 2001]. In the remainder of this chapter, the intrinsic parameters will be assumed to be known and only the extrinsic parameters will be considered, such that for each camera c , the camera model \underline{P}_c will be entirely defined by $\underline{p}_c \in \mathbb{R}^6$.

2.1.2 Coupled calibration and shape measurement problem

As depicted in Figure 2.1, the graylevel conservation assumption [Horn and Schunck, 1981] supposes that the graylevel value $\mathcal{I}_c(\underline{x}_c)$ of the projections \underline{x}_c in each image \mathcal{I}_c of any 3D point \underline{X} should be equal: $\mathcal{I}_0(\underline{x}_0) = \mathcal{I}_1(\underline{x}_1)$. Since both the actual shape and position of the specimen (with respect to the stereo rig) are not known exactly, the graylevel conservation is not fulfilled. The calibration of the stereo rig thus consists in a coupled problem aiming at finding the extrinsic parameters $\underline{p} = [\underline{p}_0, \underline{p}_1]$ in addition to a shape correction field $\underline{S}(\underline{X}), \forall \underline{X} \in \Omega_s$, such that the advection of the nominal surface Ω_s by the correction field $\underline{S}(\underline{X})$ corresponds to the

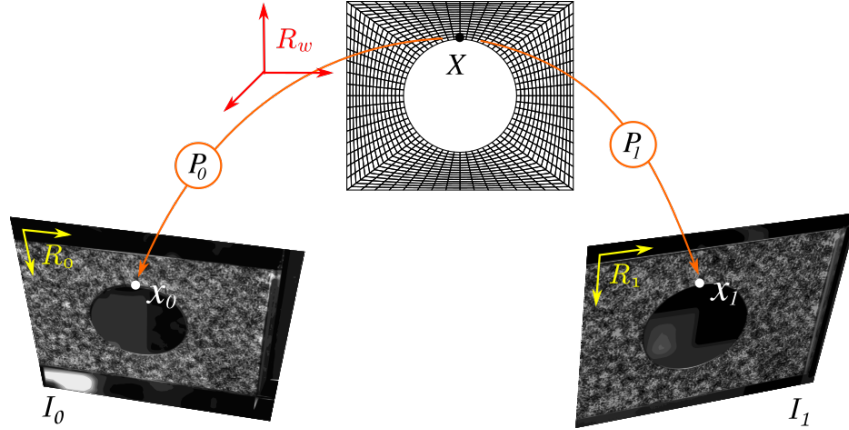


Figure 2.1: Principle of the formulation of the SDIC problem in the reference frame of the FE model. A 3D point \underline{X} and its projections \underline{x}_0 and \underline{x}_1 onto the image planes.

actual surface. More precisely, shape correction and camera parameters minimize the graylevel mismatch:

$$\begin{aligned} \underline{S}^*, \underline{p}^* &= \arg \min_{\underline{S} \in L_2(\Omega_s), \underline{p} \in \mathbb{R}^{12}} \mathcal{F}_S(\underline{S}(\underline{X}), \underline{p}) \\ \text{with } \mathcal{F}_S(\underline{S}(\underline{X}), \underline{p}) &= \frac{1}{2} \int_{\Omega_s} \left(r(\underline{S}(\underline{X}), \underline{p}) \right)^2 d\underline{X}, \end{aligned} \quad (2.2)$$

and where the graylevel residual $r(\underline{S}(\underline{X}), \underline{p})$ is defined $\forall \underline{X} \in \Omega_s$ as:

$$r(\underline{S}(\underline{X}), \underline{p}) = \mathcal{I}_0(\underline{P}_0(\underline{X} + \underline{S}(\underline{X}), \underline{p}_0)) - \mathcal{I}_1(\underline{P}_1(\underline{X} + \underline{S}(\underline{X}), \underline{p}_1)). \quad (2.3)$$

Let us highlight, at this stage, that the graylevel residual is defined in Ω_s in the reference system of the model, which differs from subset based SDIC, where it is written in the image frames.

The unknown vector \underline{p} gathering the extrinsic parameters is already discrete, but the shape correction field \underline{S} lies in an infinite space. To solve Problem (2.2) an approximation subspace for \underline{S} must be defined. To be consistent with the description of the geometry and displacements in FE simulations, \underline{S} is searched for in an analysis-suitable FE subspace [Pierré et al., 2017]:

$$\underline{S}(\underline{X}) = \sum_{i=1}^{n_{FE}} N_i(\underline{X}) \underline{S}_i = \underline{\mathbf{N}}^T(\underline{X}) \underline{\mathbf{S}}, \quad (2.4)$$

where $\underline{\mathbf{N}}$ is a $(3n_{FE} \times 3)$ matrix gathering the n_{FE} Lagrange shape functions N_i

and $\underline{\mathbf{S}}$ is a vector that collects the $3n_{FE}$ corresponding degrees of freedom (DOF):

$$\underline{\underline{\mathbf{N}}} = \begin{bmatrix} N_1 & 0 & 0 \\ \vdots & \vdots & \vdots \\ N_{n_{FE}} & 0 & 0 \\ 0 & N_1 & 0 \\ \vdots & \vdots & \vdots \\ 0 & N_{n_{FE}} & 0 \\ 0 & 0 & N_1 \\ \vdots & \vdots & \vdots \\ 0 & 0 & N_{n_{FE}} \end{bmatrix} \quad \text{and} \quad \underline{\mathbf{S}} = \begin{bmatrix} S_1^1 \\ \vdots \\ S_{n_{FE}}^1 \\ S_1^2 \\ \vdots \\ S_{n_{FE}}^2 \\ S_1^3 \\ \vdots \\ S_{n_{FE}}^3 \end{bmatrix}, \quad (2.5)$$

In addition, note that \underline{S}_i in (2.4) is the subset of $\underline{\mathbf{S}}$ gathering the three components $\{S_i^1, S_i^2, S_i^3\}$ of the field $\underline{S}(\underline{X})$ associated with shape function N_i . Problem (2.2) is a non-linear least-square problem. Its resolution is based on a fixed point algorithm which consists in alternatively minimizing the graylevel functional \mathcal{F}_S with respect to \underline{p} (calibration) and to $\underline{\mathbf{S}}$ (shape measurement).

Minimization with respect to camera parameters. The shape correction field $\underline{S}(\underline{X})$ being fixed, the set of parameters \underline{p} is the solution of the calibration problem:

$$\underline{p}^* = \arg \min_{\underline{p} \in \mathbb{R}^{12}} \mathcal{F}_S(\underline{S}(\underline{X}), \underline{p}) \quad (2.6)$$

Such a non-linear least-square problem is efficiently solved using a Gauss-Newton [Passieux and Bouclier, 2019], see [Pierré et al., 2017] for details.

Minimization with respect to shape correction field. The extrinsic camera parameters \underline{p} being fixed, the DOF vector $\underline{\mathbf{S}}$ is the solution of the shape measurement problem:

$$\underline{\mathbf{S}}^* = \arg \min_{\underline{\mathbf{S}} \in \mathbb{R}^{3n_{FE}}} \mathcal{F}_S(\underline{\underline{\mathbf{N}}}^T(\underline{X}) \underline{\mathbf{S}}, \underline{p}) \quad (2.7)$$

This non-linear least-square problem is also solved using a Gauss-Newton algorithm. At iteration k , the solution is sought as $\underline{\mathbf{S}}^{(k)} = \underline{\mathbf{S}}^{(k-1)} + \delta \underline{\mathbf{S}}^{(k)}$, where the descent direction $\delta \underline{\mathbf{S}}^{(k)}$ is the solution of the following linear system [Pierré et al., 2017]:

$$\begin{aligned} \underline{\underline{\mathbf{H}}}_S^{(k)} \delta \underline{\mathbf{S}}^{(k)} &= \underline{\mathbf{b}}_S^{(k)} \quad \text{with} & (2.8) \\ \left\{ \begin{aligned} \underline{\underline{\mathbf{H}}}_S^{(k)} &= \int_{\Omega_s} \underline{\underline{\mathbf{N}}} (\underline{J}_0^{(k)T} \underline{\nabla \mathcal{I}}_0^{(k)} - \underline{J}_1^{(k)T} \underline{\nabla \mathcal{I}}_1^{(k)}) (\underline{J}_0^{(k)T} \underline{\nabla \mathcal{I}}_0^{(k)} - \underline{J}_1^{(k)T} \underline{\nabla \mathcal{I}}_1^{(k)})^T \underline{\underline{\mathbf{N}}}^T d\underline{X} \\ \underline{\mathbf{b}}_S^{(k)} &= - \int_{\Omega_s} \underline{\underline{\mathbf{N}}} (\underline{J}_0^{(k)T} \underline{\nabla \mathcal{I}}_0^{(k)} - \underline{J}_1^{(k)T} \underline{\nabla \mathcal{I}}_1^{(k)}) r(\underline{\underline{\mathbf{N}}}^T \underline{\mathbf{S}}^{(k-1)}, \underline{p}) d\underline{X}, \end{aligned} \right. \end{aligned}$$

$\underline{\nabla \mathcal{I}}_c^{(k)} = \underline{\nabla \mathcal{I}}_c(P_c(\underline{X} + \underline{\underline{\mathbf{N}}}^T \underline{\mathbf{S}}^{(k-1)}))$ with $\underline{\nabla \mathcal{I}}_c$ defining the gradient of the graylevel image \mathcal{I}_c and $\underline{J}_c^{(k)} = \underline{J}_c(\underline{X} + \underline{\underline{\mathbf{N}}}^T \underline{\mathbf{S}}^{(k-1)})$ with \underline{J}_c being the Jacobian of Projector P_c with respect to \underline{X} , *i.e.* such that $(J_c)_{ij} = \partial(P_c)_i / \partial X_j$. The so-called DIC operator $\underline{\underline{\mathbf{H}}}_S^{(k)}$ is actually an approximation of the Hessian of \mathcal{F}_S (using first-order derivatives only) and $-\underline{\mathbf{b}}_S^{(k)}$ corresponds to its gradient with respect to $\underline{\mathbf{S}}$. A generalization to the case of n_{cam} cameras is proposed in Section 3.4.1.

Remark 3 Up to now, the shape correction field was defined as homogeneous to a displacement field, with one component along each three dimension of space. But since a shape correction field tangent to the surface does not actually modify the geometry, Problem (2.8) is solved in projection onto the normal of the nominal surface. The shape correction field becomes a scalar field. The operator and right-hand side become $\underline{\underline{\Pi}}_Z^T \underline{\underline{\mathbf{H}}}_S^{(k)} \underline{\underline{\Pi}}_Z$ and $\underline{\underline{\Pi}}_Z^T \underline{\underline{\mathbf{b}}}_S^{(k)}$ respectively, with $\underline{\underline{\Pi}}_Z$ being a $3n_{FE} \times n_{FE}$ operator representing the normal.

Remark 4 During an experiment, change in illumination may occur, which may change locally the graylevel values of images. In DIC which is based on a comparison of graylevel values, such modulations can be taken into account by an affine correction in graylevels:

$$\tilde{r}(\underline{\underline{\mathbf{S}}}, \underline{\underline{\mathbf{p}}}) = \alpha r(\underline{\underline{\mathbf{S}}}, \underline{\underline{\mathbf{p}}}) + \beta, \quad (2.9)$$

where α and β are adjusted to account for contrast and brightness modulations respectively. These values have to be considered as additional unknowns of the DIC problem. Shape and calibration rely on a measure of the discrepancy between graylevels of images taken by different cameras from different view angles. The issue of brightness and contrast modulation is much more acute. Choosing α and β as constants may be insufficient. In [Dufour et al., 2015b], α and β are sought as low order polynomials, but specular reflections may not be well described by low frequency corrections. In this chapter, such as what has been proposed by Colantonio et al., an elementary brightness and contrast adjustment is performed, considering α and β as piecewise constants [Colantonio et al., 2020, Colantonio, 2020]. Images \mathcal{I}_0 and \mathcal{I}_1 are modified at each iteration such that their average is zero and their standard deviation is one, on each finite element.

Remark 5 As any Newton type algorithm, the question of the initial guess of $\underline{\underline{\mathbf{p}}}$ and $\underline{\underline{\mathbf{S}}}$ is crucial. On the one hand, as stated above, the theoretical shape is supposed to be a good approximation of the actual shape in experimental mechanics, therefore $\underline{\underline{\mathbf{S}}} = \underline{\underline{\mathbf{0}}}$ is a good initialization. On the other hand, the extrinsic parameters are not known. It is usually initialized by picking manually some (at least 4) points on the mesh and on each image. However, even under these conditions, and particularly when the discrepancy between theoretical and real shape is significant, a pyramidal multiscale initialization technique may be relevant to improve convergence. In FE-SDIC, the idea consists in filtering images and regularizing the shape simultaneously. Instead of filtering images, pixel aggregation (to generate low-definition images) is probably the best idea because of computational speedup. More precisely, starting with coarse images and a high level of regularization, the process consists in decreasingly filtering the images while reducing the regularization level at each considered scale to reach the fine images. A classic way of regularizing is to resort to Tikhonov regularization technique, i.e. to complement system (2.8) as follows:

$$(\underline{\underline{\mathbf{H}}}_S^{(k)} + \lambda \underline{\underline{\mathbf{A}}}) \delta \underline{\underline{\mathbf{S}}}^{(k)} = \underline{\underline{\mathbf{b}}}_S^{(k)} - \lambda \underline{\underline{\mathbf{A}}} \underline{\underline{\mathbf{S}}}^{(k-1)}, \quad (2.10)$$

where $\underline{\underline{\mathbf{A}}}$ is a linear operator such that $\underline{\underline{\mathbf{A}}} \underline{\underline{\mathbf{S}}}$ expresses the gradient of $\underline{\underline{\mathbf{S}}}(\underline{\underline{\mathbf{X}}})$ and λ is a penalization parameter whose value can be interpreted as the filter cutoff frequency (see, e.g., [Dufour et al., 2016, Pierré et al., 2017] for more details). The larger λ , the higher the regularization level.

2.2 Geometric regularization based on Bézier extraction

We now propose to geometrically regularize the FE mesh-based shape measurement problem (2.7) by projecting it onto more regular spline-based subspaces. We notice that spline functions have already been successfully used in DIC given their high degree of regularity (see, *e.g.*, [Cheng et al., 2002, Xie and Farin, 2004, Elguedj et al., 2011, Réthoré et al., 2010, Kleinendorst et al., 2015]). In the context of shape measurement, their interest is expected to be even more important since these functions are particularly adapted to optimize free-form surfaces [Kiendl et al., 2014, Hirschler et al., 2019b]. In this section, we detail the CAD-based approach presented in Section 1.2.3.

2.2.1 Splines: basics and shape modification

The spline technology, which has become a standard over the years for geometric modelling in CAD and computer graphics, relies on the use of non-uniform rational B-spline (NURBS) functions [Cohen et al., 1980, Piegl and Tiller, 1997, Farin, 2002]. Only basic precisions on NURBS are given in the following to complete the fundamentals on B-splines given in Section 1.2.1. For further details, the interested reader is referred to the references cited therein. The NURBS functions lend themselves to an exact representation of many shapes used in engineering, such as conical sections (circle, ellipse, etc). NURBS are a generalization of B-splines: they can be viewed as rational projections of B-splines. Therefore, they possess many of the properties of B-splines, the most interesting one being their increased smoothness, thus implying few degrees of freedom.

A general expression for a NURBS geometry with parameter $\underline{\xi} \in \mathbb{R}^\delta$ (δ being the dimension of the parametric space) is written as:

$$\underline{\mathcal{S}}(\underline{\xi}) = \sum_{i=1}^{n_{IG}} \tilde{R}_i(\underline{\xi}) \underline{X}_i = \underline{\tilde{\mathbf{R}}}^T(\underline{\xi}) \underline{\tilde{\mathbf{X}}}, \quad (2.11)$$

where $\underline{\tilde{\mathbf{R}}}$ and $\underline{\tilde{\mathbf{X}}}$ denote the matrix of the n_{IG} NURBS basis functions and the vector collecting the location of the associated control points, respectively. Note that the same convention as in Equations (1.3) and (2.4) is used here for the notation. The multivariate NURBS basis functions are obtained from the multivariate B-spline functions \tilde{N}_i as follows:

$$\tilde{R}_i(\underline{\xi}) = \frac{\tilde{w}_i \tilde{N}_i(\underline{\xi})}{\tilde{W}(\underline{\xi})} \quad \text{with} \quad \tilde{W}(\underline{\xi}) = \sum_{k=1}^{n_{IG}} \tilde{w}_k \tilde{N}_k(\underline{\xi}), \quad (2.12)$$

and where \tilde{w}_i denotes the weight of the i^{th} control point. Given Eq. (2.12) (and verifying that the B-spline functions satisfy the partition of unity), it may be noticed that if all weights are equal, the NURBS entity turns out to be a B-spline entity.

An interesting feature of splines is their high degree of regularity. If m is the multiplicity of a given knot, the functions are C^{p-m} continuous at that location, which is in contrast with standard FE where only a C^0 regularity is encountered on the element boundaries. This property is very appealing from the design point of view since it allows to define smooth free-form shapes using few degrees of freedom. Considering Figs 2.2(a) and 2.3(a), which show geometries associated with the knot vector $\{0, 0, 0, 0.5, 1, 1, 1\}$, it means that the regularity of the curve between the two elements is C^1 . To modify the shape of the spline entities, one may thus simply

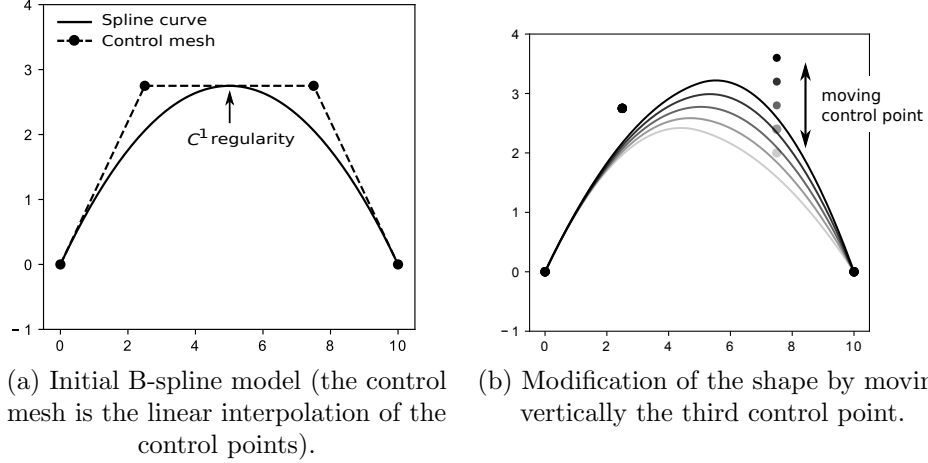


Figure 2.2: Spline generation and shape modification: example of a two-element quadratic C^1 B-spline curve.

need to move the control points, which results in a natural smooth modification of the geometry (see Fig 2.2(b) for illustration).

Furthermore, as explained in Section 1.2, spline functions present refinement procedures that allow to enhance the design space (used for updating the shape) without changing the geometry. In particular, one may refine the spline mesh by inserting knots (knot-insertion technique) while maintaining the initial smooth shape (see Fig 2.3(b) for illustration). As a result, starting with a coarse spline model, the refinement of the design space can be chosen in accordance with the desired complexity of the final shape. Even more importantly, the modification of the shape can be performed using a multilevel strategy as in IG shape optimization (see Figure 1.15 and [Nagy et al., 2011, Kiendl et al., 2014]), or in other fields such as the biomedical community for organ detection [Jiang et al., 2015]: one may begin with a coarse design model to fit the major tendencies of the surface and then refine the spline model to get the sharper variations. Similarly to Equation (1.4), the exact refinement procedure can be written for NURBS functions in matrix form (note that this refinement procedure also acts on the weights \tilde{w}_i):

$$\underline{\underline{\tilde{\mathbf{R}}}}^c = \underline{\underline{\mathbf{C}}}_{\text{ref}}^{c,f} \underline{\underline{\tilde{\mathbf{R}}}}^f \quad (n_{IG}^c \leq n_{IG}^f). \quad (2.13)$$

Such a relation offers a simple way to build the refined spline mesh from the coarse one. Denoting by $\underline{\underline{\tilde{\mathbf{X}}}}^c$ and $\underline{\underline{\tilde{\mathbf{X}}}}^f$ the location of the control points associated with the coarse and fine description, respectively, and asserting that the geometry (see Eq. (2.11)) is not modified through the refinement, we can write the following equality:

$$\left(\underline{\underline{\tilde{\mathbf{R}}}}^c(\underline{\underline{\xi}})\right)^T \underline{\underline{\tilde{\mathbf{X}}}}^c = \left(\underline{\underline{\tilde{\mathbf{R}}}}^f(\underline{\underline{\xi}})\right)^T \left(\underline{\underline{\mathbf{C}}}_{\text{ref}}^{c,f}\right)^T \underline{\underline{\tilde{\mathbf{X}}}}^c, \quad \forall \underline{\underline{\xi}}; \quad (2.14)$$

which simply leads to:

$$\underline{\underline{\tilde{\mathbf{X}}}}^f = \left(\underline{\underline{\mathbf{C}}}_{\text{ref}}^{c,f}\right)^T \underline{\underline{\tilde{\mathbf{X}}}}^c. \quad (2.15)$$

For more details on refinement strategies of splines and their matrix representations, reference is made to [Piegl and Tiller, 1997, Cottrell et al., 2007, Lee and Park, 2002].

Remark 6 *NURBS also offer the opportunity to apply shape variation by modifying the control point weights. However, unless a very coarse NURBS model is*

considered [Qian, 2010, Nagy et al., 2013], it appears from the IG shape optimization community that it is generally sufficient for free-form surfaces to only use the control point coordinates (see, e.g., [Kiendl et al., 2014]). We perform similarly in this work (as [Dufour et al., 2016]).

Remark 7 In a general context, additional attention may be required when updating the shape for a rather fine spline geometric model. If the control points are allowed to move independently in every spatial direction, fold-overs may appear. However, as noted in Remark 3, only the normal component of the displacement is considered for the update of the geometry in this study, which naturally circumvents the problem.

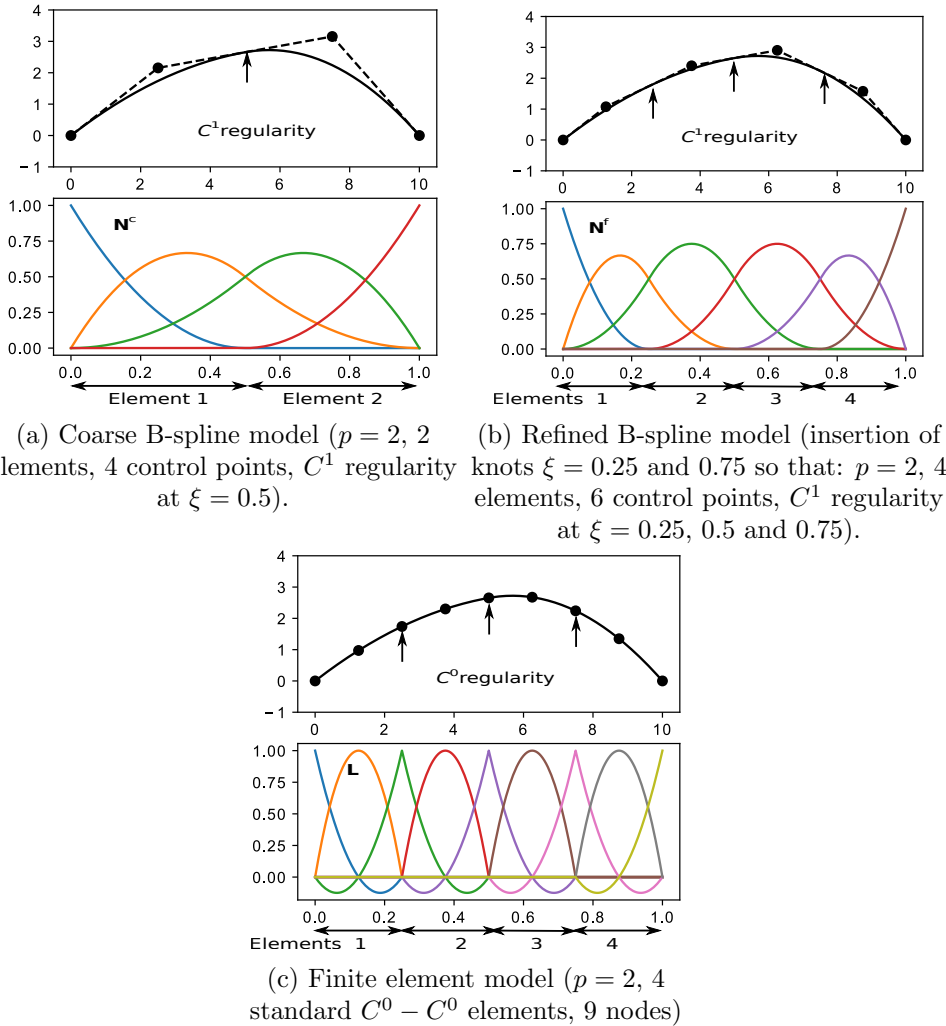


Figure 2.3: Going from a coarse spline representation to a fine (analysis-suitable) FE mesh without modifying the initial geometry.

2.2.2 IG-FE bridge

Recalling that the desired input and output in our methodology is the fine (analysis-suitable) FE mesh, it is now required to establish a link between this FE mesh and the different (multilevel) spline-based descriptions introduced in previous section. In this section, the properties of the $\underline{\underline{C}}_{\text{Lag}}$ operator (see Equation (1.5)) are first recalled, and then its construction in the case of B-spline and NURBS is detailed.

2.2.2.1 Principle

The ultimate objective is to be able to build, in an explicit and non-invasive manner, the different Hessian and gradient operators, associated with the different spline approximation subspaces, from their fine FE counterparts computed using our FE-SDIC code (see Eqs. (2.8)). Since it is already possible to communicate between the different spline models (see Eqs. (2.13) and (2.15)), the goal here is to relate a fine FE and a fine spline discretization (*i.e.*, with same number of elements and same polynomial degree). In order to do so, we make use of previous work [Tirvaudey et al., 2019] in which a global algebraic bridge between IGA and FEA is constructed by resorting to Bézier-based operators [Borden et al., 2011, Schillinger et al., 2016]. More precisely, an operator that maps a C^0 FE basis onto a smooth spline basis can be formulated. Details regarding the construction of this operator are given in the forthcoming Sections 2.2.2.2 and 2.2.2.3.

This operator has been briefly introduced in Section 1.2.3, and Equation (1.5) can be applied in the case of a fine, analysis-suitable spline mesh:

$$\underline{\underline{\mathbf{R}}}^f = \underline{\underline{\mathbf{C}}}_{\text{Lag}} \underline{\underline{\mathbf{N}}}, \quad \text{and thus} \quad \underline{\underline{\mathbf{X}}} = \underline{\underline{\mathbf{C}}}^T_{\text{Lag}} \underline{\underline{\mathbf{X}}}^f, \quad (2.16)$$

$\underline{\underline{\mathbf{N}}}$ being the standard nodal Lagrange basis functions of Eq. (2.4), and $\underline{\underline{\mathbf{C}}}_{\text{Lag}}$ being the Lagrange extractor or its approximation in the case of NURBS (its construction is detailed in the next sections).

As an example, this treatment has been performed to obtain the FE model of Fig. 2.3(c) starting with the spline model of Fig. 2.3(b). From the resulting FE mesh, we then have the opportunity to recover the refined spline Hessian and gradient operators without implementing IGA but simply by projecting the related FE operators onto the reduced, spline basis. From Eq. (2.8), we can compute the associated spline operator $\underline{\underline{\mathbf{H}}}_S^f$ such that (superscript (k) omitted):

$$\begin{aligned} \underline{\underline{\mathbf{H}}}_S^f &= \int_{\Omega_s} \underline{\underline{\mathbf{R}}}^f (J_0^T \nabla \mathcal{L}_0 - J_1^T \nabla \mathcal{L}_1) (J_0^T \nabla \mathcal{L}_0 - J_1^T \nabla \mathcal{L}_1)^T \underline{\underline{\mathbf{R}}}^{fT} dX \\ &= \int_{\Omega_s} \underline{\underline{\mathbf{C}}}_{\text{Lag}} \underline{\underline{\mathbf{N}}} (J_0^T \nabla \mathcal{L}_0 - J_1^T \nabla \mathcal{L}_1) (J_0^T \nabla \mathcal{L}_0 - J_1^T \nabla \mathcal{L}_1)^T \underline{\underline{\mathbf{N}}}^T \underline{\underline{\mathbf{C}}}_{\text{Lag}}^T dX \\ &= \underline{\underline{\mathbf{C}}}_{\text{Lag}} \underline{\underline{\mathbf{H}}}_S \underline{\underline{\mathbf{C}}}_{\text{Lag}}^T. \end{aligned} \quad (2.17)$$

As well, the spline gradient operator $\underline{\underline{\mathbf{b}}}_S^f$ can be obtained from its FE counterpart $\underline{\underline{\mathbf{b}}}_S$ (see Eq. (2.8)) as follows:

$$\underline{\underline{\mathbf{b}}}_S^f = \underline{\underline{\mathbf{C}}}_{\text{Lag}} \underline{\underline{\mathbf{b}}}_S. \quad (2.18)$$

Furthermore, the same procedure can be applied to recover the coarse spline operators from the fine FE ones:

$$\begin{cases} \underline{\underline{\mathbf{H}}}_S^c = \underline{\underline{\mathbf{C}}}_{\text{ref}}^{c,f} \underline{\underline{\mathbf{H}}}_S^f \left(\underline{\underline{\mathbf{C}}}_{\text{ref}}^{c,f} \right)^T = \underline{\underline{\mathbf{C}}}_{\text{ref}}^{c,f} \underline{\underline{\mathbf{C}}}_{\text{Lag}} \underline{\underline{\mathbf{H}}}_S \underline{\underline{\mathbf{C}}}_{\text{Lag}}^T \left(\underline{\underline{\mathbf{C}}}_{\text{ref}}^{c,f} \right)^T \\ \underline{\underline{\mathbf{b}}}_S^c = \underline{\underline{\mathbf{C}}}_{\text{ref}}^{c,f} \underline{\underline{\mathbf{b}}}_S^f = \underline{\underline{\mathbf{C}}}_{\text{ref}}^{c,f} \underline{\underline{\mathbf{C}}}_{\text{Lag}} \underline{\underline{\mathbf{b}}}_S \end{cases}. \quad (2.19)$$

Consequently, the IG regularized shape measurement systems of form $\underline{\underline{\mathbf{H}}}_S^c \delta \underline{\underline{\mathbf{S}}}^c = \underline{\underline{\mathbf{b}}}_S^c$ and $\underline{\underline{\mathbf{H}}}_S^f \delta \underline{\underline{\mathbf{S}}}^f = \underline{\underline{\mathbf{b}}}_S^f$ can be solved instead of the ill-posed fine FE shape measurement systems (2.8). Finally, note that the resulting IG DOF vectors, denoted by $\underline{\underline{\mathbf{S}}}^c$ or $\underline{\underline{\mathbf{S}}}^f$, can be back-converted in terms of nodal FE shape update $\underline{\underline{\mathbf{S}}}$:

$$\underline{\underline{\mathbf{S}}} = \underline{\underline{\mathbf{C}}}_{\text{Lag}}^T \left(\underline{\underline{\mathbf{C}}}_{\text{ref}}^{c,f} \right)^T \underline{\underline{\mathbf{S}}}^c \quad \text{or} \quad \underline{\underline{\mathbf{S}}} = \underline{\underline{\mathbf{C}}}_{\text{Lag}}^T \underline{\underline{\mathbf{S}}}^f, \quad (2.20)$$

so that a unique basis is used for the representation of the surface at each multilevel step. An overview of the different transformations is given in Figure 2.4.

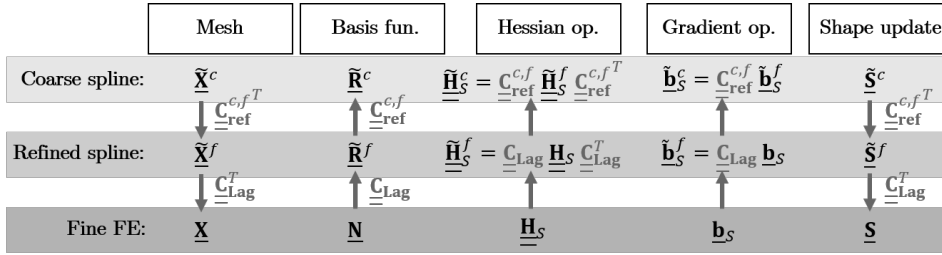


Figure 2.4: Overview of the different transformations allowing to communicate between the fine (analysis-suitable) FE mesh and the different (multilevel) spline-based discretizations.

2.2.2.2 Construction: case of B-splines

In case of a B-spline geometric model, constructing $\underline{\mathbf{C}}_{\text{Lag}}$ appears quite straightforward since both spline and FE discretizations rely on polynomials. Since the space generated by the B-Spline functions (smooth polynomials) is included in the one generated by the Lagrange functions (C^0 polynomials), the process consists in extracting the smooth part of C^0 functions.

In order to form a multivariate C^0 mesh from a multivariate smooth B-spline mesh, the starting point consists in repeating all the inside knots of the knot-vectors until they reach a p multiplicity. A specific knot-insertion process is thus performed, which allows to get the famous Bézier extraction operator whose interest to relate IGA and FEA has been intensely demonstrated (see [Borden et al., 2011, Scott et al., 2011, Evans et al., 2015, D’Angella et al., 2018] to name a few). More precisely, the Bézier extraction operator maps a Bernstein basis onto a B-Spline basis. Bernstein and Lagrange polynomials generates the same approximation subspace. Therefore, the second step consists in moving from the Lagrange basis to the Bernstein basis, which can be easily performed by evaluating the Bernstein functions at the nodal points associated with the Lagrange basis. The succession of these two steps leads to the construction of the Lagrange extraction operator $\underline{\mathbf{C}}_{\text{Lag}}$ [Schillinger et al., 2016] in case of B-splines. For more details regarding these transformations, the interested reader is advised to consult [Borden et al., 2011, Schillinger et al., 2016, Tirvaudey et al., 2019].

Remark 8 Note that for better numerical efficiency, the Lagrange extraction operator can be directly computed from the B-spline and Lagrange basis. It merely requires to evaluate the B-spline basis functions at the nodal points of the Lagrange basis.

Remark 9 The present work is restricted to quadratic functions since almost all standard FE codes do not go beyond second-order Lagrange finite elements (the famous 9-node quadrilateral element in 2D, or the 27-node cubic element in 3D). However, we emphasize that the proposed methodology could be directly applied to higher-order spline-based discretization, provided that the corresponding higher-order FE are available in a FE-SDIC environment.

2.2.2.3 Construction: case of NURBS

In this section and in this section only, $\underline{\mathbf{C}}_{\text{Lag}}$ will only refer to the exact Lagrange extractor. Its approximation will be denoted $\underline{\mathbf{C}}_{\text{Lag}}^W$. In this chapter, we undertake

to also consider NURBS (and not just B-splines) to exactly represent conic sections. The Lagrange extraction can be extended to the case of NURBS, but it cannot directly go from a Lagrange basis to a NURBS basis since the first one is based on polynomials while the other one relies on rational functions. The NURBS version of the Lagrange extraction actually consists in mapping a rational Lagrange basis onto a NURBS basis, as detailed in [Schillinger et al., 2016]. To truly start with Lagrange polynomials, the construction of an additional mapping going from polynomials to rational functions is required. Such a transformation cannot be exact since this is the space of the rational functions that includes the associated polynomials and not the other way around. A projection thus needs to be performed. In order to do so, we propose to proceed as in [Tirvaudey et al., 2019]; that is, we start with the NURBS version of the Lagrange extraction and then perform the projection at the Lagrange level. This choice offers the opportunity to follow a pragmatic yet accurate strategy.

More precisely, using the B-spline version of the Lagrange extraction operator and returning to (2.12), we can write:

$$\underline{\underline{\mathbf{R}}}^f(\underline{\xi}) = \frac{\underline{\underline{\mathbf{W}}}^f \underline{\underline{\mathbf{C}}}_{\text{Lag}} \underline{\underline{\mathbf{N}}}(\underline{\xi})}{\underline{\underline{W}}^f(\underline{\xi})}, \quad (2.21)$$

where $\underline{\underline{\mathbf{W}}}^f$ is the diagonal matrix collecting the weights of the refined NURBS discretization and $\underline{\underline{W}}^f(\underline{\xi}) = \sum_{k=1}^{n_{IG}^f} \tilde{w}_k^f \tilde{N}_k^f(\underline{\xi})$ is the associated NURBS weight function. Omitting dependency on $\underline{\xi}$, the NURBS weight function can be rewritten using the Lagrange basis as:

$$\begin{aligned} \underline{\underline{W}}^f &= \sum_{k=1}^{n_{IG}^f} \tilde{w}_k^f \tilde{N}_k^f = (\underline{\underline{\mathbf{w}}}^f)^T \underline{\underline{\mathbf{N}}}^f = (\underline{\underline{\mathbf{w}}}^f)^T \underline{\underline{\mathbf{C}}}_{\text{Lag}} \underline{\underline{\mathbf{N}}} \\ &= (\underline{\underline{\mathbf{C}}}_{\text{Lag}}^T \underline{\underline{\mathbf{w}}}^f)^T \underline{\underline{\mathbf{N}}} = (\underline{\underline{\mathbf{w}}})^T \underline{\underline{\mathbf{N}}} = W, \end{aligned} \quad (2.22)$$

where the weights associated with the rational Lagrange control points are:

$$\underline{\underline{\mathbf{w}}} = \underline{\underline{\mathbf{C}}}_{\text{Lag}}^T \underline{\underline{\mathbf{w}}}^f. \quad (2.23)$$

Note here that $\underline{\underline{\mathbf{N}}}$ is only the vector $[N_1 \dots N_{n_{FE}}]$ (it is different from $\underline{\underline{\mathbf{N}}}$ from Equation (2.4)), so $\underline{\underline{\mathbf{C}}}_{\text{Lag}}$ is in its smallest form (in other equations, $\underline{\underline{\mathbf{C}}}_{\text{Lag}}$ takes into account the number of dof per node by appropriately repeating the matrix coefficients). The rational Lagrange functions are then defined as follows:

$$\underline{\underline{\mathbf{R}}} = \frac{\underline{\underline{\mathbf{W}}} \underline{\underline{\mathbf{N}}}}{\underline{\underline{W}}}, \quad (2.24)$$

where $\underline{\underline{\mathbf{W}}}$ is the diagonal matrix of the Lagrange weights. The link between NURBS functions and rational Lagrange functions is finally made using Eqs. (2.24) and (2.22) in Eq. (2.21). Consequently, a new extraction operator $\underline{\underline{\mathbf{C}}}_{\text{Lag}}^W$ is created as described below:

$$\underline{\underline{\mathbf{R}}}^f = \underline{\underline{\mathbf{W}}}^f \underline{\underline{\mathbf{C}}}_{\text{Lag}} (\underline{\underline{\mathbf{W}}})^{-1} \underline{\underline{\mathbf{R}}} = \underline{\underline{\mathbf{C}}}_{\text{Lag}}^W \underline{\underline{\mathbf{R}}}. \quad (2.25)$$

Then, going from $\underline{\underline{\mathbf{N}}}$ to $\underline{\underline{\mathbf{R}}}$ or, in other words, from $\underline{\underline{\mathbf{X}}}^W$ (the location of the rational Lagrange control points) to $\underline{\underline{\mathbf{X}}}$, can be achieved very simply. Noticing that the control points of the rational Lagrange discretization interpolates the geometry, it appears possible to consider that the position of the FE nodes $\underline{\underline{\mathbf{X}}}$ is exactly the same

as the position of the rational Lagrange control points $\underline{\mathbf{X}}^W$. Following this strategy, we end up with:

$$\underline{\mathbf{X}} \approx \left(\underline{\mathbf{C}}_{\text{Lag}}^W \right)^T \tilde{\underline{\mathbf{X}}}^f \quad \text{and} \quad \underline{\underline{\mathbf{R}}}^f \approx \underline{\underline{\mathbf{C}}}_{\text{Lag}}^W \underline{\underline{\mathbf{N}}}. \quad (2.26)$$

The above approximations get more accurate with the refinement of the NURBS mesh, which is assumed to be the case here since it is related to the last-level NURBS model. As demonstrated in [Tirvaudey et al., 2019], this process provides sufficient accuracy with already rather coarse NURBS meshes for typical engineering geometries.

In the remainder of this work, the notation $\underline{\underline{\mathbf{C}}}_{\text{Lag}}$ will refer to both $\underline{\underline{\mathbf{C}}}_{\text{Lag}}$ or $\underline{\underline{\mathbf{C}}}_{\text{Lag}}^W$ depending on the case (B-splines or NURBS).

2.2.3 Proposed methodology

We now have all the ingredients in hand to present the proposed methodology. We remind here that the objective is to improve the mesh-based shape measurement occurring in FE-SDIC by using, in a non-invasive manner, a geometrically sound regularization. In order to do so, the main idea is to relate the multilevel spline parameterizations of the geometry (and of its update) with the multiscale images used for the initialization of the shape measurement (see Remark 5). The principle is illustrated in Fig. 2.5. The different approximation subspaces that describe the geometry are chosen in accordance with the resolution of the images so that the shape measurement problem is regularized at each scale (number of DOF versus number of pixels). The coarse scales allow to fit the major tendencies of the surface while the finer ones allow the representation of sharper variations. Moving from scale s to finer scale $s - 1$, the spline design space is enhanced while keeping the same geometry, and the initial solution for the shape measurement problem of scale $s - 1$ is taken as the final solution of scale s .

Remark 10 *In practice, the method starts from a sufficiently coarse representation of the nominal geometry. So far, in experimental mechanics, specimen shape is relatively smooth such that very compact spline representations with very few DOF are generally sufficient. In a situation where the initial CAD representation should be too fine to effectively regularize the problem, it would be possible to either reduce the number of scales or resort to additional Tikhonov-type regularization techniques. Note that even in such a case, although insufficient, a certain amount of geometric regularization is expected. The level of Tikhonov regularization should presumably be lower than the one which would be required with an analysis-suitable FE mesh.*

More precisely, an overview of the proposed regularization scheme included in the calibration of the whole stereo rig is given in Fig. 2.6. For simplicity, we denote by $\underline{\underline{\mathbf{C}}}_s$ the extraction operator that maps the fine FE space onto the spline discretization of scale s , *i.e.* $\underline{\underline{\mathbf{C}}}_s$ is defined such that:

$$\underline{\underline{\mathbf{C}}}_0 = \underline{\underline{\mathbf{C}}}_{\text{Lag}} \quad \text{and} \quad \underline{\underline{\mathbf{C}}}_s = \left(\prod_{i=0}^{s-1} \underline{\underline{\mathbf{C}}}_{\text{ref}}^{(s-i), (s-i-1)} \right) \underline{\underline{\mathbf{C}}}_{\text{Lag}}, \quad \forall s \in \{1, \dots, n_s\}, \quad (2.27)$$

where n_s is the number of scales (for initialization purposes) and $s = 0$ corresponds to the finest scale while $s = n_s$ refers to the coarsest scale. As can be observed, making use of the IG-FE bridge of previous section, the implementation is performed from standard FE-SDIC routines with minimal effort. Summarizing, we proceed as

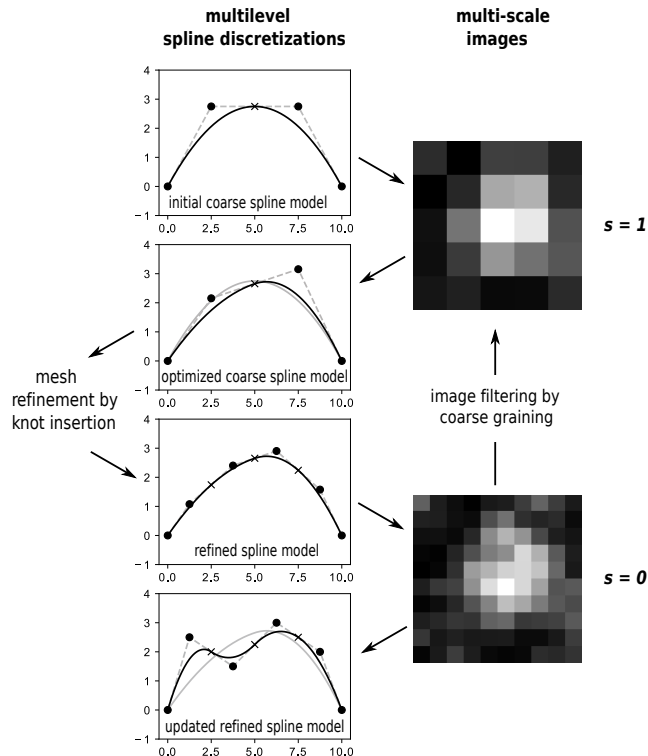


Figure 2.5: Principle of the geometric regularization: the multilevel spline optimization process is coupled with the multiscale initialization of shape measurement.

follows for the regularization. From the initial CAD representation of the theoretical surface, we build in the pre-processing step a fine analysis-suitable FE mesh and the different multilevel spline discretizations through their corresponding extraction operators $\underline{\underline{C}}_s$. Then, entering into the shape measurement loop and beginning with the coarsest scale, we project, at each iteration of the Gauss-Newton solver, the FE hessian and gradient onto the first-level spline space and solve the associated regularized IG system. We thus end up with the IG shape update that can be converted in terms of nodal FE shape update so that the FE hessian and gradient can be updated for the next iteration. Going to the finest scale, we finally repeat the previous procedure with the different refined spline spaces to regularize at each scale. The final shape can be given either in terms of splines (thereby directly compatible with CAD environments) or in terms of finite elements (thus facilitating the communication with numerical simulations).

2.3 Examples

In this section, the proposed regularization technique for mesh-based shape measurement is applied to a real experiment. A steel open-hole tensile specimen of size $180 \times 50 \times 2$ mm and hole diameter 28 mm was considered. A dedicated speckle pattern was laser printed over a layer of uniform white paint. A pair of 5 Mpx CCD cameras and 50 mm lenses was used to capture the 8bit 2452×2052 digital images presented in Figure 2.1. The stereo-angle was set around 25° which represents a good compromise between in-plane and out-of-plane uncertainties [Balcaen et al., 2017]. The intrinsic parameters of the nonlinear camera models (first order radial distortions) were calibrated prior to the experiment using a series of digital images

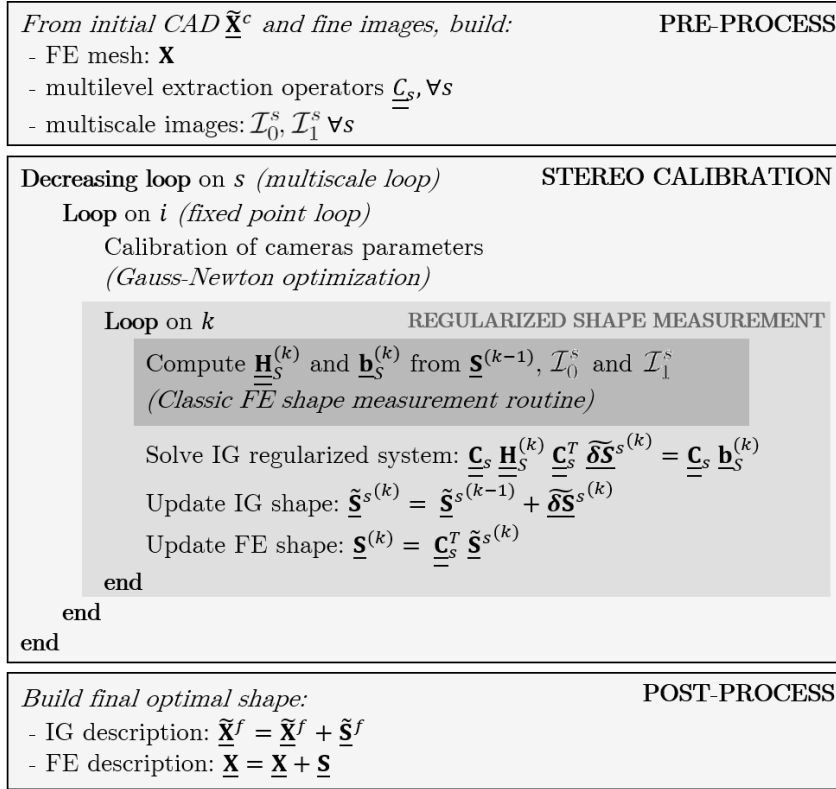


Figure 2.6: Overview of the proposed regularization scheme included in the calibration of a stereo rig.

of a calibration target made of a grid of 12x9 dots with a step size of 3 mm. The obtained intrinsic parameters are considered fixed in the remainder of the study. More precisely, two configurations were considered for the study:

- In a chronological order, the specimen was first clamped in the lower jaw of an electro-mechanical tensile testing machine. The upper part of the specimen was left free. In this first configuration, a set of images was taken and is referred to as the *flat* configuration, as the observed surface of the specimen was almost plane. This configuration is used to analyze the robustness of the method to a reasonably complex shape.
- The specimen was then clamped in the upper jaw. Since the jaws are slightly misaligned, the statically indeterminate clamping generated a torsional moment and the specimen twisted. The misalignment was around 2 or 3°, which should generate significant waviness. The corresponding set of images is referred to as the *twisted* configuration. With this case study, it is possible to analyze the method in a configuration where the difference between the theoretical (considered flat) and real (twisted) shapes is significantly greater than in standard mechanical experiments.

For a clear understanding of the results, we choose in the following to start with the twisted configuration and then turn to the flat configuration. The two pairs of digital images are analyzed by (a) the proposed geometric, Bézier-based, regularized shape measurement method, (b) a standard FE-based shape measurement possibly considering Tikhonov regularization and (c) a more standard subset-based

DIC method. It must be mentioned, at this stage, that the regions of interest of the FE-based and subset DIC are not equal. The FE (or IG) meshes do conform to the edges of the specimen, whereas subset DIC was not able to perform shape measurement too close to the boundaries. This point should be kept in mind when comparing global and local DIC solutions.

2.3.1 Pre-processing: construction of the geometric model and FE mesh

The nominal geometry of the sample consists in a plate with a circular hole. As a result, its exact representation in CAD requires the use of NURBS (rational B-splines). It is common to proceed as in Figure 2.7(a) for the building of the first NURBS model of such a geometry. Given that the four vertices of the plate imply a C^0 regularity of the geometry at those points, the coarsest NURBS model necessarily involves 4 C^0 - C^0 elements. More precisely, denoting by ξ the parameter describing the circumferential direction, we needed to start with degree $p = 2$ in that direction with knot-vector $\Xi = \{0, 0, 0, 0.25, 0.25, 0.5, 0.5, 0.75, 0.75, 1, 1, 1\}$ (for more details on NURBS constructions, see, *e.g.*, [Cottrell et al., 2009]). Along the other direction, even if degree 1 would be sufficient, we also took degree 2 so as to be consistent with the final FE-mesh that is made of standard 9-node (*i.e.* bi-quadratic) elements. Starting with the NURBS model composed of 4 quadratic elements, we thus only performed knot-insertion (inserting one knot at a time) to get the different (multi-level) NURBS parametrizations (see Figs 2.7(b) and (c)). We finally further carried out knot-insertion and applied the IG-FE mapping of Section 2.2.2 (see Eq. (2.16)) to obtain the analysis-suitable FE-mesh (see Figure 2.7(d)).

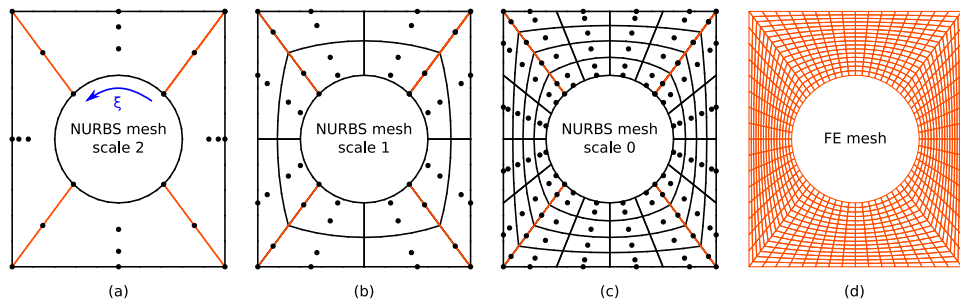


Figure 2.7: Initial CAD parametrization, multi-level NURBS meshes and final fine FE mesh. The C^0 lines are orange. The final FE mesh is composed of 1000 elements.

2.3.2 Results: twisted configuration

Let us recall that, because of the misalignment of the grips, in this clamped-clamped configuration, the specimen underwent significant twist. Note that these images were not analyzed for displacement measurement using FE-SDIC with respect to the flat configuration images. They were used for shape measurement independently as if this configuration was the initial state of the specimen.

2.3.2.1 Classic FE-based shape measurement without any regularization

A first classic FE shape measurement (using *Pyxel* [Passieux, 2018]) was performed using the FE mesh given in Figure 2.7(d) without any regularization. The obtained shape is represented in Figure 2.8. In order to compare the shape measurements ob-

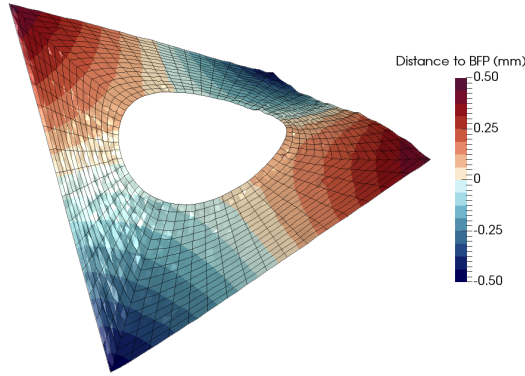


Figure 2.8: Twisted specimen: shape obtained with classic FE-SDIC without regularization (def. scale fact. $\times 30$).

tained with the different considered techniques, we chose the color data to represent the distance to the best fitting plane (BFP) instead of directly plotting the shape correction field $\underline{S}(X)$, which would not be available using the subset approach. The shape is typical of a twist test. The waviness is around one millimeter, which, at the scale of this specimen, is large. In addition, the resulting shape is relatively noisy. Even though the noise is one order of magnitude smaller than the artificially large shape correction field, it still seems large and unphysical.

2.3.2.2 Use of standard Tikhonov regularization

In order to regularize this noise, a classic Tikhonov regularization technique was first considered. The shape obtained for three different regularization lengths is given in Figure 2.9. As expected, using Tikhonov regularization, the shape mea-

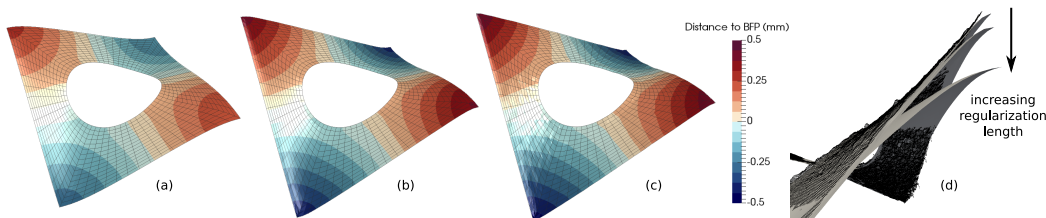


Figure 2.9: Twisted specimen: shape obtained using a classic FE-SDIC with Tikhonov regularization for different values of the regularization length: decreasing values of the regularization length from (a) to (c) respectively (def. scale fact. $\times 30$).

surements appeared smoother, especially for large values of the regularization length (see Figs. 2.9(a) and (b)). It can be seen that such high levels of regularization may also affect the shape. In Figure 2.9(d), the influence of the regularization length on the shape is depicted, with the subset approach as the reference. Using a too large regularization length reduces the displacement magnitudes and underestimates the shape waviness. Asymptotically, using very large values of regularization would lead to an almost constant correction field, which would correspond to a rigid body translation of the observed surface with respect to the theoretical CAD.

Conversely, for lower values of the regularization length, the solution looks more like the shape obtained without regularization. For instance Shape 2.9(c) is less noisy than the one illustrated in Figure 2.8, but high frequency noise is still present, which means that the regularization was still not sufficient. Even in this case, where

the regularization level was insufficient to get completely rid of noise, it can be observed in Figure 2.9(d) that the correction field at the top corner was already underestimated because of the differential nature of the chosen regularization term. As shown in this example, choosing the correct regularization length may become a tricky trade-off. In other words, a satisfying value of the regularization length may not exist, as it seems to be the case here.

2.3.2.3 Use of the proposed geometric regularization

Next, the proposed geometric regularization scheme was considered with the same image set. The multiscale initialization technique described in Section 2.2.3 was applied with three scales using the three NURBS meshes of Figure 2.7. The corresponding shapes obtained at each scale are given in Figure 2.10.

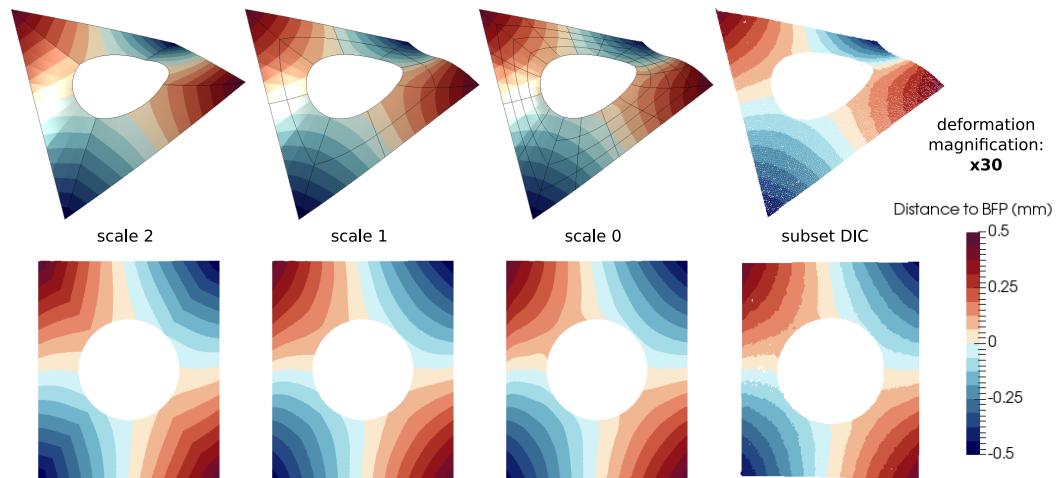


Figure 2.10: Twisted specimen with the proposed geometric regularization (def. scale fact. $\times 30$).



Figure 2.11: Unregularized FE shape measurement (black mesh) and different scales with different spline refinements with our CAD-based approach (gray surfaces) (def. scale fact. $\times 30$). This figure should be compared to Figure 1.5.

First, it can be observed that the shapes obtained at the three scales are very smooth. The very low-dimensional spline approximation subspace indeed acts as a very strong regularization technique. Each of the three shapes are very similar to

each other and also in good agreement with the shape provided by the subset DIC method. In addition, the reduction in the correction field magnitude observed when using the Tikhonov regularization did not occur here (see Figure 2.11). Even at the highest scale, where the spline representation is particularly coarse, a very good approximation of the shape was already obtained. This property of the geometric regularization is particularly interesting for the highest scales of the multiscale approach, since they are associated with high regularization levels.

Figure 2.12(left) presents the evolution of the standard deviation of the graylevel residual field in percent of the reference image dynamics (later denoted *relative residual*) as a function of the iteration number. It compares the convergence of the

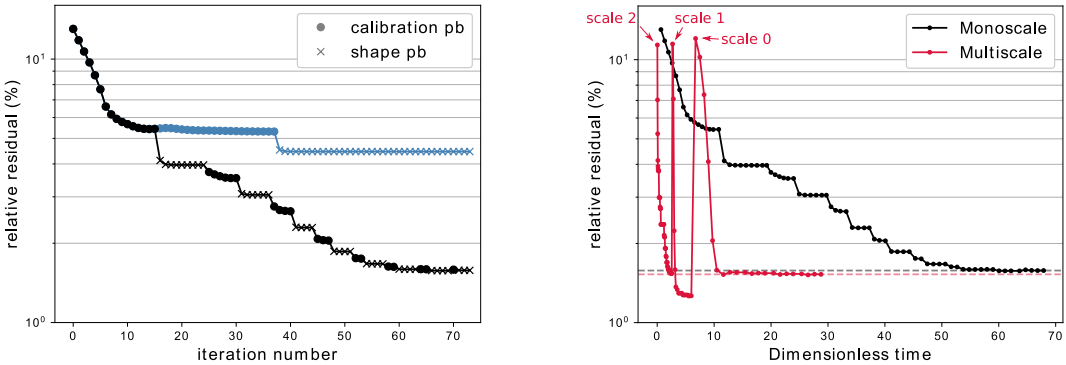


Figure 2.12: Convergence of the algorithm on the twisted use case: (left) convergence (vs iterations) of the relative residual with (black) and without (blue) the fixed point iterations and (right) convergence speed (vs dimensionless time) for the monoscale and multiscale approaches.

problem with and without iterating between calibration of extrinsic parameters (● symbols) and shape correction problems (× symbols). It can be seen that, at least on this case, converging the fixed point algorithm (by alternating between calibration and shape problems) is mandatory to converge towards an accurate solution. It is the case here because the actual shape is significantly different from the initial CAD. On the (right) side of the same figure, the relative residual is plotted as a function of CPU time normalized by the CPU time taken by one iteration at scale 0, for the monoscale (only scale 0) and multiscale approaches. It can be seen that, although the number of iterations may increase, the computational time is clearly reduced (divided by 2 in this case), since the higher scales are associated with low definition images whose interpolation is far cheaper. Note also, that when using the multiscale approach, the value of the relative residual was lower than that of the monoscale alternative. Lower relative residual emerges from the fact that the multiscale initialization, in addition to convergence acceleration, was designed to avoid local minima. In this example, the solutions seem to be similar, but the multiscale approach, by avoiding local minima, may allow to reduce significantly the relative residual and therefore improve the measurement accuracy.

Remark 11 *Note that the residual at scale $s > 0$ was estimated using the coarsened images and not with the full resolution (scale 0) images, for efficiency. This explains why the estimated residual at scale $s > 0$ is sometimes a little smaller than the one at scale 0 after convergence on Figure 2.12(right).*

2.3.2.4 A note regarding brightness and contrast correction

Another interesting point with this test case and that has been studied in [Colantonio et al., 2020, Colantonio, 2020] is the analysis of the graylevel residual field $r(\underline{S}(\underline{X}), p)$ at scale $s = 0$ before and after convergence, with and without elementary brightness and contrast correction. First, the initial graylevel map, obtained with the initial CAD (flat) shape and the initial set of extrinsic parameters, is depicted in Figure 2.13. Its value is about 70% of the dynamic of the image which means that the

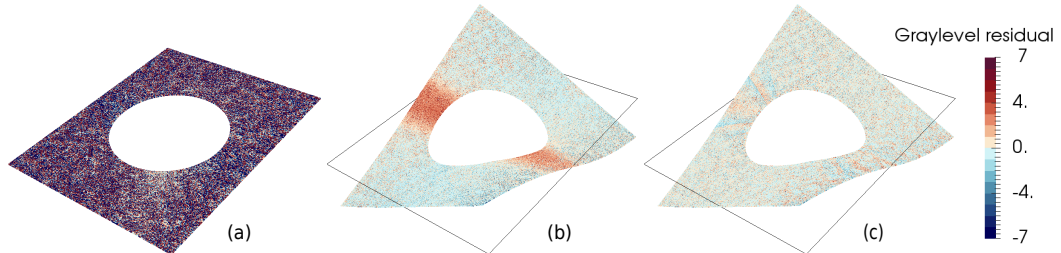


Figure 2.13: Graylevel residual $r(\underline{S}(\underline{X}), p)$ in percent of the dynamic of the images with (a) the initial CAD shape and after convergence (b) without and (c) with elementary brightness and contrast correction (def. scale fact. $\times 30$).

graylevels do not correspond at all. After 8 iterations of the fixed point algorithm, the graylevel residual dropped to less than 10% of the images dynamic. It can be seen in Figure 2.13(b) that the residual map presents a band of higher value located around the hole when using a global brightness/contrast correction. This localized worse verification of the graylevel conservation was attributed to the presence of a specular reflection of the light, which seems consistent with the twisting of the specimen. This phenomenon locally modifies the brightness and contrast (B/C). As shown here, global B/C correction methods cannot take this into account. The proposed elementary B/C correction method (see Remark 4) was applied and the resulting graylevel residual is depicted on Figure 2.13(c). It presents a homogeneous value around 2% of the dynamic in all the region of interest. This elementary correction technique is very simple but generic, and it can efficiently account for a complex local B/C variations (such as specular reflection), which would be difficult using a global descriptor.

2.3.3 Results: flat configuration

In this section, the so-called flat configuration where the specimen is clamped at the bottom end only is being analyzed. Since here the specimen is nearly flat, the shape correction field is expected to be of lower magnitude, but less regular than the twist of the previous section. Only the final shape measurements are plotted in this section to study the robustness of the geometric regularization method with respect to a more complex shape with lower signal to noise ratio. Figure 2.14 presents the shape measurement and distance to BFP when using (a) the FE-SDIC approach without regularization, (b) the local SDIC method and (c) the geometric regularization technique. First it can be noticed that all the shapes are in good agreement with each other. Note that the waviness is one order of magnitude smaller than in the twist case. The FE and local SDIC measurements are clearly affected by acquisition noise. The geometric regularization technique efficiently manages to extract a regular shape from the images. From this measurement, which provides the NURBS parametrization of the optimal shape, and using the IG-FE bridge of

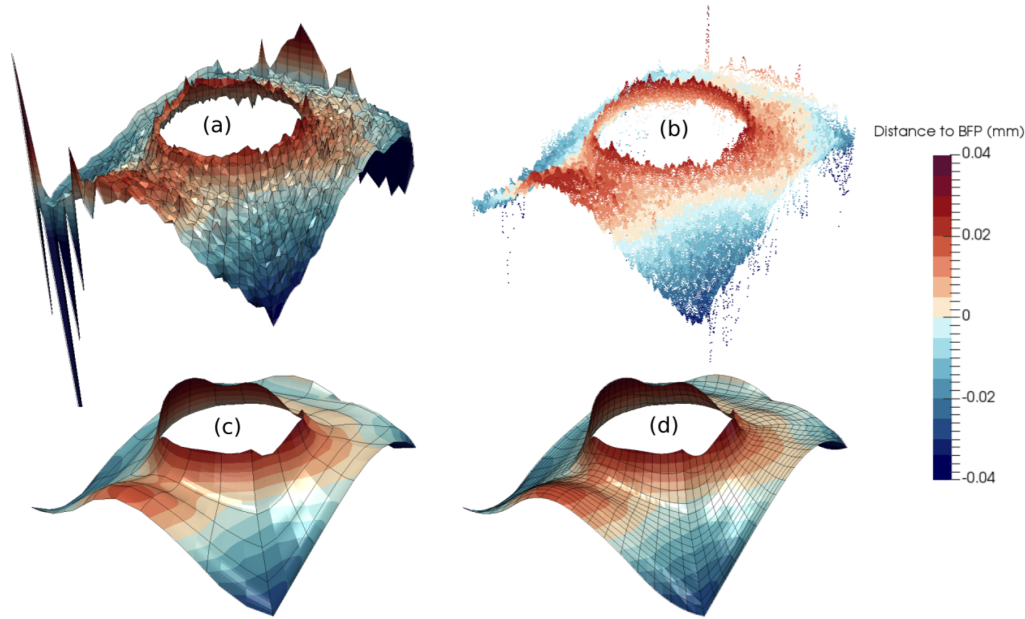


Figure 2.14: Flat specimen shapes with distance to best fitting plane (BFP) in mm: (a) measured by the FE-SDIC without regularization, (b) measured using the subset based SDIC and measured using the proposed geometric regularization: (c) Spline parametrization of the optimal shape and (d) corresponding measured finite element mesh (def. scale fact. $\times 300$).

Section 2.2.2, it is possible to build directly the FE mesh (see Figure 2.8(d)), which exactly corresponds to the same shape. Such an output may be convenient to be used for FE-SDIC displacement measurements in the context of validation/identification of FE models.

Conclusion

In this chapter, we developed a hybrid IG-FE strategy for the regularization of the mesh-based shape measurement occurring in FE-SDIC. From a regularization point of view, the proposed strategy draws inspiration from the techniques developed recently in the isogeometric shape optimization community, especially with the multilevel design concept [Kiendl et al., 2014, Hirschler et al., 2019b, Wang et al., 2018]. By making use of the advanced spline refinement procedures and of adequate Bézier-based operators, the main idea here was to extract, from the initial FE subspace, smoother multilevel spline parametrizations of the geometry and to relate them with the multiscale images used for the initialization of shape measurement. This treatment allowed to efficiently regularize, with a geometrical meaning, the problem at each scale. From a practical point of view, the proposed approach consists of nothing more than projecting the ill-posed FE shape measurement problem onto more regular spline subspaces by using appropriate operators. As a result, we ended up with a technique that draws up the best of IG and FE technologies. On the one hand, we benefit from the increased smoothness of spline functions for the description of the geometry and of its update. On the other hand, we can perform the resolution in a non-invasive manner from an existing FE-SDIC code and, we are able to describe the final shape using the same fine FE mesh as the one which could be used for displacement measurement and identification of mechanical models.

The performance of the developed methodology over existing strategies was demonstrated through the analysis of real images coming from different experiments. For each experiment, multilevel NURBS parametrizations of the geometry were built in accordance with the multiscale images used for the initialization of the shape measurement. The method was implemented from existing FE-SDIC routines with minimal efforts. Our results clearly indicated the superiority of the proposed geometric regularization, especially as the real and the theoretical shapes are far from each other. We always managed to obtain a consistent smooth final shape within a limited number of iterations, while the standard Tikhonov regularization appeared to fail when rotations were expected.

Additionally, the proposed approach allows performing a spline field measurement (such as what has been carried out by Dufour et al. [Dufour et al., 2015a, Dufour et al., 2016]) without using a dedicated spline software. Only a standard FE-DIC software is required, in addition to an analysis-suitable CAD description of the studied structure and the easy-to-compute Lagrange extractor (or its approximation in the case of NURBS).

Yet the CAD-based approach may seem limited in the case when an analysis-suitable CAD model is not available. Splines can describe a large variety of edges geometries, but they are not adapted to simply describe holes since they provide a continuous mapping between a δ -orthotope and the physical geometry. In the case of the plate with a hole, we had to define three C^0 lines to exactly create the circle, and we had to "glue" two sides of the patch together by pairing control points to close the geometry (instead, we could have used periodic B-splines along one direction, but we would have had to create C^0 lines or superimpose control points for the four corners). For a mechanical engineer who would like to regularize shape measurement on a very complex geometry, a CAD-based method may be too complicated to use, because it requires creating a CAD model with an analysis-suitable mesh. Moreover, the FE mesh thus obtained completely depends on this CAD model and on the chosen discretization and degree. In the experimental mechanics field, a FE mesh is often chosen a priori. It is not necessarily a structured quadrangular mesh, and it can have higher levels of refinement locally to better represent geometrical details and also displacement field variations, because the same mesh is then used to measure a displacement field. In the next chapter, we present a method that generalizes the spline-based regularization concept to possibly any arbitrary FE meshes, without limitations regarding geometry complexity or elements type.

Chapter 3

FFD-based regularization of DIC problems

This chapter is extracted from [Chapelier et al., 2021].

Introduction

The CAD-based technique developed in the previous chapter is interesting because it allows to measure a 3D spline shape while using a standard FE-DIC software in a non-invasive way. However, it is restricted to input FE meshes whose approximation subspaces include the initial CAD space. In practice, this means that the FE mesh needs to be at least quadratic and even made of elements exhibiting a tensor product structure, which is usually not the case for any arbitrary analysis-suitable mesh. Another issue with all the previously mentioned strategies is the construction of the input proper boundary-fitted spline parametrization of the specimen geometry from CAD data, which is not a trivial task as demonstrated by the recent developments in isogeometric analysis [Marussig and Hughes, 2018, Teschemacher et al., 2018]. Here, we place ourselves from the experimental mechanics engineer point of view who needs to perform a relevant field measurement starting from a given FE mesh coming from a simulation software. In other words, the objective is to develop a new non-invasive regularization scheme that can be applied to any FE mesh, regardless of the element size, type or spatial density.

In order to do so, we propose in this chapter to make use of the Free-Form Deformation (FFD) concept that was first introduced by Sederberg and Parry in the field of computer graphics [Sederberg and Parry, 1986] and later applied in engineering fields, in particular for the aerodynamic design of structures [Andreoli et al., 2003, Duvigneau, 2006, Kenway et al., 2010, Lassila and Rozza, 2010, Hojjat et al., 2014, Kenway and Martins, 2014, Lyu and Martins, 2015] or to more general shape optimization problems [Bletzinger, 2017, Hirschler et al., 2019a], to make structures fit given data points in mechanical and biomedical engineering [Bardinet et al., 1998, Sacharow et al., 2011, Sacharow et al., 2013], and for non-rigid image registration in medical imaging [Rueckert et al., 1999, Xie and Farin, 2004, Wang and Jiang, 2007, Sotiras et al., 2013, Jorge-Peñas et al., 2015]. The FFD approach consists in embedding an object – respectively, a CAD geometric model in computer graphics, a mechanical structure in shape optimization or in data fitting, or an image in medical imaging – into a morphing box (usually made of splines). Any deformation

inside the morphing box is then only described by the deformation of the morphing box itself. In this respect, note that what is classified as the FFD approach in medical imaging is actually very similar to the direct spline DIC method discussed previously [Elguedj et al., 2011, Kleinendorst et al., 2015] in the sense that both techniques seek to find a spline displacement field that matches different images. In contrast, we have to consider in this study, as embedded object, a mechanical structure that is described by its analysis-suitable FE mesh. Thus our situation is closer to what is encountered in FFD shape optimization [Kenway et al., 2010, Lyu and Martins, 2015, Bletzinger, 2017] in terms of definition of the design space. The FFD concept offers the opportunity to decouple the design space from that of the actual geometry to be updated. As a result, even if the geometry is not regular (*e.g.*, C^0 across elements in case of a FE mesh), the deformation of the geometry can be considered of increased smoothness so as to regularize the corresponding optimization problem. The key idea here is just to link each FE nodal dof of the field of interest to another, more regular field discretized by the morphing box. As such, the initial structure of the FE mesh is kept during the whole process and we end up with a conventional measured FE field. Furthermore, the method is non-invasive with respect to a standard FE code (classic quadrature rules, element connectivities, etc). The strategy can ultimately be interpreted as a projection on a reduced, smooth basis and actually consists in a generalization of the technique introduced in [Colantonio et al., 2020]. Any FE mesh can indeed be embedded in a morphing box and thus any FE field dof can be controlled by the deformation of the morphing box.

The presented work is organized as follows: after this introduction, Section 3.1 dwells on theoretical and numerical aspects of the proposed FFD scheme. The adopted choices and innovative treatments with respect to the general field of FFD to build the morphing box and to relate the FE field of interest to the deformation of the box are clearly accounted for and highlighted. In particular, we consider a simple cuboid spline box and thus need to develop a specific strategy to handle conditioning problems caused by non-influential control points. In addition, we provide an original point of view on the developed FFD method and discuss its connection with other existing techniques, namely projection methods [Réthoré, 2015, Tirvaudey et al., 2019, Colantonio et al., 2020, Etievant et al., 2020] and fictitious domain approaches [Rank et al., 2012, Legrain, 2013, Schillinger and Ruess, 2015, Hansbo et al., 2017]. Then, our FFD method is applied in Section 3.2 to regularize 2D-DIC for FE displacement field measurements. Note as of now that the extension to DVC could be straightforwardly performed. The minimization problem and the associated resolution are detailed before the performances of the method are demonstrated on real images taken to observe the bending of a 2D beam. Then, Section 3.4 is devoted to the delicate problem of FE mesh shape measurement. Innovative developments based on additional projections over local directions are performed to adapt to complex geometries. The results coming from real images of a twisted plate and of a spherical cap are given to assess the methodology. Finally, concluding remarks are drawn in the last section.

3.1 Free-Form Deformation projection

As most of the works dealing with FFD, we use B-spline functions to create the morphing box. NURBS functions could also be considered [Wang and Jiang, 2007]. Yet the B-spline technology is the easiest and most encountered one and appears sufficient for the applications carried out in this work. The analysis-suitable FE

mesh will thus be controlled by a simple embedding B-spline box deformation. One can already see that this method is of great interest when the structure geometry is complex, described by a fine and possibly unstructured FE mesh, since the box geometry can be chosen very simply and with a number of dof adapted to the deformation to describe.

B-spline basics have been seen in Sections 1.2.1 and 2.2. Similarly to what has been developed in the previous chapter, a refinement procedure of the morphing box will be used in a simple and flexible multilevel approach. This approach has been initially developed for shape optimization (see, *e.g.*, [Nagy et al., 2013, Kiendl, 2011, Kiendl et al., 2014, Hirschler et al., 2019b]) and it is therefore adapted to FE-DIC displacement field measurement and FE-DIC shape measurement that both aim to find a field that minimizes a certain quantity (see Sections 3.2 and 3.4).

In the following, the creation of the morphing box is outlined, before the link between the deformation of the FE mesh and the one of the morphing box is properly derived. Then, some insights regarding the implementation are given along with a discussion on good practices to avoid bad conditioning.

3.1.1 Creating the morphing box

In the remainder of the chapter, the morphing box geometry was chosen to be a one-patch B-spline δ -orthotope entity (see Equation (1.3)), *i.e.* a rectangle if $\delta = 2$ or a rectangular parallelepiped if $\delta = 3$. The choice of δ will depend on the structure geometry, and we have $\delta \leq D$, where D is the dimension of the physical domain (see Fig. 3.1 that will be further explained in the following). These geometries are particularly easy to create because the parametric domain I can be chosen so that the mapping from I to the physical domain is the identity function [Sacharow et al., 2013]. To do so, the parametric space I is defined as $I = [0, \lambda_l]^\delta$, where $(\lambda_l)_{l=1..d}$ are being directly chosen as characteristic lengths in the physical space. This is what is performed in this work, and one of the reasons that led us to use B-splines rather than NURBS. However, the defect with such a simple geometric modeling is that some morphing box control points may not have an influence on the embedded FE mesh because they are too far from the latter, in other words, because the support of the corresponding basis function does not, or only slightly, intersect the FE mesh. This issue, which is expected to lead to ill-conditioning, will be addressed in Section 3.1.4. To circumvent the problematic, most of other works preferred morphing boxes that are closer to the structure, but therefore have a mapping that is not the identity function [Andreoli et al., 2003, Duvigneau, 2006, Kenway et al., 2010, Lyu and Martins, 2015]. In this case, a step is needed to determine the position of the embedded geometry in the parametric domain of the box (inversion of a possibly non-linear mapping).

The dimensions of the morphing box $(\lambda_l)_{l=1..d}$ are defined by the embedded structure geometry so that it is tangent to some parts of the structure (see Fig. 3.1 (left) for illustration). To construct the morphing box, a simple one-element B-spline box is first created and then, automatic refinement procedures are used to get to the desired degree and number of elements in each dimension. The morphing box is finally deformed by modifying the control points locations $\tilde{\mathbf{X}}$ (the **mb** subscript used in Section 1.2.4 is not used here for simplicity as the spline quantities always refer to the morphing box in this chapter) in the physical domain of dimension D (see Fig. 3.1 (right)). In this chapter, we work with 2^{nd} -degree B-spline functions. In the following, the link between the deformation of the morphing box and that of the embedded FE mesh will be explained.

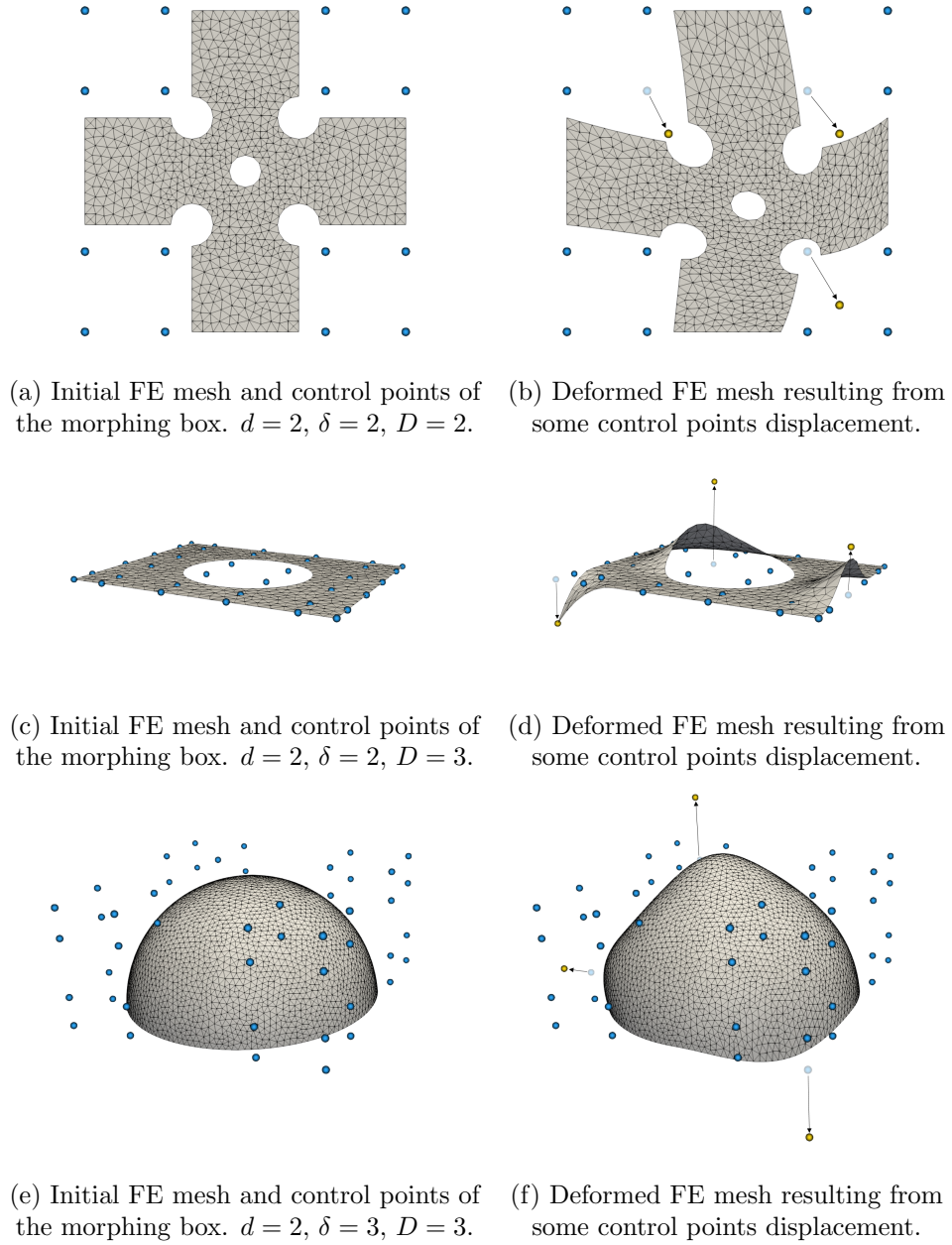


Figure 3.1: Deformation of a FE mesh using FFD. The blue dots are the control points of the morphing box. Moving these points (yellow dots, images on the right) results in a displacement of the FE mesh nodes. d is the topology of the FE elements (1: wire, 2: surface, 3: volume), δ is the dimension of the patch for the morphing box parametric domain, and D is the dimension of the physical domain. Note that the generalization to $d = 3$, $\delta = 3$ and $D = 3$ is straightforward (in this case, the surface hemisphere at the bottom just has to be viewed as a volume hemisphere).

3.1.2 Linking the deformation of the FE mesh to that of the morphing box

The FE mesh deformation is completely driven by the morphing box deformation. As stated previously, the morphing box is defined by B-spline functions and thus verifies Eq. (1.3). Let us denote by n_{FFD} the number of control points of the morphing box. In this chapter, we recall that the embedded structure is described by a FE mesh, denoted $\underline{\mathcal{M}}(\underline{\eta})$, and defined by FE nodes and shape functions such that:

$$\underline{\mathcal{M}}(\underline{\eta}) = \sum_{j=1}^{n_{FE}} N_j(\underline{\eta}) \underline{X}_j, \quad (3.1)$$

where n_{FE} is the number of FE nodes and $N_j(\underline{\eta})$ is the FE basis function associated with the j^{th} FE node ($\underline{\eta}$ is a parameter that lives in the space where FE shape functions are defined). This j^{th} node location is denoted \underline{X}_j and has D coordinates in the physical domain. For our application, the considered FE mesh is of dimension $d = 2$, which means that we only work with surface elements. Note, however, that the method easily applies in the case of a volume mesh (simple extension of Fig. 3.1(e)).

The FE structure (3.1) thus needs to be deformed according to the deformation of the morphing box, or more precisely according to the displacement of its control points. A first way of doing so would be to take every physical point in the FE mesh $\underline{\mathcal{M}}(\underline{\eta})$, to find its equivalent in the morphing box parametric domain (here, we recall that we have an identity mapping, so $\underline{\xi} = \underline{\mathcal{M}}(\underline{\eta})$ directly), and to compute the B-spline functions at these points:

$$\underline{\mathcal{S}} \circ \underline{\mathcal{M}}(\underline{\eta}) = \sum_{i=1}^{n_{FFD}} \tilde{N}_i(\underline{\mathcal{M}}(\underline{\eta})) \tilde{X}_i, \quad (3.2)$$

and thus for any other field of interest $\underline{\mathcal{U}}(\underline{\eta})$ living in the structure:

$$\underline{\mathcal{U}}(\underline{\eta}) = \sum_{i=1}^{n_{FFD}} \tilde{N}_i(\underline{\mathcal{M}}(\underline{\eta})) \tilde{U}_i, \quad (3.3)$$

with \tilde{U}_i the value of the field of interest at the i^{th} control point of the morphing box. This approach is very similar to the standard practice in the fictitious domain community where a mechanical domain with complex geometry is not meshed but embedded in a grid used for field representation, while the immersed geometry is accurately captured by means of specific quadrature rules for cut grid elements (see, *e.g.*, [Rank et al., 2012, Legrain, 2013, Schillinger and Ruess, 2015, Hansbo et al., 2017]) However, for our purposes, this method appears to be complex (sophisticated quadrature rules, specific treatment to counterbalance the ill-conditioning of the resulting system), and, more importantly, is highly invasive *w.r.t.* standard FE (see Figure 3.2(b)) so we decided to use another approach.

The aim of our work concerning data assimilation is to keep for the field description a FE mesh coming from the analysis so that a direct comparison between the measured field and a FE simulated field is possible. To this end, we apply the morphing box deformation (*i.e.* composition (3.2)) only to the nodes of the FE mesh (*i.e.* pointwise, see Figure 3.2(c)):

$$\underline{\mathcal{M}}(\underline{\eta}) = \sum_{j=1}^{n_{FE}} N_j(\underline{\eta}) \sum_{i=1}^{n_{FFD}} \tilde{N}_i(\underline{\xi}_j^{FE}) \tilde{X}_i, \quad (3.4)$$

with $\underline{\xi}_j^{FE}$ the position of the j^{th} FE node in the spline parametric domain I . We can then write Equation (3.4) in a matrix form:

$$\boxed{\underline{\mathcal{M}}(\underline{\eta}) = \underline{\mathbf{N}}^T(\underline{\eta}) \underline{\mathbf{C}}_{\mathbf{FFD}}^T \underline{\tilde{\mathbf{X}}}}, \quad (3.5)$$

where $\underline{\mathbf{C}}_{\mathbf{FFD}}$ is a $(Dn_{FFD} \times Dn_{FE})$ matrix such that has its coefficients equal to $\tilde{N}_i(\underline{\xi}_j^{FE})$. Note that $(\underline{\xi}_j^{FE})_{j=1..n_{FE}}$ is equal to the initial position of the FE nodes $(\underline{X}_j)_{j=1..n_{FE}}$ (as a consequence of the identity mapping).

The same applies to any field of interest $\underline{\mathcal{U}}(\underline{\eta}) = \sum_{j=1}^{n_{FE}} N_j(\underline{\eta}) \underline{U}_j$, where \underline{U}_j is the value of the field at the j^{th} FE node. Since this field is defined at the nodes of the FE mesh, the FE nodes value can be controlled by the control variables $(\underline{\tilde{U}}_i)_{i=1..n_{FFD}}$ attached to the morphing box, similarly to (3.4):

$$\boxed{\underline{\mathcal{U}}(\underline{\eta}) = \sum_{j=1}^{n_{FE}} N_j(\underline{\eta}) \sum_{i=1}^{n_{FFD}} \tilde{N}_i(\underline{\xi}_j^{FE}) \underline{\tilde{U}}_i}. \quad (3.6)$$

The above relation reads in matrix form:

$$\boxed{\underline{\mathcal{U}}(\underline{\eta}) = \underline{\mathbf{N}}^T(\underline{\eta}) \underline{\mathbf{C}}_{\mathbf{FFD}}^T \underline{\tilde{\mathbf{U}}}}. \quad (3.7)$$

It results in a conventional FE field, but where the dof are controlled by the morphing box. This approach can thus be seen as a kind of discretization of the (pure) fictitious domain approach (3.2)-(3.3) (for an illustration, see Figure 3.2). Unlike the latter, it has the strong interest of being non-invasive *w.r.t.* a standard FE code in the sense that classic FE quadrature rules can be applied and the element connectivities remain the same. This also enables to straightforwardly reconstruct the mesh after deformation (see again Fig. 3.1 for illustration). The non-invasive aspect of the method will be further accounted for in next section. Note finally that if the FE mesh is infinitely fine, the present approach is equivalent to the fictitious domain approach.

At this point, we can see that this work is a generalization of what has been proposed in Chapter 2 and [Colantonio et al., 2020]. It encompasses the CAD-based approach and offers more possibilities. As pointed out in [Bletzinger, 2017], in general, a CAD patch can be seen as a morphing box. Eq. (3.4) reads:

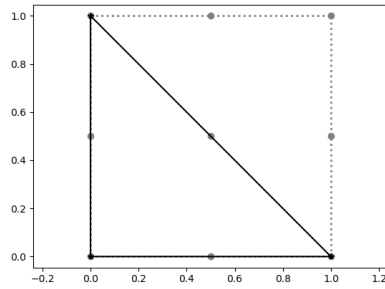
$$\underline{\mathcal{M}}(\underline{\eta}) = \sum_{i=1}^{n_{FFD}} \left(\sum_{j=1}^{n_{FE}} N_j(\underline{\eta}) \tilde{N}_i(\underline{\xi}_j^{FE}) \right) \underline{\tilde{X}}_i. \quad (3.8)$$

In the case when the morphing box fits the CAD geometry (without being necessarily a rectangle, and in the general case when the identity mapping is not ensured), and when lower-regular lines created by knots coincide with FE element edges, a B-spline function can be expressed as a linear combination of Lagrange polynomials of same degree ([Schillinger et al., 2016, Tirvaudey et al., 2019]) as:

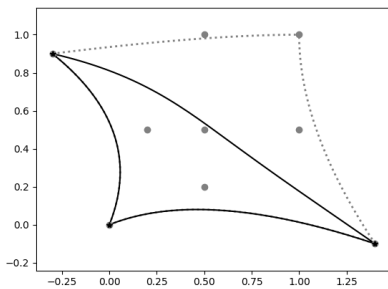
$$\tilde{N}_i(\underline{x}) = \sum_{j=1}^{n_{FE}} N_j(\underline{\eta}) \tilde{N}_i(\underline{\xi}_j^{FE}), \quad \forall i \in \{1, \dots, n_{FFD}\}, \quad (3.9)$$

or, in matrix form,

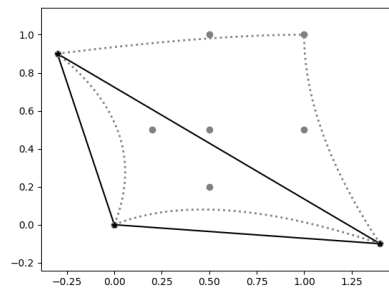
$$\underline{\tilde{\mathbf{N}}} = \underline{\mathbf{C}}_{\mathbf{FFD}} \underline{\mathbf{N}}, \quad (3.10)$$



(a) FE mesh (in black) made of a single $T3$ element embedded in a morphing box (in gray).



(b) Deformation of the FE element according to the morphing box deformation with a (pure) fictitious domain approach. Every point in the element follow the deformation. The FE element is not a $T3$ triangle in the physical domain anymore.



(c) Deformation of the FE element according to the morphing box deformation with our FFD-based approach, which can be seen as a kind of discretization of the (pure) fictitious domain approach. Only the FE nodes follow the deformation. The FE element remains a $T3$ triangle in the physical domain.

Figure 3.2: Comparison of a (pure) fictitious domain approach with our FFD-based approach on a FE mesh made of a single $T3$ element (1^{st} -degree triangular element), in the physical domain.

where $\underline{\underline{\mathbf{C}}}_{\text{FFD}}$ becomes the Lagrange extraction operator here. Equation (3.9) makes a linear combination of Lagrange functions appear, in which the coefficients are the spline functions evaluated in specific points (see the first remark in Section 2.2.2.2).

The main advantage of the general FFD approach in this work is that any FE mesh can be embedded in an FFD morphing box, while in the CAD-based approach, the FE space needed to include the CAD space. The FE mesh can now be made of low-order elements, triangles and quadrangles, and can be refined, either globally or locally, allowing for instance the integration of small geometry features (holes, etc) and accurate representation of the solution close to these areas. All information is described by the control points, thus only the morphing box refinement level matters for problem solving.

Remark 12 *For a geometry that is initially a plane, we choose the morphing box to be a bivariate patch ($\delta = 2$), and the geometry can then be deformed in a space of dimension $D = 3$ (see Figs. 3.1(c) and 3.1(d)). The geometry thus obtained is not a plane anymore. One may wonder whether a non-planar surface FE mesh, which could however be described using B-splines, could be embedded in a bivariate patch ($\delta = 2$) with a 3D mapping. If the B-spline description is known, it is possible to do so but that means the mapping is no longer the identity function (see Section 3.1.1). In our work, in this case, we will rather create a trivariate patch ($\delta = 3$) morphing box (see Figs. 3.1(e) and 3.1(f)).*

3.1.3 Implementation: projection over the morphing box

The implementation of the FFD method mainly consists in implementing the matrix $\underline{\underline{\mathbf{C}}}_{\text{FFD}}$ as described in Equation (3.5). As we have seen, this matrix makes the link between the FE nodes position and the morphing box control points position.

The $(Dn_{FE} \times Dn_{FFD}) \underline{\underline{\mathbf{C}}}_{\text{FFD}}^T$ matrix can be seen as a collection of modes, each mode being a column of the matrix [Lassila and Rozza, 2010]. For instance, if the field of interest is a displacement field, each of these modes is the displacement of all FE nodes caused by a unitary displacement of a control point. This collection of modes is a basis for a vector subspace of the vector space generated by the FE functions. We use this basis for model reduction in Sections 3.2 and 3.4 where equations of the following form, emanating from the FE discretization of variational formulations, appear:

$$\text{Find } \underline{\underline{\mathbf{U}}} \in \mathbb{R}^{Dn_{FE}} \text{ such that } \underline{\underline{\mathbf{H}}} \underline{\underline{\mathbf{U}}} = \underline{\underline{\mathbf{b}}}, \quad (3.11)$$

where $\underline{\underline{\mathbf{H}}}$ comes from a positive symmetric bilinear form and $\underline{\underline{\mathbf{b}}}$ comes from a linear form. $\underline{\underline{\mathbf{U}}}$ will either gather FE displacement or FE shape correction dof in this chapter.

From Equation (3.7), we have:

$$\underline{\underline{\mathbf{U}}} = \underline{\underline{\mathbf{C}}}_{\text{FFD}}^T \tilde{\underline{\underline{\mathbf{U}}}}. \quad (3.12)$$

In accordance with the Ritz-Galerkin method, the reduced-order problem thus writes:

$$\text{Find } \tilde{\underline{\underline{\mathbf{U}}}} \in \mathbb{R}^{Dn_{FFD}} \text{ such that } \underline{\underline{\mathbf{C}}}_{\text{FFD}} \underline{\underline{\mathbf{H}}} \underline{\underline{\mathbf{C}}}_{\text{FFD}}^T \tilde{\underline{\underline{\mathbf{U}}}} = \underline{\underline{\mathbf{C}}}_{\text{FFD}} \underline{\underline{\mathbf{b}}}. \quad (3.13)$$

$\tilde{\underline{\underline{\mathbf{U}}}}$ is then back converted in terms of FE dof using (3.12). At this stage, the non-invasiveness feature of the method clearly appears: it does not require any modifications in how $\underline{\underline{\mathbf{H}}}$ and $\underline{\underline{\mathbf{b}}}$ are computed from a standard FE code. Similarly

to Chapter 2, the developed method consists in nothing more than projecting the (expected ill-posed) FE problem onto a more regular vector subspace made of spline functions. In this sense, the proposed approach may also be related to other current reduced order techniques encountered in the broad field of DIC (which will constitute our application, see Sections 3.2 and 3.4). In particular, one can mention [Réthoré, 2015] where Williams’ modes are used to predict crack propagation, and [Etievant et al., 2020] where free vibrations modes are used to quantify the shape defects of machined surfaces. Here, we enforce less pronounced *a priori* knowledge so as to be able to regularize a large range of FE optimization problems: we only prescribe some regularity of the reduced basis by resorting to the family of B-spline functions. An associated interest is that it leads to a projection matrix that is very sparse. B-spline functions have local supports and for a patch of parametric dimension δ and of degree p , the maximum number of non-zero functions at a given point $\underline{\xi}$ is $(p + 1)^\delta$. It means that for each column of $\underline{\underline{C}}_{\text{FFD}}$, only $(p + 1)^\delta$ values or less are non-zero values.

3.1.4 Conditioning concerns

As in any immersed-like method, it may be necessary to make some corrections before getting a proper basis in $\underline{\underline{C}}_{\text{FFD}}$. In some cases, especially when the morphing box is very finely discretized, some control points may not have an influence on the embedded FE mesh, because no FE node intersects its associated B-spline support. In other words, if $\forall j, \tilde{N}_i(\underline{\xi}_j^{FE}) = 0$, then the control point in $\tilde{\underline{X}}_i$ is non-influential (see Fig. 3.3). The basis is therefore corrected by removing the columns that are full of zeros in $\underline{\underline{C}}_{\text{FFD}}^T$, *i.e.* removing the non-influential control points. The

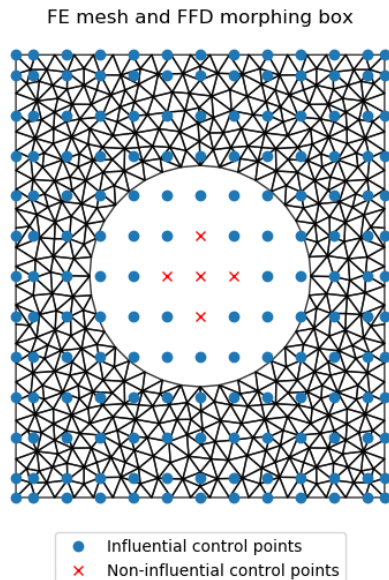


Figure 3.3: Non-influential points in a 2D structure with a hole.
 FE structure of size 60×50 with hole of diameter 28. Nodes: 503. Elements: 884.
 Element type: T3.
 Morphing box degree: 2, 2. Morphing box elements: 11×11 .

obtained basis may still not be optimal, since some control points may have very little influence on the FE mesh, even though it is not strictly zero. It has consequences

on the $\underline{\underline{\mathbf{C}}}_{\text{FFD}} \underline{\underline{\mathbf{H}}} \underline{\underline{\mathbf{C}}}_{\text{FFD}}^T$ condition number as will be seen in Section 3.4.4. For that reason, we decided to use a criterion on the influence of a control point (through its corresponding function) derived from criteria that are used by the fictitious domain community [Schillinger and Ruess, 2015, Verhoosel et al., 2015, Rouwane et al., 2021]. The idea is to see what proportion of a function support actually overlaps with the embedded structure. When the structure and the morphing box are of same dimension ($d = \delta$), we propose the following criterion for a control point in $\underline{\underline{\tilde{X}}}_i$:

$$Q_i = \frac{\int_{\mathcal{M}} \tilde{N}_i(\underline{\underline{\xi}}) d\underline{\underline{\xi}}}{\int_I \tilde{N}_i(\underline{\underline{\xi}}) d\underline{\underline{\xi}}}, \quad (3.14)$$

where Q_i is the influence of the control point in $\underline{\underline{\tilde{X}}}_i$. However, when the structure and the morphing box are of different dimensions ($d \neq \delta$), as in Section 3.4.4 and Figs. 3.1(c) and 3.1(d) where $d = 2$ and $\delta = 3$, we need to define an equivalent surface from the integral along the volume, by raising it to the power d/δ . Our criterion is thus generalized as follows:

$$Q_i = \frac{\int_{\mathcal{M}} \tilde{N}_i(\underline{\underline{\xi}}) d\underline{\underline{\xi}}}{\left(\int_I \tilde{N}_i(\underline{\underline{\xi}}) d\underline{\underline{\xi}}\right)^{d/\delta}}. \quad (3.15)$$

This criterion could be directly coupled with the choice of a threshold to remove control points that do not have enough influence on the FE geometry. In Section 3.4.4, we chose to use this criterion to only sort the points by increasing influence and then we removed the minimum of points so as to lower the $\underline{\underline{\mathbf{C}}}_{\text{FFD}} \underline{\underline{\mathbf{H}}} \underline{\underline{\mathbf{C}}}_{\text{FFD}}^T$ condition number below a chosen value.

Finally, note that for the sake of simplicity, we numerically compute Q_i as:

$$Q_i = \frac{\sum_j \tilde{N}_i(\underline{\underline{\xi}}_j)}{\left(\int_I \tilde{N}_i(\underline{\underline{\xi}}) d\underline{\underline{\xi}}\right)^{d/\delta}}. \quad (3.16)$$

The numerator is not exactly an integral (at least a mean element size is needed to get an integral approximation), but with FE elements sizes that are comparable with one another, as is the case in this chapter, this criterion allows us to compare control points influences. The interest is that the numerator is also easily accessible because it is the sum of coefficients in the i^{th} line of $\underline{\underline{\mathbf{C}}}_{\text{FFD}}$. This sum is zero for non-influential control points, as explained above. Moreover, considering the value of B-spline functions \tilde{N}_i at the nodes of the FE mesh makes sense, because they are the only points of the mesh that exactly follow the deformation of the morphing box. For instance, in the case where $\delta = 2$ and $D = 3$ (see Figs. 3.1(c) and 3.1(d)), Gauss points are not a priori in the morphing box, due to tessellation. To the best of our knowledge, this is the first time that such a treatment is applied in the general field of FFD.

3.2 Digital Image Correlation (DIC)

As a first application of our FFD approach, we investigate the measurement of FE displacement fields carried out by Digital Image Correlation (DIC). As mentioned in the introduction, spline functions have shown their potential for regularization in the broad field of image registration (see, *e.g.*, [Jorge-Peñas et al., 2015, Sotiras et al., 2013] related to the biomedical area and [Elguedj et al., 2011, Kleinendorst et al., 2015, Dufour et al., 2015a] in the experimental solid mechanics community). Unlike

these works, we aim here at taking advantage of spline properties, while obtaining as an output a FE displacement field, which simplifies the communication with a simulation software in view of performing data assimilation. A first approach in this direction was proposed in Chapter 2 and [Colantonio et al., 2020]. Here we extend this work to any FE mesh, regardless of the element size or type. The developed technique is particularly adapted for mechanical solutions over complex geometries that necessitate very fine FE meshes, thereby making the corresponding inverse DIC problems highly ill-posed.

3.2.1 Mesh-based DIC

Measuring a displacement field with DIC requires taking pictures of a specimen before and after deformation. The specimen is covered with a black and white speckle pattern in order to correlate the images of the deformed and reference state. More precisely, we seek to measure at the surface of the specimen the displacement field $\underline{u}(\underline{x})$ related to any pixel position \underline{x} of the region of interest ω_s in the reference image. The graylevel conservation at each pixel states [Horn and Schunck, 1981]:

$$\forall \underline{x} \in \omega_s, \quad \mathcal{I}(\underline{x}) = \mathcal{J}(\underline{x} + \underline{u}(\underline{x})), \quad (3.17)$$

with \mathcal{I} the reference stage image and \mathcal{J} the deformed state image. This equality cannot generally be satisfied (due to noise, brightness, speckle choice, graylevel quantization...). Thus the problem is classically reformulated as the minimization of a least-square functional:

$$\underline{u}^* = \arg \min_{\underline{u} \in (L_2(\omega_s))^D} \mathcal{F}_u(\underline{u}(\underline{x})) \quad \text{with } \mathcal{F}_u(\underline{u}(\underline{x})) = \frac{1}{2} \int_{\omega_s} [\mathcal{I}(\underline{x}) - \mathcal{J}(\underline{x} + \underline{u}(\underline{x}))]^2 d\underline{x}. \quad (3.18)$$

The problem can be discretized using a FE basis (leading to so-called FE-DIC [Sun et al., 2005, Besnard et al., 2006, Fedele et al., 2013, Wittevrongel et al., 2015, Passieux et al., 2018b]), which means that the displacement field is constructed thanks to standard nodal Lagrange polynomial functions: $\underline{u}(\underline{x}) = \underline{\mathbf{N}}^T(\underline{x}) \underline{\mathbf{u}}$. In the case of 2D-DIC, we have $D = d = 2$ (see Figs. 3.1(a) and 3.1(b)). Note however that the developed FFD-based methodology could be straightforwardly applied to DVC [Leclerc et al., 2012, Gomes Perini et al., 2014]. These functions are linked to a FE mesh that we suppose to have *a priori*. It usually comes from FE simulations to then faster the dialog between measured and simulated fields for data assimilation in experimental mechanics [Périé et al., 2009, Réthoré, 2010, Mathieu et al., 2015]. We recall that the proposed FFD approach does not prescribe any constraint on the FE mesh construction (see Section 3.1).

The FE-DIC problem writes:

$$\underline{\mathbf{u}}^* = \arg \min_{\underline{\mathbf{u}} \in \mathbb{R}^{Dn_{FE}}} \mathcal{F}_u(\underline{\mathbf{N}}^T(\underline{x}) \underline{\mathbf{u}}). \quad (3.19)$$

This problem is solved using a modified Gauss-Newton algorithm [Passieux and Bouclier, 2019]. An initialization of the displacement $\underline{\mathbf{u}}^{(0)}$ at each dof is chosen (see discussion at the end of the section), and at each iteration k , a correction $\underline{\delta \mathbf{u}}^{(k)}$ is sought so that $\underline{\mathbf{u}}^{(k)} = \underline{\mathbf{u}}^{(k-1)} + \underline{\delta \mathbf{u}}^{(k)}$. The descent direction $\underline{\delta \mathbf{u}}^{(k)}$ is the solution of

the following linear system:

$$\begin{aligned} \underline{\underline{\mathbf{H}}}_u \delta \underline{\mathbf{u}}^{(k)} &= \underline{\mathbf{b}}_u^{(k)} \quad \text{with} \quad (3.20) \\ \left\{ \begin{aligned} \underline{\underline{\mathbf{H}}}_u &= \int_{\omega_s} \underline{\underline{\mathbf{N}}}(x) \underline{\nabla \mathcal{I}}(x) \underline{\nabla \mathcal{I}}^T(x) \underline{\underline{\mathbf{N}}}^T(x) dx \\ \underline{\mathbf{b}}_u^{(k)} &= \int_{\omega_s} \underline{\underline{\mathbf{N}}}(x) \underline{\nabla \mathcal{I}}(x) \left[\mathcal{I}(x) - \mathcal{J} \left(x + \underline{\underline{\mathbf{N}}}^T(x) \underline{\mathbf{u}}^{(k-1)} \right) \right] dx \end{aligned} \right. \end{aligned}$$

where $\underline{\nabla \mathcal{I}}(x)$ is the gradient of image \mathcal{I} evaluated at position x . A brightness correction is applied at the element level so that the graylevel values in each element have the same mean and standard deviation [Colantonio et al., 2020]. In case of a too fine mesh compared to the data provided by the experimental instrumentation, the FE-DIC problem (3.19) is highly ill-posed. As a strong regularization, we apply the FFD projection strategy described in Section 3.1. More precisely, we seek the displacement field in the reduced basis coming from a morphing box; that is, we express the unknown field as in (3.7) which leads to modify, at each iteration, system (3.20) by the one given in (3.13).

For the initialization, we use a multiscale approach, inspired from [Colantonio et al., 2020], which combines coarse graining techniques used in DIC and multilevel properties of splines. Coarse graining [Hild et al., 2002, Besnard et al., 2006, Pierré et al., 2017] is a well-known tool in DIC to avoid local minima when solving the problem. It consists in aggregating pixels in the images f and g to create images with lower resolution, and consider them to run the DIC algorithm first. The solution is then used as an initialization of the DIC problem on the well-resolved images. This process can be repeated several times (see Fig. 3.4). In our approach, since splines can be refined automatically and efficiently, it is interesting to couple the morphing box refinement with the coarse graining procedure. When the images resolution is low, we need a spline box with few elements to regularize the corresponding coarse DIC problem. More precisely, at each scale s , the final coarse spline dof $\tilde{\underline{\mathbf{u}}}_{scale\ s}^{(n)}$ is back converted in terms of FE dof $\underline{\mathbf{u}}_{scale\ s}^{(n)}$ following (3.12), and then taken as the initialization for the finer scale $s - 1$, such as $\underline{\mathbf{u}}_{scale\ s}^{(n)} = \underline{\mathbf{u}}_{scale\ s-1}^{(0)}$ (see Fig. 3.4).

The multilevel properties of B-splines avoid computing the FFD matrix at each scale. Only the computation of $\underline{\underline{\mathbf{C}}}_{\text{FFD}}$ at the finest scale, namely scale 0, as described in Section 3.1.2, is needed. Then, similarly to Equation (2.27), we can write:

$$\underline{\underline{\mathbf{C}}}_0 = \underline{\underline{\mathbf{C}}}_{\text{FFD}} \quad \text{and} \quad \underline{\underline{\mathbf{C}}}_s = \left(\prod_{i=0}^{s-1} \underline{\underline{\mathbf{C}}}_{\text{ref}}^{(s-i), (s-i-1)} \right) \underline{\underline{\mathbf{C}}}_{\text{FFD}}, \quad \forall s \in \{1, \dots, n_s\}, \quad (3.21)$$

where $\underline{\underline{\mathbf{C}}}_s$ is the FFD projection operator at scale s . In the end, the resolution of the regularized DIC problem at each scale simply consists in modifying system (3.20) by the one given in (3.13) with $\underline{\underline{\mathbf{C}}}_{\text{FFD}}$ replaced by $\underline{\underline{\mathbf{C}}}_s$.

3.2.2 2D digital image correlation: Bending of a beam

In order to validate our method for mesh-based DIC, we applied it on a bending beam, using *Pyxel* as a FE-DIC software [Passieux, 2018]. A 2D simply supported horizontal PMMA beam is subjected to vertical loads on two points (see Fig. 3.5(a)). The displacement field is then measured on a 1006×5500 -pixel region of interest. The chosen FE discretization is a structured quadrangular mesh (20×110 4-node elements) but could be any mesh. Each FE node can move along the two planar directions. A 3-scale initialization is chosen, which means that the pixels of images

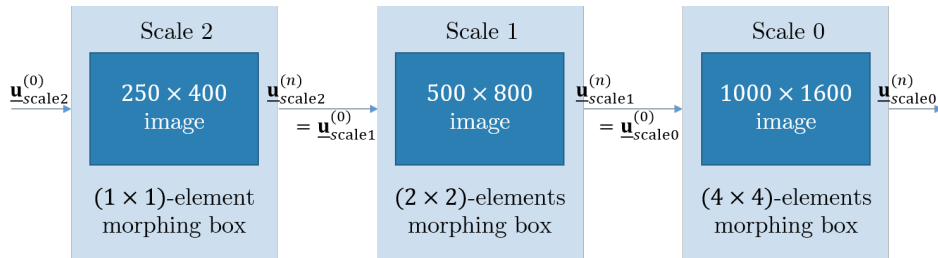
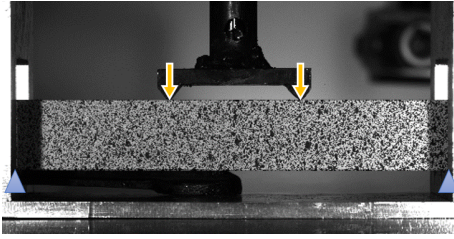


Figure 3.4: Example of a multiscale approach. At scale 0, the images \mathcal{I} and \mathcal{J} are used with their initial resolution, and a number of spline elements is chosen for the FFD morphing box. For each scale, the pixels in \mathcal{I} and \mathcal{J} are aggregated by $2^{2 \times \text{scale}}$, and similarly, the number of spline elements is reduced to achieve a sufficient regularization level. The number of scales can be chosen freely, but the images must still contain enough graylevel gradient (contrast).

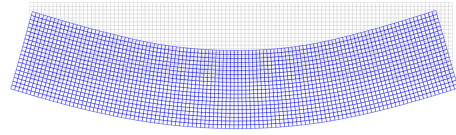
\mathcal{I} and \mathcal{J} are aggregated 8 by 8 at the coarsest scale. This initialization was carried out using FFD regularization with a single 2-dimensional quadratic patch of 1×1 , 2×2 and 4×4 spline elements at scale 3, 2 and 1 respectively.

The deformed configuration eventually obtained at scale 0 is shown in Fig. 3.5(b). The final displacement field was computed with the proposed FFD regularization technique with 8×8 spline elements. We compared our results with two classical solutions obtained with the same initialization, only changing the way of solving the problem at scale 0: (i) what is commonly called Tikhonov regularization in the field of DIC [Passieux and Périé, 2012, Dufour et al., 2016, Pierré et al., 2017] and (ii) no regularization. Tikhonov regularization consists here in a penalization of the L_2 -norm of the gradient of each component of the displacement field. In this case, the penalization coefficient was chosen so as to obtain a characteristic regularization length comparable to the smallest regularization length that we get with the FFD regularization at scale 0. The smallest FFD regularization length is set along y because the FFD spline elements are smaller in that direction. This choice comes from the fact that the variations of the sought displacement field are known to be greater along y . The FFD characteristic regularization length in that direction is thus 2 times the size of the spline elements in the y direction. In order to set the Tikhonov penalization coefficient, the procedure described in [Leclerc et al., 2012] was followed, with the choice of a reference displacement field in the form of a plane wave. Note here that defining a physical regularization length is intuitive and straightforward with the FFD method, whereas additional computations are required for its estimation with the Tikhonov regularization.

The FFD regularization shows great potential for reducing the noise impact on the result. The obtained displacement field with FFD regularization is consistent and very smooth, as shown in Fig. 3.6. Two harmful effects can be reported with the standard alternatives to solve the problem (see the region within the dotted and solid circles in Fig. 3.6). The dotted circle indicates the impact of dust on the camera. A speck of dust creates a small black spot in the images, and that spot remains stationary relatively to the images. Thus it does not follow the displacement of the specimen. This explains why a node of the FE mesh has a smaller displacement than its neighbors when no regularization is applied (black mesh). Tikhonov regularization (red mesh) smooths this impact, and the chosen FFD regularization (blue mesh) completely removes the problem. The solid circle shows Tikhonov defects on



(a) Experimental set-up. Yellow arrows and blue triangles represent respectively applied loads in the y direction and points where the beam is simply supported.



(b) Gray and blue meshes represent respectively the undeformed FE mesh and its deformed configuration after running DIC with our FFD regularization. Amplification factor: $\times 30$.

Figure 3.5: Experimental application: bending beam.

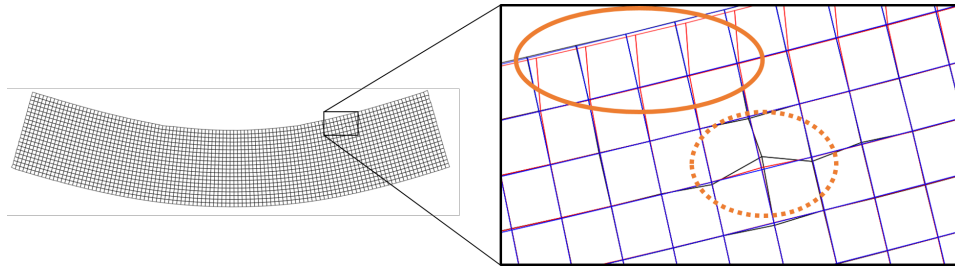


Figure 3.6: Zoom on defects that are not part of the displacement field. The black mesh results from the unregularized problem, the red mesh is obtained using Tikhonov regularization, and the blue mesh shows the deformed configuration with FFD regularization. The dotted circle shows the impact on the results of dust on the camera, which affects the black and red meshes. The solid circle shows artifacts inherent to the standard Tikhonov regularization.

the curved edges of the specimen. It reduces a part of the rotations that is relevant, which creates artifacts on the edges. This harmful effect of the standard Tikhonov regularization has already been underlined in [Colantonio et al., 2020] for the specific case of mesh-based shape measurement.

The differences between FFD regularization, Tikhonov regularization and no regularization are all more noticeable when displaying the strain field, since the impact of noise tends to be increased when taking a derivative. Fig. 3.7 shows the strain fields obtained with no regularization, Tikhonov regularization, FFD regularization and an idealized analytical solution obtained with a standard beam model and simple boundary conditions. Clearly, using no regularization gives noisy results (see Figs. 3.7(a) to 3.7(c)). Color scales have been adjusted in order to see the relevant components of the strain field. The edges of the region of interest and the region where there is the dust spot are undergoing unrealistic off-scale values. For example, the top right corner of the region of interest has values of ε_{yy} up to $1.3e - 2$, that is 10 times higher than expected. Tikhonov regularization reduces the impact of the noise, makes the edges much less erratic and smooths the impact of dust on the result. However, as pointed out in Fig. 3.6, the rotations of the edges are dampened, and that leads to measuring some spurious shear (see near to the top and bottom boundaries of the region of interest in Fig. 3.7(f) in comparison to the reference in Fig. 3.7(1)). The FFD regularization gives smooth results thanks to the projection of the DIC problem onto a smaller, more regular, spline basis. It gives satisfying results compared to the idealized analytical solution. This result appears totally

3.3. A LESS REGULAR CASE

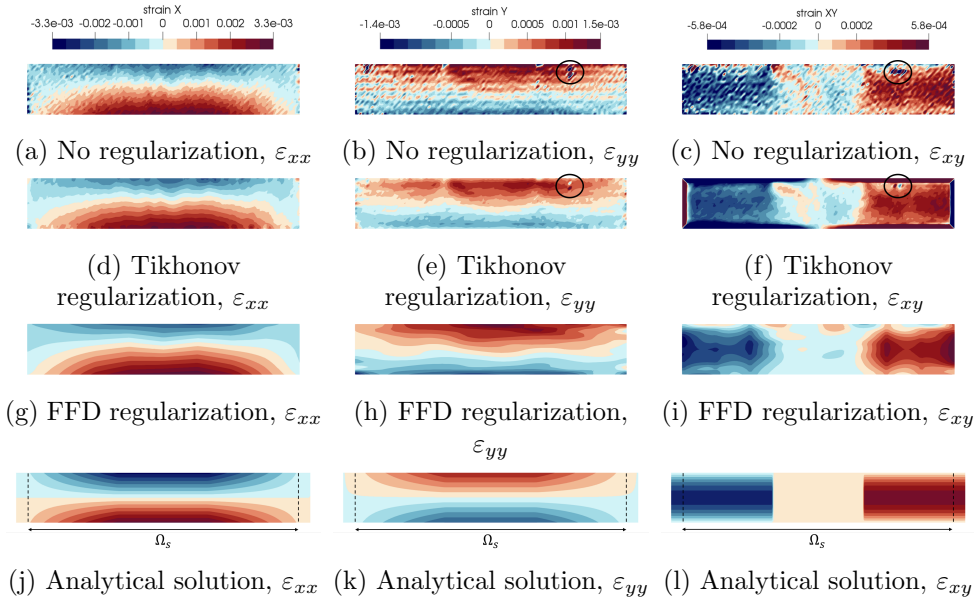


Figure 3.7: Comparison of our regularization method (third line, FFD regularization) with the results obtained with no regularization (first line), with Tikhonov regularization (second line) and with an idealized beam solution (fourth line) for the measured strain coming from DIC on the bending beam shown in Figure 3.5(a). The beam for the analytical solution is longer because it represents the whole beam while the other figures only represent the region of interest. The impact of dust has been circled.

relevant since the aim of the experiment was to measure a global displacement field, in accordance with Saint Venant’s principle.

Remark 13 Here we used FFD regularization for the initialization in each case (process illustrated in Fig. 3.4). Note that in case another regularization technique is chosen to compute an initialization $\mathbf{u}_{scale\ 0}^{(0)}$ (such as Tikhonov regularization as is often done in the field [Passieux and Périé, 2012, Dufour et al., 2016, Pierré et al., 2017]), a projection is needed before starting the developed FFD-DIC resolution process at scale 0. When performing an optimization, it is indeed essential to start with the initialization in the research space. In other words, we have to make sure that the initialization performed is not adding features that cannot be modified in the FFD subspace. In this case, the projection of $\mathbf{u}_{scale\ 1}^{(n)}$ consists in finding $\tilde{\mathbf{u}}_{scale\ 0}^{(0)}$ that minimizes the L_2 -error $\left\| \mathbf{u}_{scale\ 1}^{(n)} - \underline{\underline{\mathbf{C}}}_{\text{FFD}}^T \tilde{\mathbf{u}}_{scale\ 0}^{(0)} \right\|^2$. The resulting FE field used for initialization is finally $\mathbf{u}_{scale\ 0}^{(0)} = \underline{\underline{\mathbf{C}}}_{\text{FFD}}^T \tilde{\mathbf{u}}_{scale\ 0}^{(0)}$.

Remark 14 Note that other types of regularization techniques exist, such as mechanical regularization [Réthoré et al., 2009b, Tomičević et al., 2013]. This technique is not detailed in this manuscript as we mainly consider shape measurement problems.

3.3 A less regular case

In order to demonstrate the regularizing potential of splines even in cases when an irregular feature has to be measured, the following numerical example shows how to apply the method in the case of a less regular displacement field in 2D

DIC. For this purpose, a pair of synthetic images was generated. They represent a specimen containing a bi-material interface before and after applying a tension in the horizontal direction. The Young modulus ratio was 10 and the Poisson's ratio was chosen to be zero. Across this interface, the displacement field is C^0 and thus the strain field is discontinuous, see Fig. 3.8(b). A structured finite element mesh made of 4-node linear quadrilaterals was constructed, see Fig. 3.8(a). The size of the finite elements was chosen to be small enough to well represent the strain discontinuity, but not large enough to allow for direct measurement without regularization.

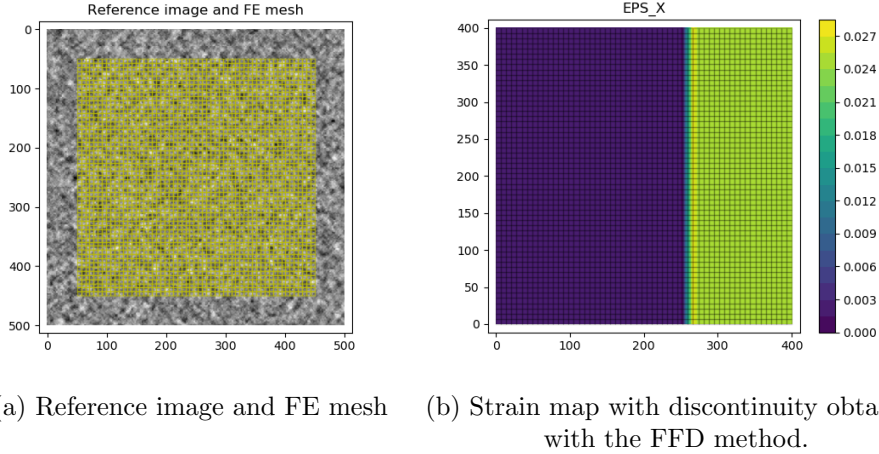


Figure 3.8: Virtual test showing the ability of the method to describe a less regular displacement field. More details are shown in Figure 3.9

An initial morphing box of 1 quadratic element was built around the FE mesh. A first FFD measurement with this morphing box has been performed. Not surprisingly, it is not at all adapted to the irregularity of the field to be measured, see Figure 3.9(top). This results in a particularly high correlation residual which reflects the fact that the (regular) kinematics chosen is not sufficient to represent the complexity of the field. This residual provides extremely valuable information for enriching the approximation space, since it is possible to locate areas where the approximation is insufficient.

As an illustration, we performed a naive technique, which consists in locating the abscissa corresponding to the maximum of the residual function and adding a knot in the knot vector at this very same place. The measurement was then performed once again with the new spline parametrization of the FFD morphing box. The corresponding spline mesh is depicted in Figure 3.9 (middle-left). It is still C^1 which means that it is not surprising to find again high residual levels although they are reduced compared to the first measurement. The same adaptive knot-insertion procedure is performed once more. As the maximum of the residual is located at the same point, the new knot is duplicated in the knot vector, which reduces the regularity of the space and allows to represent C^0 line in the morphing box. This time the displacement is perfectly measured with its C^0 line and the residual map is homogeneous, at a level comparable to noise. It is possible to generalize such a procedure to create C^0 or discontinuous lines in the morphing box, either *a priori*, or during the refinement phase. As illustrated here, criteria such as the graylevel residual value can help identify the regions that should be refined [Kleinendorst et al., 2015].

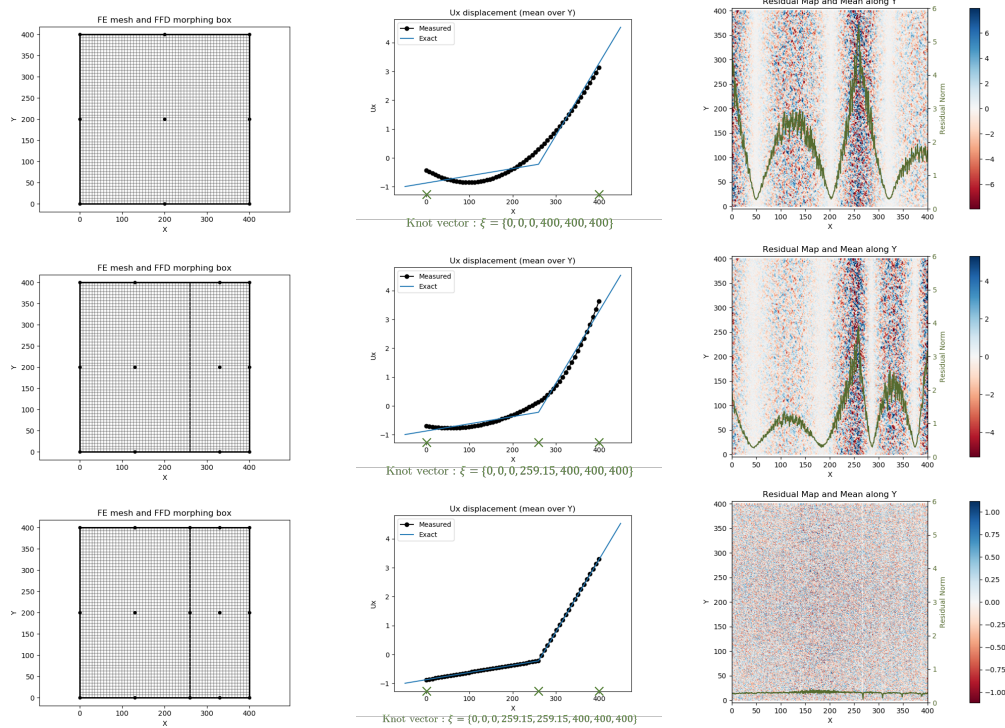


Figure 3.9: The first line shows an initial morphing box of 1×1 quadratic element, the measured displacement along x (mean over y) compared to the exact one, and the residual map resulting from the FFD-DIC problem in this case (which shows a maximum for $x = 259.15$). In the second line, a knot has been added in the morphing box for $x = 259.15$. The residual is still maximum for this value. In the third line, a second knot has been added for $x = 259.15$, creating a C^0 line, which enables us to properly capture the irregular solution.

3.4 Shape measurement

As seen in the previous chapter, spline-based regularization is particularly well adapted when the measured field is expected to be smooth [Dufour et al., 2016]. It is the case when measuring a shape before performing 3D displacement field measurement. In this chapter, the context is slightly different from that of Chapter 2. In the last chapter, the measured shape correction was expressed on a CAD model of the structure, and a FE software could be used thanks to the non-invasive implementation of the exact link between B-spline functions and FE standard functions. The core, the starting point of the CAD-based method is an analysis-suitable CAD model, which makes sense for shape correction since a structure geometry model often starts with a CAD description. In this chapter, the proposed FFD-based approach does not offer a CAD description of the shape correction, but it allows working with any arbitrary FE mesh. This approach is thus perfectly adapted to experimental mechanics engineers who are given a FE mesh as a starting point.

This section aims at showing the potential of the FFD-based approach on possibly complex geometries. To do so, an example on a non-planar specimen with pictures taken at 360° is presented. Therefore, the theoretical aspects of shape measurement with n_{cam} cameras (with $n_{cam} \geq 2$) are first given. Then, the FFD projection is detailed, and finally, the method is validated on two examples: the twisted specimen from Chapter 2 and a spherical cap.

3.4.1 Mesh-based shape measurement: generalization to n_{cam} cameras

As we have seen in Section 2.1.2, mesh-based shape measurement consists in correcting the theoretical geometry of a structure using its FE mesh by analyzing several pictures of the structure taken from different points of view [Pierré et al., 2017]. These corrections are needed because the real geometry may slightly differ from the nominal geometry, due to machining imperfections or to the experimental set-up that can induce small deformations. This mismatch between the idealized CAD and the actual specimen shape may be detrimental to the displacement measurement.

We now generalize the shape measurement problem and consider that the specimen is observed with n_{cam} cameras (which may correspond to the same physical sensor in different positions and/or orientations). Each camera c is modelled by a mapping $\underline{x}_c = \underline{P}_c(\underline{X})$ from any point \underline{X} of the physical space $\Omega_s \in \mathbb{R}^3$ to the coordinate in pixels $\underline{x}_c \in \mathbb{R}^2$ of its projection in the image plane [Sutton et al., 2000] (see Section 2.1). Such models depend on a number of parameters that are considered to be determined in a photogrammetric calibration phase carried out beforehand [Garcia, 2001].

The goal of shape measurement is to find a geometry correction field $\underline{S}(\underline{X})$ such that the projection of a physical point $\underline{X} + \underline{S}(\underline{X})$ of the structure has the same graylevel in all images taken pair by pair. The problem thus writes:

$$\underline{S}^* = \arg \min_{\underline{S} \in (L_2(\Omega_s))^D} \sum_{i=1}^{n_{cam}} \sum_{j=i+1}^{n_{cam}} \int_{\Omega_s} V_i(\underline{X}) V_j(\underline{X}) r_{ij}^2(\underline{S}(\underline{X})) d\underline{X}, \quad (3.22)$$

with r_{ij} the graylevel residual fields between images \mathcal{I}_i of camera i and image \mathcal{I}_j of camera j :

$$r_{ij}(\underline{S}(\underline{X})) = [\mathcal{I}_i \circ \underline{P}_i(\underline{X} + \underline{S}(\underline{X})) - \mathcal{I}_j \circ \underline{P}_j(\underline{X} + \underline{S}(\underline{X}))]. \quad (3.23)$$

Function $V_c(\underline{X})$ is a mask associated with camera c , such that $V_c(\underline{X}) = 1$ if a point on the FE model \underline{X} is correctly seen by the camera c and $V_c(\underline{X}) = 0$ otherwise. With 3D structures, a given camera may indeed not see the whole region of interest at once (see Section 3.4.4). Moreover, when measuring the shape from several points of view, two cameras are very unlikely to have equal visible structure parts. For that reason, the contribution of a pair of cameras is restricted to the intersection of visible regions of each camera. $\alpha_{ij}(\underline{X}) = V_i(\underline{X}) V_j(\underline{X})$ is thus a mask associated with the pair of cameras i and j .

As for DIC (see Section 3.2), we discretized the problem using a FE basis and solved it with a modified Gauss-Newton algorithm. An initialization of the shape correction at each degree of freedom $\underline{\mathbf{S}}^{(0)}$ is set (often to zero since the discrepancy between theoretical and actual shape is usually small) and the shape correction at each iteration, $\underline{\delta\tilde{\mathbf{S}}}^{(k)}$ such that $\underline{\mathbf{S}}^{(k)} = \underline{\mathbf{S}}^{(k-1)} + \underline{\delta\tilde{\mathbf{S}}}^{(k)}$, is computed by solving the following linear system (\underline{X} -dependence omitted for clarity):

$$\begin{aligned}
 \underline{\underline{\mathbf{H}}}_S^{(k)} \delta \underline{\mathbf{S}}^{(k)} &= \underline{\mathbf{b}}_S^{(k)} \quad \text{with} & (3.24) \\
 \left\{ \begin{aligned}
 \underline{\underline{\mathbf{H}}}_S^{(k)} &= \sum_{i=1}^{n_{cam}} \sum_{j=i+1}^{n_{cam}} \int_{\Omega_s} \alpha_{ij} \underline{\mathbf{N}} \left(\underline{\underline{J}}_i^{(k)T} \underline{\nabla} \underline{\mathcal{I}}_i^{(k)} - \underline{\underline{J}}_j^{(k)T} \underline{\nabla} \underline{\mathcal{I}}_j^{(k)} \right) \\
 &\quad \times \left(\underline{\underline{J}}_i^{(k)T} \underline{\nabla} \underline{\mathcal{I}}_i^{(k)} - \underline{\underline{J}}_j^{(k)T} \underline{\nabla} \underline{\mathcal{I}}_j^{(k)} \right)^T \underline{\mathbf{N}}^T d\underline{\mathbf{X}} \\
 \underline{\mathbf{b}}_S^{(k)} &= - \sum_{i=1}^{n_{cam}} \sum_{j=i+1}^{n_{cam}} \int_{\Omega_s} \alpha_{ij} \underline{\mathbf{N}} \left(\underline{\underline{J}}_i^{(k)T} \underline{\nabla} \underline{\mathcal{I}}_i^{(k)} - \underline{\underline{J}}_j^{(k)T} \underline{\nabla} \underline{\mathcal{I}}_j^{(k)} \right) \\
 &\quad \times r \left(\underline{\mathbf{N}}^T \underline{\mathbf{S}}^{(k-1)}, p \right) d\underline{\mathbf{X}}
 \end{aligned} \right. ,
 \end{aligned}$$

where $\underline{\underline{J}}_c^{(k)}$ is the jacobian matrix of the mapping \underline{P}_c with respect to $\underline{\mathbf{X}}$, calculated at the physical point $\underline{\mathbf{X}} + \underline{\mathbf{N}}^T(\underline{\mathbf{X}}) \underline{\mathbf{S}}^{(k-1)}$, and $\underline{\nabla} \underline{\mathcal{I}}_c^{(k)} = \underline{\nabla} \underline{\mathcal{I}}_c \circ \underline{P}_c \left(\underline{\mathbf{X}} + \underline{\mathbf{N}}^T(\underline{\mathbf{X}}) \underline{\mathbf{S}}^{(k-1)} \right)$ defines the gradient of the graylevel image.

It can be seen that the computation of the matrix $\underline{\underline{\mathbf{H}}}_S^{(k)}$ and the vector $\underline{\mathbf{b}}_S^{(k)}$ involves a sum of all pair contribution. It is worth noting that for many pairs of cameras, $V_i(\underline{\mathbf{X}})V_j(\underline{\mathbf{X}}) = 0, \forall \underline{\mathbf{X}}$, because both cameras see different regions of the structure. This significantly reduces the number of terms in the double sum.

Practically speaking, V_c is defined for each FE element. Elements whose outward normal unit vector \underline{n}_e is pointing to the background are not visible. As a result, the value of V_c is set to 0 for any FE elements that meet the criterion $\underline{z}_c \cdot \underline{n}_e < 0$, where $-\underline{z}_c$ is the unit direction the camera c is looking at.

We also did not consider surfaces that are seen too inclined by the camera, because the speckle pattern is not accurately captured due to a too small pixel size to structure surface ratio. When this criterion is below a given threshold ϵ_n , the element e is considered not correctly visible for the camera c , and $V_c(\underline{\mathbf{X}}) = 0$ on this element. In other terms:

$$V_c(\underline{\mathbf{X}}) = \begin{cases} 1 & \text{if } \underline{z}_c \cdot \underline{n}_e(\underline{\mathbf{X}}) > \epsilon_n, \\ 0 & \text{otherwise.} \end{cases} \quad (3.25)$$

Note here that the greater we choose the threshold ϵ_n , the more elements are "correctly" seen by each camera, and the more cameras see a given element. The minimum number of cameras that are needed for shape measurement is thus defined by this threshold, since each FE element should be seen by at least two cameras for the FE problem to be solvable if not regularized.

Note also that all elements are not seen by the same number of cameras (zones that are seen by a given camera overlap), which means some dof have more weight than others by construction of $\underline{\underline{\mathbf{H}}}_S^{(k)}$. We decided to normalize each element contribution by the number of pairs of cameras that can see it, such that no dof is predominant in the minimization of the functional. Note that an appropriate, physically-based weighting has been proposed in [Fouque et al., 2021b].

Similarly to Section 3.2, the matrix $\underline{\underline{\mathbf{H}}}_S^{(k)}$ and the vector $\underline{\mathbf{b}}_S^{(k)}$ being computed by any pre-existing FE-SDIC software, we regularize the problem by projecting it on the smoother FFD space thanks to the matrix $\underline{\underline{\mathbf{C}}}_{\text{FFD}}$.

The multiscale initialization approach as described in the previous chapter and [Colantonio et al., 2020] was also used for shape measurement.

3.4.2 FFD projection of the shape measurement problem

So far shape correction consists in moving nodes (or control points) in the 3 dimensions of space. However, moving a node/control point in the direction tangent to

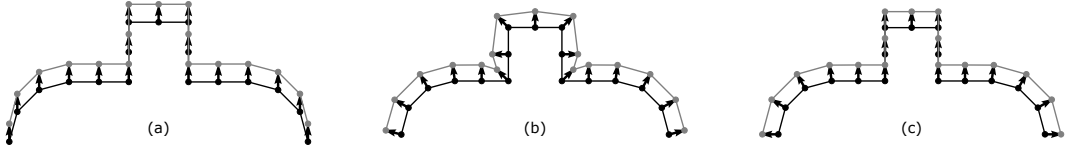


Figure 3.10: Examples of normal direction fields defined on the FE mesh for shape measurement.

the surface does not change the geometry and thus makes the shape measurement problem ill-posed. To avoid mesh distortion or elements overlapping and to improve the spectral properties of the Hessian, the shape correction is sought in one single direction, usually the normal to the surface [Dubreuil et al., 2016, Pierré et al., 2017]. As such, we end up with a scalar problem, namely, with only one dof per node. In FFD-based 3D shape optimization, the usual practice consists in proceeding in two successive steps: (i) first the 3D FE optimization problem is projected onto the 3D Spline shape functions, then (ii) the control points are constrained to move in one direction only [Kenway et al., 2010].

Defining a direction vector field at the FFD control points is not completely satisfactory in our context because of the multiscale process. To prevent the final result from depending on the minimization algorithm, it is important to ensure that each research space is included in the next one. This condition implies that the direction field variations in each scale are given by the coarsest FFD direction field. This constraint may be restrictive especially when dealing with complex geometries.

In the spirit of the approach developed from the finite element mesh point of view, we propose to define a local normal direction field \underline{n} defined at the nodes of the FE mesh and along which the nodes will be moved to update the geometry. It means we look for a shape correction written $\underline{\mathbf{S}} = \underline{\underline{\mathbf{\Pi}}}_n \underline{\mathbf{S}}_n$, where $\underline{\mathbf{S}}_n$ contains dofs in the chosen direction and $\underline{\underline{\mathbf{\Pi}}}_n$ is the corresponding extraction $Dn_{FE} \times n_{FE}$ matrix gathering the components of unit normal vectors \underline{n} at each node, n_{FE} being the number of FE nodes as introduced in (3.1). The 3D FE optimization problem is then first projected according to this normal field so that the operator and right-hand side become $\underline{\underline{\mathbf{\Pi}}}_n^T \underline{\underline{\mathbf{H}}}_S^{(k)} \underline{\underline{\mathbf{\Pi}}}_n$ and $\underline{\underline{\mathbf{\Pi}}}_n^T \underline{\mathbf{b}}_S^{(k)}$, respectively. Hence, the FE shape correction field becomes a scalar problem (one dof per node). Only then is this scalar problem projected onto the FFD space, which means we look for a shape correction $\underline{\mathbf{S}}_n = \underline{\underline{\mathbf{C}}}_{\text{FFD}}^T \underline{\tilde{\mathbf{S}}}_n$. The FFD projected problem eventually writes:

$$\underline{\underline{\mathbf{C}}}_{\text{FFD}} \underline{\underline{\mathbf{\Pi}}}_n^T \underline{\underline{\mathbf{H}}}_S^{(k)} \underline{\underline{\mathbf{\Pi}}}_n \underline{\underline{\mathbf{C}}}_{\text{FFD}}^T \underline{\tilde{\mathbf{S}}}_n^{(k)} = \underline{\underline{\mathbf{C}}}_{\text{FFD}} \underline{\underline{\mathbf{\Pi}}}_n^T \underline{\mathbf{b}}_S^{(k)}. \quad (3.26)$$

The corresponding dofs $\underline{\tilde{\mathbf{S}}}_n$ do no longer correspond to displacements of the control points, but to magnitudes of the correction along the FE nodes normals. This choice makes it possible to keep a normal that is constant throughout the scales but not constrained by the coarsest length scale. The method is general, since the normals can be defined in many different ways, see Fig. 3.10: for instance a field of local normals (nodes by nodes) (Fig. 3.10(b)), a field of non-local normals taking into account the geometry of the neighborhood (Fig. 3.10(a)) or even user-defined normals (Fig. 3.10(c)).

To the best of our knowledge, such an approach is original in the general field of FFD, since in our work the direction of the correction is defined on the FE mesh and only the magnitude of the correction field is defined by the FFD control points.

Remark 15 *In this chapter, we used the regularity properties of spline functions to regularize the FE-DIC and FE shape measurement problems. However, we may*

sometimes face situations where the measured quantity is not regular. Firstly, for the shape measurement problem, it must be emphasized that the regularity is imposed on the shape correction field and not on the shape itself. The basic assumption of this work is that we have a theoretical CAD shape representative of the object. An initial CAD containing sharp edges can be used without limitations with the proposed regularization method. Only the construction of the local normal field needs special attention, see Fig. 3.10. Conversely, there is no reason for a sharp edge to exist in the object shape (before mechanical loading) without existing in the CAD. Under these conditions, the shape correction field will always be regular. Secondly, for displacement measurement, the appearance of a discontinuity in the strain or displacement fields can occur during a test (bi-material interface, crack, etc.). If the morphing box is regular, this will result in locally high residuals near the discontinuity. In such situation, it is possible to adapt the morphing box using spline reparametrization from the residual map. A very simplified illustrative example is provided in 3.3 to show the potential of the method in this situation.

3.4.3 Twisted plate with a hole

We applied the proposed regularization method to the shape measurement of a set of real images already studied in Chapter 2.

In this example, the initial FE mesh is flat. Consequently, a bivariate patch is chosen for the morphing box. Since the outer shape of the structure is a rectangle, we choose a FFD morphing box that coincides with the structure on the edges. The high resolution of our images allows to use 4 scales for the shape measurement problem resolution. We chose to start at the coarsest scale with a 1-element FFD morphing box, and then subdivide each spline element into 4 elements at each finer scale, so that the finest scale has a 64-element FFD morphing box. In practice, the number of scales should be chosen in accordance with the desired regularization length.

The problem to solve is the one given in Equation (3.26). In the case of an initial flat configuration, the obvious choice for \underline{n} at each FE node is the normal to the surface, which is the same direction for all nodes. In this special case where all nodes can be corrected in the same direction, it is possible to see the correction as a displacement of the FFD control points along that same direction, which made the visualization of the deformed FFD morphing box possible in Fig. 3.11.

The results are shown Fig. 3.11. As expected, we observe very smooth results with the FFD regularization, because we benefit from the regularity of spline functions and the very low number of dof in the regularized problem. The coarsest scale already gives satisfying results and finer scales slightly improve this shape correction field. Results are in good agreement with the shape correction field obtained with subset DIC. Here, VIC 3D software was used.

On the right, Fig. 3.11 shows the shape correction field expressed in each point of the FFD morphing box, using 2^{nd} -degree B-spline functions. Higher values in the center can be noticed at the finest scale. This feature results from the too little influence that control points inside the center hole have on the FE mesh. It can be interpreted as a fictitious extension of the shape correction field outside the region of interest, *i.e.* outside the FE mesh, that inevitably exists when the mesh does not occupy the whole morphing box. It does not have a physical meaning, but it does not affect the solution if the problem is not ill-conditioned. For this example, it does not negatively impact the results.

An advantage of this method compared to a standard CAD-based method as in Chapter 2 is the absence of C^0 lines that appear when creating a boundary-fitted

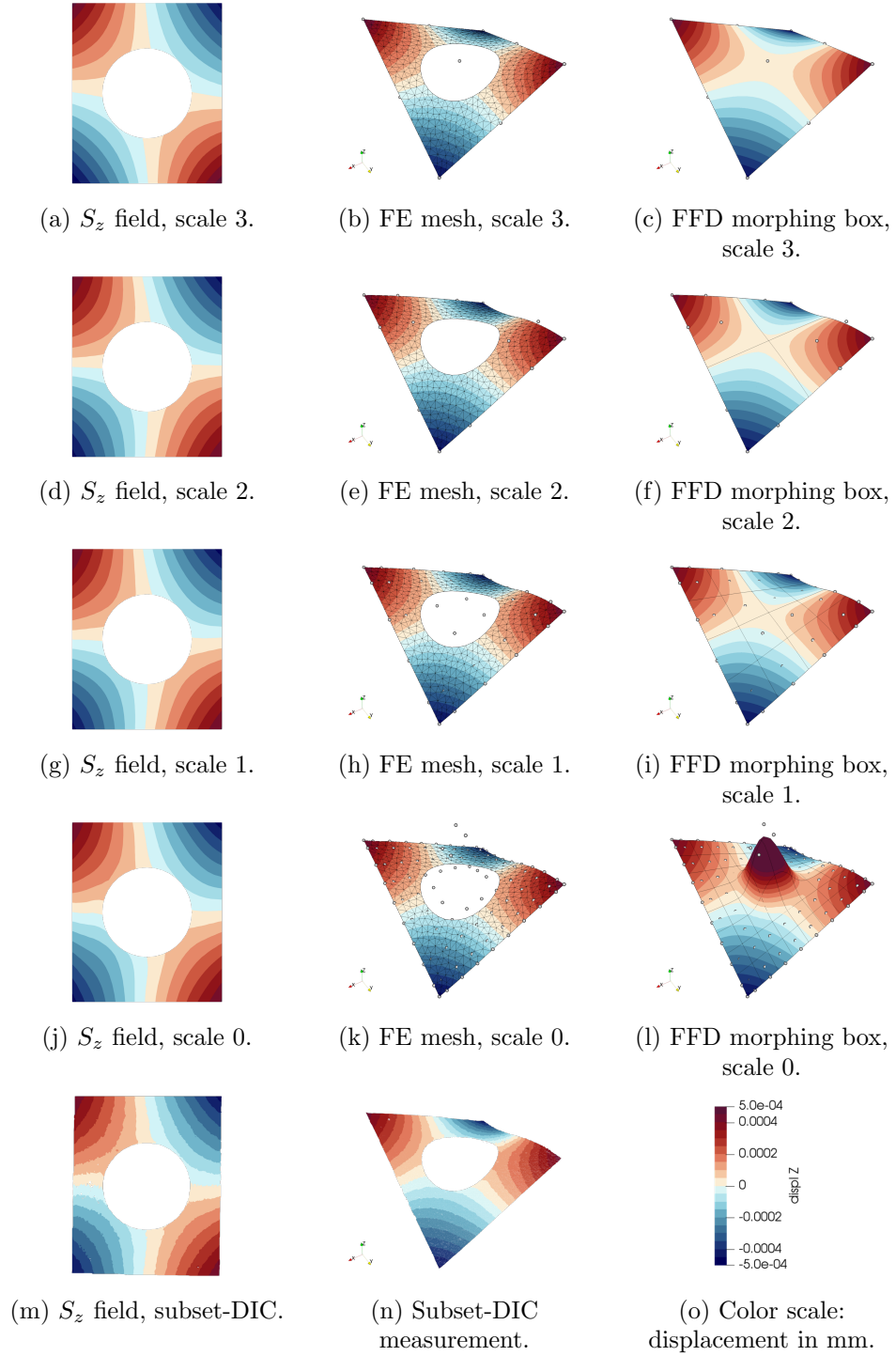


Figure 3.11: Experimental application: Twisted plate with a hole. We compare the shape measured with our method using a 3-scale initialization with the shape measured thanks to the industrial software VIC. S_z is the shape correction along the normal direction z .

patch. The FFD regularization is a generalization of the CAD-based regularization proposed in Chapter 2, where we eliminated the need for an analysis-suitable boundary-fitted spline mesh. As a result, the FFD regularization can be applied to any geometry. Another advantage coming from the fact that the FE mesh does not have to derive from a spline mesh is that any type of FE element can be chosen, and not only 9-node quadrilaterals ($Q9$ elements), that are not implemented in all FE softwares. The next example illustrates a case on an initially non-planar geometry.

3.4.4 Spherical cap

The proposed FFD approach offers great possibilities to regularize shape measurement on complex 3D shapes. In this section, we apply this method to a spherical cap (see Fig. 3.12). The initial mesh for the spherical cap is 35.45 mm large and 77.10 mm high. This FE mesh was constructed as a part of a sphere with a 38.686-mm radius.

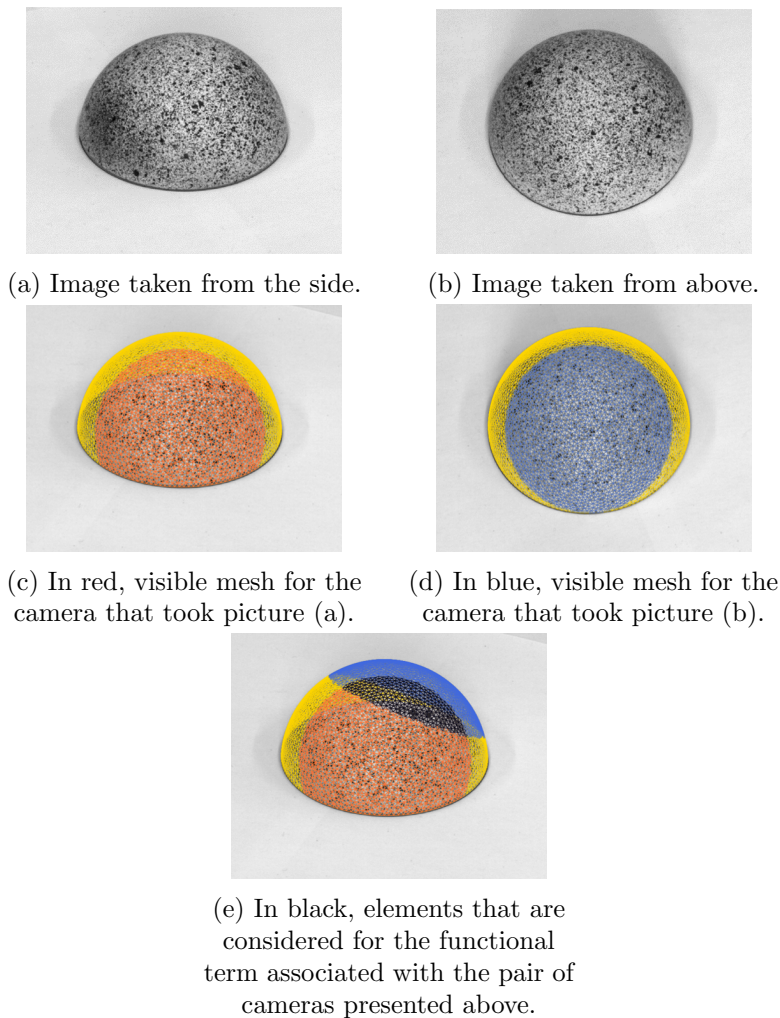


Figure 3.12: Spherical cap and chosen FE mesh. Visible parts of the mesh for 2 of the 14 cameras are red and blue, the intersection is black, and the rest of the mesh is yellow.

A set of 14 images of size 2560×2048 -pixels was taken, including 11 from different sides of the spherical cap (Fig. 3.12(a)), with view points placed all over the structure, and 3 from above (Fig. 3.12(b)), with different view angles. On the

images, on the "correctly visible" part of the sphere, one pixel represents approximately 0.125mm. Because each camera cannot correctly see the whole region of interest, we applied the mask V_c defined in (3.25) with an ϵ_n value of 0.6. Examples of the elements that are correctly seen by a given camera are shown in Figs. 3.12(c) and 3.12(d), and an example of the elements that are correctly seen by a pair of cameras is given in Fig. 3.12(e).

We used a total of three scales, with three image resolutions from 640×512 to 2560×2048 pixels using coarse graining and three refinements for the morphing box from $1 \times 1 \times 1$ element to $4 \times 4 \times 4$ elements. 2^{nd} -degree B-splines were chosen. As explained previously, the FE-mesh number of elements and connectivity remain unchanged. A 6571-element triangular FE mesh with first-degree FE basis is used, shown in Fig. 3.12. For numerical integration, we use Gauss points that are uniformly distributed on the sphere, so that there is at least one Gauss point per pixel (Gauss points are defined in the 3D physical space).

As explained in Section 3.4.2, the correction is sought along a normal direction. In this example, the surface normal vectors at each FE node are computed as the mean of outward-pointing normal vectors \underline{n}_e of the adjacent elements, which is a good approximation of the normal direction at the FE node for regular shapes with fine FE meshes. It is important to note here that unlike in the previous example, $\tilde{\mathbf{S}}_n$ cannot be seen as a displacement of the morphing box control points. $\tilde{\mathbf{S}}_n$ depicts a scalar field inside the morphing box that is the magnitude of the shape correction, and the direction of this correction is only defined at the FE nodes. The same scalar field applied to a different structure would not result in the same shape correction field.

The spherical cap is a surface FE mesh ($d = 2$) embedded in a trivariate patch ($\delta = 3$). As explained in Section 3.1.4, some morphing box control points may not have – or may not have enough – influence on the FE mesh. Therefore, we used the criterion Q_i defined in (3.16) to determine the influence of each control point, and considered the condition number of $\underline{\mathbf{C}}_{\text{FFD}} \underline{\mathbf{\Pi}}_n^T \underline{\mathbf{H}}_S^{(k)} \underline{\mathbf{\Pi}}_n \underline{\mathbf{C}}_{\text{FFD}}^T$ as described in Section 3.1.4 to spot the less influential control points that make this condition number greater than 10^8 . We then removed the corresponding lines of $\underline{\mathbf{C}}_{\text{FFD}}$ as follows:

- 1 removed line over 27 for scale 2
- 1 removed line over 64 for scale 1
- 37 removed lines over 216 for scale 0 (see Fig. 3.13)

We obtained the results shown in Fig. 3.14. More precisely, Fig. 3.14(d) shows the results with no regularization at scale 0. One-element-wavelength noise appears in this case, with unrealistic values at some FE nodes. We observe in Figs. 3.14(a), 3.14(b) and 3.14(c) that the FFD regularization successfully smooths the shape correction field.

All tested image sets give similar results. The correction on the top of the spherical cap is small, but the size of the spherical cap base seems to be initially underestimated (about 0.27 mm on the base radius). This result is validated by a shape measurement with the laser scanner Handyscan developed by Creaform3D. A sphere is well fitted by the points measured by the laser scan, and the radius of the least-square best fitting sphere on the laser scan data points is slightly greater than the radius used for our initial FE mesh. The correction we measure in Fig. 3.14 is schematized in Fig. 3.15.

The laser scan measured points best fitting sphere has a radius of 38.885 mm. We also calculated the least-square best fitting sphere to our measured shape (showed

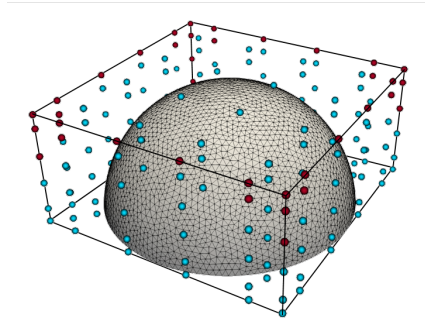
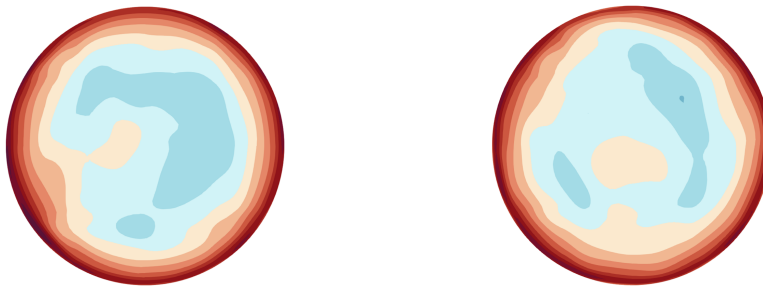
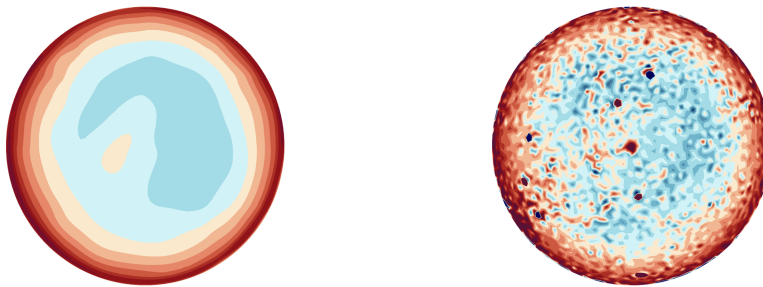


Figure 3.13: FE mesh embedded in the FFD morphing box at the finest scale, with $4 \times 4 \times 4$ spline elements. The dots are the control points of the morphing box. The red dots are the 37 control points that do not have enough influence, and the blue dots are the remaining dofs.



(a) Results with a first set of 14 images. (b) Results with a second similar set of 14 images.



(c) Results with all 50 images. (d) Results with a first set of 14 images, no regularization at scale 0.



(e) Color scale for the shape correction along the outer-pointing normal (in m).

Figure 3.14: Shape measurement on the spherical cap presented in Figure 3.12. The normal correction fields are shown with the spherical cap seen from below.

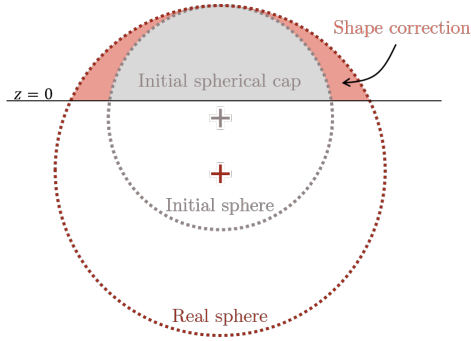


Figure 3.15: Measured shape correction schematization.

Fig. 3.14(a)) by considering the Gauss points, which are the points where graylevel is measured to correct the shape in the modified Gauss-Newton procedure. This sphere has a radius of 38.873 mm, which corresponds to a 0.012mm (*i.e.* a 0.03% error) on the radius if we take the laser measure as a reference. We also compared the sphericity defects of the FFD-measured shape and the laser-measured shape (see Table 3.1). For each Gaussian point \underline{M}_i (resp. measured point for the laser scan), we defined this sphericity defect as $d(\underline{M}_i, \underline{Q}) - R$ with \underline{Q} the center of the least-square best-fitting sphere, R its radius and $d(\underline{M}_i, \underline{Q})$ the distance between \underline{M}_i and \underline{Q} . We obtained the mean and standard deviation values given table 3.1, which shows that our method gives a correct measure of the shape.

	DIC with FFD regularization	laser scan
LS radius	38.873 mm	38.885 mm
Mean of sphericity defects	2.126×10^{-5} mm	-1.720×10^{-7} mm
Standard deviation of sphericity defects	0.02934 mm	0.02760 mm

Table 3.1: Comparison of sphere shape measurement with the FFD method (with 14 images) and with the laser scan.

Another shape measurement was carried out with a initial finite element mesh whose geometry is taken a little farther from the actual shape. The initial FE mesh is chosen with the same center as the previous initial FE mesh, but its radius is decreased by 1 mm, so this spherical cap is a part of a 37.686-mm radius sphere. Figure 3.16 shows the results after the modified Gauss-Newton minimization. FFD regularization allows finding the right correction, with a 1-mm correction on all the spherical cap and the expected additional 0.27-mm correction near the base of the structure (see Fig. 3.16(b)). Without regularization, some FE nodes fail to measure the shape correctly and even take unrealistic correction values.

These results show the capacity of the multiscale FFD regularization to be applied, not only to 2D initial FE meshes, but meshes of any dimension, and with any type of FE elements. Using splines helps obtaining smooth, more realistic shapes, and the proposed regularization method appears robust to initialization compared to a result without regularization (see Fig. 3.16 where it is clear that smoothing the FE field *a posteriori* would not lead to the right shape correction).

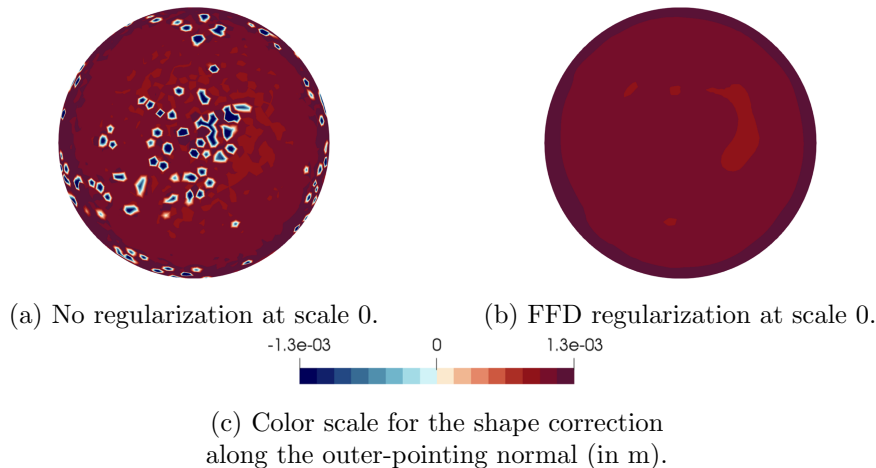


Figure 3.16: Shape correction field (along the normal) for the spherical cap of Figure 3.12, for an initialization with a radius that is 1 mm smaller than in the first experience (Figure 3.14).

Conclusion

A non-invasive FFD-based regularization method has been proposed for general full-field measurement in experimental solid mechanics. FE meshes that are used in FE-DIC for easy comparison with simulation results are usually very fine and thus contain too many dof compared to the available amount of data, which makes the corresponding inverse problems highly ill-posed. Embedding the mesh into a cuboid spline morphing box, similarly as in shape optimization for instance [Kenway et al., 2010, Lyu and Martins, 2015, Bletzinger, 2017], offered a way of decoupling the design space from that of the input FE mesh. Each nodal FE dof of the measured field is controlled by a spline field that is defined over much less control points. In other words, the deformation of the FE mesh follows the smooth spline deformation of the morphing box. This regularization method showed competitive advantages in the experimental mechanics community compared to other published methods.

First, the regularization length directly derives from the morphing box refinement, which can easily be set to a desired value thanks to the multilevel properties of B-splines. Then, it can be adapted to any kind of measured fields, without any *a priori* physical knowledge. In this chapter, applications to a displacement field measurement and to shape measurements have been shown. Moreover, the FFD regularization method released the constraints imposed by a CAD-based method, which are the need of an input boundary-fitted spline mesh and, in case it is made non-invasive from standard FE following [Colantonio et al., 2020], of an input FE mesh that has to encompass a spline parametrization. The proposed FFD regularization allows to deal with any structure topology and any FE element type or size. The choice of the FE mesh is independent of the FFD regularization method. The method can also be applied to structures and fields of any dimension, as has been shown in the three given examples with 2D and 3D fields.

Formally, the FFD regularization can be seen as a discretization of a fictitious domain approach [Schillinger and Ruess, 2015, Verhoosel et al., 2015, Rouwane et al., 2021]. Consequently, it has similar problems to address, as the handling of conditioning problems caused by non-influential control points over the region of interest, which led us to the definition of a criterion to quantify the influence of a control variable. For this purpose, we extended the criteria emanating from the current

practice in fictitious domain methods to be adapted to the discretized aspect of our method and to the possible dimension differences between the studied FE-meshed structure and the morphing box. To the best of our knowledge, this is the first time that such a treatment is applied in the general field of FFD.

From a practical point of view, the proposed FFD regularization method can be seen as the projection of the DIC problem, which is originally solved in a FE space, onto a reduced, smoother space. We gave the matrix form of the projection from the FE space to the spline-controlled space. Its computation is easy and it has the advantage of being sparse. This explicit projection matrix allows the use of a standard FE-DIC software in a non-invasive way, which makes this method easily applicable. For shape measurement, we proposed a novel double projection approach to avoid undesired tangential corrections and help the algorithm convergence. In this case, the morphing box controls a scalar field, and the correction direction is defined at the FE nodes and freely chosen, thus widening the range of possible corrections.

We illustrated our method with the analysis of real images coming from three different experiments. The first one consisted in measuring a 2D displacement field on a planar bending beam. A comparison with the standard Tikhonov regularization showed the high potential of the FFD method to strongly regularize without adding artifacts on the resulting measured field. The second example validated the hybridization of a 3D shape measurement problem with a bivariate FFD morphing box. The superiority of the proposed method over standard CAD-based method was highlighted. The last example showed the capacity of the FFD method to be applied for the shape measurement of a more complex 3D geometry. Results of a quality comparable to that of a laser scanner were presented. The robustness to initialization was also demonstrated.

The developed method proved its efficiency for the measurement of relatively regular fields and shapes. It may be easily applied to less regular shapes and extended to less regular fields by defining C^0 lines in the FFD patch, or by creating a multi-patch FFD morphing box with potentially C^{-1} lines between them, which could be adapted to measuring the propagation of cracks [Réthoré, 2015]. Hierarchical splines [Kleinendorst et al., 2015, Verhoosel et al., 2015] could also be used to allow for local refinement, which would be particularly adapted to multiscale DIC experiment [Passieux et al., 2015].

Chapter 2 and this chapter demonstrate the ability of splines to regularize measured fields that are still expressed on possibly very fine, analysis-suitable FE meshes. In particular, this chapter shows that any FE mesh of any geometry can be used for displacement field or shape measurement. With this result, it is now possible to deal with the third optimization problem, namely the shape optimization of mechanical specimen for constitutive parameters identification. The constitutive parameters identification procedure requires performing FE-DIC displacement field measurement, and the shape optimization process may create specimens that necessitate a locally fine FE mesh for an accurate description of the geometry. Yet, in order to get relatively smooth specimen edges and guarantee that the specimen geometry is physically-sound, we develop in the next chapter a FFD-based shape optimization strategy.

Chapter 4

Shape optimization for constitutive parameters identification

Introduction

Along with the creation of new materials, such as new alloys (with new forming and additive manufacturing techniques) or composite materials, comes the need to characterize them. It is necessary to know how they behave so they can be modeled and used for simulation on complex structures, such as airplanes or satellites.

Nowadays, identifying several constitutive parameters requires designing several different experiments, and identifying a single parameter requires carrying out up to dozens of experiments, which makes the overall process very costly and time consuming [D3518/D3518M, 1994]. It is therefore an impediment to innovation, especially in some fields which have rigorous certification procedures and need to know precisely the behavior of the materials they use.

As explained in Section 1.1.4, a way of reducing the costs is to design an experiment that allows identifying several parameters at once with the lowest possible uncertainty. To do so, several articles have focused on designing dedicated specimens to improve their identification ability, either by choosing shapes that widen the range of obtained stress states in the specimens (no *a priori* material model) [Pottier et al., 2012, Conde et al., 2021], or by choosing shapes that make the specimens more sensitive to given constitutive parameters (a material model is chosen *a priori*) [Feld et al., 2015, Bertin et al., 2016, Chamoin et al., 2020]. A few works, in particular [Bertin et al., 2015, Bertin et al., 2016], [Feld et al., 2015] and more recently [Chamoin et al., 2020] proposed to optimize the shape of the specimen to minimize the uncertainties coming from the whole metrological chain, using the covariance matrix of the identified material parameters. All these works are based on (variants of) the Finite Element Model Updating (FEMU) method, which is widely used coupled to DIC for measurement to identify the parameters of a chosen constitutive law [Robert et al., 2012, Gras et al., 2013].

As has been seen in Section 1.1.4, proposed optimizations by Feld et al., Bertin et al. and Chamoin et al. are either carried out in very small spaces, where only geometrical parameters such as radiuses and hole positions are modified – this is generally known as *parametric optimization* – [Feld et al., 2015, Bertin et al., 2016], or in very large spaces – for *topology optimization* – [Chamoin et al., 2020], but in that case, the shape specimen was optimized to identify only one parameter (no physically sound final specimen design is proposed in the case of topology optimiza-

tion for several parameters). We propose here to use *geometric shape optimization* because it allows free form geometry modifications, as long as the topology remains unchanged, and it is possible to keep a low number of design variables thanks to B-spline functions. Moreover, we aim at improving the sensitivity to several constitutive parameters, for the purposes of identifying several parameters at once.

In this chapter, we make use of the FFD tools developed in the previous chapter to control a FE mesh with splines, and we extend this non-invasive FFD approach to a larger range of morphing boxes. This chapter is organized as follows: the first section quickly describes the process of parameter identification, namely the FEMU method and its functional, and the covariance matrix that comes from coupling FEMU to DIC and that gives a representation of the uncertainty over the identified constitutive parameters. The second section details the proposed modeling of the specimen shape optimization problem. In particular, we explain our choices regarding cost function and constraint functions so that the optimization results are physically meaningful and the obtained geometry is adapted to the associated test. These choices are illustrated and validated with a simple beam example. Finally, the third section focuses on the development of a proper resolution strategy and applies it to a more complex structure. A specific handling of the geometry, based on FFD, is proposed, in order to make the method suitable to any possible geometry.

4.1 Parameter identification

In this work, we consider the FEMU method for material constitutive parameter identification, in the context of 2D-DIC. However, note again that under certain conditions detailed in [Mathieu et al., 2015], this work can be extended to IDIC.

4.1.1 FEMU method

Similarly to other constitutive parameters identification methods such as those mentioned in Section 1.1.4.1, the FEMU method consists in comparing a measured quantity to a simulated one, typically a measured displacement field on a specimen obtained with DIC to a simulated displacement field obtained with similar boundary conditions and the chosen material constitutive law [Kavanagh and Clough, 1971, Collins et al., 1974]. The aim is to find constitutive parameters values that minimize the discrepancy between the simulated field \underline{v} and the measured field \underline{u} . The functional to minimize thus reads:

$$\mathcal{F}_p(\underline{p}) = \|\underline{v}(\underline{x}, \underline{p}) - \underline{u}(\underline{x})\|^2, \quad (4.1)$$

where \underline{p} is the set of sought constitutive parameters. One can see that the quality of the method depends on the quality of the measurement. A consequence is that there exists a "best" norm to choose in order to quantify the discrepancy between the two fields, that takes into account some information about the measurement quality: the $\underline{\mathbf{H}}_u$ -norm, denoted $\|\cdot\|_{\underline{\mathbf{H}}_u}$, where $\underline{\mathbf{H}}_u$ is the hessian matrix of the DIC problem and more importantly, the inverse of the covariance matrix of the noise on measured displacements coming from Gaussian noise in the images, as will be detailed in Section 4.1.2. This metric, which is the Mahalanobis distance, was shown to be optimal with respect to sensitivity to measurement noise [Roux and Hild, 2020]. This norm gives to each dof a weight that is linked to local quality of the measurement due to the speckle pattern quality. With continuous fields, this norm translates into an approximation of the hessian of the image \mathcal{I} , denoted $\underline{\underline{H}}_{\mathcal{I}}$ in Equation (4.2). In our

work, we thus considered this weighted FEMU functional [Réthoré, 2010, Mathieu et al., 2015, Roux and Hild, 2020]:

$$\mathcal{F}_p(\underline{p}) = \|\underline{v}(\underline{x}, \underline{p}) - \underline{u}(\underline{x})\|_{\underline{H}_{\mathcal{I}}}^2, \quad (4.2)$$

which can be written thanks to the 2D-DIC developments in Section 3.2.1:

$$\mathcal{F}_p(\underline{p}) = \int_{\omega_s} (\underline{u}(\underline{x}) - \underline{v}(\underline{x}, \underline{p}))^T \nabla \mathcal{I}(\underline{x}) \nabla \mathcal{I}^T(\underline{x}) (\underline{u}(\underline{x}) - \underline{v}(\underline{x}, \underline{p})) d\underline{x}, \quad (4.3)$$

where ω_s is the region of interest in the images, and \mathcal{I} is the reference image of the DIC measurement.

To find \underline{p} that minimizes $\mathcal{F}_p(\underline{p})$, we perform a Gauss-Newton optimization. Starting from an initial set $\underline{p}^{(0)}$, each Gauss-Newton iteration k updates the values of the constitutive parameters as follows:

$$\forall k \in \mathbb{N}, \quad \underline{p}^{(k+1)} = \underline{p}^{(k)} + \underline{\delta p}^{(k)}. \quad (4.4)$$

$\underline{\delta p}^{(k)}$ is computed as the solution of a linear system:

$$\int_{\omega_s} \underline{\underline{\nabla_p v}}^{(k)} \nabla \mathcal{I} \nabla \mathcal{I}^T \left(\underline{\underline{\nabla_p v}}^{(k)} \right)^T \underline{\delta p}^{(k)} d\underline{x} = \int_{\omega_s} \underline{\underline{\nabla_p v}}^{(k)} \nabla \mathcal{I} \nabla \mathcal{I}^T (\underline{u} - \underline{v}^{(k)}) d\underline{x}, \quad (4.5)$$

where ∇_p is the gradient with respect to the sought constitutive parameters, *i.e.* line i is $\frac{\partial}{\partial p_i}$, the sensitivity field to parameter p_i . For example, with a set of two constitutive parameters and a 2D displacement field:

$$\underline{\underline{\nabla_p v}} = \begin{bmatrix} \frac{\partial v_x}{\partial p_1} & \frac{\partial v_y}{\partial p_1} \\ \frac{\partial v_x}{\partial p_2} & \frac{\partial v_y}{\partial p_2} \\ \frac{\partial v_x}{\partial p_3} & \frac{\partial v_y}{\partial p_3} \end{bmatrix} \quad (4.6)$$

Equation (4.5) can also read:

$$\underline{\underline{H}}_{FEMU}^{(k)} \underline{\delta p}^{(k)} = \underline{\underline{b}}_{FEMU}^{(k)}. \quad (4.7)$$

Simulated displacement fields generally come from FE software and therefore are expressed at the nodes of a FE mesh. An easy way to compare a measured displacement field with a simulated one is to seek the measured displacement field in the same FE space as used for the simulation. This is the idea of FE-DIC described in Section 3.2.1. Note that thanks to the FFD-DIC technique developed in Chapter 3, it is possible to perform FE-DIC on arbitrarily fine FE meshes, which removes any limitation for element size in the simulation. Using the same FE basis for u and v leads to the following expressions for $\underline{\underline{H}}_{FEMU}^{(k)}$ and $\underline{\underline{b}}_{FEMU}^{(k)}$:

$$\begin{cases} \underline{\underline{H}}_{FEMU}^{(k)} = \underline{\underline{\nabla_p v}}^{(k)} \underline{\underline{H}}_u \underline{\underline{\nabla_p v}}^{(k)T} \\ \underline{\underline{b}}_{FEMU}^{(k)} = \underline{\underline{\nabla_p v}}^{(k)} \underline{\underline{H}}_u (\underline{u} - \underline{v}(\underline{p}^{(k)})) \end{cases}, \quad (4.8)$$

where \underline{v} and \underline{u} represent the FE values of the displacement field at the nodes of the FE mesh, and $\underline{\underline{H}}_u$ is first described in Section 3.2.1 and will be further developed in Section 4.2.2. In this manuscript, $\underline{\underline{H}}_{FEMU}$ will not be written in bold because its size is independent of mesh refinement, in accordance with notation choices, even if the mesh is used to compute its values.

4.1.2 Covariance matrix

To quantify how well a set of constitutive parameters is identified thanks to the FEMU method, in the sense that the identified values are precise, we rely on the covariance matrix of the sought constitutive parameters, which characterizes the uncertainty on these parameters. Errors can arise from any step of the whole DIC and FEMU procedure. Here is a non-exhaustive list:

- speckle pattern quality,
- ambient noise (light, air temperature gradient, ...),
- camera resolution,
- camera noise,
- camera calibration,
- sub-pixel interpolation algorithm (nearest, bilinear, bicubic, splines),
- interpolation functions and research space for the displacement field,
- numerical approximation,
- choice of constitutive law.

Considering that the main contribution to errors comes from camera noise, it is possible to derive the covariance of the measured displacements at each FE node, thanks to the DIC problem resolution detailed in Section 3.2.1, and then derive the covariance of the identified parameters with FEMU method, thanks to Equations (4.7) and (4.8).

4.1.2.1 Noise modeling in the images

We can assume that the reference image \mathcal{I} and the deformed image \mathcal{J} are independently affected by Gaussian white noise of:

- zero-mean,
- variance γ^2 .

Hence, we can consider that only \mathcal{J} is affected by white noise $\varepsilon_{\mathcal{J}}$ of zero-mean and variance $2\gamma^2$ [Besnard et al., 2006, Réthoré, 2010, Hild and Roux, 2012, Bertin et al., 2016], *i.e.* $\mathcal{J}(\underline{x})$ is actually $\mathcal{J}(\underline{x}) + \varepsilon_{\mathcal{J}}(\underline{x})$ with:

- $\langle \varepsilon_{\mathcal{J}}(\underline{x}) \rangle = 0$ (zero-mean),
- $\langle \varepsilon_{\mathcal{J}}(\underline{x}) \varepsilon_{\mathcal{J}}(\underline{x}') \rangle = 2\gamma^2 \delta(\underline{x} - \underline{x}')$ (variance $2\gamma^2$),

where $\delta(\underline{x} - \underline{x}')$ is the Dirac delta function (noise is supposed spatially uncorrelated).

4.1.2.2 Noise impact on the measured displacement field

Let $\varepsilon_{\underline{u}}$ be the impact of that noise on the measured displacements at each FE node, so that \underline{u} is actually $\underline{u} + \varepsilon_{\underline{u}}$. From Equation (3.20), we get that the noise on \underline{u} follows [Besnard et al., 2006, Réthoré, 2010, Hild and Roux, 2012, Bertin et al., 2016]:

- $\langle \varepsilon_{\underline{u}} \rangle = 0$ (zero-mean),
- $\langle \varepsilon_{\underline{u}} \varepsilon_{\underline{u}}^T \rangle = 2\gamma^2 \underline{\underline{\mathbf{H}}}_u^{-1}$.

Note that to get this result, in addition to considering all the noise on the image \mathcal{J} , the impact of the noise is not considered on $\underline{\nabla \mathcal{I}}$ even though its presence in $\underline{\underline{\mathbf{H}}}_u$ expression initially comes from an approximation of $\underline{\nabla \mathcal{J}}$ used in the modified Gauss-Newton algorithm for computational cost reduction purposes.

4.1.2.3 Noise impact on the identified constitutive parameters

From Equations (4.7) and (4.8), and with ε_p being the noise on the identified parameters coming from the noise in the images, we get that this noise follows [Réthoré, 2010, Bertin et al., 2016]:

4.2. APPROPRIATE MODELING OF THE SPECIMEN SHAPE OPTIMIZATION PROBLEM

- $\langle \varepsilon_{\underline{p}} \rangle = 0$ (zero-mean),
- $\langle \varepsilon_{\underline{p}} \varepsilon_{\underline{p}}^T \rangle = 2\gamma^2 \underline{\underline{H}}_{FEMU}^{-1}$.

The covariance matrix $\langle \varepsilon_{\underline{p}} \varepsilon_{\underline{p}}^T \rangle$ has a size $n_p \times n_p$ with n_p the number of sought constitutive parameters. It contains helpful information in order to derive a representative criterion of a "good" constitutive parameter identification.

4.2 Appropriate modeling of the specimen shape optimization problem

Based on this knowledge, we can define a cost function for the purposes of optimizing the shape of a specimen to minimize the identification ability of several constitutive parameters. This section details our choices for the cost function with respect to what has been proposed in [Feld et al., 2015, Bertin et al., 2016, Chamoin et al., 2020], and we then propose to complete the optimization problem with constraint functions in order to get a physically sound geometry. In this section, \underline{s} will denote the design variables, which are quantities that modify the shape of the specimen. They will be further detailed in Section 4.3.1. Note also that for simplicity, we place ourselves in the linear elastic context for 2D static tests only. When appropriate and to improve understandability, examples will be given on a simple tension sample. Its shape will be modified thanks to a rectangle FFD morphing box (see Chapter 3 for details on the FFD method).

4.2.1 Cost function

As explained in Section 4.1.2, as well as in [Feld et al., 2015, Bertin et al., 2016, Chamoin et al., 2020], the covariance matrix provides an estimation of the quality of the identified parameters. Improving the quality of the identification can thus be achieved by "minimizing" this covariance matrix that expresses the uncertainty on the constitutive parameter values, *i.e.* by "minimizing" $\underline{\underline{H}}_{FEMU}^{-1}(\underline{s})$ with respect to design variables \underline{s} that modify the geometry of the specimen. We will later specify what "minimize" can mean for a matrix (see Section 4.2.1.3).

This section is divided as follows: first, preliminary explanations on how to compute the covariance matrix are given. Then, we explicit the cost function formulation in the single-parameter case where H_{FEMU} is simply a scalar, and in the case where several constitutive parameters are sought. Finally, we propose the addition of a physically sound coefficient to take into account the size of the specimen.

4.2.1.1 Preliminaries

4.2.1.1.1 Approximating the unknown DIC matrix The optimization of the specimen geometry is intended to be carried out before any experiment. It means that neither images nor information on their gradient are available. Furthermore, the speckle pattern is generally not known *a priori*. Hence the $\underline{\underline{H}}_u$ matrix cannot be computed as such, because \mathcal{I} and thus $\underline{\nabla} \mathcal{I}$ does not exist yet. To circumvent this issue, Feld et al. [Feld et al., 2015] propose to replace $\underline{\underline{H}}_u$ with an identity matrix. [Bertin et al., 2016] and [Chamoin et al., 2020] recommend the use of a mean-field assumption. This assumption consists in considering that the graylevel gradient $\underline{\nabla} \mathcal{I}$ varies a lot more than the shape functions $\underline{\underline{N}}$ in the following expression:

$$\underline{\underline{H}}_u = \int_{\omega_s} \underline{\underline{N}}^T \underline{\nabla} \mathcal{I} \underline{\nabla} \mathcal{I}^T \underline{\underline{N}} dx . \quad (4.9)$$

As a consequence, we can make the following approximation:

$$\underline{\underline{\mathbf{H}}}_u \approx \int_{\omega_s} \underline{\underline{\mathbf{N}}}^T \begin{bmatrix} \left\langle \left(\frac{\partial \mathcal{I}}{\partial x} \right)^2 \right\rangle & \left\langle \frac{\partial \mathcal{I}}{\partial x} \frac{\partial \mathcal{I}}{\partial y} \right\rangle \\ \left\langle \frac{\partial \mathcal{I}}{\partial x} \frac{\partial \mathcal{I}}{\partial y} \right\rangle & \left\langle \left(\frac{\partial \mathcal{I}}{\partial y} \right)^2 \right\rangle \end{bmatrix} \underline{\underline{\mathbf{N}}} d\underline{x}, \quad (4.10)$$

where $\langle \cdot \rangle$ is the mean operator, such that $\langle \cdot \rangle = \frac{1}{|\omega_s|} \int_{\omega_s} \cdot d\underline{x}$, with $|\omega_s| = \int_{\omega_s} d\underline{x}$ the size of the ROI in the image. We also consider that $\frac{\partial \mathcal{I}}{\partial x}$ and $\frac{\partial \mathcal{I}}{\partial y}$ are independent, which gives $\langle \frac{\partial \mathcal{I}}{\partial x} \frac{\partial \mathcal{I}}{\partial y} \rangle = 0$. Finally, we suppose that $\left\langle \left(\frac{\partial \mathcal{I}}{\partial x} \right)^2 \right\rangle = \left\langle \left(\frac{\partial \mathcal{I}}{\partial y} \right)^2 \right\rangle = \frac{G_{\mathcal{I}}^2}{2}$, where:

$$G_{\mathcal{I}}^2 = \langle \|\nabla \mathcal{I}\|^2 \rangle = \frac{1}{|I|} \int_I \left(\frac{\partial \mathcal{I}}{\partial x} \right)^2 + \left(\frac{\partial \mathcal{I}}{\partial y} \right)^2 d\underline{x}, \quad (4.11)$$

which gives:

$$\underline{\underline{\mathbf{H}}}_u \approx \frac{G_{\mathcal{I}}^2}{2} \int_{\omega_s} \underline{\underline{\mathbf{N}}}^T \underline{\underline{\mathbf{N}}} d\underline{x}. \quad (4.12)$$

As a result, $\underline{\underline{\mathbf{H}}}_u$ can be replaced by a pseudo-mass matrix (no density parameter) in this case, the $\frac{G_{\mathcal{I}}^2}{2}$ factor being ignored for two reasons: its value is unknown because it only depends on a speckle we do not have, and this factor does not influence the minimization result, because it is constant with respect to the design variables \underline{s} .

We also chose the mean-field assumption, that leads to the following approximation:

$$\underline{\underline{H}}_{FEMU}(\underline{s}) \approx \underline{\underline{\nabla}}_{\mathbf{p}} \mathbf{v}(\underline{s}) \underline{\underline{\mathbf{M}}}(\underline{s}) \underline{\underline{\nabla}}_{\mathbf{p}} \mathbf{v}^T(\underline{s}), \quad (4.13)$$

which only involves a mass matrix and the derivatives of a simulated displacement field with respect to the sought constitutive parameters, which are all quantities that can be computed with a FE software program.

The addition of a normalizing coefficient will be described in Section 4.2.2 but is not necessary for the following developments.

4.2.1.1.2 Choosing numerical constitutive parameter values In order to compute $\underline{\underline{H}}_{FEMU}$, it is necessary to choose values for the different constitutive parameters of the selected constitutive law, because of the need to know $\underline{\mathbf{v}}$. These parameters are defined numerically before the optimization process. They are not modified during or after the process, since they are considered as the exact parameter values throughout the process. Hence, it may be preferable to choose values that are not too different than those expected, as these values can impact the cost function and thus the optimized final geometry.

4.2.1.1.3 Computing parameter sensitivities analytically Because we aim at identifying linear elastic constitutive parameters, it is possible to compute the analytical derivative of the simulated field with respect to a given parameter p . $\underline{\mathbf{v}}$ comes from a FE static problem resolution $\underline{\underline{\mathbf{K}}}\underline{\mathbf{v}} = \underline{\mathbf{F}}$, where the stiffness matrix $\underline{\underline{\mathbf{K}}}$ depends on the constitutive parameter p and the applied load $\underline{\mathbf{F}}$ does not. The derivative reads:

$$\underline{\underline{\mathbf{K}}}_{,p} \underline{\mathbf{v}} + \underline{\underline{\mathbf{K}}}\underline{\mathbf{v}}_{,p} = 0, \quad (4.14)$$

which leads to:

$$\underline{\mathbf{v}}_{,p} = -\underline{\underline{\mathbf{K}}}^{-1} \underline{\underline{\mathbf{K}}}_{,p} \underline{\mathbf{v}}. \quad (4.15)$$

Since the FE basis functions do not depend on p , only the Hooke matrix derivative is needed to compute $\underline{\underline{\mathbf{K}}}_{,p}$. This derivative can be computed exactly when the

4.2. APPROPRIATE MODELING OF THE SPECIMEN SHAPE OPTIMIZATION PROBLEM

constitutive law is linear. $\underline{\underline{\mathbf{K}}}_{,p}$ can then be assembled with the same routines as for the stiffness matrix $\underline{\underline{\mathbf{K}}}$, the only difference being the use of the Hooke matrix derivative instead of the Hooke matrix.

Naturally, for numerical concerns (balance of the sensitivities of different parameters), each parameter p is normalized with its chosen initial value p_0 in the FEMU minimization process. Let us denote by \bar{p} the normalized parameter such that $p = p_0 \bar{p}$. \bar{p} is 1 at the beginning of the FEMU process. As a result, we use $\frac{\partial \mathbf{v}}{\partial \bar{p}}$ instead of $\frac{\partial \mathbf{v}}{\partial p}$, and we have the following relation:

$$\frac{\partial \mathbf{v}}{\partial \bar{p}} = p_0 \frac{\partial \mathbf{v}}{\partial p}. \quad (4.16)$$

4.2.1.2 For a single parameter

4.2.1.2.1 Expression When only one parameter is to be identified, $\nabla_{\mathbf{p}} \mathbf{v}$ is a vector equal to $\frac{\partial \mathbf{v}}{\partial p}$ and H_{FEMU} is a scalar. In this case, the cost function can simply read [Bertin et al., 2016, Chamoin et al., 2020]:

$$f_{cost}(\underline{s}) = \frac{1}{H_{FEMU}(\underline{s})} = \frac{1}{\frac{\partial \mathbf{v}}{\partial p}^T(\underline{s}) \underline{\underline{\mathbf{M}}}(\underline{s}) \frac{\partial \mathbf{v}}{\partial p}(\underline{s})}. \quad (4.17)$$

Note that with the choice $\underline{\underline{\mathbf{H}}}_u = \underline{\underline{\mathbf{M}}}$, the denominator term is equivalent to integrating the sensitivity field over the region of interest ω_s :

$$\frac{\partial \mathbf{v}}{\partial p}^T \underline{\underline{\mathbf{M}}} \frac{\partial \mathbf{v}}{\partial p} = \int_{\omega_s} \frac{\partial v}{\partial p}^T \frac{\partial v}{\partial p} d\underline{x} = \int_{\omega_s} \left\| \frac{\partial v}{\partial p} \right\|^2 d\underline{x}. \quad (4.18)$$

This observation justifies the choice of $\underline{\underline{\mathbf{M}}}$ as a weighting matrix for the scalar product with $\nabla_{\mathbf{p}} \mathbf{v}$. Sensitivity values at nodes that are in fine regions of the FE mesh have a smaller weight because the elements in the region are smaller, which compensates for the high number of contributing nodes in that region, and conversely, higher weights are applied to nodes in coarse regions of the FE mesh. Equation (4.18) also gives another physical meaning to our cost function. By minimizing f_{cost} , we maximize the mean sensitivity to the sought parameter over the whole region of interest.

4.2.1.2.2 Semi-analytical sensitivity To reduce computational time and errors, and in the case of a single parameter to identify, it is possible to perform a semi-analytical gradient of the cost function, similarly to what is called *semi-analytical sensitivity analysis* in structural shape optimization [Kiendl et al., 2014], but adapted to our cost function. An advantage of this method lies in that instead of using Finite Difference Methods (FDM) on quantities that come from system solving (such as \mathbf{v}), we first use FDM on quantities obtained directly (such as $\underline{\underline{\mathbf{K}}}$, $\underline{\underline{\mathbf{M}}}$ or $\underline{\underline{\mathbf{F}}}$) and then solve a system. Errors coming from solving the system are thus not aggravated by the finite difference process and many computational time savings can be reported since it avoids numerous system resolutions.

Taking the derivative with respect to one design variable s_i , we get:

$$f_{cost,s_i}(\underline{s}) = - (f_{cost}(\underline{s}))^2 (2 \underline{\mathbf{v}}_{,ps_i}^T \underline{\underline{\mathbf{M}}} \underline{\mathbf{v}}_{,p} + \underline{\mathbf{v}}_{,p}^T \underline{\underline{\mathbf{M}}}_{,s_i} \underline{\mathbf{v}}_{,p}) . \quad (4.19)$$

$\underline{\mathbf{v}}_{,p}$ can be computed thanks to Equation (4.15), $\underline{\underline{\mathbf{M}}}_{,s_i}$ derives from FDM, and $\underline{\mathbf{v}}_{,ps_i}$ can be determined as follows:

$$\underline{\mathbf{v}}_{,ps_i} = \underline{\underline{\mathbf{K}}}^{-1} (\underline{\underline{\mathbf{K}}}_{,p} \underline{\underline{\mathbf{K}}}^{-1} \underline{\underline{\mathbf{K}}}_{,s_i} + (\underline{\underline{\mathbf{K}}}_{,p} \underline{\underline{\mathbf{K}}}^{-1} \underline{\underline{\mathbf{K}}}_{,s_i})^T - \underline{\underline{\mathbf{K}}}_{,ps_i}) \underline{\mathbf{v}} - \underline{\underline{\mathbf{K}}}^{-1} \underline{\underline{\mathbf{K}}}_{,p} \underline{\underline{\mathbf{K}}}^{-1} \underline{\underline{\mathbf{F}}}_{,s_i}, \quad (4.20)$$

with $\underline{\underline{\mathbf{K}}}_{,s_i}$, $\underline{\underline{\mathbf{K}}}_{,ps_i}$ and $\underline{\underline{\mathbf{F}}}_{,s_i}$ computed thanks to FDM.

4.2.1.3 For several parameters

When several constitutive parameters are to be identified, $\underline{\underline{H}}_{FEMU}$ is no longer a scalar. "Minimizing" its inverse is then not straightforward. The idea proposed in [Feld et al., 2015, Bertin et al., 2016, Chamoin et al., 2020] is to work on the eigenvalues of this matrix.

4.2.1.3.1 Physical meaning of the eigenvalues These eigenvalues have a physical meaning when looking at the multivariate normal distribution associated with the covariance matrix $\underline{\underline{H}}_{FEMU}^{-1}$. In fact, the isosurface where $\underline{p}^T \underline{\underline{H}}_{FEMU} \underline{p}$ equals 1 is an ellipsoid where each principal semi-axis direction is given by an $\underline{\underline{H}}_{FEMU}^{-1}$ eigenvector, and their size squared is the associated eigenvalue. An illustration is shown with 2 variables on Figure 4.1.

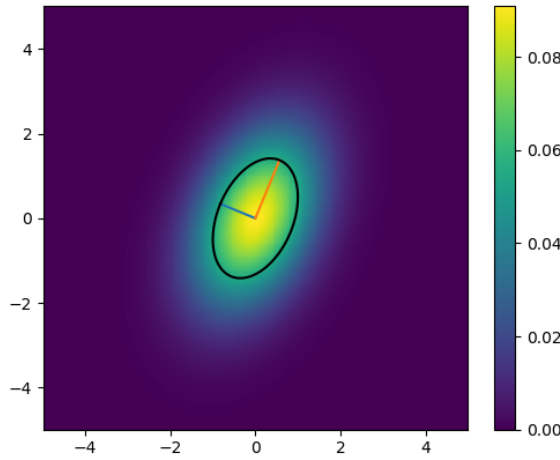


Figure 4.1: Bivariate normal distribution associated with variances 1. and 2. and covariance 0.5. Eigenvalues are $\Lambda_1 = 0.79$ and $\Lambda_2 = 2.21$, associated with eigenvectors $[-0.92, 0.38]$ and $[0.38, 0.92]$. In black, the ellipse with semi-axes of lengths $\sqrt{\Lambda_1}$ and $\sqrt{\Lambda_2}$.

To minimize the uncertainty on the identified constitutive parameters, this ellipse should be as small as possible, meaning that $\underline{\underline{H}}_{FEMU}^{-1}$ eigenvalues should be as small as possible. These eigenvalues also correspond to the FEMU functional curvature near the optimum set of constitutive parameters, since $\underline{\underline{H}}_{FEMU}$ is an approximation of the hessian matrix. With this point of view, decreasing $\underline{\underline{H}}_{FEMU}^{-1}$ eigenvalues improves the FEMU functional convexity, which also translates into a better confidence in the identified constitutive parameters.

4.2.1.3.2 Defining a criterion over eigenvalues In order to perform an optimization of the constitutive parameter identification procedure, we need to derive a unique scalar criterion from $\underline{\underline{H}}_{FEMU}^{-1}$ eigenvalues. Several choices exist.

[Feld et al., 2015] minimize the ratio of the largest eigenvalue over the lowest. This choice improves the conditioning of $\underline{\underline{H}}_{FEMU}$. Hence, the numerical errors are reduced during the Gauss-Newton minimization performed in FEMU. However, it does not necessarily enhance the sensitivity to the sought parameters. An increase of both eigenvalues can lead to a decrease of this ratio, which means that the optimized

4.2. APPROPRIATE MODELING OF THE SPECIMEN SHAPE OPTIMIZATION PROBLEM

experiment may be less sensitive to the sought constitutive parameters. Graphically, with the example of Figure 4.1, this criterion leads to an ellipse looking more like a circle (because at a minimum, $\frac{\Lambda_{max}}{\Lambda_{min}} = 1$), but it does not affect the size of that circle.

[Bertin et al., 2016] and [Chamoin et al., 2020] suggest that the determinant of $\underline{H}_{FEMU}^{-1}$ can be used as a criterion – they call it the *uncertainty volume*. In this case, all eigenvalues are contained equally in the criterion. But once again, it does not necessarily enhance the sensitivity to all constitutive parameters. As a matter of fact, the optimization procedure can lead to decreasing some eigenvalues and increasing others at the same time. In this case, parameters that were not well identified with the initial experiment can be even less well identified in the optimized experiment. Graphically, with the example of Figure 4.1, this choice results in an ellipse with a smaller surface. Yet it does not prevent the ellipse from getting thinner and longer.

[Bertin et al., 2016] and [Chamoin et al., 2020] minimize the largest $\underline{H}_{FEMU}^{-1}$ eigenvalue. In this case, only the worst parameter sensitivity matters (or the worst correlation between parameters). This choice assures that each constitutive parameter will be identified with an uncertainty that will not be greater than the initial maximum uncertainty. Graphically, this choice makes the circumscribed circle of the ellipse smaller. The shape of the ellipse can vary but its largest semi-axis is necessarily smaller at the end of the optimization than the largest initial semi-axis.

Note that normalizing the constitutive parameters allows comparing the given uncertainties because they are all expressed in percentage of the chosen p_0 value.

It is interesting to mention that none of these criteria take the orientation of the ellipse into account (they only consider the sizes of its axes), and hence they do not consider separately variances on each parameter and correlation between parameters. This correlation is visible in the non-diagonal terms of the covariance matrix, as illustrated in Figure 4.2. Nonetheless, the variance values of the different constitutive parameters cannot be greater than the largest eigenvalue.

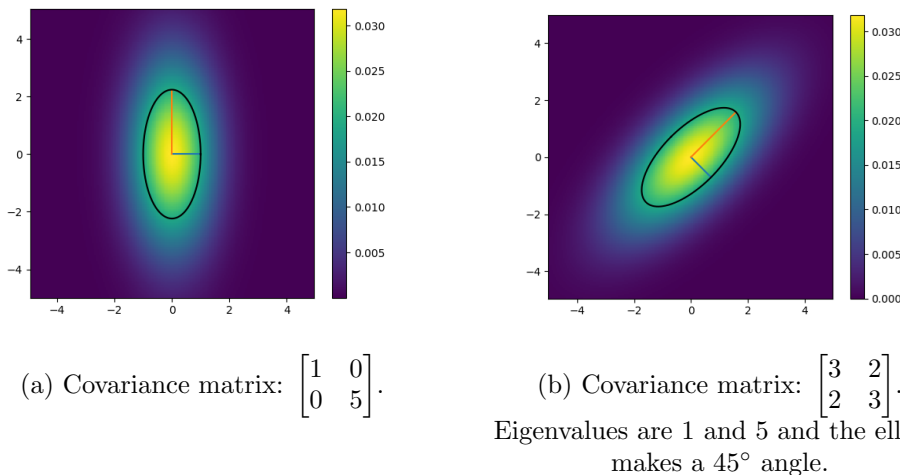


Figure 4.2: Parameter correlation impact on covariance matrices and covariance ellipse.

Of course, the result of the optimization procedure depends on the choice of the cost function. In the light of the above, we chose to minimize the largest eigenvalue

of the covariance matrix. Our cost function is therefore:

$$f_{cost}(\underline{s}) = \max_i \Lambda_i, \quad (4.21)$$

where Λ_i are the eigenvalues of $(\underline{\nabla}_{\mathbf{p}}\mathbf{v}(\underline{s}) \underline{\mathbf{M}}(\underline{s}) \underline{\nabla}_{\mathbf{p}}\mathbf{v}^T(\underline{s}))^{-1}$.

4.2.2 Normalizing coefficient

Since we aim at optimizing the shape of the specimen, its size may change. Consequently, the experimental set-up may have to be adapted, especially the camera position. If the specimen is larger, the camera has to be placed farther away in order to capture the whole region of interest. By doing so, a given physical displacement will lead to a smaller displacement in pixels in the deformed state image. To take this effect into account, we write the $\underline{\mathbf{H}}_u$ matrix by considering physical fields. This novel approach with respect to the literature [Bertin et al., 2016, Chamoin et al., 2020] avoids obtaining a geometry with a greater area to minimize f_{cost} . A greater area indeed affects $\underline{\mathbf{M}}$ without necessarily improving the sensitivity to the sought parameters. To this end, we make the change of variables $\omega_s = \underline{P}(\Omega_s)$, where Ω_s is the physical region of interest on the specimen, and \underline{P} is the camera projector model (see Equation (4.23) below). To improve readability, we redefine $\underline{\mathbf{N}}$ to be FE shape functions in the physical ROI Ω_s , as if we had written $\underline{\mathbf{N}} \circ \underline{P}^{-1}$ instead of $\underline{\mathbf{N}}$ in all the previous equations where quantities are defined in the image. $\underline{\mathbf{H}}_u$ becomes:

$$\underline{\mathbf{H}}_u \approx \frac{G_I^2}{2} \int_{\Omega_s} |\det(\underline{\nabla}P)| \underline{\mathbf{N}}^T \underline{\mathbf{N}} dX. \quad (4.22)$$

Considering a pin-hole camera model (see, *e.g.*, page 10 of [Garcia, 2001]), which is a low order camera model, it is possible to express $\underline{\nabla}P$. The pinhole model states:

$$\underline{P} : X, Y \mapsto x = -f_x \frac{X}{Z} + x_0, \quad y = -f_y \frac{Y}{Z} + y_0, \quad (4.23)$$

where f_x and f_y , in pixels, are the camera focal sampling parameters along the 2 image directions, Z is the distance between the specimen and the camera, and x_0 and y_0 are the center of the image (in pixels). The projector gradient can then be obtained:

$$\underline{\nabla}P = \begin{bmatrix} -\frac{f_x}{Z} & 0 \\ 0 & -\frac{f_y}{Z} \end{bmatrix}. \quad (4.24)$$

$\underline{\mathbf{H}}_u$ thus reads:

$$\underline{\mathbf{H}}_u \approx \frac{f_x f_y}{Z^2} \int_{\Omega_s} \underline{\mathbf{N}}^T \underline{\mathbf{N}} dX. \quad (4.25)$$

We get the mass matrix with a weighting coefficient. f_x and f_y depend on the focal length F with a parameter k_x (resp. k_y) that is intrinsic to the camera (it corresponds to a number of pixels per meter on the sensor), such that $f_x = k_x F$ (resp. $f_y = k_y F$) (see again page 10 of [Garcia, 2001]).

By application of Thales theorem (see Figure 4.3), and assuming that (i) pictures are always taken so as to maximize the images resolution on the ROI and (ii) $k_x = k_y$, the coefficient $\frac{f_x f_y}{Z^2}$ can be linked to the surface S of the ROI thanks to the camera sensor surface S_0 :

$$\frac{f_x f_y}{Z^2} = \frac{k^2 F^2}{Z^2} = k^2 \frac{S_0}{S}. \quad (4.26)$$

4.2. APPROPRIATE MODELING OF THE SPECIMEN SHAPE OPTIMIZATION PROBLEM

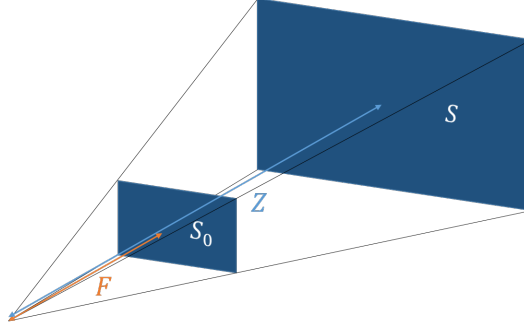


Figure 4.3: Camera sensor (surface S_0) at a distance F (focal length) from the camera reference origin, and pictured surface (surface S) at a distance Z of the camera reference origin. Inspired from [Garcia, 2001]

S depends on the specimen geometry. Therefore, we add it in our cost function, in the form of the surface of the rectangle that is tangent to the region of interest. In other words, the Λ_i in Equation (4.21) now becomes the eigenvalues of $\left(\frac{1}{S(\underline{s})} \underline{\nabla}_{\underline{\mathbf{p}}} \underline{\mathbf{v}}(\underline{s}) \underline{\mathbf{M}}(\underline{s}) \underline{\nabla}_{\underline{\mathbf{p}}} \underline{\mathbf{v}}^T(\underline{s})\right)^{-1}$. This rectangle choice could be improved by adding knowledge on the sensor dimension ratio. For a single parameter, it reads:

$$f_{cost}(\underline{s}) = S(\underline{s}) \frac{1}{H_{FEMU}(\underline{s})} = S(\underline{s}) \frac{1}{\frac{\partial \underline{\mathbf{v}}^T}{\partial \underline{\mathbf{p}}}(\underline{s}) \underline{\mathbf{M}}(\underline{s}) \frac{\partial \underline{\mathbf{v}}}{\partial \underline{\mathbf{p}}}(\underline{s})}. \quad (4.27)$$

This normalizing coefficient has its importance. Some geometries minimize the cost function better than others without this coefficient, but worse with the coefficient. Figures 4.4 and 4.5 show an example, on a tension beam, of two geometries that lead to different results when using the normalizing coefficient or not. The material is isotropic linear elastic and symmetry Dirichlet boundary conditions are applied on the right and bottom edges. A uniformly distributed tensile load is applied on the left edge (the resultant force is the same in each case). The top edge remains free.

The cost function is defined so as to improve the sensitivity to Young's modulus E , and we used the value of the cost function on the reference geometry shown in Figure 4.4 to normalize the value of the cost function on the two geometries shown Figure 4.5, so its value is around 1. Results with or without the normalizing coefficient are gathered in Table 4.1.

	Without $\frac{1}{S}$	With $\frac{1}{S}$
Rectangle geometry	0.667	0.444
Butterfly geometry	0.345	0.518

Table 4.1: Cost function values for the geometries shown Figure 4.5, with or without $\frac{1}{S}$ normalizing coefficient.

Without the normalizing coefficient, the rectangle geometry (Figure 4.5(a)) minimizes less the cost function than the butterfly geometry (Figure 4.5(b)). The regions that are more sensitive to Young's modulus, namely the left part of the specimen whose displacement is the greatest, are larger than for the rectangular geometry. Yet, the butterfly geometry is higher than the rectangular geometry and would require taking pictures from farther away. Hence, with the normalizing coefficient, the rectangular geometry minimizes more the cost function than the butterfly geometry,

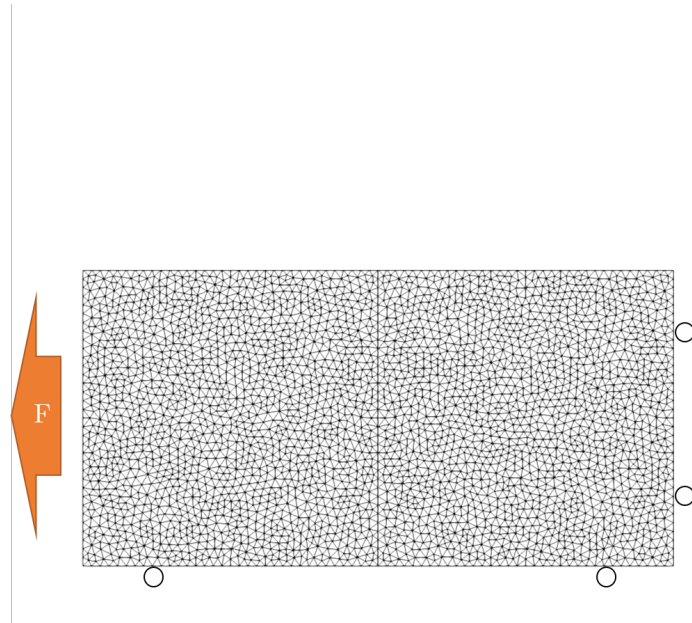
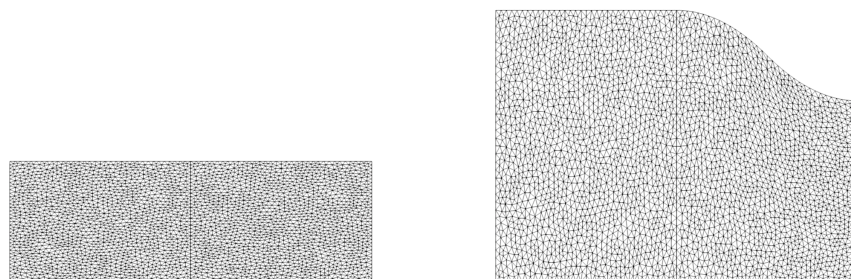


Figure 4.4: Reference geometry (to normalize the cost function so that its value is around 1), and boundary conditions. The material is isotropic linear elastic with Poisson's ratio equal to zero.



(a) Rectangle geometry.

(b) Butterfly geometry.

Figure 4.5: Different tension beam geometries. Their performance with respect to Young's modulus sensitivity depends on the normalizing coefficient S in the cost function.

4.2. APPROPRIATE MODELING OF THE SPECIMEN SHAPE OPTIMIZATION PROBLEM

which is in accordance with the classic specimen shape choice to identify Young's modulus. This simple example indicates that the normalizing coefficient may appear necessary to avoid obtaining large, unadapted geometries.

4.2.3 Restricting to permissible geometries

Although the cost function is now properly determined (see Equations (4.21) and (4.27)), non-physically sound geometry can still appear because of a too large design space. In order to forbid non permissible geometries, we add constraints to our optimization problem.

4.2.3.1 Transformation Jacobian determinant

A typical issue that we want to avoid is the intersection of an edge with itself or another edge (see Figure 4.6). This issue can happen if control points (of the FFD box), whose positions are design variables, cross each other. It results in geometries that have no physical meaning, and some mesh elements can be totally or partially flipped.

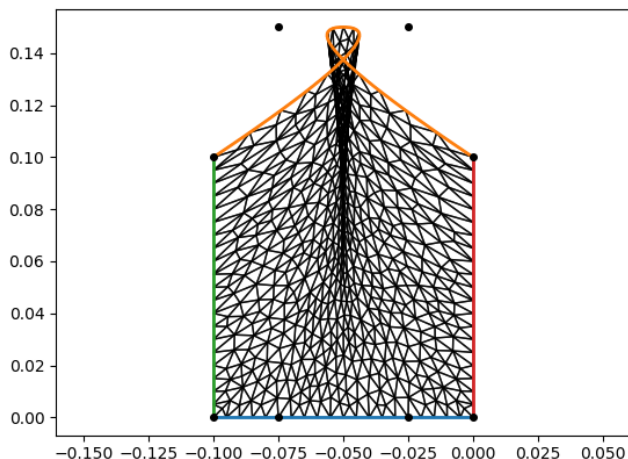


Figure 4.6: Non permissible geometry, due to the loop made by the upper edge.

Flipped elements lead to a transformation Jacobian determinant – transformation that links the reference element to the physical one – that is negative. Therefore, we make use of it to define a constraint function that helps keep this quantity positive at each Gauss point throughout the optimization process. Besides, this quantity is already computed to obtain the stiffness matrix needed for the cost function, so it is possible to benefit from that. Another advantage of this constraint function is that we can set a threshold above zero if we also want to avoid distorted elements. In other words, this constraint also allows ensuring the quality of the mesh. For computation purposes, we normalized the constraint function with the initial values of the transformation Jacobian determinant. The constraint reads:

$$\forall k \in [1..n_{pg}], \quad \frac{(\det(\underline{J}(\underline{s})))_k}{(\det(\underline{J}^{(0)}))_k} \geq \epsilon_{Jac} , \quad (4.28)$$

where n_{pg} is the number of Gauss points in the FE model, $(\det(\underline{J}))_k$ is the transformation Jacobian determinant at Gauss point k , $(\det(\underline{J}^{(0)}))_k$ is the initial transformation Jacobian determinant at Gauss point k , and ϵ_{Jac} is the chosen threshold.

4.2.3.2 Specimen integrity

We consider tests for the identification of elastic constitutive law parameters. In this work, only the shape is optimized. Boundary conditions are fixed during the optimization process. In order to get a geometry that will not cause the specimen to break during the experiment, we have to set a maximum equivalent stress that should not be outreached. This equivalent stress can be computed thanks to the displacement field $\underline{\mathbf{v}}$ that can be retrieved from the cost function sensitivity field computations (see Equation (4.15) where $\underline{\mathbf{v}}$ also has to be computed to get $\underline{\mathbf{v}}_{,p}$). Hence, the second constraint function takes into account the equivalent stress values on the specimen under load, and these values should remain below a given threshold σ_{max} . Once again, we normalize the studied quantity with its initial value. The constraint thus reads:

$$\forall k \in [1..n_{pg}], \quad \frac{(\sigma_{eq})_k(\underline{\mathbf{s}})}{(\sigma^{(0)})_k} \leq (\epsilon_\sigma)_k, \quad (4.29)$$

where $(\sigma_{eq})_k$ is the equivalent stress value at the Gauss point k , $(\sigma^{(0)})_k$ is the initial equivalent stress value at the Gauss point k , and $(\epsilon_\sigma)_k = \frac{\sigma_{max}}{(\sigma^{(0)})_k}$. Here, the threshold is noted ϵ_σ to make a parallel with the other constraint function, but it is not meant to be small. In this work, we use the Von Mises equivalent stress (with plane stress assumption, see Equation (4.30) below), but other equivalent stresses could be chosen:

$$\sigma_{eq} = \sqrt{\sigma_{xx}^2 + \sigma_{yy}^2 - \sigma_{xx}\sigma_{yy} + 3\sigma_{xy}^2} \quad (4.30)$$

4.2.3.3 Constraint function formulations

For these constraint functions, several formulations are possible. In the `Scipy` module of `Python`, constraint functions are defined to remain positive throughout the optimization procedure:

$$g(\underline{\mathbf{s}}) \geq 0. \quad (4.31)$$

Note that it is possible to collect values for all Gauss points in a single vector. In that case, there is no ambiguity and all components of the vector must be positive. The simplest formulation is therefore the following:

$$g_{Jac}(\underline{\mathbf{s}}) = \frac{\det(\underline{J}(\underline{\mathbf{s}}))}{\det(\underline{J}^{(0)})} - \epsilon_{Jac} \quad \text{for Jacobian determinant}, \quad (4.32)$$

$$g_\sigma(\underline{\mathbf{s}}) = \epsilon_\sigma - \frac{\sigma_{eq}(\underline{\mathbf{s}})}{\sigma^{(0)}} \quad \text{for the maximum stress}. \quad (4.33)$$

This formulation is the one used in Section 4.2.4. However, with the case studied in Section 4.3.2, this formulation for g_σ leads to results that are not compatible with the constraint function. This issue was solved by replacing the expression of g_σ with the following:

$$g_\sigma(\underline{\mathbf{s}}) = \frac{\sigma^{(0)}}{\sigma_{eq}(\underline{\mathbf{s}})} - \frac{1}{\epsilon_\sigma}. \quad (4.34)$$

The formulation of Equation (4.34) does not yet give consistent results with the following example, which explains that we keep the one of Equation (4.33) for Section 4.2.4. The causes for this issue are not well known. They can come from the

4.2. APPROPRIATE MODELING OF THE SPECIMEN SHAPE OPTIMIZATION PROBLEM

dependence of constraint functions on the design variable (this dependence is difficult to predict in our case), the boundary conditions (Neumann in Section 4.2.4, Dirichlet in Section 4.3.2), or the choice of the geometry part that is being optimized (exterior edges, holes), and they certainly depend on the chosen optimization algorithm. In this work, we used the built-in SLSQP function from `Scipy`.

4.2.4 Validation on a beam

In order to validate our modeling choices of the optimization problem, we first consider the simple tension beam presented in Figure 4.4. In this case, an analytical solution can be found when only the height of the rectangle is a design variable. An isotropic linear elastic material is chosen, with two parameters: the Young's modulus E and the Poisson's ratio ν . Only the sensitivity to the Young's modulus is optimized here.

4.2.4.1 Analytical developments

The beam has a given length L and the design variable is its height h . Symmetry conditions are applied at the bottom and right edges, the upper edge remains free, and the left edge is under uniformly distributed load. We denote by F the resultant force, which is kept constant. The resulting displacement field is the following:

$$u_x(x, y) = \frac{F}{hE}x, \quad (4.35)$$

$$u_y(x, y) = -\frac{\nu F}{hE}y. \quad (4.36)$$

The normalized sensitivity field to the Young's modulus reads:

$$E \frac{\partial u_x}{\partial E} = -\frac{F}{hE}x, \quad (4.37)$$

$$E \frac{\partial u_y}{\partial E} = \frac{\nu F}{hE}y. \quad (4.38)$$

Finally, and according to Equations (4.18) and (4.27), the cost function is defined as follows:

$$f_{cost}(h) = \frac{Lh}{\int_{x=-L}^0 \int_{y=0}^h \frac{F^2 x^2}{h^2 E^2} + \frac{\nu^2 F^2 y^2}{h^2 E^2} dy dx} = \frac{3E^2 h^2}{F^2 (L^2 + \nu^2 h^2)}, \quad (4.39)$$

which we can write, using the initialization value $h = \frac{L}{2}$:

$$f_{cost}(h) = f_{cost}\left(\frac{L}{2}\right) \frac{(4 + \nu^2)}{L^2 + \nu^2 h^2} h^2. \quad (4.40)$$

In practice, we use $\frac{f_{cost}(h)}{f_{cost}(L/2)}$ as a cost function, to normalize it, and so that the initial value is one.

In the following optimization test, we use $\nu = 0$, which simplifies the cost function since in this case:

$$\frac{f_{cost}(h)}{f_{cost}(L/2)} = 4 \frac{h^2}{L^2}. \quad (4.41)$$

If we impose that the stress value should remain below σ_{max} , *i.e.* $\frac{F}{h} \leq \sigma_{max}$, we get the following constraint:

$$h \geq \frac{F}{\sigma_{max}}. \quad (4.42)$$

4.2.4.2 Numerical test

Figure 4.7 shows the optimization result on the tension beam with 1 design variable. The finite difference method was used to compute the different derivatives, but in this case where only one constitutive parameter is to be identified, semi-analytical derivatives could be used as well (see Section 4.2.1.2). The design variable used here is not exactly h but the equivalent vertical displacement of upper control points of a one-element, 1st-degree FFD morphing box, normalized by the initial beam height (which is $L/2$ in our case, with $L = 0.2$ m). The resultant of the applied force is 5×10^4 N and the maximum admissible stress is 3×10^6 Pa. The SLSQP minimization algorithm from `scipy.minimize` is used.

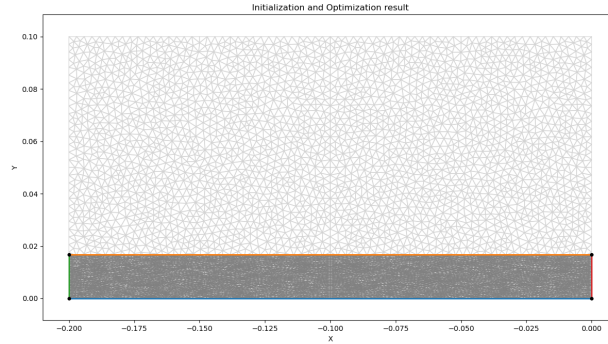


Figure 4.7: Tension beam with a single design variable. Initial geometry in light gray (that normalizes the cost function so that its value starts at 1), and optimized geometry (in gray) with the associated morphing box (colored edges and black control points).

The evolution of the cost function and constraint functions is shown in Figure 4.8. In this example, the final value for the design variable is -0.8333 which leads to an optimal height of 0.01667 (the single design variable controls all upper points). As expected, the cost function is minimized (h is decreased, which is in accordance with Equation (4.41)), and the beam could not be thinner because this height corresponds to the lower bound due to the maximum stress constraint (see Equation (4.42)). The stress state in the beam is now uniform and its value is σ_{max} .

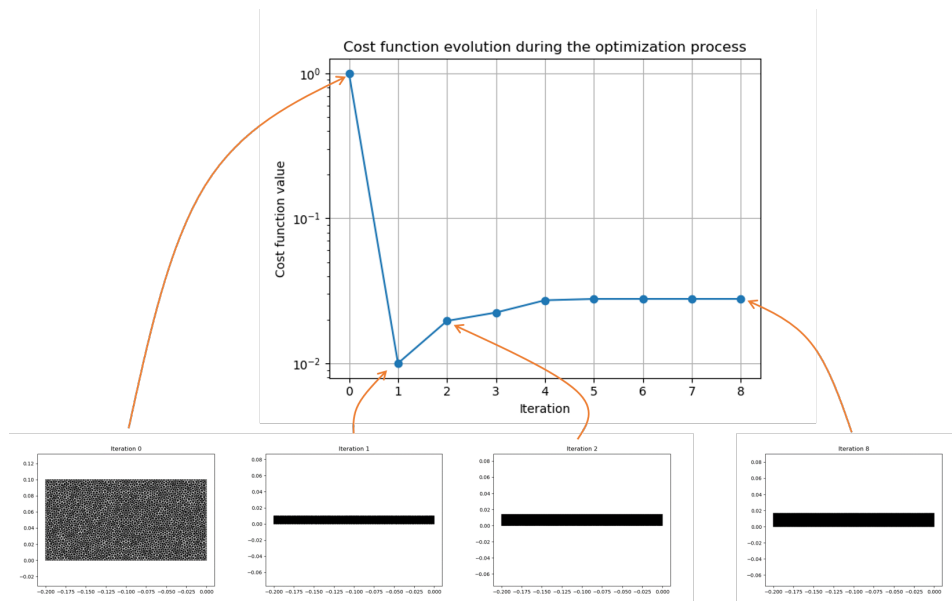
4.2.4.3 Example with more design variables

Figures 4.9 and 4.10 show the results with the same algorithm with more design variables. These design variables were chosen so as to keep the left part upper edge horizontal (to describe the tip of the specimen, see Figure 4.9). To do so, a C^0 line was added at $x = -0.1$ by repeating a knot. C^1 -continuity was then enforced by imposing some control points to move like their neighbors (see Fig. 4.9), hence enforcing tangential directions [Kiendl et al., 2009, Hirschler et al., 2019b].

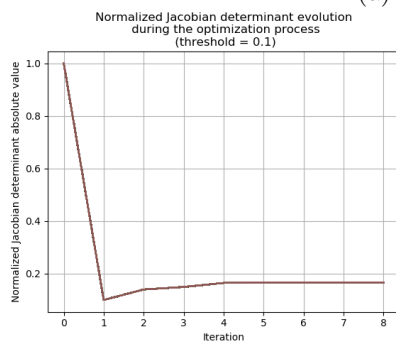
4.2.5 Influence of boundary conditions

When setting a maximum stress σ_{max} that is greater than the initial maximum stress (*i.e.* when choosing $\epsilon_\sigma > 1$), as has been done in the previous example, an important issue remains. The cost function is not only dependent on shape, but also on boundary conditions (BC), via the $\frac{\partial \mathbf{v}}{\partial p}$ term. In a linear elastic context,

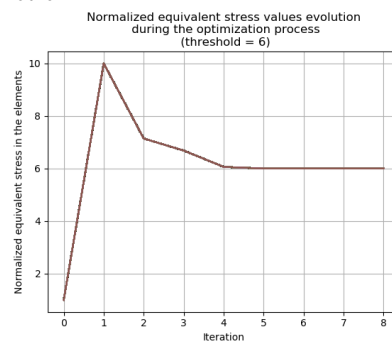
4.2. APPROPRIATE MODELING OF THE SPECIMEN SHAPE OPTIMIZATION PROBLEM



(a) Cost function.



(b) Transformation Jacobian constraint.



(c) Maximum stress constraint.

Figure 4.8: Cost and constraint functions evolution throughout the optimization process for the tension beam with a single design variable.

4.2. APPROPRIATE MODELING OF THE SPECIMEN SHAPE OPTIMIZATION PROBLEM

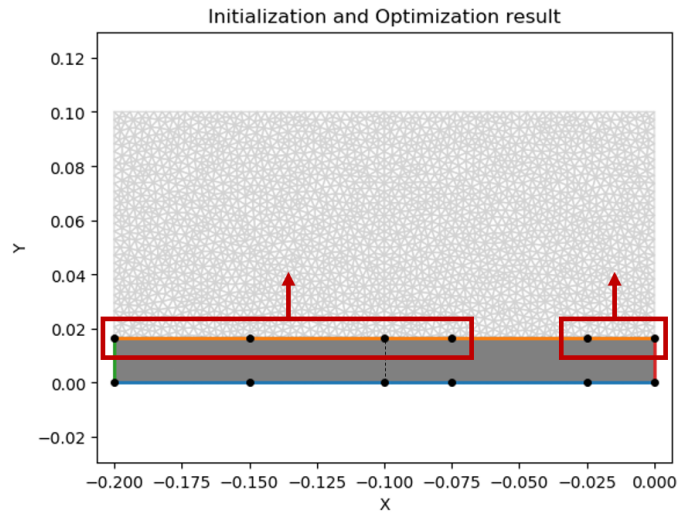


Figure 4.9: Same tension beam optimization problem, two design variables. First design variable: four upper left control points, along y . Second design variable: two upper right control points, along y .

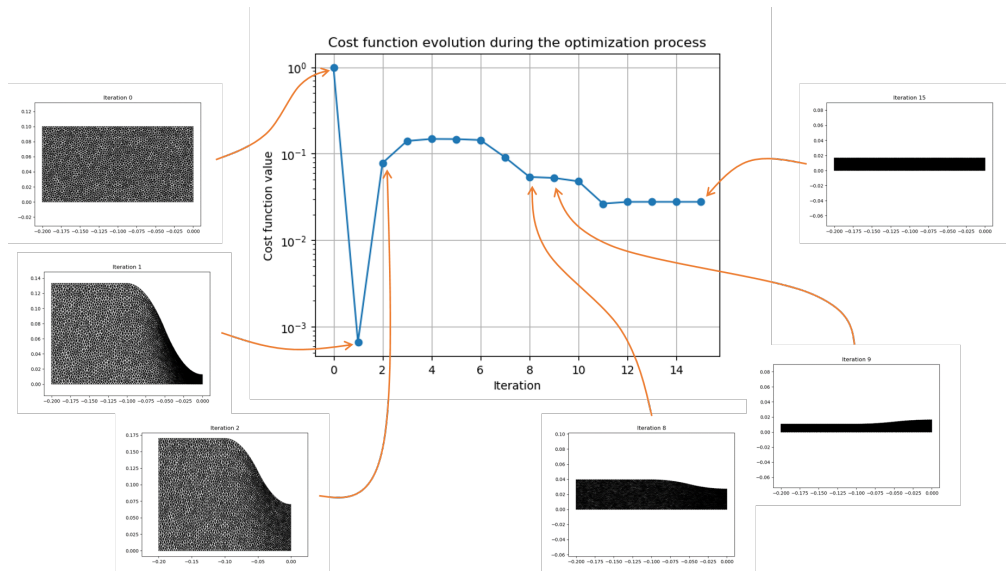


Figure 4.10: Evolution of cost function and geometry throughout the optimization process for the tension beam with two design variables.

4.2. APPROPRIATE MODELING OF THE SPECIMEN SHAPE OPTIMIZATION PROBLEM

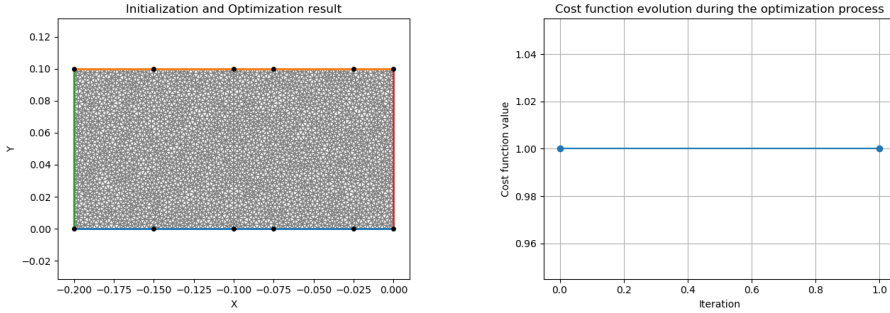
multiplying the BC (applied load or prescribed displacement) intensity by a factor α also multiplies $\underline{\mathbf{v}}$, and thus $\frac{\partial \underline{\mathbf{v}}}{\partial p}$, by α . For a given geometry, the cost function value is divided by α^2 . This observation is particularly relevant for the initial geometry in the optimization process, with regard to the chosen BC. If the maximum initial equivalent stress value $\max_{k \in [1..n_{pg}]} (\sigma^{(0)})_k$ is strictly smaller than σ_{max} , a simple

modification of the BC would lead to a cost function value that is $\left(\frac{\max_{k \in [1..n_{pg}]} (\sigma^{(0)})_k}{\sigma_{max}} \right)^2$

smaller, and the whole mechanical problem would still meet the maximum stress constraint. The issue comes from the fact that this cost function value on the initial geometry could be smaller than the one obtained with the unmodified BC on the final geometry, hence questioning the relevance of performing such an optimization.

To remove the influence of boundary conditions and solve this issue, we chose $\sigma_{max} = \max_{k \in [1..n_{pg}]} (\sigma^{(0)})_k$. As stated above, with this choice, the initial geometry meets the maximum stress constraint. This choice can also be understood as follows: the initial geometry is the one of an existing specimen that is adapted to an experimental set-up, including chosen boundary conditions. Therefore, the optimized specimen should not reach stress values that are greater than those of the initial specimen. In other words, the goal of the optimization process is to improve the geometry with regard to constitutive parameters sensitivity without the material taking a higher amount of stress. As a consequence, ϵ_σ does no longer depend on the Gauss point k and its value is 1.

Applying this choice to the simple tension beam mentioned above with two design variables causes the optimized geometry to be identical to the initial geometry, as expected.



(a) Final geometry (identical to the initial geometry) and FFD morphing box.

(b) Evolution of the cost function. Only one iteration is performed and the geometry is unchanged.

Figure 4.11: Optimization results when setting the maximum admissible equivalent stress equal to the initial one ($\epsilon_\sigma = 1$).

Remark 16 *From our experience, if no other constraint has been reached, the stress constraint is the one that stops the optimization. This could be explained by the fact that making geometries thinner causes displacements to be larger, which reduces the cost function value.*

4.3 Improving a specimen shape with a robust FFD-based optimization strategy

The methodology developed in the previous section for the optimization process can be applied to a more complex specimen. However, the choice of the FFD morphing box may not be as simple as with the rectangular plain beam shown in Figure 4.4. In this section, we propose a way of performing FFD on such more complex specimens, knowing the issues that typically arise in optimization processes. Then, the geometry of holes in a tension beam, inspired from [Feld et al., 2015] (see Figure 4.12), is improved with respect to the sensitivity to orthotropic linear elastic constitutive parameters.

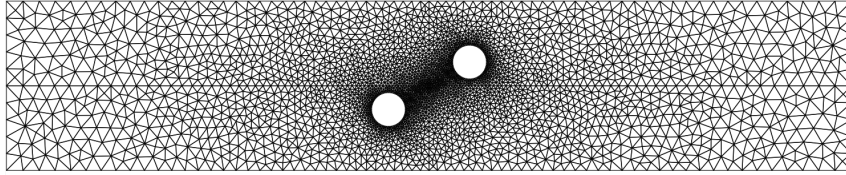


Figure 4.12: Geometry to improve (inspired from [Feld et al., 2015]).

4.3.1 Shape modification with FFD

4.3.1.1 Choice of the FFD morphing box

4.3.1.1.1 Solution 1 The simplest idea, illustrated in Figure 4.13, is to embed the whole specimen FE mesh (or at least, the central part, without the tips) into a single bivariate FFD morphing box, and define which control points are the design variables. The main advantage is that it is possible to deform the whole FE mesh directly with control points, as has been presented in Chapter 3. This choice is well adapted when only the edges of the morphing box matter, typically when they fit the specimen edges (see the rectangular plain beam in Figure 4.7 or the yellow control points in Figure 4.13), or when almost all control points are design variables (as it was the case in Chapter 3). However, for geometrical features that are strictly inside the morphing box, choosing the relevant design variables can be difficult. Some B-spline functions indeed have a support that intersects the feature to be modified, yet without having a significant influence on it. To keep a reasonable number of design variables, it is necessary to select just a few. Since geometry modifications can be important, other control points, which are not design variables, need to be handled as well so they do not interfere with the control points of the (spline) mesh morphing that are design variables. A simple way of doing so is by considering a mechanical problem $\underline{\mathbf{K}} \underline{\mathbf{v}} = \underline{\mathbf{0}}$ to modify the spline mesh with respect to imposed displacement applied on the design control points [Andreoli et al., 2003]. Yet when features are too close from one another, the embedded FE mesh can be severely deteriorated because the morphing box is not refined enough in the in-between region to allow for a nice distribution of FE nodes (see Figure 4.14(a)).

Refining the morphing box can also be an issue because it affects the number of knot spans, and thus control points, on a whole row or column, due to the tensor product that creates the bivariate B-spline functions. Refining the morphing box for a specific feature could affect the morphing box refinement near another feature, and would increase the number of control points. Even though solutions can be found to tackle these issues, such as the use of hierarchical B-spline functions to perform

4.3. IMPROVING A SPECIMEN SHAPE WITH A ROBUST FFD-BASED OPTIMIZATION STRATEGY

local refinement [Kleinendorst et al., 2015, D'Angella et al., 2018], these solutions require additional, potentially long and costly programming.

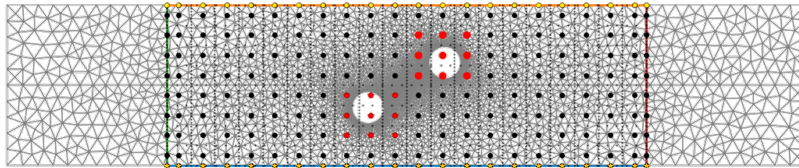
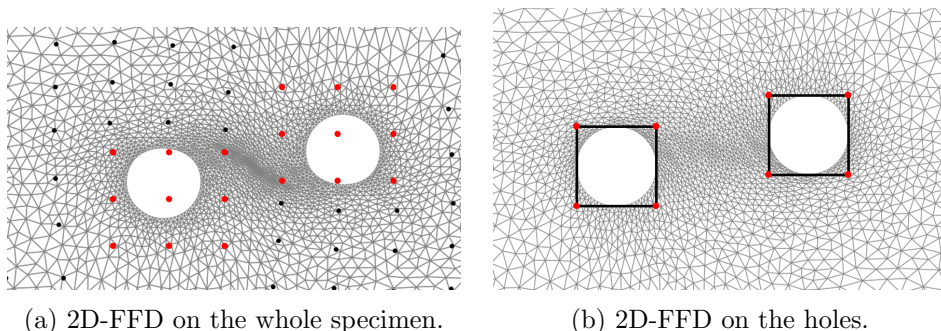


Figure 4.13: FFD morphing box on the whole specimen (except tips). Red dots and stars are the design variables for the holes shape, and yellow dots and stars for the edges. Black dots are the other control points, and small black dots show the spline elements (or knot spans).

4.3.1.1.2 Solution 2 We thus propose to create one morphing box per geometrical feature (see Figure 4.14(b)). First, we considered bivariate rectangle morphing boxes, so as to create an identity mapping between their parametric space and the physical space. However, some of the issues mentioned above still occur in this case, namely the choice of design variables and the handling of other control points. A solution is to consider only 1-element FFD morphing box of low order, which is quite restrictive.



(a) 2D-FFD on the whole specimen.

(b) 2D-FFD on the holes.

Figure 4.14: Comparing the effect on the FE mesh of (a) 2D-FFD on the whole specimen and (b) 2D-FFD on the holes only, for an imposed vertical displacement of the holes. In the first case, the FE mesh is very distorted because the $\underline{\mathbf{K}} \underline{\mathbf{v}} = \underline{\mathbf{0}}$ mesh modification is performed on the spline mesh and very few dof control the region between the holes because the control points around the holes are not dof (their displacement is fixed as they are the design variables that control the holes shapes). In the second case, the $\underline{\mathbf{K}} \underline{\mathbf{v}} = \underline{\mathbf{0}}$ mesh modification is performed on the

FE mesh (richer space, only the FE nodes of the holes edges have their displacement fixed), which allows for a better distribution of FE nodes between the holes.

4.3.1.1.3 Solution 3 To avoid any issue coming from control points that are not design variables, we create a univariate morphing box for each feature. Unlike the two other proposed solutions, and unlike Chapter 3, the FE mesh is not created *a priori* in this case. It is created from the initial morphing box geometry to get the parametric coordinates of FE nodes directly, by setting them first, and avoid solving a possibly non-linear system to find both the morphing box control points

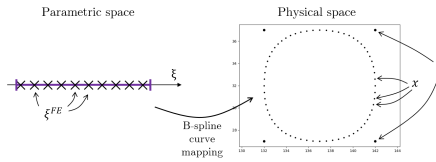
4.3. IMPROVING A SPECIMEN SHAPE WITH A ROBUST FFD-BASED OPTIMIZATION STRATEGY

position and FE nodes parametric coordinates (this problem has been mentioned in Section 3.1.1). Therefore, the morphing box, which is a line, defines the initial geometry for the feature it controls, which is not an issue because in this case the geometry of the specimen is not fixed and neither is the FE mesh.

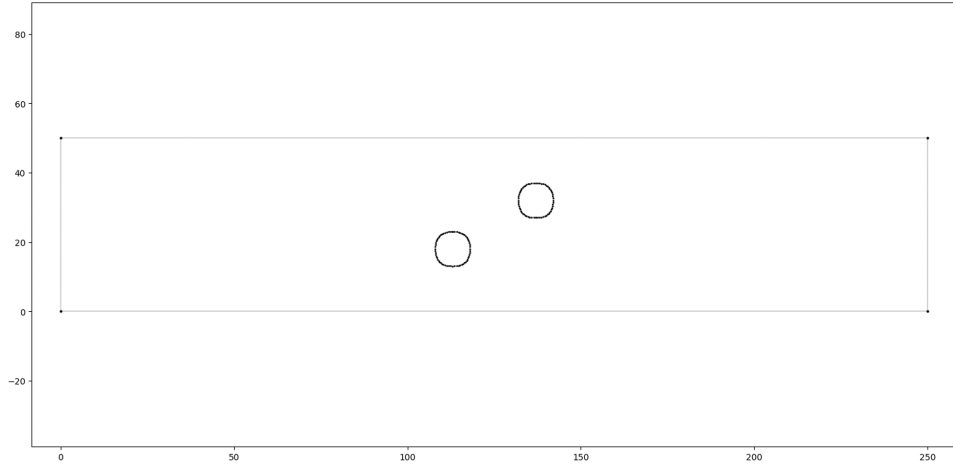
More precisely, to create the initial geometry, we first determine the position and shape of the 1D morphing boxes, that can be periodic in the case of holes. Then, we discretize the parametric domain of each morphing box and compute their images in the physical domain to create FE nodes (see Figure 4.15(a)). A FFD matrix $\underline{\underline{\mathbf{C}}}_{\text{FFD}}$ can be derived from this step, linking the FE nodes physical coordinates to the FFD control points, knowing the FE nodes parametric coordinates:

$$\underline{\mathbf{X}} = \underline{\underline{\mathbf{C}}}_{\text{FFD}}^T (\underline{\xi}^{FE}) \underline{\tilde{\mathbf{X}}}, \quad (4.43)$$

where $\underline{\mathbf{X}}$ and $\underline{\xi}^{FE}$ collect respectively all FE nodes physical and parametric coordinates, and $\underline{\tilde{\mathbf{X}}}$ gathers control points coordinates. These FE nodes are given as boundary inputs to GMSH [Geuzaine and Remacle, 2009] to get the FE mesh of the initial geometry (see Figures 4.15(b) and 4.16). With this technique, all control points have the same influence on the edges they control, which eliminates the issues coming from the choice of design variables and the handling of other control points. Moreover, refinement is easy if needed.



(a) 1D-FFD morphing box control points (4 large points) and position of the controlled FE nodes (small points), which come from the discretization of the B-spline curve.



(b) In black, FE nodes position that are given to GMSH to create the complete FE mesh. In gray, loops that are given as input to GMSH.

Figure 4.15: Construction steps of the mesh. The complete mesh is shown in Figure 4.16.

4.3.1.2 Link between design variables and complete mesh

In some cases, typically to enforce C^1 -continuity where the morphing box is C^0 , it can be necessary to impose that some control point coordinates should vary together

4.3. IMPROVING A SPECIMEN SHAPE WITH A ROBUST FFD-BASED OPTIMIZATION STRATEGY

(see *e.g.* Figure 4.9). In this case, there are less design variables than expected, and we can define a matrix $\underline{\underline{\mathbf{C}}}_{\text{dv}}$ that links the design variables of a morphing box $\tilde{\mathbf{X}}_{hole}^{dv}$ (attached to master control points) to all control points $\tilde{\mathbf{X}}_{hole}$ of the considered morphing box: $\tilde{\mathbf{X}}_{hole} = \underline{\underline{\mathbf{C}}}_{\text{dv}} \tilde{\mathbf{X}}_{hole}^{dv}$.

Similarly to [Feld et al., 2015] and to reduce the number of design variables, the specimen geometry is treated so as to keep the central symmetry, which divides the number of design variables by a factor 2. This symmetry can be expressed in a sparse matrix form $\underline{\underline{\mathbf{C}}}_{\text{Sym}}$ such that $\tilde{\mathbf{X}} = \underline{\underline{\mathbf{C}}}_{\text{Sym}} \tilde{\mathbf{X}}_{hole}$.

Then, once the edges are deformed thanks to the design variables and the symmetry, the whole mesh has to be modified in accordance with this deformation. This procedure is sometimes referred to as *mesh morphing* [Galland et al., 2011]. To do so, as mentioned above, we solve an isotropic linear elastic problem $\underline{\underline{\mathbf{K}}} \underline{\mathbf{v}} = \underline{\mathbf{0}}$ on the FE mesh [Belegundu and Rajan, 1988]. A simple orthotropic linear elastic model is chosen with a unitary Young's modulus ($E = 1$) and a Poisson's ratio equal to zero ($\nu = 0$). The deformation of the edges is considered as an imposed displacement on the corresponding dof, and the goal is to obtain the resulting displacement of all FE nodes, which is the sought mesh modification. This mesh modification can be written in a matrix form, similarly to Guyan reduction in dynamics [Guyan, 1965]. If we note $\underline{\mathbf{v}} = [\underline{\mathbf{v}}_m, \underline{\mathbf{v}}_r]^T$ with $\underline{\mathbf{v}}_m$ the imposed shape modification on the edges and $\underline{\mathbf{v}}_r$ the displacement of the remaining dof, and $\underline{\underline{\mathbf{K}}} = \begin{bmatrix} \underline{\underline{\mathbf{K}}}_{mm} & \underline{\underline{\mathbf{K}}}_{mr} \\ \underline{\underline{\mathbf{K}}}_{rm} & \underline{\underline{\mathbf{K}}}_{rr} \end{bmatrix}$, it is possible to link $\underline{\mathbf{v}}_r$ to $\underline{\mathbf{v}}_m$ as follows:

$$\underline{\mathbf{v}}_r = -\underline{\underline{\mathbf{K}}}_{rr}^{-1} \underline{\underline{\mathbf{K}}}_{rm} \underline{\mathbf{v}}_m. \quad (4.44)$$

Therefore, we denote the associated matrix $\underline{\underline{\mathbf{C}}}_{\text{Guyan}}$ such that $\underline{\mathbf{v}} = \underline{\underline{\mathbf{C}}}_{\text{Guyan}} \underline{\mathbf{v}}_m$:

$$\underline{\underline{\mathbf{C}}}_{\text{Guyan}} = \begin{bmatrix} \mathbf{I} \\ -\underline{\underline{\mathbf{K}}}_{rr}^{-1} \underline{\underline{\mathbf{K}}}_{rm} \end{bmatrix}, \quad (4.45)$$

and we have $\underline{\mathbf{X}}_{all} = \underline{\underline{\mathbf{C}}}_{\text{Guyan}} \underline{\mathbf{X}}$.

From all these steps, we can define a unique matrix $\underline{\underline{\mathbf{C}}}_{\text{modif}}$ that links the design variables to the modification of all FE nodes position:

$$\underline{\underline{\mathbf{C}}}_{\text{modif}} = \underline{\underline{\mathbf{C}}}_{\text{Guyan}} \underline{\underline{\mathbf{C}}}_{\text{FFD}}^T \underline{\underline{\mathbf{C}}}_{\text{Sym}} \underline{\underline{\mathbf{C}}}_{\text{dv}}. \quad (4.46)$$

4.3.2 Optimizing hole shapes

We now apply the developed procedure to the specimen shown in Figure 4.12. To create two 1D FFD morphing box (one for each hole, but only one is used for design variables, the other one is determined thanks to symmetry), we use a B-spline description of the holes geometry (see Figure 4.16). The hole shape is thus not exactly a circle, thus the initialization geometry is slightly different from the geometry that we aim to improve, but the cost function value and the maximum equivalent stress have similar values in both geometries, which justifies the choice of this geometry as an initial geometry.

The goal is to improve this geometry with respect to its sensitivity to the four orthotropic linear elastic constitutive parameters, namely the longitudinal Young's modulus E_1 , the transverse Young's modulus E_2 , the shear modulus G_{12} and the Poisson's ratio ν_{12} . Similarly to [Feld et al., 2015], we impose Dirichlet boundary conditions and do not use information other than the displacement field. As a consequence, the Young's moduli and the shear modulus cannot be identified as such (a simple example on a rectangular plain beam where $u_x = x u_{imp}/L$ and

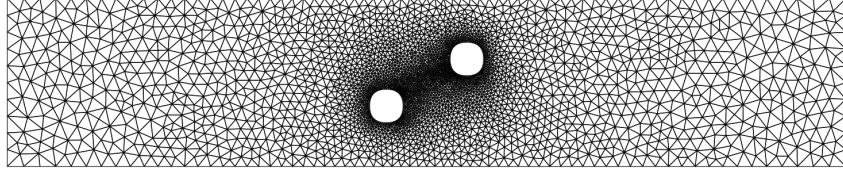


Figure 4.16: Initial geometry with B-spline description of the holes geometry.

therefore is independent of any Young's modulus can help understand the problem). Therefore, the ratios $\frac{E_2}{E_1}$, $\frac{G_{12}}{E_1}$ are used, together with ν_{12} , as constitutive parameters of interest in this example.

As explained in Section 4.2.3.3, the stress constraint function is expressed as in Equation (4.34). Since the initial geometry, with a B-spline description of the holes, is different (even slightly) from the initial geometry with round holes, we take as references for the cost function and the equivalent stress constraint the values coming from the geometry to improve (*i.e.* the one with exact circles), so that the final geometry can effectively be compared to the geometry with circle holes.

4.3.2.1 First optimization phase

The optimization leads to the geometry shown in Figure 4.17, and the deformed morphing box is shown in Figure 4.18. Figure 4.19 shows the evolution of the cost and constraint function. We can see that it is possible to improve the cost function value by a factor 10 without reaching higher equivalent stress values. That means the uncertainty on the worst identified parameters is lowered by approximately 3 and that the same experimental set-up than with the initial specimen can be used, which is of great interest to make the most out of the experiment with regard to constitutive parameters identification.

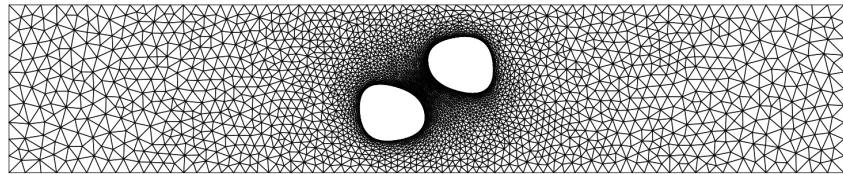


Figure 4.17: Improved geometry after the shape optimization of the holes.

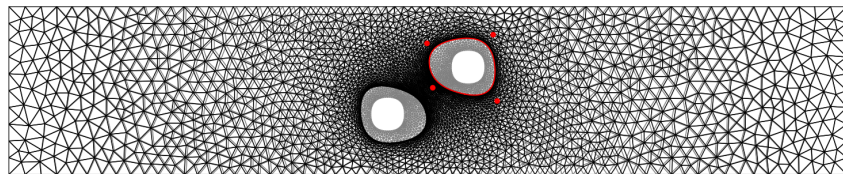
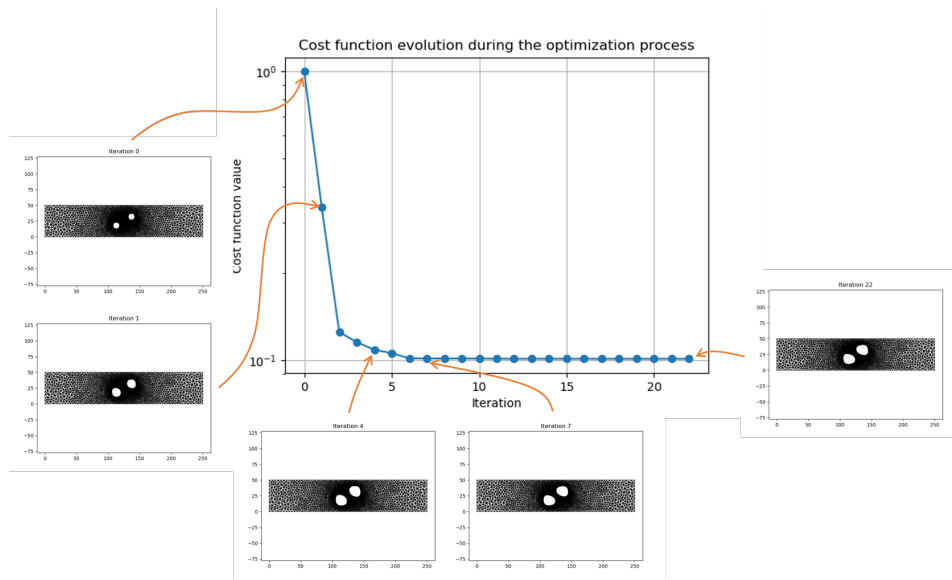
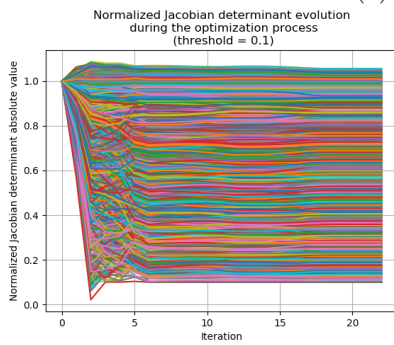


Figure 4.18: Improved geometry (in black) compared to the initial geometry (in gray), and 1D FFD morphing box and its control points position at the end (in red)

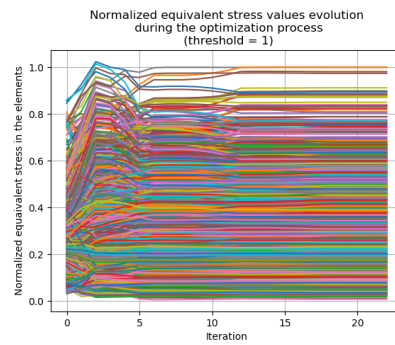
4.3. IMPROVING A SPECIMEN SHAPE WITH A ROBUST FFD-BASED OPTIMIZATION STRATEGY



(a) Cost function.



(b) Transformation Jacobian constraint.



(c) Maximum stress constraint.

Figure 4.19: Cost and constraint functions evolution throughout the optimization process to improve sensitivity to orthotropic linear elastic constitutive parameters by modifying hole shapes.

4.3.2.2 Second optimization phase

We noticed that at the end of the optimization process, the Jacobian constraint is reached (see Figure 4.19). However, this is not due to purely geometrical issues such as loops on the edges, but it comes from the mesh modification that propagates the edges deformation to the rest of the FE nodes. When the edge deformation is too large, solving a $\underline{\mathbf{K}} \underline{\mathbf{v}} = \underline{\mathbf{0}}$ problem can lead to flipped elements, even if the specimen edges remain physically sound (see Figure 4.20). A solution is then to

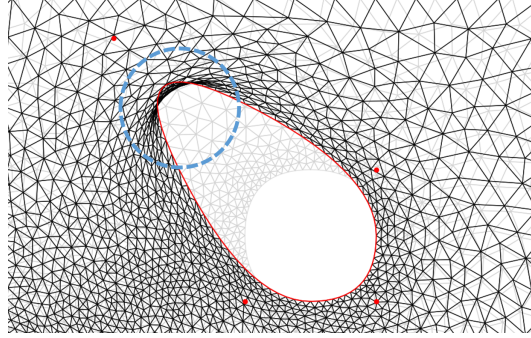


Figure 4.20: Flipped elements when the deformation of the edges is too important (circled in blue).

remesh the interior of the specimen at the end of the optimization process, and to launch another shape optimization on this new mesh. By keeping the same nodes as the old mesh on the edges, in particular for the optimized holes, we can keep the same FFD matrix $\underline{\mathbf{C}}_{\text{FFD}}$ than for the first optimization process. Hence, only $\underline{\mathbf{C}}_{\text{Guyan}}$ is to be recomputed. The results obtained after the second optimization step are shown in Figures 4.21 to 4.23. With the new mesh, it is possible to reach higher deformations and obtain bigger holes. What stops the optimization are bounds that were arbitrarily chosen for the design variables. During this step, the cost function value is reduced by a factor 3, which brings the overall reduction factor up to 30.

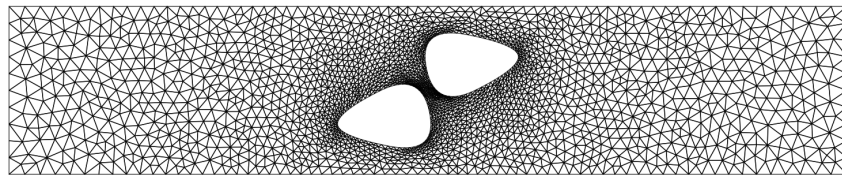


Figure 4.21: Improved geometry after the shape optimization of the holes.

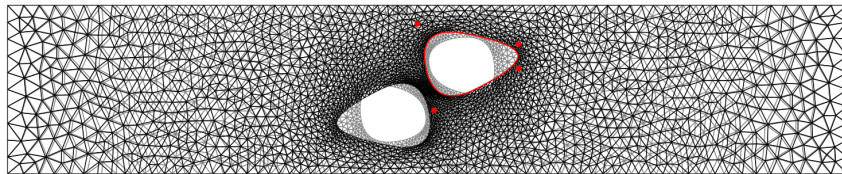
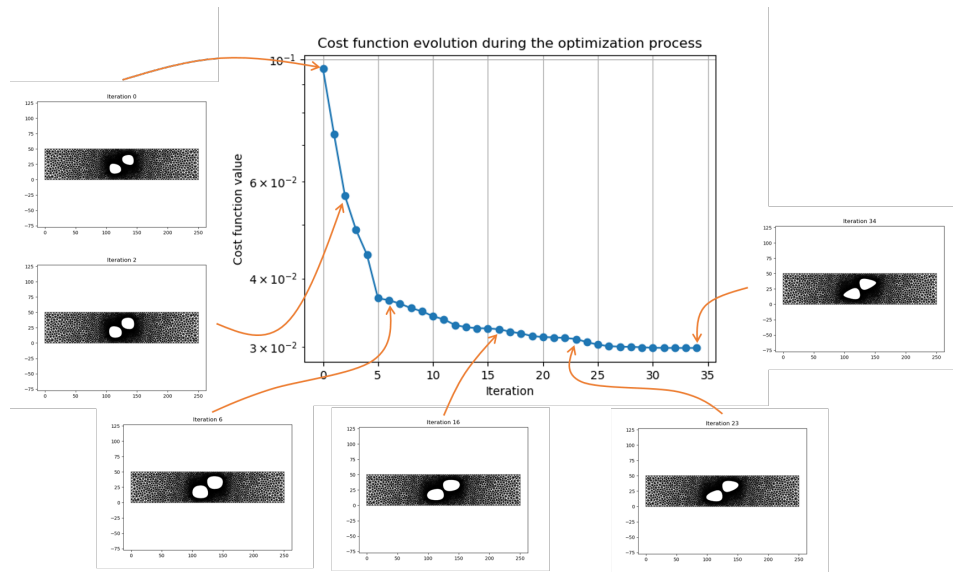
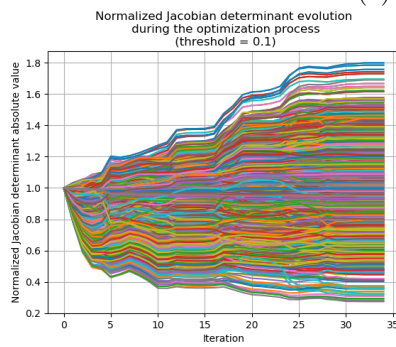


Figure 4.22: Improved geometry (in black) compared to the initial geometry (in gray), and 1D FFD morphing box and its control points position at the end (in red)

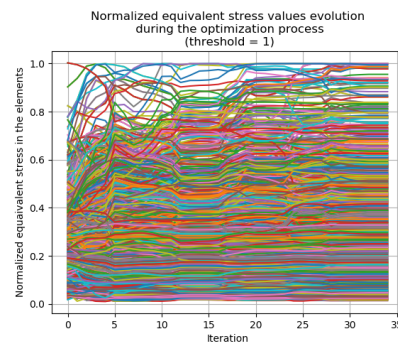
4.3. IMPROVING A SPECIMEN SHAPE WITH A ROBUST FFD-BASED OPTIMIZATION STRATEGY



(a) Cost function.



(b) Transformation Jacobian constraint.



(c) Maximum stress constraint.

Figure 4.23: Cost and constraint functions evolution throughout the second optimization process to improve sensitivity to orthotropic linear elastic constitutive parameters by modifying hole shapes.

4.3.2.3 Overview of the results

To have an overview of how all three parameters sensitivity have been impacted by the optimization process, looking at $\underline{\underline{H}}_{FEMU}^{-1}$ and its eigenvalues is convenient (see Table 4.2). Here, the parameters are rather decoupled (covariance values are small compared to variance values), and the worst initially identifiable parameter is $\frac{E_2}{E_1}$. At the end of the first optimization step, its variance is divided by 10 and parameters are still rather decoupled. At the end of the second optimization step, its variance decreases again. We note that some parameters are now coupled ($\frac{E_2}{E_1}$ and ν_{12}). We also observe that $\frac{G_{12}}{E_1}$ variance decreases at each step, and ν_{12} variance slightly increases, in such a way that the eigenvector associated with the greatest eigenvalue at the last step has its larger component on this constitutive parameter.

Initial geometry	End of 1 st optim. step	End of 2 nd optim. step
$\begin{bmatrix} 27 & -0.50 & -0.047 \\ -0.50 & 1.6 & 0.0072 \\ -0.047 & 0.0072 & 0.31 \end{bmatrix}$	$\begin{bmatrix} 2.6 & -0.28 & 0.24 \\ -0.28 & 0.29 & -0.020 \\ 0.24 & -0.020 & 0.47 \end{bmatrix}$	$\begin{bmatrix} 0.63 & -0.050 & 0.14 \\ -0.050 & 0.14 & -0.017 \\ 0.14 & -0.017 & 0.67 \end{bmatrix}$
0.31 1.5 27	0.26 0.45 2.7	0.14 0.51 0.80
$\begin{bmatrix} 0.0017 & 0.020 & -1.0 \\ -0.0051 & 1.0 & 0.020 \\ 1.0 & 0.0051 & 0.0018 \end{bmatrix}$	$\begin{bmatrix} 0.12 & 0.10 & -0.99 \\ 0.99 & -0.058 & 0.12 \\ -0.046 & -0.99 & -0.11 \end{bmatrix}$	$\begin{bmatrix} 0.099 & 0.74 & -0.66 \\ 1.0 & -0.070 & 0.070 \\ 0.0056 & -0.67 & -0.74 \end{bmatrix}$

Table 4.2: The first line gives $\underline{\underline{H}}_{FEMU}^{-1}$ matrix at each optimization step (the three parameters are in the following order: $\frac{E_2}{E_1}$, $\frac{G_{12}}{E_1}$, ν_{12}). The second line gives $\underline{\underline{H}}_{FEMU}^{-1}$ eigenvalues, and the third line the associated eigenvectors (matrix columns, in the same order the eigenvalues above). (values rounded to 2 digits).

These observations can also be made by looking at the sensitivity fields for each constitutive parameter. Indeed, Figure 4.24 shows that the sensitivity magnitude increase for $\frac{E_2}{E_1}$ and $\frac{G_{12}}{E_1}$, and slightly decrease for ν_{12} .

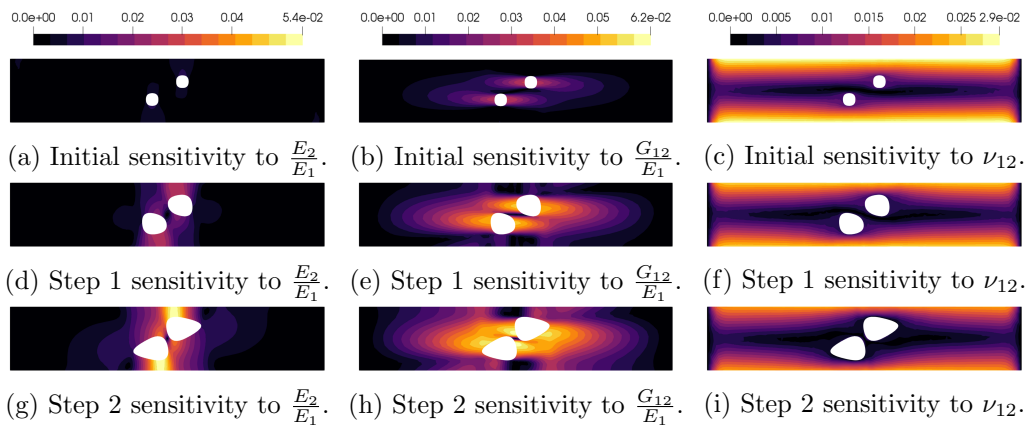


Figure 4.24: Sensitivity fields magnitude for each constitutive parameter, initially and at each optimization step (in mm).

Finally, to visualize the FEMU functional aspect near the exact values of the constitutive parameters, we compute, for a given geometry, $(\mathbf{v}(p_{ex}) - \mathbf{v}(p))^T \frac{\mathbf{M}}{S} (\mathbf{v}(p_{ex}) - \mathbf{v}(p))$, where p_{ex} is the set of exact parameter values (that were chosen to compute all mechanical quantities in the optimization process). The results are shown in

4.3. IMPROVING A SPECIMEN SHAPE WITH A ROBUST FFD-BASED OPTIMIZATION STRATEGY

Figure 4.25. An improvement of the FEMU functional convexity is observed.

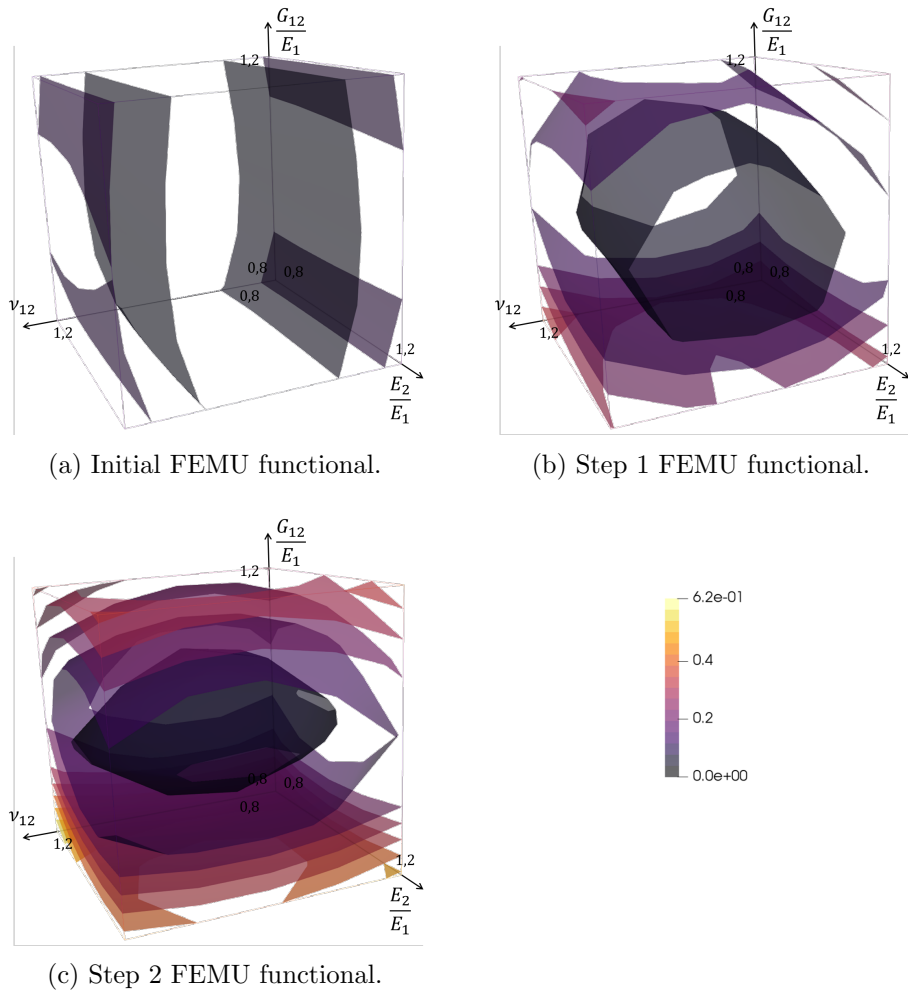


Figure 4.25: FEMU functional improvement after the optimization steps. It is plotted for all parameters that vary between 80% to 120% of their exact value. A greater convexity of the FEMU functional is reached with the optimized geometry.

4.3.3 An ill-posed problem

Despite the use of splines to regularize the optimization problem, its ill-posedness makes the result still very sensitive to initialization (see Figure 4.26), demonstrating the presence of several local minima of comparable objective function values.

To a lesser extent, the results may also depend on other variables such as the FE mesh (especially its discretization size near the holes). Furthermore, the cost function could depend on the choice of the exact constitutive parameter values that we set before the shape optimization. It is therefore recommended to choose numerical exact values close to what we think are the real values.

These observations justify our choice to improve an existing specimen rather than finding the optimal geometry to identify a given set of constitutive parameters. In this respect, we recall that we were able to decrease the uncertainty on the identified constitutive parameters by a factor of 6, which appears of interest for practical applications. In this problem where the evolution of the cost and constraint functions with respect to design variables are very complex (several local minima, high computational costs on fine FE meshes), one could also prefer using other

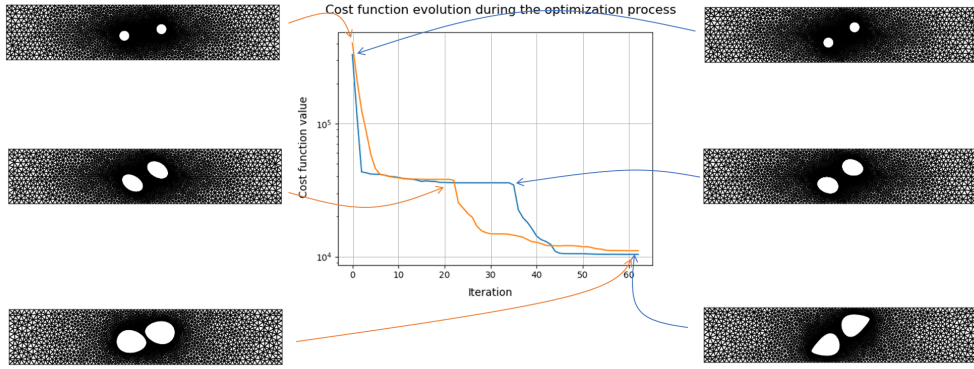


Figure 4.26: Cost function and geometries for a 2-step optimization, for 2 different initializations (initial position of the holes). 2D FFD was used with bivariate 1st-degree morphing boxes.

approaches, such as the use of kriging and surrogate models [Bouhleb et al., 2016] or other optimization algorithms, for instance a genetic algorithm, to avoid being trapped in a local minimum.

Conclusion

In this chapter, a methodology has been proposed to improve the sensitivity of a test to chosen constitutive parameters through shape optimization of the specimen. Our approach relies on the non-invasive spline tools developed in the previous sections and is meant to fill the gap between the existing approaches in terms of design space used in shape optimization problems with regard to constitutive parameters identification. Our FFD-based approach indeed allows working with few design variables, yet keeping a search space that leads to a vast range of geometries, provided that their topology is the same. We placed ourselves in the case where a pre-design of the specimen is available and the goal is to improve its geometry, with respect to the sensitivity to constitutive parameters for given boundary conditions.

For the modeling of the optimization problem, we relied on the cost function formulation of [Bertin et al., 2016] and [Chamoïn et al., 2020], which makes sense from an experimental point of view, because the covariance matrix comes from noise propagation through the whole metrological chain, but also from a physical point of view, because for a single parameter we have shown that the cost function is directly linked to the sensitivity field integral to that parameter, and finally from a mathematical point of view, because the FEMU Hessian eigenvalues contain information on the convexity of the FEMU functional. We then added information coming from the camera modeling to that cost function, in order to tackle possible size changes throughout the optimization process. Furthermore, sensitivity fields, which are the derivatives of the displacement field with respect to constitutive parameters, were computed analytically, *i.e.* without using Finite Differences methods. Constraint functions were also added to ensure that the obtained geometry was physically sound. The first one involved the Jacobian of the FE mesh transformation from the reference elements to the physical element and ensured that no element flipped. The second one set a maximum equivalent stress, which was kept equal to the initial maximum equivalent stress in order to guarantee that the cost function

4.3. IMPROVING A SPECIMEN SHAPE WITH A ROBUST FFD-BASED OPTIMIZATION STRATEGY

decrease could not be impacted by the boundary conditions values. Let us notice at this stage that these modeling ingredients could be applied to other optimization resolution strategies (independently of the design variables definition).

The resolution was then carried out on a tension beam with two holes thanks to our non-invasive FFD-based approach enhanced from Chapter 3 and [Chapelier et al., 2021]. C^1 -continuous periodic B-splines were used to create univariate morphing boxes that control the FE nodes on the edge of each hole. The edge deformation then propagates to the rest of the mesh via the resolution of a $\underline{\mathbf{K}} \underline{\mathbf{v}} = \underline{\mathbf{0}}$ morphing problem so that no remeshing is necessary during the optimization process. The cost function value was reduced by a factor 10. However, this propagation had its limitations, so a second step of optimization was carried out after remeshing to reach a lower cost function value, reducing the cost function value by a factor 3, leading to an overall reduction by a factor 30. Overall, the developed resolution strategy consisted in a CAD-based shape optimization strategy that was weakly invasive with respect to FE method and allowed for considerable geometry deformation. Such a strategy could be applied to other optimization problems (such as structural optimization).

This work offers many opportunities for future investigations. Considering only the resolution of the optimization problem, a multilevel optimization of the shape could be performed, similarly to what has been presented in the previous chapters. Other algorithms or multi-start procedures could also be employed to avoid being too dependent on initialization [Bartoli et al., 2019]. From the problem modeling point of view, a first improvement could consist in making a difference between the region of interest (where a good sensitivity is needed) and the whole structure (on which the mechanical problem is solved). The position and size of the ROI could also be defined as design variables. Boundary conditions could be considered as design variables as well (which is also a perspective from [Bertin et al., 2016]). Finally, more complex constitutive laws could be tested.

General conclusion

Spline functions have shown their potential in the context of the three studied optimization problems, namely FE displacement field measurement using DIC, FE mesh-based 3D shape measurement with stereo-correlation and shape optimization of a mechanical specimen with regard to constitutive parameters identification.

The first chapter has introduced the three problems through the review of recent articles, and highlighted some of their issues. For FE-DIC, the use of what we refer to as analysis-suitable FE meshes, which is necessary for the direct coupling with FE simulation software, leads to noisy results, both for displacement field measurement and shape measurement. The noise comes from the high number of nodes and thus design variables, and from the low regularity between FE elements. In the shape optimization of specimen, parametric optimization does not offer a large variety of geometries, but topology optimization (in particular based on the SIMP method) requires setting cumbersome penalty factors value and proceeding to a tedious post-processing step to get a physically-sound specimen geometry, because there are too many design variables and the edges are not smooth. In all cases, the issues come from the high dimension of the search space together with basis functions that are not regular enough. Spline functions appear to be convenient to tackle these issues. Their high regularity and their other properties such as their local support and their efficient and robust refinement procedures are ideal in a shape optimization context, and more broadly in any regular optimization problem. Furthermore, they are part of the FE vector subspace, which makes the spline basis an excellent candidate for a non-invasive CAD-based approach (we remind here that p^{th} -degree spline functions are C^{p-1} and thus C^0 and not the other way round, which explains that spline functions describe a vector subspace of the FE vector space). A more general FFD-approach is also a useful tool to parameterize fields defined in physical points with splines.

In the second chapter, the developed non-invasive CAD-based strategy is presented and applied to mesh-based 3D shape measurement. The Lagrange extractor (or its approximation in the case of NURBS) is expressed in a global matrix form and applied to DIC shape measurement operators, together with a projection matrix along the normal to avoid shape corrections that do not have a real influence on the geometry. A multilevel approach, which couples coarse graining on images with exact refinement of splines, has led to a faster convergence of the shape measurement algorithm. A specific care has been taken regarding brightness and contrast correction so as to take into account specular reflection on the specimen. The method has been validated on real images of a plate with a hole in two configurations, namely a twisted and a flat configuration. The proposed non-invasive multilevel CAD-based strategy is well suited when a boundary-fitted analysis-suitable CAD description of the structure is available, and has the advantage of providing both the FE solution field and the CAD solution field. It allows performing a true CAD shape measure-

ment simply from the use of classic FE routines. Yet the method is restricted to FE meshes of which the associated vector space is contained within the CAD vector space. Consequently, they have $Q9$ quadrangular elements (and not $Q8$) when 2^{nd} -degree is used.

The third chapter widens the range of possible handled FE meshes to any geometry and element type, and not only FE meshes that come from a boundary-fitted analysis-suitable CAD model. The developed approach, based on the Free-Form Deformation concept, consists in embedding the FE description of the geometry into a spline morphing box. The box has been chosen to be a δ -orthotope, so that the spline mapping from the parametric domain to the physical domain is the identity. This approach can be seen as a generalization of the CAD-based approach and we have shown that it leads to a similar non-invasive scheme, based on a projection onto a smooth space defined by spline functions thanks to a sparse operator. A parallel between the proposed method and a fictitious domain approach, and then with a model reduction approach, has been drawn. Similarly to what is done in the fictitious domain community, we have proposed a criterion to eliminate non-influential design variables that deteriorate the problem conditioning. The proposed criterion is easy and fast to compute because it only depends on sums on the sparse operator coefficients. The FFD-based strategy has been applied both on the displacement field measurement and on the shape measurement with stereo-correlation problems. A comparison with common Tikhonov regularization on the displacement field measurement of a bending beam has shown the FFD strategy potential to avoid adding artifacts, and the simplicity of a regularization length definition. The FFD strategy has then been successfully applied to the plate with a hole of Chapter 2 in the twisted configuration, improving even further the smoothness of the search space thanks to the absence of C^0 lines. Finally, a proof of concept on a more complex 3D structure has been presented, via the shape measurement of a spherical cap. Several significant issues have been addressed on this specific example:

- Images have been taken at 360° all around the structure and thus the functional must take all the images into account. Therefore, a sum over all camera pairs has been done.
- Each camera can only see a part of the structure. A mask has been added to select visible elements for each camera, and the product of these masks selects elements seen by a pair of cameras.
- On an initially planar structure, moving the FE nodes along the normal to the structure is equivalent to moving the FFD control points in the same direction. In the case of more complex 3D structures, defining a normal direction at a control point that is not physically on the surface is not straightforward, and, more importantly, defining these direction on the control points of the coarsest spline model sets the directions on the finest spline model (since we use exact spline refinement). Hence, the normal field has been defined on FE nodes and the control points define a scalar field that is the norm of the shape correction field.
- To define the normal field on the FE nodes, the user can choose to impose "global" or "local" normal directions, depending on the typical sought shape correction length. It is common to seek "global" shape corrections first and then to seek more and more "local" corrections. Here again, a multilevel approach could be carried out in the choice of the normal field (first "global" normal and then "local" normal field).

A final numerical example on an irregular displacement field measurement and based

on DIC residual analysis to refine the morphing box shows the potential of the method to be used on more complex problems. This FFD approach offers the possibility to regularize a field measurement on any arbitrary FE mesh, which is of interest for experimental mechanics engineers that are given a FE mesh to perform the measurement.

The last chapter applied the FFD approach to the shape optimization of a mechanical specimen with regard to constitutive parameters identification. In this case, the morphing box was chosen so that all control points were equally influential. We made it fit the geometry boundaries, and created several, possibly periodic morphing boxes if necessary. An operator that links the control points position to the position of all FE nodes was created, composed of the FFD non-invasive link, a symmetry operator and a Guyan reduction matrix. This global operator was used throughout the optimization procedure and avoids remeshing. Specific care has also been paid to the modeling of the optimization problem:

- The cost function is based on the constitutive parameters covariance matrix (and thus the FEMU hessian), and physically sound approximation have been proposed to take into account the size of the specimen and the fact that the covariance matrix is computed before a specimen and a speckle are defined.
- The sensitivity fields to constitutive parameters are computed analytically.
- A semi-analytical gradient is proposed for the cost function in the case of the identification of a single parameter.
- A constraint function that takes the transformation Jacobian determinant ensures that the FE mesh is still analysis-suitable.
- A constraint function based on maximum equivalent stress values prevents the specimen from being damaged during the experiment and, more importantly, guarantees that the gains in term of constitutive parameters identifiability could not be outperformed by a simple increase in the boundary conditions intensity.

The proposed optimization strategy has been validated on a tension beam and then the shape of holes in an orthotropic linear elastic tension beam has been improved with regard to constitutive parameters identification, leading to a maximum uncertainty on the constitutive parameters values divided by 6.

The obtained results on the three studied optimization problems confirm the ability of splines to be used as a non-invasive regularization method. A CAD-based, or in more general cases, a FFD-based method can be used to replace a too large and irregular search space by a reduced, smooth search space, thanks to an easily built and sparse projection matrix that makes the link between the spline framework and FE software. A multilevel approach can be adopted by simply relying on the exact refinement properties of spline functions. Advantages over other regularization techniques have also been underlined, in particular the direct link between the refinement of a spline mesh and a characteristic regularization length, and the possibility to perform DIC on FE meshes with elements that are too small to allow the measurement with the standard FE functions basis.

This work brings many interesting perspectives for future investigations. In the short term, the developed non-invasive spline-based optimization strategies could be applied to regularize stereo-DIC displacement field measurement and also DVC (Digital Volume Correlation) displacement field measurement. It could also be used

in all FE-DIC problems as an initialization method if another, more problem specific method is preferred to get the final solution. In the longer term, the developed strategies could benefit from hierarchical splines. In FE-DIC displacement field measurement, it would allow measurement of locally richer or less regular deformations [Kleinendorst et al., 2015]. In shape measurement, it could be used on smaller parts or details of the structure that are of interest for the experiment. In both DIC problems, hierarchical splines could be used together with a set of cameras that have different resolutions in order to accurately take into account the higher density of information in some regions of the structure. Regarding the FFD-based approach with the identity mapping, the question could be raised of the orientation of the structure with respect to the morphing box, and its impact on the number of influential control points and on the obtained measured field, especially for complex geometries. Finally, in the three studied optimization problems, a comparison with a RBF-based method (Radial Basis Functions), that can be found in the Computer Graphics Community in the context of shape modification, could be of interest [Kojekine et al., 2002].

Other aspects of the developed optimization strategies that are not related to splines may also provide relevant perspectives. In FE-DIC displacement field and shape measurement, the used brightness and contrast correction becomes less efficient if the FE mesh is fine and cannot be used if the elements are too small. A more physical lighting model could solve this issue [Fouque et al., 2021a]. A second issue encountered during this work was the non-unique solution to the shape measurement / extrinsic calibration problem, which, in some cases, led the edges of the spherical cap to slide on the surface. Hence the resulting shape correction did not take the edges into account. Adding a constraint to keep the FE mesh edges on the structure edges could help solve this issue. The shape optimization problem also raised interesting questions that could not be explored in this work. Since the cost function often contains several local minima, using a minimization algorithm that is not gradient-based could increase the chances of improving the experiment sensitivity to the sought constitutive parameters (see for instance the work of [Bartoli et al., 2019] who developed a constrained gradient-free optimization methodology). Furthermore, other constitutive laws could be tested, potentially non-linear and dependent on load history. Eventually, boundary conditions could be considered as design variables, especially in the case when load histories influence the material response [Bertin et al., 2016].

Appendix A

Appendix

A.1 Interactions between Python and Abaqus

Some details on how we interacted with *Abaqus* from a Python script are given here. It completes Figure 1.20(a) that gives a global overview of a non-invasive implementation of spline-based shape optimization using *Abaqus*.

A.1.1 *Abaqus* job creation

In *Abaqus*, a *job* associates loads and boundary conditions to a mesh-material pair. When defining this *job* on the *Abaqus* user interface, a text file with the `.inp` extension is generated. This text file can also be directly written with Python and given as input to *Abaqus*.

We give here an example of such a file. The `**` sign indicates comments. After a small heading, the mesh is defined, with nodes coordinates and elements connectivity (in this example, 971 nodes and 300 elements were used so we use `[...]` to indicate that the rest of the data is also written in the file). The element type is also given (SR8 for Q8 elements, *i.e.* 2nd-degree quadrangle FE elements with 8 nodes). The shell thickness is written (0.1), as well as the orientation of the reference axes. Groups of nodes and elements are created for the definition of boundary conditions later in the file.

```
*Heading
** Job name: Job-1 Model name: Model-1
** Generated by: authorName
*Preprint, echo=NO, model=NO, history=NO, contact=NO

*Node
    1, 1.2000000000000000e+02, 0.0000000000000000e+00,
      0.0000000000000000e+00
    2, 1.1978888888888889e+02, 6.555555555555554e+00,
      0.0000000000000000e+00
    [...]
*Element, type=S8R
    1, 1, 3, 50, 48, 2, 33, 49, 32
    2, 3, 5, 52, 50, 4, 34, 51, 33
    [...]
*Nset, nset=Set-1, generate
1, 971, 1
*Elset, elset=Set-1, generate
```

```

    1,    300,    1
*Orientation, name=Ori-1
1., 0., 0., 0., 1., 0.
1, 0.
** Section: Section-1
*Shell General Section, elset=Set-1, material=Material-1,
    orientation=Ori-1
0.1,
*Nset, nset=Set-2
941, 942, 943, 944, 945, 946, 947, 948, 949, 950, 951, 952,
    953, 954, 955, 956
957, 958, 959, 960, 961, 962, 963, 964, 965, 966, 967, 968,
    969, 970, 971

```

Now that the mesh is described, a material can be defined, thanks to its associated mechanical properties. The following example is for a orthotropic linear elastic behavior (values of E_1 , E_2 , ν_{12} , G_{12} , G_{13} , G_{23} are given).

```

** MATERIALS
*Material, name=Material-1
*Density
1600.,
*Elastic, type=LAMINA
    230e+9, 15e+09,    0.166, 6432e+06, 6432e+06, 5357e+06

```

The next phase is the definition of Dirichlet boundary conditions. Here, symmetry and anti-symmetry conditions are imposed on two different sets of nodes.

```

** BOUNDARY CONDITIONS
** Name: BC-1 Type: Asym
*Boundary
Set-2, ZASYMM
** Name: BC-2 Type: Sym
*Boundary
Set-3, ZSYMM

```

The final phase consists in defining the loads (and if needed, the loading history) and the requested calculations. Here, two steps are created: one for the generation of the stiffness matrix, the mass matrix and the load vector, and the other for the displacement vector U . All the data are written by *Abaqus* in different text files (see Appendix A.1.3).

```

** STEP: Step-1
*STEP
*MATRIX GENERATE, STIFFNESS, MASS, LOAD
*MATRIX OUTPUT, STIFFNESS, MASS, LOAD
*INCLUDE, INPUT=Example_load.inp
*END STEP

```

```

*STEP
*STATIC
*INCLUDE, INPUT=Example_load.inp
** OUTPUT REQUESTS
** FIELD OUTPUT: F-Output-1

```

```
*Output, field, variable=PRESELECT
** HISTORY OUTPUT: H-Output-1
*Output, history, variable=PRESELECT
*FILE FORMAT, ASCII
*NODE FILE
U
*END STEP
```

The line that starts with `INCLUDE` calls another `.inp` file. When reading this line, *Abaqus* goes to the called file. In this example, Neumann boundary conditions are defined in this other file. This file does not need a heading and looks like the following:

```
** LOADS
** Name: Load-1    Type: Ponct
*Cload
Set-6, 1, -1000.0
```

Note that a first test case can be created in *Abaqus* user interface to generate an example of `.inp` file and use this file as a base to fill some of the items with a correct syntax, typically the reference orientation, the material description or the boundary conditions definition.

A.1.2 Calling *Abaqus* from Python

To make *Abaqus* run without manually opening the software, we use the Python `os` library. The command we write in the script is the following:

```
os.system('call abaqus job=%s output_precision=full
double=both ask_delete=OFF'% filename)
```

To speed up the computation of the gradient with finite differences, we can compute the numerical derivative of each design variable independently and simultaneously (parallel computing). To do so, a batch file (which is a text file with the `.bat` extension) can be written. It collects the different command lines to execute simultaneously. In our example, one of these lines is similar to the following:

```
call abaqus job=filename output_precision=full double=both
ask_delete=OFF\n
```

When calling *Abaqus* repeatedly, one should pay attention to the time taken by *Abaqus* to run the files. Files cannot be read if their creation is not complete and it may cause errors. Adding a condition to check the existence of a file before reading it solves this issue. The condition can also rely on `.lck` files, that only exist when *Abaqus* is running, or `.odb` files, that are the last created *Abaqus* results files.

A.1.3 Reading *Abaqus* data

The stiffness matrix, the mass matrix and the load vector are written in `.mtx` files with `STIF`, `MASS`, and `LOAD` respectively in the files names. These files allow creating easily sparse matrices with Python.

The displacement vector U can be read from a `.fil` file where the relevant lines start with given characters (for example, `I19I3101I` in our case). If a greater numerical precision is desired, another method consists in writing an *Abaqus python* script to create a file that contains U , (*i.e.* by using Python inside the *Abaqus* software).

Finally, the total mass of the model can be read in a `.dat` file. We used this total mass to add a constraint in the compliance minimization problem of Figures 1.20(a) and 1.20(b).

Notations

Except for a few exceptions, the main notations have been chosen as follows:

- Capital letters for quantities that live in the physical domain;
- Small letters for quantities that live in the images (for DIC);
- Greek letters for the spline parametric domain.

Moreover, quantities that result from a discretization (FE or spline) and that gather many degrees of freedom are generally in bold, and spline quantities written with a tilde.

Finally, all quantities have been underlined with respect to their dimension:

- no line: scalar;
- 1 line: vector;
- 2 lines: matrix.

List of the main notations

p	Spline degree (parts 1, 2, 3)
\underline{p} or p	Constitutive parameters (part 4)
δ	Dimension of the spline parametric domain
D	Dimension of the physical domain
I	Spline parametric domain
m	knot multiplicity
$\underline{\underline{\mathbf{N}}}$	FE standard functions (Lagrange functions)
$\underline{\underline{\tilde{\mathbf{N}}}}$	B-spline functions
$\underline{\underline{\mathbf{R}}}$	Rational Lagrange functions
$\underline{\underline{\tilde{\mathbf{R}}}}$	NURBS functions
$\underline{\underline{\mathbf{X}}}$	FE nodes positions
$\underline{\underline{\tilde{\mathbf{X}}}}$	Spline control points positions
$\underline{\underline{\mathbf{X}}}^W$	Rational Lagrange nodes positions
$\underline{\underline{\xi}}^{FE}$	Positions of FE nodes in the spline parametric domain
$\underline{\underline{\mathbf{U}}}$	Any field defined at FE nodes
$\underline{\underline{\tilde{\mathbf{U}}}}$	Any field defined at spline control points

$\underline{\mathbf{S}}$	Shape correction field defined at the FE nodes
$\underline{\delta\mathbf{S}}$	Descent direction in the FE shape measurement problem
$\tilde{\underline{\mathbf{S}}}$	Shape correction field defined at the control points
$\underline{\delta\tilde{\mathbf{S}}}$	Descent direction in the spline shape measurement problem
$\underline{\mathbf{u}}$	Displacement field defined at the FE nodes
$\underline{\delta\mathbf{u}}$	Descent direction in the FE displacement field measurement problem
$\underline{\underline{\mathbf{H}}}_S$	Hessian approximation of the FE shape measurement problem
$\underline{\mathbf{b}}_S$	Right-hand side of the FE shape measurement problem
$\underline{\underline{\tilde{\mathbf{H}}}}_S$	Hessian approximation of the spline shape measurement problem
$\underline{\tilde{\mathbf{b}}}_S$	Right-hand side of the spline shape measurement problem
$\underline{\underline{\mathbf{H}}}_u$	Hessian approximation of the FE displacement field measurement problem
$\underline{\mathbf{b}}_u$	Right-hand side of the FE displacement field measurement problem
$\underline{\underline{\mathbf{C}}}_{\text{ref}}$	Spline refinement operator (exponents can be added to indicate the refinement levels)
$\underline{\underline{\mathbf{C}}}_{\text{Lag}}$	Lagrange extractor
$\underline{\underline{\mathbf{C}}}_{\text{FFD}}$	FFD projector
$\underline{\underline{\mathbf{C}}}_s$	Combined operator (refinement and FE-spline link) at scale s
Q_i	Criterion to determine the non-influential control points
$\underline{\underline{\mathbf{\Pi}}}_Z$	Restriction matrix to vertical displacements or shape corrections
$\underline{\underline{\mathbf{\Pi}}}_n$	Restriction matrix to normal displacements or shape corrections
\mathcal{F}_u	Functional to minimize in the displacement field measurement problem
\mathcal{F}_S	Functional to minimize in the shape measurement problem
\mathcal{F}_p	Functional to minimize in the FEMU problem
f_{cost}	Cost function to minimize in the shape optimization problem
g	Inequality constraint functions (<i>e.g.</i> g_σ and g_{Jac})
$\underline{\mathbf{s}}$	Design variables
\underline{P}_c	Camera c model (projector from physical space to 2D image)
\underline{J}_c	Jacobian of the projector \underline{P}_c
\underline{p}_c	Camera c parameters
\mathcal{I}	Reference state image (a subscript is added to indicate the camera if needed)
\mathcal{J}	Deformed state image

NOTATIONS

V_c	Mask associated to camera c
$\underline{\underline{H}}_{FEMU}$	Hessian approximation of the FEMU problem
$\underline{\underline{\mathbf{K}}}$	Stiffness matrix
$\underline{\underline{\mathbf{M}}}$	Mass matrix
$\underline{\mathbf{v}}$	FE simulated displacement field

Bibliography

- [Affagard et al., 2017] Affagard, J.-S., Wijanto, F., and Allain, J.-M. (2017). Improving the experimental protocol for a more accurate identification of a given mechanical behaviour in a single assay: Application to skin. *Strain*, 53(5):e12236. *Cited on page 14*
- [Andreoli et al., 2003] Andreoli, M., Ales, J., and Désidéri, J.-A. (2003). Free-form-deformation parameterization for multilevel 3d shape optimization in aerodynamics. *Cited on pages 53, 55, and 100*
- [Balcaen et al., 2017] Balcaen, R., Reu, P., Lava, P., and Debruyne, D. (2017). Stereo-DIC uncertainty quantification based on simulated images. *Experimental Mechanics*, 57(6):939–951. *Cited on pages 1 and 44*
- [Bardinet et al., 1998] Bardinet, E., Cohen, L. D., and Ayache, N. (1998). A parametric deformable model to fit unstructured 3D data. *Computer vision and image understanding*, 71(1):39–54. *Cited on page 53*
- [Bartoli et al., 2019] Bartoli, N., Lefebvre, T., Dubreuil, S., Olivanti, R., Priem, R., Bons, N., Martins, J. R., and Morlier, J. (2019). Adaptive modeling strategy for constrained global optimization with application to aerodynamic wing design. *Aerospace Science and technology*, 90:85–102. *Cited on pages 111 and 116*
- [Bay et al., 1999] Bay, B. K., Smith, T. S., Fyhrie, D. P., and Saad, M. (1999). Digital volume correlation: three-dimensional strain mapping using X-ray tomography. *Experimental mechanics*, 39(3):217–226. *Cited on page 1*
- [Beaubier et al., 2014] Beaubier, B., Dufour, J., Hild, F., Roux, S., Lavernhe, S., and Lavernhe-Taillard, K. (2014). CAD-based calibration and shape measurement with StereoDIC - principle and application on test and industrial parts. *Experimental Mechanics*, 54(3):329–341. *Cited on pages 1, 3, 18, and 32*
- [Belegundu and Rajan, 1988] Belegundu, A. and Rajan, S. (1988). A shape optimization approach based on natural design variables and shape functions. *Computer Methods in Applied Mechanics and Engineering*, 66(1):87–106. *Cited on page 103*
- [Berny et al., 2018] Berny, M., Jailin, C., Bouterf, A., Hild, F., and Roux, S. (2018). Mode-enhanced space-time DIC: applications to ultra-high-speed imaging. *Measurement Science and Technology*, 29(12):125008. *Cited on page 10*
- [Bertin et al., 2015] Bertin, M., Hild, F., Roux, S., Mathieu, F., and Leclerc, H. (2015). Optimization and validation of a cruciform geometry for the identification of elastoplastic models. In *Photomechanics 15 (Delft, NL)*. *Cited on pages 14 and 81*

- [Bertin et al., 2016] Bertin, M. B., Hild, F., and Roux, S. (2016). Optimization of a cruciform specimen geometry for the identification of constitutive parameters based upon full-field measurements. *Strain*, 52(4):307–323.
Cited on pages 2, 14, 15, 81, 84, 85, 87, 88, 89, 90, 110, 111, and 116
- [Besnard et al., 2006] Besnard, G., Hild, F., and Roux, S. (2006). “Finite-element” displacement fields analysis from digital images: application to Portevin–Le Châtelier bands. *Experimental Mechanics*, 46(6):789–803.
Cited on pages 1, 9, 63, 64, and 84
- [Bletzinger, 2014] Bletzinger, K.-U. (2014). A consistent frame for sensitivity filtering and the vertex assigned morphing of optimal shape. *Structural and Multidisciplinary Optimization*, 49(6):873–895.
Cited on page 17
- [Bletzinger, 2017] Bletzinger, K.-U. (2017). Shape optimization. *Encyclopedia of Computational Mechanics Second Edition*, pages 1–42.
Cited on pages 53, 54, 58, and 79
- [Bletzinger et al., 1992] Bletzinger, K.-U., Kimmich, S., and Ramm, E. (1992). Efficient modeling in shape optimal design. *Computing Systems in Engineering*, 2:483–495.
Cited on page 31
- [Borden et al., 2011] Borden, M. J., Scott, M. A., Evans, J. A., and Hughes, T. J. (2011). Isogeometric finite element data structures based on Bézier extraction of NURBS. *International Journal for Numerical Methods in Engineering*, 87(1-5):15–47.
Cited on pages 21, 25, 32, 40, and 41
- [Bouclier, 2020] Bouclier, R. (2020). *Some numerical tools based on IGA for optimization applications in structural mechanics*. HDR, Université Toulouse 3-Paul Sabatier.
Cited on page 22
- [Bouclier and Hirschler, 2021] Bouclier, R. and Hirschler, T. (2021). *IGA: non-conforming coupling and shape optimization of complex multipatch structures*, volume 1st volume of the series: Isogeometric analysis tools for optimization applications in structural mechanics. ISTE-Wiley.
Cited on page 18
- [Bouclier et al., 2019] Bouclier, R., Passieux, J.-C., Tirvaudey, M., Chamoin, L., and Chapelier, M. (2019). Un pont global entre AIG et MEF: Calcul et optimisation de forme, isogéométrique, non-intrusif à partir d’un code EF industriel. In *14e Colloque National en Calcul des Structures*.
Cited on page 26
- [Bouhleb et al., 2016] Bouhleb, M. A., Bartoli, N., Otsmane, A., and Morlier, J. (2016). Improving kriging surrogates of high-dimensional design models by partial least squares dimension reduction. *Structural and Multidisciplinary Optimization*, 53(5):935–952.
Cited on page 110
- [Braibant and Fleury, 1984] Braibant, V. and Fleury, C. (1984). Shape optimal design using B-splines. *Computer Methods in Applied Mechanics and Engineering*, 44(3):247–267.
Cited on pages 3, 17, and 31
- [Chamoin et al., 2020] Chamoin, L., Jailin, C., Diaz, M., and Quesada, L. (2020). Coupling between topology optimization and digital image correlation for the design of specimen dedicated to selected material parameters identification. *International Journal of Solids and Structures*, 193:270–286.
Cited on pages 2, 14, 15, 16, 17, 22, 24, 81, 85, 87, 88, 89, 90, and 110

- [Chapelier et al., 2021] Chapelier, M., Bouclier, R., and Passieux, J.-C. (2021). Free-Form Deformation Digital Image Correlation (FFD-DIC): a non-invasive spline regularization for arbitrary finite element measurements. *Computer Methods in Applied Mechanics and Engineering*, 384:113992. *Cited on pages 10, 53, and 111*
- [Cheng et al., 2002] Cheng, P., Sutton, M. A., Schreier, H. W., and McNeill, S. R. (2002). Full-field speckle pattern image correlation with B-spline deformation function. *Experimental mechanics*, 42(3):344–352. *Cited on pages 18 and 37*
- [Claire et al., 2004] Claire, D., Hild, F., and Roux, S. (2004). A finite element formulation to identify damage fields: the equilibrium gap method. *Int J. Numer Methods Eng*, 61(2):189–208. *Cited on page 12*
- [Cohen et al., 1980] Cohen, E., Lyche, T., and Riesenfeld, R. (1980). Discrete B-splines and subdivision techniques in computer-aided geometric design and computer graphics. *Computer graphics and image processing*, 14(2):87–111. *Cited on pages 17, 19, 31, and 37*
- [Colantonio, 2020] Colantonio, G. (2020). *Stéréo-corrélation d’images numériques éléments finis : de l’étalonnage à l’identification*. PhD thesis, Institut National des Sciences Appliquées de Toulouse (INSA Toulouse). *Cited on pages 36 and 50*
- [Colantonio et al., 2020] Colantonio, G., Chapelier, M., Bouclier, R., Passieux, J.-C., and Marenicé, E. (2020). Noninvasive multilevel geometric regularization of mesh-based three-dimensional shape measurement. *International Journal for Numerical Methods in Engineering*, 121(9):1877–1897. *Cited on pages 1, 10, 12, 13, 31, 36, 50, 54, 58, 63, 64, 66, 71, and 79*
- [Collins et al., 1974] Collins, J. D., Hart, G. C., Hasselman, T., and Kennedy, B. (1974). Statistical identification of structures. *AIAA journal*, 12(2):185–190. *Cited on page 82*
- [Conde et al., 2021] Conde, M., Andrade-Campos, A., Oliveira, M. G., and Martins, J. M. P. (2021). Design of heterogeneous interior notched specimens for material mechanical characterization. *Cited on pages 2, 14, 18, and 81*
- [Cottrell et al., 2009] Cottrell, J., Hughes, T., and Bazilevs, Y. (2009). *Isogeometric analysis: toward Integration of CAD and FEA*. 1st edn. Wiley. *Cited on pages 31 and 46*
- [Cottrell et al., 2007] Cottrell, J.-A., Hughes, T.-J.-R., and Reali, A. (2007). Studies of refinement and continuity in isogeometric structural analysis. *Computer Methods in Applied Mechanics and Engineering*, 196:4160–4183. *Cited on pages 21, 22, 32, and 38*
- [D3518/D3518M, 1994] D3518/D3518M (1994). Standard test method for in-plane shear response of polymer matrix composite materials by tensile test of a +/- 45 degree laminate. Technical report, American Society for Testing and Materials, ASTM. *Cited on pages 2 and 81*
- [Dapogny and Frey, 2014] Dapogny, C. and Frey, P. (2014). An introduction to shape optimization, with applications in fluid mechanics. *Cited on page 18*
- [Decultot, 2009] Decultot, N. (2009). *Formage incrémental de tôle d’aluminium: étude du procédé à l’aide de la mesure de champs et identification de modèles de*

- comportement*. PhD thesis, Université de Toulouse, Université Toulouse III-Paul Sabatier. *Cited on page 13*
- [Demmerle and Boehler, 1993] Demmerle, S. and Boehler, J. (1993). Optimal design of biaxial tensile cruciform specimens. *Journal of the Mechanics and Physics of Solids*, 41(1):143–181. *Cited on page 14*
- [Dubreuil et al., 2016] Dubreuil, L., Dufour, J.-E., Quinsat, Y., and Hild, F. (2016). Mesh-based shape measurements with stereocorrelation. *Experimental Mechanics*, 56(7):1231–1242. *Cited on pages 10, 12, and 72*
- [Dufour et al., 2015a] Dufour, J.-E., Beaubier, B., Hild, F., and Roux, S. (2015a). CAD-based displacement measurements with stereo-DIC. *Experimental Mechanics*, 55(9):1657–1668. *Cited on pages 1, 3, 18, 32, 52, and 62*
- [Dufour et al., 2015b] Dufour, J.-E., Hild, F., and Roux, S. (2015b). Shape, displacement and mechanical properties from isogeometric multiview stereocorrelation. *The Journal of Strain Analysis for Engineering Design*, 50(7):470–487. *Cited on pages 2, 32, and 36*
- [Dufour et al., 2016] Dufour, J.-E., Leclercq, S., Schneider, J., Roux, S., and Hild, F. (2016). 3D surface measurements with isogeometric stereocorrelation—application to complex shapes. *Optics and Lasers in Engineering*, 87:146–155. *Cited on pages 1, 3, 18, 32, 36, 39, 52, 65, 67, and 69*
- [Duvigneau, 2006] Duvigneau, R. (2006). Adaptive parameterization using free-form deformation for aerodynamic shape optimization. *Research Report INRIA*. *Cited on pages 53 and 55*
- [D’Angella et al., 2018] D’Angella, D., Kollmannsberger, S., Rank, E., and Reali, A. (2018). Multi-level Bézier extraction for hierarchical local refinement of isogeometric analysis. *Computer Methods in Applied Mechanics and Engineering*, 328:147–174. *Cited on pages 41 and 101*
- [Elguedj et al., 2011] Elguedj, T., Réthoré, J., and Buteri, A. (2011). Isogeometric analysis for strain field measurements. *Computer Methods in Applied Mechanics and Engineering*, 200(1-4):40–56. *Cited on pages 3, 18, 37, 54, and 62*
- [Etievant et al., 2020] Etievant, D., Quinsat, Y., Thiebaut, F., and Hild, F. (2020). A modal approach for shape defect measurement based on global stereocorrelation. *Optics and Lasers in Engineering*, 128:106030. *Cited on pages 18, 54, and 61*
- [Evans et al., 2015] Evans, E., Scott, M., Li, X., and Thomas, D. (2015). Hierarchical T-splines: Analysis-suitability, Bézier extraction, and application as an adaptive basis for isogeometric analysis. *Computer Methods in Applied Mechanics and Engineering*, 284:1–20. *Cited on page 41*
- [Farin, 2002] Farin, G. (2002). *Curves and surfaces for CAGD: a practical guide*. Morgan Kaufmann Publishers Inc., San Francisco. *Cited on pages 19, 31, and 37*
- [Fedele et al., 2013] Fedele, R., Galantucci, L., and Ciani, A. (2013). Global 2D digital image correlation for motion estimation in a finite element framework: a variational formulation and a regularized, pyramidal, multi-grid implementation. *International Journal for Numerical Methods in Engineering*, 96(12):739–762. *Cited on pages 1 and 63*

- [Fehrenbach and Masmoudi, 2008] Fehrenbach, J. and Masmoudi, M. (2008). A fast algorithm for image registration. *Comptes Rendus Mathématique*, 346(9-10):593–598. *Cited on page 8*
- [Feld et al., 2015] Feld, N., Laeuffer, H., and Roux, S. (2015). Mesure de champs hétérogènes pour l’identification du comportement de matériaux composites stratifiés. In *Comptes-Rendus des JNC 19*. *Cited on pages 2, 14, 15, 81, 85, 88, 100, and 103*
- [Firl et al., 2013] Firl, M., Wüchner, R., and Bletzinger, K.-U. (2013). Regularization of shape optimization problems using FE-based parametrization. *Structural and Multidisciplinary Optimization*, 47(4):507–521. *Cited on page 17*
- [Fouque et al., 2021a] Fouque, R., Bouclier, R., Passieux, J.-C., and Périé, J.-N. (2021a). Photometric DIC: A Unified Framework for Global Stereo Digital Image Correlation based on the Construction of Textured Digital Twins. *Cited on page 116*
- [Fouque et al., 2021b] Fouque, R., Bouclier, R., Passieux, J.-C., and Périé, J.-N. (2021b). Stereo digital image correlation: Formulations and perspectives. *Cited on page 71*
- [Galland et al., 2011] Galland, F., Gravouil, A., Malvesin, E., and Rochette, M. (2011). A global model reduction approach for 3d fatigue crack growth with confined plasticity. *Computer Methods in Applied Mechanics and Engineering*, 200(5-8):699–716. *Cited on page 103*
- [Garcia, 2001] Garcia, D. (2001). *Mesure de formes et de champs de déplacements tridimensionnels par stéréo-corrélation d’images*. PhD thesis, Institut National Polytechnique de Toulouse - INPT. *Cited on pages 8, 10, 33, 70, 90, and 91*
- [Garcia and Orteu, 2001] Garcia, D. and Orteu, J.-J. (2001). 3D deformation measurement using stereo-correlation applied to experimental mechanics. In *Proceedings of the 10th FIG international symposium deformation measurements*, pages 19–22. *Cited on page 1*
- [Geuzaine and Remacle, 2009] Geuzaine, C. and Remacle, J.-F. (2009). Gmsh: A 3-D finite element mesh generator with built-in pre-and post-processing facilities. *International journal for numerical methods in engineering*, 79(11):1309–1331. *Cited on page 102*
- [Gomes Perini et al., 2014] Gomes Perini, L., Passieux, J.-C., and Périé, J.-N. (2014). A multigrid PGD-based algorithm for volumetric displacement fields measurements. *Strain*, 50(4):355–367. *Cited on pages 1 and 63*
- [Gras et al., 2013] Gras, R., Leclerc, H., Roux, S., Otin, S., Schneider, J., and Périé, J.-N. (2013). Identification of the Out-of-Plane Shear Modulus of a 3D Woven Composite. *Experimental Mechanics*, 53(5):719–730. *Cited on page 81*
- [Grediac, 1989] Grediac, M. (1989). Principe des travaux virtuels et identification/principe of virtual work and identification. *Comptes Rendus de l’Académie des Sciences*, 302:1–5. *Cited on page 12*
- [Guyan, 1965] Guyan, R. (1965). Reduction of stiffness and mass matrices. *AIAA Journal*, 3(2):380. *Cited on page 103*

- [Hansbo et al., 2017] Hansbo, P., Larson, M. G., and Larsson, K. (2017). Cut finite element methods for linear elasticity problems. In *Geometrically unfitted finite element methods and applications*, pages 25–63. Springer. *Cited on pages 54 and 57*
- [Hasan Imam, 1982] Hasan Imam, M. (1982). Three-dimensional shape optimization. *International Journal for Numerical Methods in Engineering*, 18:661 – 673. *Cited on page 31*
- [Hild et al., 2002] Hild, F., Raka, B., Baudequin, M., Roux, S., and Cantelaube, F. (2002). Multiscale displacement field measurements of compressed mineral-wool samples by digital image correlation. *Applied optics*, 41(32):6815–6828. *Cited on page 64*
- [Hild and Roux, 2012] Hild, F. and Roux, S. (2012). Comparison of local and global approaches to digital image correlation. *Experimental Mechanics*, 52(9):1503–1519. *Cited on pages 1, 8, and 84*
- [Hirschler et al., 2019a] Hirschler, T., Bouclier, R., Duval, A., Elguedj, T., and Morlier, J. (2019a). The embedded isogeometric Kirchhoff–Love shell: From design to shape optimization of non-conforming stiffened multipatch structures. *Computer Methods in Applied Mechanics and Engineering*, 349:774–797. *Cited on page 53*
- [Hirschler et al., 2019b] Hirschler, T., Bouclier, R., Duval, A., Elguedj, T., and Morlier, J. (2019b). Isogeometric sizing and shape optimization of thin structures with a solid-shell approach. *Structural and Multidisciplinary Optimization*, 59(3):767–785. *Cited on pages 3, 17, 22, 26, 32, 37, 51, 55, and 96*
- [Hojjat et al., 2014] Hojjat, M., Stavropoulou, E., and Bletzinger, K.-U. (2014). The vertex morphing method for node-based shape optimization. *Computer Methods in Applied Mechanics and Engineering*, 268:494–513. *Cited on pages 17 and 53*
- [Horn and Schunck, 1981] Horn, B. K. and Schunck, B. G. (1981). Determining optical flow. In *Techniques and Applications of Image Understanding*, volume 281, pages 319–331. International Society for Optics and Photonics. *Cited on pages 33 and 63*
- [Hughes et al., 2005] Hughes, T. J., Cottrell, J. A., and Bazilevs, Y. (2005). Isogeometric analysis: CAD, finite elements, NURBS, exact geometry and mesh refinement. *Computer Methods in Applied Mechanics and Engineering*, 194(39–41):4135–4195. *Cited on pages 19, 21, 22, and 31*
- [Jailin et al., 2018] Jailin, C., Buljac, A., Bouterf, A., Hild, F., and Roux, S. (2018). Fast 4D tensile test monitored via X-CT: Single projection based Digital Volume Correlation dedicated to slender samples. *Journal of Strain Analysis for Engineering Design*, 53(7):473–484. *Cited on page 10*
- [Jiang et al., 2019] Jiang, Z., Mayeur, O., Witz, J.-F., Lecomte-Grosbras, P., Dequidt, J., Cosson, M., Duriez, C., and Brieu, M. (2019). Virtual image correlation of magnetic resonance images for 3D geometric modelling of pelvic organs. *Strain*, 55(3):e12305. *Cited on pages 3 and 18*
- [Jiang et al., 2015] Jiang, Z., Witz, J.-F., Lecomte-Grosbras, P., Dequidt, J., Duriez, C., Cosson, M., Cotin, S., and Brieu, M. (2015). B-spline Based Multi-organ Detection in Magnetic Resonance Imaging. *Strain*, 51(3):235–247. *Cited on pages 3, 18, and 38*

- [Jorge-Peñas et al., 2015] Jorge-Peñas, A., Izquierdo-Alvarez, A., Aguilar-Cuenca, R., Vicente-Manzanares, M., Garcia-Aznar, J. M., Van Oosterwyck, H., de Juan-Pardo, E. M., Ortiz-de Solorzano, C., and Muñoz-Barrutia, A. (2015). Free form deformation-based image registration improves accuracy of traction force microscopy. *PloS one*, 10(12):e0144184. *Cited on pages 53 and 62*
- [Kavanagh and Clough, 1971] Kavanagh, K. T. and Clough, R. W. (1971). Finite element applications in the characterization of elastic solids. *International Journal of Solids and Structures*, 7(1):11–23. *Cited on pages 12 and 82*
- [Kenway et al., 2010] Kenway, G., Kennedy, G., and Martins, J. (2010). A CAD-free approach to high-fidelity aerostructural optimization. In *13th AIAA/ISSMO multidisciplinary analysis optimization conference*, page 9231. *Cited on pages 28, 53, 54, 55, 72, and 79*
- [Kenway and Martins, 2014] Kenway, G. K. and Martins, J. R. (2014). Multi-point high-fidelity aerostructural optimization of a transport aircraft configuration. *Journal of Aircraft*, 51(1):144–160. *Cited on page 53*
- [Kiendl, 2011] Kiendl, J. (2011). *Isogeometric analysis and shape optimal design of shell structures*. PhD thesis, Technische Universität München. *Cited on pages 8, 17, and 55*
- [Kiendl et al., 2009] Kiendl, J., Bletzinger, K.-U., Linhard, J., and Wüchner, R. (2009). Isogeometric shell analysis with kirchhoff-love elements. *Computer methods in applied mechanics and engineering*, 198(49-52):3902–3914. *Cited on page 96*
- [Kiendl et al., 2014] Kiendl, J., Schmidt, R., Wüchner, R., and Bletzinger, K.-U. (2014). Isogeometric shape optimization of shells using semi-analytical sensitivity analysis and sensitivity weighting. *Computer Methods in Applied Mechanics and Engineering*, 274:148–167. *Cited on pages 8, 17, 22, 23, 26, 32, 37, 38, 39, 51, 55, and 87*
- [Kleinendorst et al., 2015] Kleinendorst, S., Hoefnagels, J., Verhoosel, C., and Ruybalid, A. (2015). On the use of adaptive refinement in isogeometric digital image correlation. *International Journal for Numerical Methods in Engineering*, 104(10):944–962. *Cited on pages 3, 18, 37, 54, 62, 68, 80, 101, and 116*
- [Kojekine et al., 2002] Kojekine, N., Savchenko, V. V., Senin, M., and Hagiwara, I. (2002). Real-time 3D Deformations by Means of Compactly Supported Radial Basis Functions. In *Eurographics (Short Presentations)*. *Cited on page 116*
- [Ladevèze et al., 1994] Ladevèze, P., Nedjar, D., and Reynier, M. (1994). Updating of finite element models using vibration tests. *AIAA journal*, 32(7):1485–1491. *Cited on page 12*
- [Lassila and Rozza, 2010] Lassila, T. and Rozza, G. (2010). Parametric free-form shape design with PDE models and reduced basis method. *Computer Methods in Applied Mechanics and Engineering*, 199(23-24):1583–1592. *Cited on pages 28, 53, and 60*
- [Lava et al., 2020] Lava, P., Jones, E. M., Wittevrongel, L., and Pierron, F. (2020). Validation of finite-element models using full-field experimental data: Levelling finite-element analysis data through a digital image correlation engine. *Strain*, 56(4):e12350. *Cited on page 9*

- [Lavest et al., 1998] Lavest, J.-M., Viala, M., and Dhome, M. (1998). Do we really need an accurate calibration pattern to achieve a reliable camera calibration? In Burkhardt, H. and Neumann, B., editors, *Computer Vision — ECCV’98*, pages 158–174, Berlin, Heidelberg. Springer Berlin Heidelberg. *Cited on page 33*
- [Le et al., 2011] Le, C., Bruns, T., and Tortorelli, D. (2011). A gradient-based, parameter-free approach to shape optimization. *Computer Methods in Applied Mechanics and Engineering*, 200(9-12):985–996. *Cited on page 17*
- [Leclerc et al., 2012] Leclerc, H., Périé, J.-N., Hild, F., and Roux, S. (2012). Digital volume correlation: What are the limits to the spatial resolution? *Mechanics & Industry*, 13(6):361–371. *Cited on pages 10, 63, and 65*
- [Leclerc et al., 2009] Leclerc, H., Périé, J.-N., Roux, S., and Hild, F. (2009). Integrated digital image correlation for the identification of mechanical properties. *Lectures Notes in Computer Sciences*, 5496:161–171. *Cited on page 13*
- [Leclerc et al., 2011] Leclerc, H., Périé, J.-N., Roux, S., and Hild, F. (2011). Voxel-scale digital volume correlation. *Experimental Mechanics*, 51(4):479–490. *Cited on page 10*
- [Lecompte et al., 2007] Lecompte, D., Smits, A., Sol, H., Vantomme, J., and Van Hemelrijck, D. (2007). Mixed numerical–experimental technique for orthotropic parameter identification using biaxial tensile tests on cruciform specimens. *International Journal of Solids and Structures*, 44(5):1643–1656. *Cited on page 14*
- [Lee and Park, 2002] Lee, B.-G. and Park, Y. (2002). Degree elevation of NURBS curves by weighted blossom. *Korean Journal of Computational & Applied Mathematics*, 9(1):151–165. *Cited on pages 21 and 38*
- [Legrain, 2013] Legrain, G. (2013). A NURBS enhanced extended finite element approach for unfitted CAD analysis. *Computational Mechanics*, 52:913–929. *Cited on pages 54 and 57*
- [Lucas and Kanade, 1981] Lucas, B. D. and Kanade, T. (1981). An iterative image registration technique with an application to stereo vision. *IJCAI paper*. *Cited on pages 1 and 8*
- [Lyu and Martins, 2015] Lyu, Z. and Martins, J. R. (2015). Aerodynamic shape optimization of an adaptive morphing trailing-edge wing. *Journal of Aircraft*, 52(6):1951–1970. *Cited on pages 53, 54, 55, and 79*
- [Marussig and Hughes, 2018] Marussig, B. and Hughes, T. J. (2018). A review of trimming in isogeometric analysis: challenges, data exchange and simulation aspects. *Archives of computational methods in engineering*, 25(4):1059–1127. *Cited on page 53*
- [Mathieu et al., 2015] Mathieu, F., Leclerc, H., Hild, F., and Roux, S. (2015). Estimation of elastoplastic parameters via weighted FEMU and integrated-DIC. *Experimental Mechanics*, 55(1):105–119. *Cited on pages 2, 13, 63, 82, and 83*
- [Mendoza et al., 2019] Mendoza, A., Neggers, J., Hild, F., and Roux, S. (2019). Complete mechanical regularization applied to digital image and volume correlation. *Computer Methods in Applied Mechanics and Engineering*, 355:27–43. *Cited on pages 9 and 10*

- [Mitukiewicz and Głogowski, 2016] Mitukiewicz, G. and Głogowski, M. (2016). Cruciform specimen to obtain higher plastic deformation in a gauge region. *Journal of Materials Processing Technology*, 227:11–15. Cited on pages 2 and 13
- [Nagy et al., 2011] Nagy, A. P., Abdalla, M. M., and Gürdal, Z. (2011). Isogeometric design of elastic arches for maximum fundamental frequency. *Structural and Multidisciplinary Optimization*, 43(1):135–149. Cited on pages 22, 32, and 38
- [Nagy et al., 2013] Nagy, A. P., IJsselmuiden, S. T., and Abdalla, M. M. (2013). Isogeometric design of anisotropic shells: optimal form and material distribution. *Computer Methods in Applied Mechanics and Engineering*, 264:145–162. Cited on pages 22, 32, 39, and 55
- [Olhoff et al., 1991] Olhoff, N., Bendsøe, M. P., and Rasmussen, J. (1991). On CAD-integrated structural topology and design optimization. *Computer Methods in Applied Mechanics and Engineering*, 89(1-3):259–279. Cited on pages 17 and 31
- [Orteu, 2009] Orteu, J.-J. (2009). 3-D computer vision in experimental mechanics. *Optics and lasers in engineering*, 47(3-4):282–291. Cited on page 8
- [Passieux, 2015] Passieux, J.-C. (2015). *Quelques outils numériques pour la simulation et la mesure en mécanique des structures*. HDR, Université de Toulouse (Paul Sabatier). Cited on page 8
- [Passieux, 2018] Passieux, J.-C. (2018). Pyxel: an open source FE-DIC library. <https://github.com/jcpassieux/pyxel>. Cited on pages 46 and 64
- [Passieux and Bouclier, 2019] Passieux, J.-C. and Bouclier, R. (2019). Classic and inverse compositional Gauss-Newton in global DIC. *International Journal for Numerical Methods in Engineering*, 119(6):453–468. Cited on pages 35 and 63
- [Passieux et al., 2018a] Passieux, J.-C., Bouclier, R., and Périé, J.-N. (2018a). A space-time PGD-DIC algorithm. *Experimental Mechanics*, 58(7):1195–1206. Cited on page 10
- [Passieux et al., 2018b] Passieux, J.-C., Bouclier, R., and Périé, J.-N. (2018b). A space-time PGD-DIC algorithm: Application to 3D mode shapes measurements. *Experimental Mechanics*, 58(7):1195–1206. Cited on pages 1, 2, and 63
- [Passieux et al., 2015] Passieux, J.-C., Bugarin, F., David, C., Périé, J.-N., and Robert, L. (2015). Multiscale displacement field measurement using digital image correlation: Application to the identification of elastic properties. *Experimental Mechanics*, 55(1):121–137. Cited on pages 9 and 80
- [Passieux and Périé, 2012] Passieux, J.-C. and Périé, J.-N. (2012). High resolution digital image correlation using proper generalized decomposition: PGD-DIC. *International Journal for Numerical Methods in Engineering*, 92(6):531–550. Cited on pages 3, 65, and 67
- [Périé et al., 2009] Périé, J. N., Leclerc, H., Roux, S., and Hild, F. (2009). Digital image correlation and biaxial test on composite material for anisotropic damage law identification. *International journal of solids and structures*, 46(11-12):2388–2396. Cited on pages 2 and 63
- [Piegl and Tiller, 1997] Piegl, L. and Tiller, W. (1997). *The NURBS book*. 2Nd. Springer, New york. Cited on pages 17, 19, 20, 21, 22, 31, 37, and 38

- [Pierré, 2016] Pierré, J.-E. (2016). *Stéréo Corrélation d’Images Numériques Éléments Finis*. PhD thesis, Université de Toulouse; Université Toulouse 3 Paul Sabatier (UT3 Paul Sabatier). *Cited on pages 9, 10, 12, and 32*
- [Pierré et al., 2017] Pierré, J.-E., Passieux, J.-C., and Périé, J.-N. (2017). Finite element stereo digital image correlation: framework and mechanical regularization. *Experimental Mechanics*, 57(3):443–456. *Cited on pages 1, 2, 3, 34, 35, 36, 64, 65, 67, 70, and 72*
- [Pottier et al., 2012] Pottier, T., Vacher, P., Toussaint, F., Louche, H., and Couder, T. (2012). Out-of-plane testing procedure for inverse identification purpose: application in sheet metal plasticity. *Experimental Mechanics*, 52(7):951–963. *Cited on pages 2, 14, and 81*
- [Qian, 2010] Qian, X. (2010). Full analytical sensitivities in NURBS based isogeometric shape optimization. *Computer Methods in Applied Mechanics and Engineering*, 199:2059–2071. *Cited on page 39*
- [Rank et al., 2012] Rank, E., Ruess, M., Kollmannsberger, S., Schillinger, D., and Düster, A. (2012). Geometric modeling, isogeometric analysis and the finite cell method. *Computer Methods in Applied Mechanics and Engineering*, 249:104–115. *Cited on pages 54 and 57*
- [Réthoré, 2010] Réthoré, J. (2010). A fully integrated noise robust strategy for the identification of constitutive laws from digital images. *International Journal for Numerical Methods in Engineering*, 84(6):631–660. *Cited on pages 2, 13, 63, 83, and 84*
- [Réthoré, 2015] Réthoré, J. (2015). Automatic crack tip detection and stress intensity factors estimation of curved cracks from digital images. *International Journal for Numerical Methods in Engineering*, 103(7):516–534. *Cited on pages 54, 61, and 80*
- [Réthoré et al., 2010] Réthoré, J., Elguedj, T., Simon, P., and Coret, M. (2010). On the use of NURBS functions for displacement derivatives measurement by digital image correlation. *Experimental Mechanics*, 50:1099–1116. *Cited on pages 3 and 37*
- [Réthoré et al., 2013] Réthoré, J., Muhibullah, Elguedj, T., Coret, M., Chaudet, P., and Combescure, A. (2013). Robust identification of elasto-plastic constitutive law parameters from digital image using 3D kinematics. *Int. J. Solids and Structures*, 50:73–85. *Cited on page 2*
- [Réthoré et al., 2009a] Réthoré, J., Roux, S., and Hild, F. (2009a). An extended and integrated digital image correlation technique applied to the analysis of fractured samples: The equilibrium gap method as a mechanical filter. *European Journal of Computational Mechanics/Revue Européenne de Mécanique Numérique*, 18(3-4):285–306. *Cited on page 10*
- [Réthoré et al., 2009b] Réthoré, J., Roux, S., and Hild, F. (2009b). An extended and integrated digital image correlation technique applied to the analysis of fractured samples: The equilibrium gap method as a mechanical filter. *European Journal of Computational Mechanics/Revue Européenne de Mécanique Numérique*, 18(3-4):285–306. *Cited on page 67*

- [Robert et al., 2012] Robert, L., Velay, V., Decultot, N., and Ramde, S. (2012). Identification of hardening parameters using finite element models and full-field measurements: some case studies. *The Journal of Strain Analysis for Engineering Design*, 47(1):3–17. *Cited on pages 14 and 81*
- [Rouwane et al., 2021] Rouwane, A., Bouclier, R., Passieux, J.-C., and Périé, J.-N. (2021). Adjusting fictitious domain parameters for fairly priced image-based modeling: Application to the regularization of Digital Image Correlation. *Computer Methods in Applied Mechanics and Engineering*, 373:113507. *Cited on pages 10, 62, and 79*
- [Roux and Hild, 2020] Roux, S. and Hild, F. (2020). Optimal procedure for the identification of constitutive parameters from experimentally measured displacement fields. *International Journal of Solids and Structures*, 184:14–23. *Cited on pages 12, 82, and 83*
- [Roux et al., 2008] Roux, S., Hild, F., Viot, P., and Bernard, D. (2008). Three-dimensional image correlation from X-ray computed tomography of solid foam. *Composites Part A: Applied science and manufacturing*, 39(8):1253–1265. *Cited on page 1*
- [Rueckert et al., 1999] Rueckert, D., Sonoda, L. I., Hayes, C., Hill, D. L., Leach, M. O., and Hawkes, D. J. (1999). Nonrigid registration using free-form deformations: application to breast MR images. *IEEE transactions on medical imaging*, 18(8):712–721. *Cited on page 53*
- [Sacharow et al., 2013] Sacharow, A., Odendahl, S., Peuker, A., Biermann, D., Surmann, T., and Zabel, A. (2013). Iterative, simulation-based shape modification by free-form deformation of the NC programs. *Advances in Engineering Software*, 56:63–71. *Cited on pages 53 and 55*
- [Sacharow et al., 2011] Sacharow, A., Surmann, T., and Biermann, D. (2011). Adaptive free-form deformation for the modification of CAD/CAM data. In *ADVCOMP 2011: The Fifth International Conference on Advanced Engineering Computing and Applications in Sciences*. *Cited on page 53*
- [Schemmann et al., 2018] Schemmann, M., Lang, J., Helfrich, A., Seelig, T., and Böhlke, T. (2018). Cruciform specimen design for biaxial tensile testing of smc. *Journal of Composites Science*, 2(1):12. *Cited on pages 2 and 13*
- [Schillinger and Ruess, 2015] Schillinger, D. and Ruess, M. (2015). The finite cell method: A review in the context of higher-order structural analysis of CAD and image-based geometric models. *Archives of Computational Methods in Engineering*, 22(3):391–455. *Cited on pages 54, 57, 62, and 79*
- [Schillinger et al., 2016] Schillinger, D., Ruthala, P. K., and Nguyen, L. H. (2016). Lagrange extraction and projection for NURBS basis functions: A direct link between isogeometric and standard nodal finite element formulations. *International Journal for Numerical Methods in Engineering*, 108(6):515–534. *Cited on pages 26, 27, 32, 40, 41, 42, and 58*
- [Schmaltz and Willner, 2014] Schmaltz, S. and Willner, K. (2014). Comparison of different biaxial tests for the inverse identification of sheet steel material parameters. *Strain*, 50(5):389–403. *Cited on pages 2 and 14*

- [Scott et al., 2011] Scott, M., Borden, M., Verhoosel, C., Sederberg, T., and J. R. Hughes, T. (2011). Isogeometric finite element data structures based on Bézier extraction of T-splines. *International Journal for Numerical Methods in Engineering*, 88:126 – 156. *Cited on page 41*
- [Sederberg and Parry, 1986] Sederberg, T. W. and Parry, S. R. (1986). Free-form deformation of solid geometric models. In *Proceedings of the 13th annual conference on Computer graphics and interactive techniques*, pages 151–160. *Cited on pages 28 and 53*
- [Serra et al., 2017] Serra, J., Pierré, J.-E., Passieux, J.-C., Périé, J.-N., Bouvet, C., and Castanié, B. (2017). Validation and Modeling of Aeronautical Composite Structures Subjected to Combined Loadings: the VERTEX Project. Part 1: Experimental Setup, FE-DIC Instrumentation and Procedures. *Composite Structures*, 179:224–244. *Cited on page 2*
- [Sotiras et al., 2013] Sotiras, A., Davatzikos, C., and Paragios, N. (2013). Deformable medical image registration: A survey. *IEEE transactions on medical imaging*, 32(7):1153–1190. *Cited on pages 8, 53, and 62*
- [Sun et al., 2005] Sun, Y., Pang, J. H., Wong, C. K., and Su, F. (2005). Finite element formulation for a digital image correlation method. *Applied optics*, 44(34):7357–7363. *Cited on pages 1, 9, and 63*
- [Sutton et al., 2009] Sutton, M., Orteu, J.-J., and Schreier, H. (2009). *Image correlation for shape, motion and deformation measurements: Basic Concepts, Theory and Applications*. Springer, New York, NY (USA). *Cited on page 8*
- [Sutton et al., 2000] Sutton, M. A., McNeill, S. R., Helm, J. D., and Chao, Y. J. (2000). Advances in two-dimensional and three-dimensional computer vision. In *Photomechanics*, pages 323–372. Springer. *Cited on pages 1, 8, and 70*
- [Sutton et al., 1983] Sutton, M. A., Wolters, W., Peters, W., Ranson, W., and McNeill, S. (1983). Determination of displacements using an improved digital correlation method. *Image and vision computing*, 1(3):133–139. *Cited on pages 1 and 8*
- [Sutton et al., 1999] Sutton, M. A., Zhao, W., McNeill, S. R., Helm, J. D., Piascik, R. S., and Riddell, W. T. (1999). Local crack closure measurements: Development of a measurement system using computer vision and a far-field microscope. In *Advances in fatigue crack closure measurement and analysis: second volume, STP 1343*, R. C. McClung and J. C. Newman Jr., eds., pages 145–156. *Cited on page 33*
- [Teschemacher et al., 2018] Teschemacher, T., Bauer, A., Oberbichler, T., Breitenberger, M., Rossi, R., Wüchner, R., and Bletzinger, K.-U. (2018). Realization of CAD-integrated shell simulation based on isogeometric B-Rep analysis. *Advanced Modeling and Simulation in Engineering Sciences*, 5(1):19. *Cited on page 53*
- [Tirvaudey et al., 2019] Tirvaudey, M., Bouclier, R., Passieux, J.-C., and Chamoin, L. (2019). Non-invasive implementation of nonlinear isogeometric analysis in an industrial FE software. *Engineering Computations*. *Cited on pages 18, 26, 27, 32, 40, 41, 42, 43, 54, and 58*
- [Tirvaudey et al., 2017] Tirvaudey, M., Bouclier, R., Passieux, J.-C., Chamoin, L., and Ha-Minh, C. (2017). Méthode d’implémentation non intrusive de

- l'analyse isogéométrique dans un code éléments finis: vers la prédiction de l'endommagement dans les composites. In *Congrès français de mécanique*. AFM, Association Française de Mécanique. *Cited on page 20*
- [Tomičević et al., 2013] Tomičević, Z., Hild, F., and Roux, S. (2013). Mechanics-aided digital image correlation. *The Journal of Strain Analysis for Engineering Design*, 48(5):330–343. *Cited on page 67*
- [Urlick and Marussig, 2017] Urlick, B. and Marussig, B. (2017). Why CAD Surface Geometry is Inexact. *Cited on page 23*
- [Verhoosel et al., 2015] Verhoosel, C.-V., van Zwieten, G.-J., van Rietbergen, B., and de Borst, R. (2015). Image-based goal-oriented adaptive isogeometric analysis with application to the micro-mechanical modeling of trabecular bone. *Computer Methods in Applied Mechanics and Engineering*, 284:138–164. *Cited on pages 62, 79, and 80*
- [Wall et al., 2008] Wall, W. A., Frenzel, M. A., and Cyron, C. (2008). Isogeometric structural shape optimization. *Computer Methods in Applied Mechanics and Engineering*, 197(33-40):2976–2988. *Cited on pages 3, 17, and 22*
- [Wang and Jiang, 2007] Wang, J. and Jiang, T. (2007). Nonrigid registration of brain MRI using NURBS. *Pattern Recognition Letters*, 28(2):214–223. *Cited on pages 53 and 54*
- [Wang et al., 2018] Wang, Y., Wang, Z., Xia, Z., and Poh, L. H. (2018). Structural design optimization using isogeometric analysis: A comprehensive review. *Computer Modeling in Engineering and Sciences*, 117:455–507. *Cited on pages 32 and 51*
- [Wittevrongel et al., 2015] Wittevrongel, L., Lava, P., Lomov, S. V., and Debruyne, D. (2015). A self adaptive global digital image correlation algorithm. *Experimental Mechanics*, 55(2):361–378. *Cited on pages 1 and 63*
- [Xie and Farin, 2004] Xie, Z. and Farin, G. E. (2004). Image registration using hierarchical B-splines. *IEEE Transactions on visualization and computer graphics*, 10(1):85–94. *Cited on pages 37 and 53*
- [Yang, 2021] Yang, J. (2021). 2D Finite Element Global Digital Image Correlation (FE-DIC). https://github.com/jyang526843/2D_FE_Global_DIC. *Cited on page 11*
- [Zhang et al., 2021] Zhang, Y., Coppieters, S., Gothivarekar, S., Van de Velde, A., and Debruyne, D. (2021). Independent validation of generic specimen design for inverse identification of plastic anisotropy. *Cited on pages 2 and 14*